Radiation Damage and Helium Bubble Formation in A-site Deficient $Ca_{1-x}La_{2x/3}TiO_3$ Perovskite Ceramics

Sebastian M. Lawson

A thesis submitted in partial fulfilment of the requirements for the degree of Doctor of Philosophy

The University of Sheffield

Faculty of Engineering

Department of Materials Science and Engineering

June 2018

To my mother Marianne,

thank you.

Contents

Acknowledgements

As suits a man of my character, I would raise a series of toasts.

Firstly, to my funders, the Nuclear FiRST Doctoral Training Centre and the Engineering and Physical Sciences Research Council of the United Kingdom, for making it possible to fulfil this dream.

To my supervisors over the past years, Prof Neil C. Hyatt, Prof Karl R. Whittle and Dr Amy S. Gandy, for the priceless drive, patience and perseverance. Further, to Dr Claire Corkhill, Dr Martin Stennett, Prof Steve E. Donnelly, Dr Graeme Greaves, Dr Rob Harrison, Prof Robert G. Elliman, Dr Nik-Reeves McLaren, Dr Karl Travis, Dr Laura Casey, Dr Daniel Bailey and Dr Kerry Abrams, for support without which this thesis would be incomplete.

For the whisky, Paul, for your charming composure, Colleen, and for the eye-candy, Mehul. For your limitless energy, Steph, for your boundless positivity, Becky, and for the fresh-air, Shishir. For the carbonara, Antonia, for QOTSA, Rita, and for the ale, Dale. For the pizza, Hilmi, for all huge Welshmen, Luke, and of course, for the gin, Silvia. To Mikey, Dan and Sean, because we made it. Finally, to Richard, for your comradeship through all. For the beer, late nights and never-ending support, everyone in the Immobilisation Science Laboratory and elsewhere at the University of Sheffield, past and present.

For the unbreakable solidarity, George, for your indescribable strength, Emily, and for your eternal kindness, Jessica. For your endless charm, Alastair, for your boundless wit, Ricky, and for your timeless friendship, Matthew. For your impassable loyalty, Richard, for your never-ending energy, Jim, and for your effortlessly brilliant distraction, Wesley. To Oliver, Sam and Ellis, for your enduring friendship. For being my rock, my escape and my determination, all of the unmentioned who make the Steel City my home.

To Dr Phil Lightfoot, for unlocking and instilling a passion for research that I will never shake, and for not impaling me.

To my sixth form physics teachers, David Dennis and Dr Paul Jukes, for enlightening a boy from Sheffield with the wonders of the physical world. Without you, none of this happens. This is as much your achievement as mine.

To my brothers, Liam, Steve and Oliver, my sisters-in-law Carolyn, Jess and Claire and my nieces and nephews Ben, Emma, Mia, Isaac and Ruby, for being the foundation of who I am.

To my father, Clive, for your belief and wisdom.

To my mother, Marianne, for your strength and devotion. We made it.

Cheers to you all, I love you eternally.

Abbreviations

c-a: Crystalline-Amorphous

EDS: Electron Dispersive X-ray Spectroscopy

EELS: Electron Energy-loss Spectroscopy

ELNES: Electron Energy-loss Near Edge Spectroscopy

GAXRD: Glancing-angle X-ray Diffraction

HRTEM: High-resolution Transmission Electron Microscopy

IMF: Inert Matrix Fuel

MIAMI: Microscope and Ion Accelerator for Materials Investigation

NRT: Norgett-Robinson-Torrens

PIPS: Precision Ion Polishing System

PKA: Primary Knock-on Atom

PVTEM: Plan-view TEM

SAED: Selective Area Electron Diffraction

SAEDP: Selective Area Electron Diffraction Pattern

SEM: Scanning Electron Microscope

SRIM: Stopping and Ranges of Ions in Matter

STEM: Scanning Transmission Electron Microscope

TEM: Transmission Electron Microscope

XRD: X-ray Diffraction

XTEM: Cross-Sectional Transmission Electron Microscopy

List of Figures

List of Tables

Abstract

Phase transitions within the $Ca_{1-x}La_{2x/3}TiO_3$ A-site deficient perovskite system using XRD and electron diffraction have been identified as *Pbnm* for $0 \leq x \leq 0.5$, *Ibmm* for $x = 0.6$, *I4/mcm* for $x = 0.7$, *Cmmm* for $x = 0.9$, while a single-phase product for the $x = 0.8$ sample could not be confirmed. A-site cation/vacancy ordering was observed in the $x = 0.7$ and 0.9 samples through electron diffraction. Nanocrystallite formation within A-site deficient samples was observed due to low energy Ar^+ ion milling.

Bulk 1 MeV Kr^+ and 5 MeV Au^+ ion implantation of the A-site deficient perovskite system $Ca_{1-x}La_{2x/3}TiO_3$ was undertaken to fluences of 1×10^{15} ions cm^{-2} and 5×10^{14} ions cm^{-2}, respectively. A-site deficiency enhanced resistance to amorphisation has been observed for the $0.2 \leq x \leq 0.4$ region, followed by a reduced resistance to amorphisation region for $x \geq 0.5$. A saturation of radiation damage induced volume swelling was observed for the $x = 0$ and 0.5 samples, while volume swelling was not observed for $x \geq 0.6$ samples. The enhanced resistance to amorphisation observed was not related to structure and is likely directly related to the induction of A-site vacancies.

Helium bubble formation was investigated within the $Ca_{1-x}La_{2x/3}TiO_3$ system, investigated using 6 keV He^+ ion implantation *in-situ* in a TEM. The fluence for observable bubble formation remained within error for the $x = 0$, 0.2 and 0.4 samples, suggesting enhanced resistance to amorphisation supresses helium bubble formation in the $x = 0.2$ and 0.4 samples. Preferential bubble formation was observed within grain boundaries, increasing the required fluence for helium bubble formation in the bulk. The fluence required for helium bubble formation was reduced in the $x = 0.2$ sample when ion implanted at 823 K.

1. Introduction

The perovskite family of materials are suitable for numerous applications. Its chemical flexibility has led to the synthesis of a wide-ranging suite of structures and compositions, receiving interest as anodes for solid oxide fuel cells [1,2], memory storage [3] and dielectric resonators [4]. The occurrence of actinide bearing natural perovskites within the Earth's crust has given rise to the use of perovskite as an actinide bearing ceramic phase for the disposition of high-level nuclear waste [5–11], in particular the large quantity of reprocessed plutonium. As of 2016, the United Kingdom has a high-level waste inventory of 3,000 tonnes [12], while 140 tonnes of civil-grade plutonium is forecast to be stockpiled on completion of the UK's current reprocessing programme [13]. This presents the need for highly durable waste forms to immobilise such waste streams. Perovskite structured ceramics have been extensively studied to this end as part of the SYNROC family of ceramic waste forms [6,14,15], allowing for the immobilisation of several waste streams, including trivalent fuel products.

Furthermore, the next generation of nuclear reactors are being designed with increased levels of radiation when compared with those they will replace. This will include the use of next-generation concept fuels, one example of which is the inert matrix fuel (IMF) [16,17]. The IMF concept allows for the burn-up of fertile material in a reactor core whilst minimising the production of further nuclear waste. Traditional mixed oxide fuel uses ^{238}U mixed with fissile Pu and U as a volumetric safety constraint, leading to a significant amount of ^{239}Pu breading. The IMF concept replaces ^{238}U with a transition metal such as Zr or Ti, to minimise waste production. Post burn-up, the material is already immobilised within a ceramic matrix ready for disposal. Perovskite materials are prime IMF candidates as they readily accommodate actinides, with Pu and U doped $CaTiO_3$, $BaUO_3$ and $ZrUO_3$ all studied to this end [18].

Both potential deployment options involve subjecting materials to highly radiation intensive environments and directly incorporating actinides into a ceramic structure. Radiation damage in such environments has the potential to amorphise materials, leading to volume swelling, cracking and the loss of intrinsically desirable material properties. The recoil nuclei created during the alpha-decay process can dislocate thousands of atoms per decay [19], while the release of helium through alpha decay events presents a further materials challenge for wasteform and fuel performance. The insolubility of noble gases within ceramic materials allows for the agglomeration of helium at point defect sites within the crystalline lattice. At sufficient levels this will lead to inevitable nanoscale helium bubble formation. It is estimated that in current fission reactors the helium concentration in materials is negligible, however considering new reactor types, such as fusion reactors, helium concentration could reach 1 at% over a reactors lifetime [20].

Understanding the fundamental mechanisms that govern radiation damage tolerance will be key to meeting these goals. Perovskites have been reported to exhibit several phenomena when subjected to radiation damage, including undergoing phase transitions. A-site deficient perovskites have been reported to exhibit particularly interesting behaviour. These perovskites formulate with a deficient A-site, that is the inclusion of cation vacancy defects in the intrinsic structure of the material. At certain doping levels, this has been observed to both increase and hinder radiation damage tolerance, however limited research has been conducted into these phenomena. Within this study, the $Ca_{1-x}La_{2x/3}TiO_3$ A-site deficient perovskite system has been synthesised and investigated. The effects of radiation damage have been probed using bulk ion implantation and helium bubble formation has been investigated using ion implantation *in-situ* in a transmission electron microscope (TEM). While such a system is unlikely to be directly employed within a fission or fusion reactor, A-site deficiency may be induced through doping with multivalent elements, and the presence of A-site vacancies within these ceramics allows for fundamental effects that may produce materials with increased resistance to radiation damage to be probed.

This thesis is structured with this introduction (chapter 1) acting as a preface to contextualise the research. Chapter 2 contains a brief introduction to perovskites and radiation damage, and a survey of the relevant literature within the field of research and research aims are given in chapter 3. An experimental methodology is given in chapter 4, followed by characterisation of synthesised $Ca_{1-x}La_{2x/3}TiO_3$ samples prior to ion implantation in chapter 5. A study is presented in chapter 6 reporting the effects of ion milling used as preparation for TEM on the samples. Characterisation of the bulk ion implanted $Ca_{1-x}La_{2x/3}TiO$ samples is presented in chapter 7 and *in-situ* helium ion implantation in chapter 8. Finally, chapter 9 contains the final research conclusions and summary of this thesis, preceding a section on possible future work in chapter 10.

2. Background

2.1 Perovskite

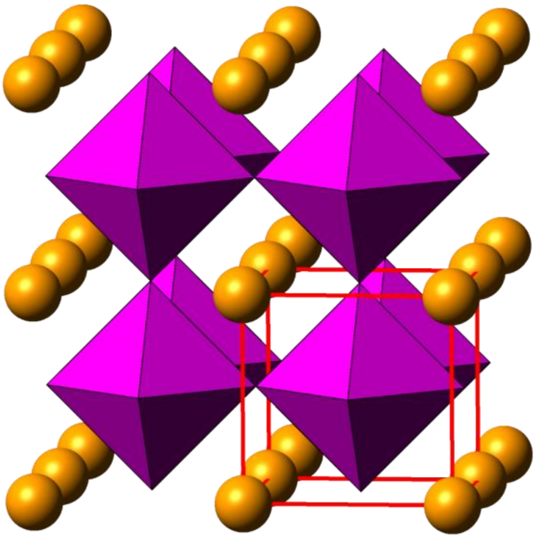

Figure 2.1 The $SrTiO_3$ structure, with TiO_6 octahedra in purple, and Sr^{2+} cations in orange. The unit cell is shown in red. No tilting of TiO_6 octahedra is observed in the tilt system $a^0a^0a^0$.

Perovskite structured materials are denoted by the base oxide structural formula ABO_3, with typical charge configurations $A^{2+}B^{4+}O^{-2}{}_3$, $A^{3+}B^{3+}O^{-2}{}_3$ and $A^{1+}B^{5+}O^{-2}{}_3$. The ideal perovskite structure takes the cubic form with space group *Pm-3m*, exemplified by the aristotype $SrTiO_3$, consisting of a body centred B-site cation and A-site cations located at the unit cell corners with coordination numbers 6 and 12, respectively. The oxygen ions are face-centred to form corner-sharing layered BO_6 octahedra, as visualised by the purple corner sharing octahedra in figure 2.1. Perovskite structures will distort from this ideal structure as the A and B-site cation radii vary. This is governed by the Goldschmidt tolerance factor, *t*, [21] given by

$$t = \frac{(r_A + r_O)}{1.4\,(r_B + r_O)}, \qquad (2.1)$$

where r_A and r_B are the ionic radii of the A and B-site cations, respectively, and r_o the ionic radius of oxygen. As this value drops from t = 1, the structure progressively distorts, as the cubic structure requires a larger A-site cation radius. This causes the BO_6 octahedra to tilt, leading to the formation of non-aristotype perovskites. For example, $SrTiO_3$ has no tilted octahedra in the *Pm-3m* configuration, with t = 1.002, while $MgTiO_3$ (t = 0.747) will not synthesise as a perovskite and instead the ilmenite structure is formed [22,23].

Octahedral tilting is commonly described using Glazer notation [24]. This uses the Cartesian coordinates of the BO_6 octahedra, with the rotations about each axis *x*, *y* and *z* denoted as *a*, *b* and *c*. Each is given a superscript, either positive, negative or zero. A positive superscript indicates an in-phase tilt, i.e. the octahedra in successive layers tilt in the same direction along that axis. Negative indicates an anti-phase tilt, i.e. the rotation in the adjacent layer is opposite to the previous. Zero indicates no rotations about that axis. If the amplitude of tilt in one axis is identical to the next, the notation is carried forward. These relationships are exhibited in figure 2.2 graphically. The first

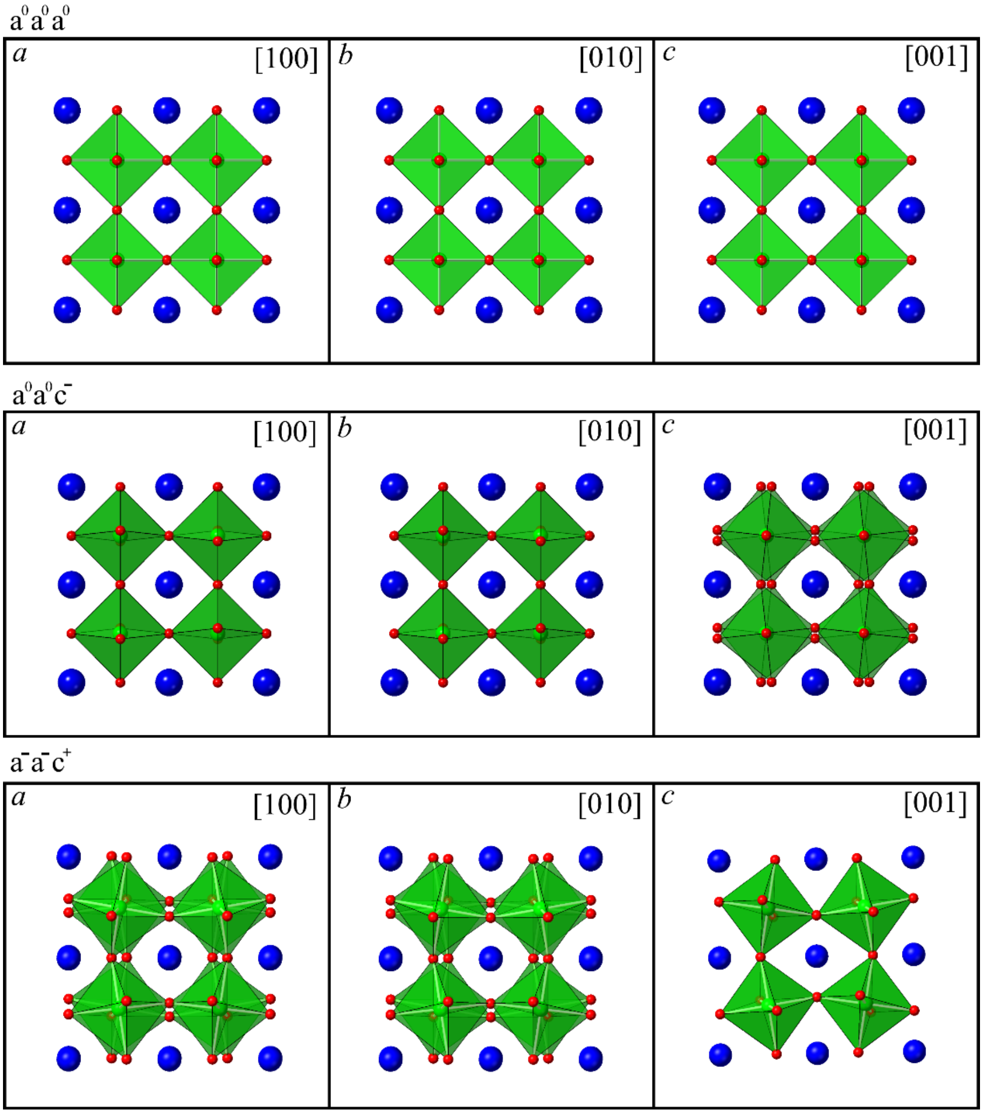

Figure 2.2 The $a^0a^0a^0$, $a^0a^0c^-$ and $a^-a^-c^+$ perovskite tilt groups as indicated. The *a, b* and *c* axes are denoted representing the [100], [010] and [001] zone axes. The A-site cations are represented in blue, BO_6 octahedra shown in green with red oxygen atoms.

example is $a^0a^0a^0$ whereby no tilting is observed and the a^0 identifier carries forward. In the second example the $a^0a^0c^-$ system is presented, with only anti-phase octahedral tilting observed in the c axis, donated by the c^- identifier. In the last example of $a^-a^-c^+$, two identical anti-phase tilt axes are found in the a and b axes, with the a^- identifier carried forward in the notation. The c axis octahedral tilting is in-phase, finishing the notation with c^+.

It is possible to consider the relationship between non-aristotype perovskites with regard to the aristotype structure. In this manner, perovskites can be considered with relation to a pseudo-cubic perovskite unit cell, and examples of these relationships are presented graphically in Figure 2.3. For example, if the undistorted aristotype *Pm-3m* unit cell parameters are denoted a_p, b_p and c_p, a drop in symmetry to orthorhombic *Pbnm* produces a pseudo-cubic unit cell of the form $a/\sqrt{2} \times b/\sqrt{2} \times c/2$. Similarly, the tetragonal phase *I4/mcm* will take the pseudo-cubic form $a/\sqrt{2} \times a/\sqrt{2} \times c/2$, while the orthorhombic *Cmmm* structure has the pseudo-cubic unit cell $a/2 \times b/2 \times c/2$. In practice, these changes are commonly characterised through X-ray diffraction (XRD) and electron diffraction. Reflections can be indexed with relation to their space-group formation but are commonly indexed with relation to the aristotype perovskite structure, and unit cell calculations can be suitably reduced for ease of comparison. The tilt structures of perovskites can be indexed based on the additional reflections that are induced by non-aristotype structures. Rules have been developed based on simulations and experimental data, first reported by Glazer [25] and refined by Woodward and Reaney [26]. The rules consider the aristotype perovskite unit cell for all perovskite structures and within this thesis all aristotype reflections are denoted by a subscript p, $(hkl)_p$, to reflect this. Additional reflections are indexed based on miller indices $(hkl)_p$, with indices labelled as either odd, *o*, or even, *e*. In this manner, in-phase tilting will produce additional reflections with two half-integral indices and one integral, i.e. ½(*eoo*), anti-phase with all half-integral indices, i.e. ½(*ooo*) and further ‘concert’ reflections as a result of combined in-phase/anti-phase tilting arise as one integral and two half integral indices, i.e. ½(*eeo*). Reaney *et al* [23] experimentally determined that anti-phase tilting reflections present in ⟨110⟩ zone axes, while in-phase tilting is present in the ⟨100⟩ and ⟨111⟩ zone axes. Additional reflections will not be present in all zone axes when considering electron diffraction, depending on the specific axis of tilting and how many axes are tilted [27]. For example, the $a^-b^-c^-$

tilt system will exhibit additional anti-phase tilt reflections in all $\langle 110 \rangle$ zone axes, but the $a^0a^0c^-$ system will not as two axes exhibit no tilting. These rules can used to identify phase transitions by observing several zone axis electron diffraction patterns, with the number of additional reflections for each tilt system reported by Woodward and Reaney [26]. This is also the case for X-ray diffraction, whereby specific reflections, following the same (*hkl*) rules for anti-phase tilting, in-phase tilting and concert reflections will be present depending on the perovskite tilt system in question.

(a) *Pm-3m*

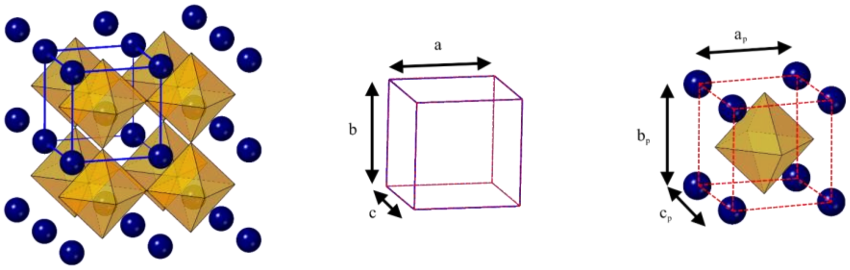

(b) *Pbnm*

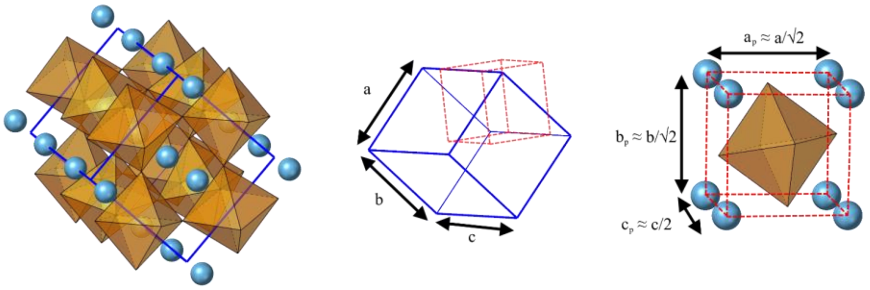

(c) *Cmmm*

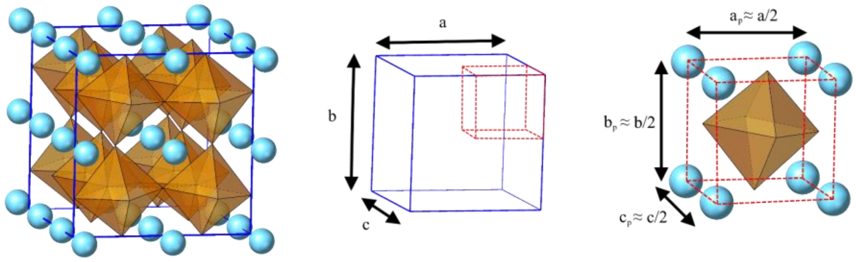

Figure 2.3 Relationship between (a) the aristotype perovskite unit cell and the (b) *Pbnm* unit cell and (c) *Cmmm* unit cell. The real unit cells of the labelled structures are presented with a blue solid line, while the pseudo-cubic unit cell is presented with a red dashed line. Non-subscripted parameters refer to the real lattice parameter. Those with a subscript "*p*" refer to the aristotype or pseudo-cubic parameter. A-sites are presented in shades of blue, with BO_6 octahedra in orange.

2.2 Radiation Damage

Radiation damage can manifest from several sources, the primary mechanisms being α-decay/recoil, β-decay and γ-emission. Atomic displacement of atoms occurs through elastic scattering interactions between incoming particles and the crystalline structure. Due to the low mass of β particles, high energy levels are required for atomic displacement, with the subsequent recoil events also insufficiently energetic to cause displacement. γ-emission is generally insufficiently energetic to cause displacements [28]. However, actinide α-decay events emit helium nuclei in the energy range of 4.5-5.0 MeV, with daughter recoil nuclei in the 70-90 keV range [28]. Reeve and Woolfrey [29] estimate this α-recoil event accounts for 94% of the damage imparted to the structure, with the remainder from the light helium nuclei. The range of the helium nucleus is < 10 µm, and will produce hundreds of displacements at the end of its damage track, whilst the recoil nuclei has a range of < 10 nm and will produce thousands of displacements across this damage track. This is the result of the low energy and high mass of the daughter nuclei producing ballistic collisions, while the energy loss of the helium nucleus is predominantly through electronic stopping. These processes are expanded upon in section 2.2.2. Recoil nuclei can cause significant damage to crystalline structures, while the production of inert helium can lead to helium bubble formation and agglomeration.

2.2.1 Defects

Once a system has been damaged, an end state can be induced in which defects are present. Various forms of defects exist, but it is easiest to first consider the simplest form of defect, the vacancy. Vacancies are a consequence of atoms that have escaped from established equilibrium positions within the lattice. Defects do exist in undamaged structures, and a clear example in the context of this research is the intrinsic A-site vacancies within the $Ca_{1-x}La_{2x/3}TiO_3$ solid solution. This requires a provision of energy sufficient to allow atomic vibrations, or oscillations, to reach amplitudes sufficient to dislocate an atom [30]. Most often this is provided by thermal energy, but within the context of radiation damage, sufficient energy can be transferred from energetic particles to cause dislocations through ballistic collisions and electronic energy transfer.

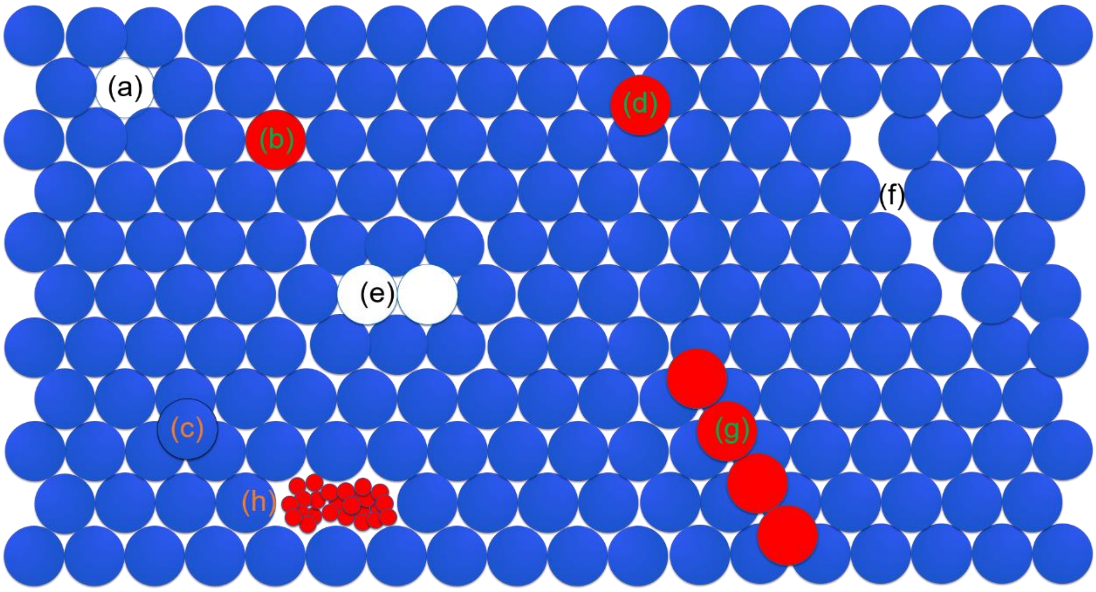

Figure 2.4 Graphical representation of various defect types: (a) vacancy (b) substitution impurity (c) interstitial (d) impurity interstitial (e) di-vacancy (f) vacancy-loop (g) interstitial-loop (h) gas bubble formation

Vacancies are an example of a point defect, that is a single deviation from lattice symmetry [30]. Atoms that do not occupy a lattice site of the crystal structure are known as interstitials, another point defect. Interstitials are a common feature of radiation damage, due to both displaced lattice ions and the stopping of any radiative species. A displacement will also create a vacancy, with the linked defects known as a Frenkel pair, the most common defect when considering radiation damage. Alternatively, substitution defects occur when a non-native ion occupies a lattice site of a displaced atom. These could further be described as impurities, and are a common consequence of the ion implantation processes used to induce radiation damage effects in this study. Further defects include dislocations or ‘line’ defects, in that no point defects are necessary to maintain equilibrium conditions within the structure. This often manifests as a shift in structural atoms, for example an edge dislocation is established as an extra half-plane of atoms within the structure. Volume defects are generally local amorphous regions or regions with altered stoichiometry, and can suffer localised expansion, swelling and strain. Similarly, the production of vacancy/interstitial pairs can lead to modified lattice parameters, increased or decreased density and induced stress. Voids are regions that have suffered a high number of atomic displacements, creating a porous region and inducing stress on surrounding grains [31]. Graphical representations of several defect types are presented in figure 2.4. This diagram includes gas bubble formation, which is described in section 3.3.

2.2.2 Stopping

As an initial particle diffuses through a solid mass, it causes damage by transferring energy to lattice ions through nuclear and electrostatic collisions. Such collisions can be described as having nuclear and electronic ‘stopping’ components. Nuclear stopping manifests as ballistic collisions between atomic nuclei, which can lead to atomic displacements and significantly change the trajectory of the incident ion. This is favourable for heavier ions and lower energies, with most damage occurring over a short ion track. Electronic stopping transfers energy to a systems electronic structure through interactions between the incident ion and the surrounding lattice electrons. This process is favourable for lighter ions with higher energies. In general, nuclear stopping leads to the most severe damage and highest number of displacements. The total energy-loss to the sample is described by,

$$\frac{dE}{dx} = \left(\frac{dE}{dx}\right)_n + \left(\frac{dE}{dx}\right)_e , \tag{2.2}$$

where dE/dx donates the energy transferred per unit length travelled, and n and e donates the nuclear and electronic stopping contributions, respectively [31]. Both contributions are dependent on the incident ion mass and energy, and which mechanism dominates influences the damage incurred. It can, therefore, be more useful to describe the process in terms of the electronic to nuclear stopping power ratio, given by

$$\mathrm{ENSP} = {\left(\frac{dE}{dx}\right)_e} \Big/ {\left(\frac{dE}{dx}\right)_n} . \tag{2.3}$$

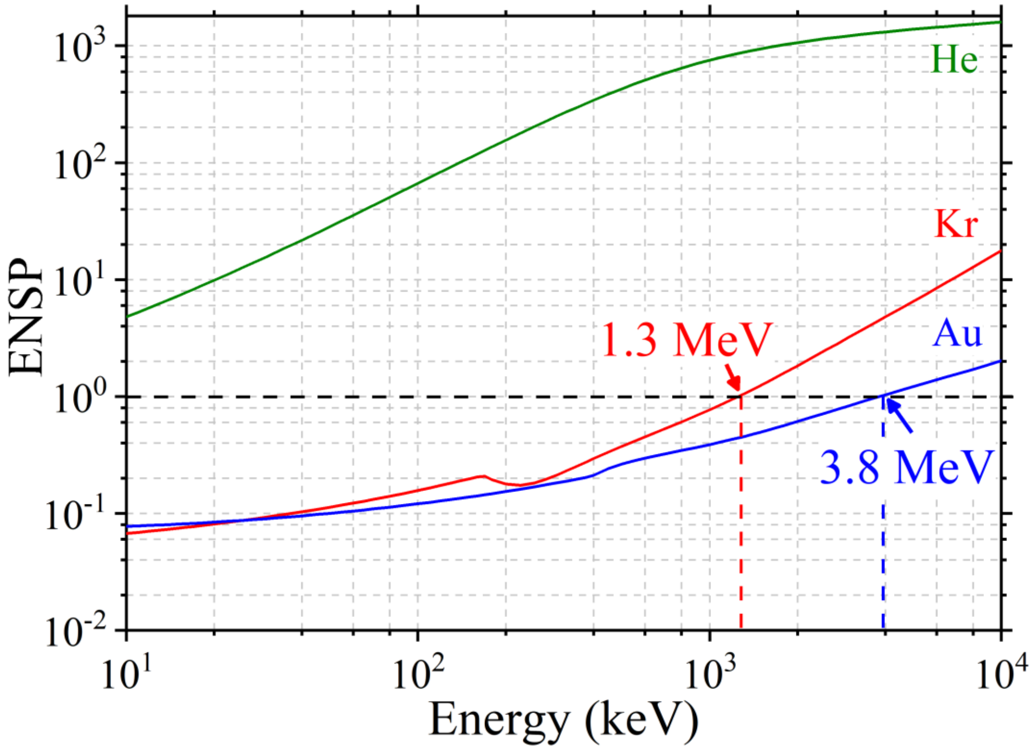

Figure 2.5 The ENSP ratio for He, Kr and Au in the energy range 10 keV – 10 MeV, implanted in $CaTiO_3$, calculated using SRIM [98].

Figure 2.5 shows ENSP plotted against ion energy for $CaTiO_3$, with He, Kr and Au ions. For He, electronic stopping is always dominant, but cross-overs for Kr and Au electronic stopping occur at 1.3 MeV and 3.8 MeV, respectively, illustrating the effects of ion mass and energy upon stopping power.

The maximum energy transfer, E_{max}, of a particle of mass m_1, with incident energy E, transferred to a lattice ion of mass m_2 is derived by Kinchin and Pease as

$$E_{max} = E\left(\frac{4m_1m_2}{(m_1+m_2)^2}\right), \tag{2.4}$$

for non-relativistic processes [32]. When considering electron bombardment, relativistic processes are relevant, with E_{max} given by

$$E_{max} = \frac{2E(E\text{-}2m_ec^2)}{m_2c^2}, \tag{2.5}$$

where m_e is the electron mass and c the velocity of light in a vacuum [32]. This derivation can be described as a hard-sphere model, assuming a series of two-body collisions that create a damage cascade within a random arrangement of atoms.

A displacement energy, E_d, is defined as the energy required to displace an atom from its lattice position, and below which the probability of said displacement is zero. Kinchin and Pease [32] define the number of displacements due to an incoming particle as

$$N_d = \frac{E_c}{2E_d}, \tag{2.6}$$

where N_d represents the number of displaced atoms and, assuming no recombination events, the number of vacancies produced, with E_c the critical energy level accounting for electron energy loses, defined as the incident ions mass in keV, i.e. $E_c(\mathrm{Kr}) = 84$ keV. This definition is improved by the Norgett-Robinson-Torrens (NRT) modification that accounts for the electronic excitations that occur as displaced particles pass through a lattice structure [33], defined as

$$N_d = 0.8\frac{E_c}{2E_d}. \tag{2.7}$$

The first initial displaced lattice ion is referred to as the primary knock-on atom, or PKA. The irradiating particle or PKA may be sufficiently energetic, i.e. with energy $> 2E_d$, to continue to create defects and cause displacements. These displaced lattice ions become ‘secondary knock-on atoms’, which if energetic enough will cause further displacements and defect production. This creates a ‘collision cascade’ and is the primary damage mechanism in crystalline structures, which can be further enhanced by the overlapping of cascades increasing defect density. The extent to which these cascades damage the structure is usually described in terms of displacements per atom (dpa). Using this unit, 1 dpa is equivalent to on average every atom in a specific volume being displaced once, for a given fluence, and is calculated as,

$$\mathrm{dpa} = \frac{\mathrm{Fluence\ (ions\ cm^{-2})} \times \mathrm{Displacements\ (displacements\ cm^{-1}\ ion^{-1})}}{\mathrm{Density\ (atoms\ cm^{-3})}}. \tag{2.8}$$

The value of E_d is considered to be atom specific and is often theoretically derived. Several values are reported for Ca, Ti, La and O using various techniques [59–63], with a wide range of values reported in each case based on the technique used and the specific compound investigated. The value of E_d is required when conducting SRIM calculations (see section 4.7), and due to the range of values reported this value is frequently set to 50 eV for all species as an estimation. It must be considered that this value is unlikely to be wholly accurate but is commonly employed as a good estimation based on comparisons of SRIM calculations and experimental data.

While it is ignored by the Kinchin and Pease and NRT models, it should be noted that E_d can be significantly altered by ‘directionality’. This is centred on the fact that radiation damage is not isotropic, and indeed there is preferred directionality for damage propagation. This modifies displacement energies and leads to ‘easy’ and ‘hard’ directions for displacement cascades to propagate. Such directionality arises from the crystal structure of the material, as shown in rutile TiO_2 by Robinson *et al* [36]. These processes are particularly prominent in single crystals with a specific orientation, commonly referred to as ion channelling.

2.2.3 Radiation Damage Recovery

Discussions of radiation damage have so far ignored any damage recovery processes. The mobility of defects has a large bearing on the damage tolerance of materials. For instance, the commonly induced Frenkel pair defects may migrate and recombine either with each other or another interstitial/vacancy pair within the structure. Furthermore, interstitial defects or vacancies may migrate to form defect loops and stacking faults, relieving stress induced by the initial damage process [39]. These processes can be enhanced by providing external energy inputs through both thermal and dynamic means. Thermally enhanced recovery provides an entire specimen with thermal energy through increased specimen temperature. In this manner defect mobility is increased, leading to enhanced recovery. A temperature may be reached where the rate of damage recovery equals the rate of damage induced, leading to a suppression of amorphisation. This temperature is defined as the critical temperature, T_c, of amorphisation. Dynamic recovery refers to local increases in energy imparted directly by radiation damage and collisions between atoms increasing defect mobility.

Various models have been derived to describe radiation damage, including the effects of radiation damage recovery. Weber [40] provides a thorough summary of such models. Of most relevance to this research are the models used by Smith *et al* [5] when conducting T_c of amorphisation experiments on the $Sr_{1-x}La_{2x/3}TiO_3$ system, details of which are expanded upon in chapter 3. These are based on equations derived by

Weber *et al* [41] and are widely used in the literature [8,67-85]. The first model describes the fluence required to amorphise a sample

$$F_c = {F_{c0}} \Big/ \left\{1\text{-}\exp\left[\left({E_a}/{k_B}\right)\left({1}/{T_c} - {1}/{T}\right)\right]\right\}, \tag{2.9}$$

where F_c is the critical amorphisation fluence, F_{c0} the critical amorphisation fluence at 0 K, E_a the activation energy for radiation damage recovery, k_B the Boltzmann constant, T_c the critical temperature of amorphisation and T the sample temperature. The second defines the critical temperature of amorphisation, and the activation energies for thermal and dynamic recovery as

$$T_c = {E_a} \Big/ \left[k\ \ln\left({1}/{\phi\sigma\nu}\right)\right], \tag{2.10}$$

Where E_a represents the activation energy for thermal or dynamic recovery (E_{th} and E_{irr}, respectively), ϕ the ion flux, ν the effective jump frequency and σ the amorphisation cross-section.

3. Literature Review

3.1 $Ca_{1-x}La_{2x/3}TiO_3$ and A-site Deficiency

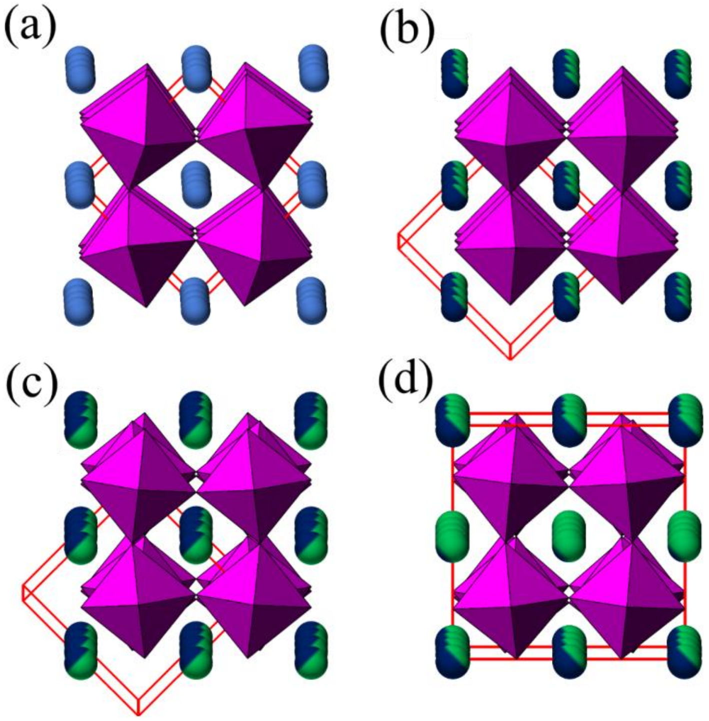

Figure 3.1 Structures of the $Ca_{1-x}La_{2x/3}TiO_3$ system with unit cells outlined, as reported by Zhang *et al* [72]. Ca atoms are represented in light blue, A-site Ca/La sites are represented in dark blue, with TiO_6 octahedra shown in purple. Green is used to donate A-site vacancy content. (a) x = 0 *Pbnm* (b) x = 0.6 *Ibmm* (c) x = 0.7 *I4/mcm* (d) x = 0 .9 *Cmmm*. Note the A-site vacancy ordering in the x = 0.9 sample.

The $Ca_{1-x}La_{2x/3}TiO_3$ solid solution is the subject of interest for this research. The system is A-site deficient, with the induction of A-site vacancies through charge balancing of the form,

$$3\mathrm{Ca}_{\mathrm{Ca}}^{\cdot\cdot} \rightarrow 2\mathrm{La}_{\mathrm{Ca}}^{\cdot\cdot\cdot} + \mathrm{v}_{\mathrm{Ca}}^{''},$$

using Kröger-Vink notation [61]. In this instance, the sub-script refers to the site occupied considering the $CaTiO_3$ structure, the number of superscript dots (positive) and apostrophes (negative) refer to the site charge. The end member $CaTiO_3$ has been widely studied [1,2,4,23,26,29-47]. With tolerance factor t = 0.856, the structure distorts to orthorhombic *Pbnm* with tilt series $a^-a^-c^+$. Two phase transitions at elevated temperatures are reported [81]. The structure transitions into the tetragonal *I4/mcm* phase at 1498 ± 25 K with the tilt series $a^0a^0c^-$, before a transition at 1634 ± 13 K to the *Pm-3m* phase with tilt series $a^0a^0a^0$ [81]. Structural characterisation of the La solid-solution series as a whole has been previously undertaken. Phase identification by Vashook *et al* [1,2] is reported as *Pbnm* for $0 \leq x \leq 0.3$, *Ibmm* for $0.4 \leq x \leq 0.6$, *I4/mcm* $0.7 \leq x \leq 0.75$ and *Cmmm* for $0.8 \leq x \leq 0.96$. These structures were amended by Zhang *et al* [72], who report the disappearance of the ½$(310)_p$ in-phase tilt reflection at x = 0.6, extending the *Pbnm* range to $0 \leq x \leq 0.5$. Discrepancies in the indexing of the $0.4 \leq x \leq 0.6$ region are due to the use of XRD by Vashook *et al* [1,2] and neutron diffraction by Zhang *et al* [72], the latter of which is more sensitive to octahedral phase transitions. Zhang *et al* [72] tentatively confirm the transition to *I4/mcm* at x = 0.7 and amend the x = 0.8 structure to *I4/mcm*. The *I4/mcm* structure was indexed based on the position of the ½$(311)_p$ anti-phase tilt reflection and the extrapolation of high-temperature structural determinations across the system. Mixed-phase tilt reflections were observed for the x = 0.8 structure and Zhang *et al* [72] argue these reflections indicate cation/vacancy ordering. They did not include such reflections in their refinements, and index the structure as *I4/mcm*, while Vashook *et al* [1,2] indexed the structure as *Cmmm*, including such reflections in their analysis. The *Pbnm* structured x = 0, *Ibmm* structured x = 0.6, *I4/mcm* structured x = 0.7 and *Cmmm* structured x = 0.9 are presented graphically in figure 3.1, with BO_6 octahedra in purple, A-site cations/vacancies in blue/green and the unit cell outlined in red. The oxygen deficient perovskite $La_{2/3}TiO_{3-\delta}$ has been synthesised, first by Abe and Uchino [82], however various studies have found that fully oxidised $La_{2/3}TiO_3$ cannot be stabilised [83,84], and a solubility limit for La is reported by Vashook *et al* [2] of x = 0.96 for the $Ca_{1-x}La_{2x/3}TiO_3$ system when synthesised in air.

Elevated temperature phase transitions in the $Ca_{1-x}La_{2x/3}TiO_3$ system are reported by Vashook *et al* [1] and Zhang *et al* [72], and a full phase transition diagram is shown in figure 3.2. A transition from *Pbnm* → *I4/mcm* is reported for the x = 0.3 and 0.4 phases at 1100 K and 850 K, respectively. The x = 0.5 phase undergoes a transition from *Pbnm* → *Ibmm* at 525 K, followed by a transition *Ibmm* → *I4/mcm* at 470 K. A transition from *Ibmm* → *I4/mcm* is reported for the x = 0.6 phase at 650 K, followed by a transition from *I4/mcm* → *Pm-3m* at 1170 K. The x = 0.8 phase undergoes a transition from *I4/mcm* → *Pm-3m* at 775 K, with the x = 0.9 phase undergoing a transition from *Cmmm* → *P4/mmm* at 675 K.

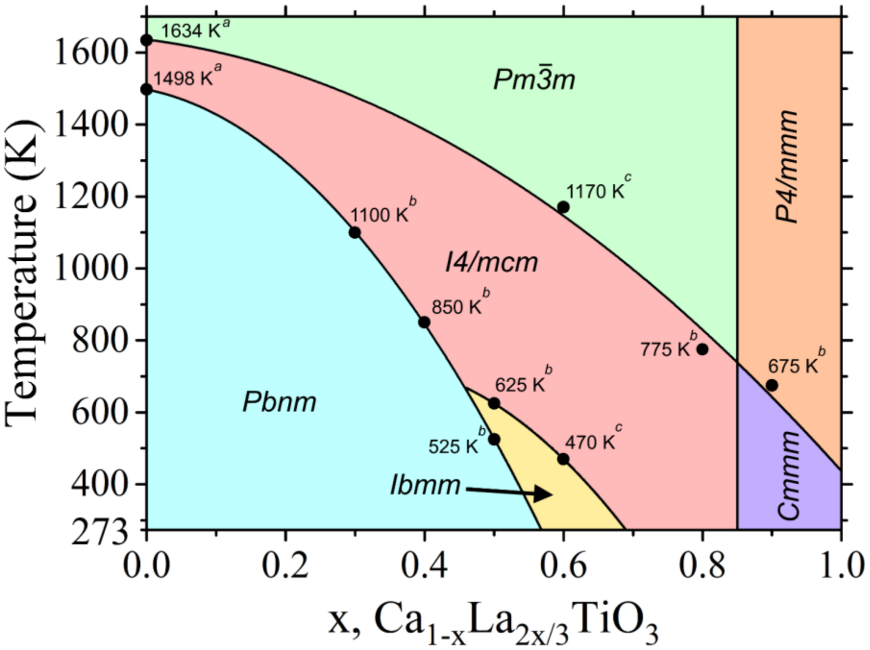

Figure 3.2 Structural phase diagram of the $Ca_{1-x}La_{2x/3}TiO_3$ solid solution. Phase transition temperatures are labelled and referenced. For $0.96 < x \leq 1.0$, the phase diagram refers to $Ca_{1-x}La_{2x/3}TiO_{3-\delta}$ as only oxygen deficient perovskites have been reported in this formula unit region.

[a] Ali, R. & Yashima, M. (2005) *Journal of Solid State Chemistry*, 178, 2867–2872.

[b] Zhang, Z. et al (2007) *Journal of Solid State Chemistry*, 180(**3**), 1083–1092.

[c] Vashook, V, et al (2003) *Journal of Alloys and Compounds*, 354, 13–23.

Within highly A-site deficient perovskites, A-site vacancy ordering has been reported. This includes the $La_{2/3}TiO_3$ end member in which layers of 1/3 and full A-site occupation are present [82], while various instances of vacancy ordering in perovskites are present in the literature, including compounds rich in La such as $La_{1/3}NbO_3$ and $La_{1/3}TaO_3$ [85]. These compounds will form layered structures of 2/3 A-site occupied layers and layers devoid of A-site cations. This is particularly prominent within compounds with a divalent A-site, in which A-site vacancies are induced as opposed to the reduction of the B-site cation, in this instance Ti^{4+}. The $Sr_{1-x}La_{2x/3}TiO_3$ system has been shown to exhibit A-site ordering by HRTEM for $x \geq 0.7$, requiring significant La^{3+} substitution before ordering is observed [75]. Ordering has also been reported in the $Ca_{1-x}La_{2x/3}TiO_3$ system, with Zhang *et al* [72] reporting short range A-site vacancy ordering for $0.7 \leq x < 0.9$, followed by long range ordering for $x \geq 0.9$. These conclusions are drawn by the inclusion of concert reflections forbidden by *Cmmm* and

I4/mcm symmetries and identified as evidence of ordering of A-site vacancies. This has been further reinforced by Danaie *et al* [10], research conducted in collaboration with the current author. Comparison of bright field and high-angle annular dark field images using scanning transmission electron microscopy (STEM) showed no evidence of A-site vacancy ordering in the *Pbnm* phase, but definitive long-range ordering within the $Ca_{0.1}La_{0.6}TiO_6$ *Cmmm* phase was observed. The ordering forms a layered perovskite-like structure along the c axis, with alternate layers of La-rich and La-poor planes.

3.2 Radiation Damage in Perovskites

3.2.1 Calcium Titanate, $CaTiO_3$

The first initial attempts to study the long-term effects of radiation damage in oxide structures were undertaken by observations of natural analogue systems. However, data of this form is limited for perovskites and doses are typically quoted in α-decays g^{-1} (α g^{-1}) within these studies. Sinclair and Ringwood [86] took several natural perovskite samples, of varied ages and uranium/thorium contents, with doses of 1.6×10^{18} α g^{-1} and 2.6×10^{18} α g^{-1}, respectively, and a loparite phase with a dose of 1.3×10^{18} α g^{-1}. In each case, the samples remained highly crystalline by XRD, with a maximum volume expansion observed of 1.82 ± 0.05%. More recent studies by Lumpkin *et al* [87] report a range of geological samples, with the first appearance of a crystalline-amorphous transition in perovskite observed at a dose of $3\text{-}6 \times 10^{18}$ α g^{-1} and ‘moderately’ damaged perovskite observed at $8\text{-}12 \times 10^{18}$ α g^{-1}, both by electron diffraction.

Following attempts to simulate damage were undertaken by irradiating samples with neutrons. This allowed for the direct irradiation of laboratory synthesised perovskites. Woolfrey *et al* [88] conducted fast neutron irradiation, defined as > 1 MeV, on all five constituents of the SYNROC family of materials, including $CaTiO_3$, to neutron doses of 4.8×10^{20} n cm^{-2}. Reeve and Woolfrey [29] use an estimation of 7×10^{21} α $g^{-1} \approx 3.6 \times 10^{20}$ n cm^{-2}, and further equivalate this to ≈ 1 dpa in these studies. This conversion is not perfect, and ignores the effects of minor active phases such as U^{235} [89]. Perovskite was found to exhibit a bulk volume increase of 6.01% after a 2.48×10^{20} n cm^{-2} dose. Ball *et al* [90] conducted further fast neutron irradiations on pure $CaTiO_3$ to a dose of 2.2×10^{20} n cm^{-2} and found that whilst volume

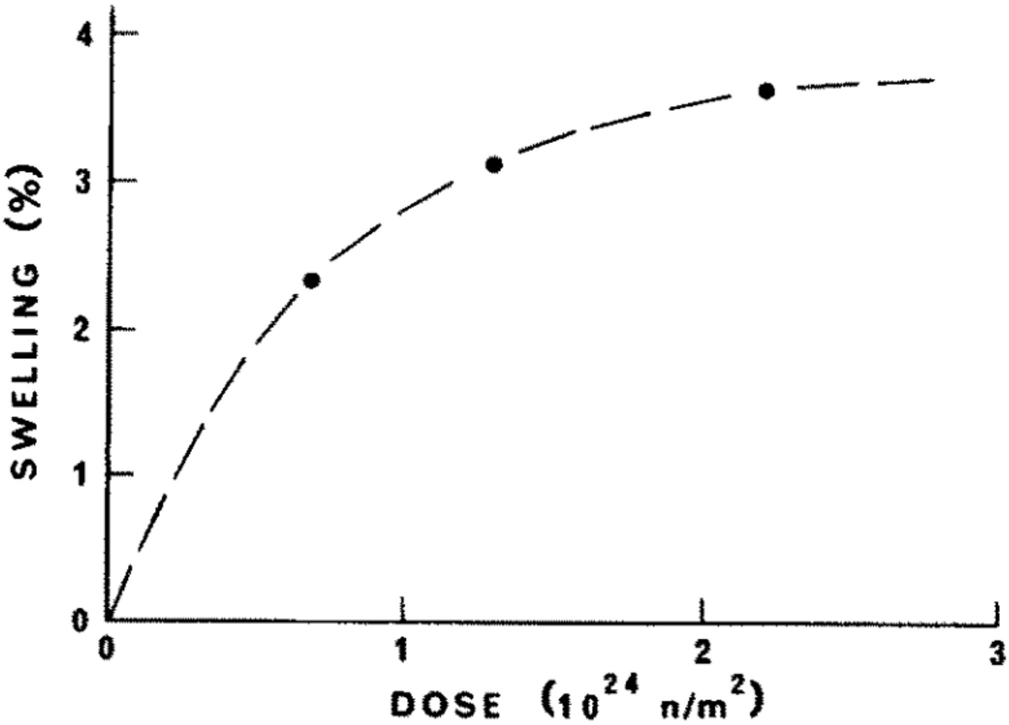

Figure 3.3 Saturation of volume swelling in $CaTiO_3$ under neutron irradiation. Reprinted Fig 3. from C.J. Ball, R.G. Blake, D.J. Cassidy and J.L. Woolfrey, "Neutron irradiation effects in perovskite ($CaTiO_3$)" *Journal of Nuclear Materials* 151, p153, 1988 with permission from Elsevier 2019. Available: http://dx.doi.org/10.1016/0022-3115(88)90067-0

swelling was observed by XRD, it saturated at an expansion of 3.67 ± 0.05%, as can be observed in figure 3.3, with *a* and *c* saturating at the maximum dose. Such volume swelling was anisotropic, with the *b* lattice parameter saturating at 1 x 10^{20} n cm^{-2}. They report the initial rate of volume expansion in agreement with Woofrey *et al* [88], but bulk density measurements are not in agreement. This is likely due to irradiation induced microscopic cracking rather than solely due to lattice expansion. These calculations were made by geometric measurement which was subject to significant influence from microcracking, preventing accurate quantification of unit cell expansion as is possible with XRD. Line attenuation and broadening is also reported post-irradiation, likely due to increased disorder. The key difference between these techniques is the inevitable variation in the mechanisms for damage accumulation. Alpha-recoil events will produce more knock-on events, leading to more damaging localised individual cascades, compared to neutrons which will produce displacement events over a longer cascade.

Further attempts to determine the effects of α-decay upon oxides used a method of directly doping a ceramic structure with actinides such as Pu and Cm. The resulting effects of α-decay and recoil nuclei can then be investigated, whilst doping with Cm is commonly employed to achieve higher dose rates. Perovskite doped with 5 wt% Pu is reported by Evans *et al* [15] as exhibiting a maximum volume expansion of 7.4% at a dose of 4.2×10^{18} α g^{-1}. Once more these are geometric measurements, suggesting microcracking leads to a higher bulk volume increase when compared with X-ray diffraction data. No saturation is reported, and it is likely microcracking occurs as a result of the saturation limit being breached. In general, the long-term nature of actinide doping experiments is disadvantageous, although Strachan *et al* [91] report that ^{238}Pu and ^{239}Pu doped zirconolite and pyrochlore matrices showed levels of damage to enable the study of early-stage damage processes within a year. Moreover, it is the need for equipment capable of handling highly active samples, in particular for synthesis and characterisation, that makes actinide doping most troublesome.

Modern investigations have employed ion implantation, the process of bombarding samples with high flux ion beams, allowing for high fluences to be achieved in short timescales. This process also allows for surrogate, non-active samples to be analysed without the use of active-handling facilities, whilst also providing the capability to tune ion beam species and energies to an experiment. The process is readily used in various industrial processes, most well-known for the surface modification of semiconductors. Of concern when employing ion implantation is the high flux employed, unrepresentative of the slow α-decay processes that occur over a nuclear wasteforms lifetime. Frequently Kr^+ ion implantation is used to simulate the effects of actinide recoil damage, as this configuration has been found to produce similar amorphisation dosages to those reported in actinide doping experiments [92]. In all the previous studies mentioned, while perovskite undergoes significant volume swelling, amorphisation is not reported. Ion implantation was undertaken using 3 MeV Au^+ ions by Karioris *et al* [93] on perovskite, although the exact composition is not reported. XRD analysis showed decreasing peak intensities with increasing dose until fully amorphous. This was the first suggestion that ion implantation is capable of amorphising the perovskite structure. Studies on single crystal $CaTiO_3$ followed by White *et al* [94], using 250 keV and 540 keV Pb^+ ion implantation to fluences of $1\text{-}4 \times 10^{15}$ ions cm^{-2} at liquid nitrogen temperatures. This study employed Rutherford backscatter spectroscopy (RBS) to measure the relative disorder of the Ti, O and Ca sublattices. The Ti, O and Ca sublattices are reported to amorphise $CaTiO_3$ following 250 keV Pb^+ implantation to a fluence of 4 x 10^{15} ions cm^{-2}, with amorphisation reported at 1 x 10^{15} ions cm^{-2} when employing 540 keV Pb^+ implantation. After annealing for 1 hour at 500 °C, the 250 keV Pb^+ implanted sample is reported to yield recrystallisation that replicates pristine regions, suggesting epitaxial recrystallisation of the damaged structure. Annealing of the 540 keV Pb^+ implanted sample at 425 °C for 15 hours demonstrates partial recrystallisation, shifting the crystalline-amorphous (c-a) interface closer to the sample surface. White *et al* [95] suggest this behaviour is indicative of recrystallisation occurring via solid-phase epitaxy. This is further reinforced by *in-situ* heating of the 540 keV Pb^+ sample in an electron microscope at 480 °C, in which the partial epitaxial recrystallisation is observed with a shift in the c-a interface toward the sample surface. Activation energies were derived by measuring

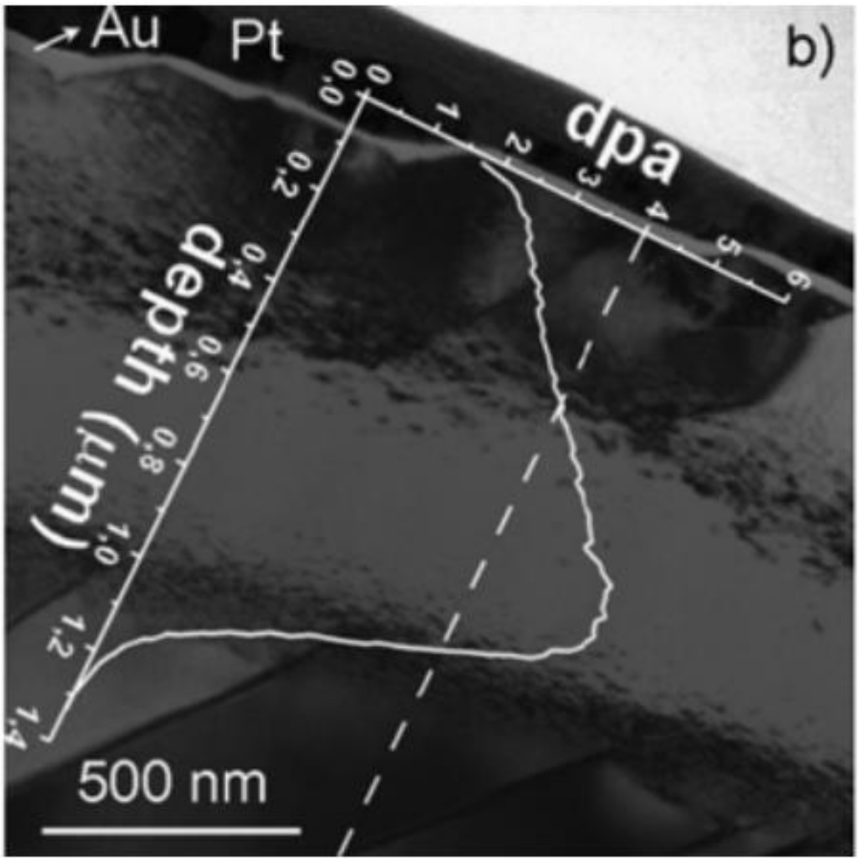

Figure 3.4 TEM micrograph of 2 MeV Kr^+ irradiated $CaTiO_3$ with SRIM profile superimposed. Reprinted Fig 4b. from C. Davoisne, M. C. Stennett, N. C. Hyatt, N. Peng, C. Jeynes, W.E. Lee, "Krypton irradiation damage in Nd-doped zirconolite and perovskite" *Journal of Nuclear Materials* 415, p69, 2011 with permission from Elsevier 2019. Available: http://dx.doi.org/10.1016/j.actamat.2011.05.043

recrystallisation growth velocities with temperature, giving 1.3 eV for a low-symmetry [100] and [010] crystals and 3.76 eV for [001] samples. The ‘growth velocity’ is determined by the length of annealed material after a specific annealing period. It should be noted these are thermally activated processes, rather than dynamic. Rankin *et al* [96] built on *in-situ* annealing of the Pb^+ irradiated single crystal $CaTiO_3$ samples. Once again, they report inward epitaxial recrystallisation from the c-a amorphous interface toward the surface, in this instance using a 475 °C anneal, across both the [010] and [100] directions.

Cross-sectional TEM was performed by Davoisne *et al* [11] on a Nd doped perovskite of composition $(Ca_{0.9}Nd_{0.1})(Ti_{0.9}Al_{0.1})O_3$, used as a surrogate for plutonium due to its comparable oxidation state and ionic radii, with Nd^{3+} (r = 0.983 Å) and Pu^{3+} (r = 1 Å). Such a sample was not considered A-site deficient due to Al^{3+} B-site doping to compensate charge balancing. Implantation was conducted using 2 MeV Kr^+ at room temperature, to a dose of 5×10^{15} ions cm^{-2} (maximum dose = 5.71 dpa). The amorphisation fluence is reported as 4 dpa, as can be observed from the SRIM profile superimposed on the TEM micrograph of the perovskite sample in question in figure 3.4. In this case, the light contrast regions are damaged/amorphous material, while the darker contrast represents crystalline regions. The authors report the oxidation state of Ti remains in the Ti^{4+} state, through analysis of electron energy loss near-edge spectroscopy (ELNES) data. Furthermore, a drop in coordination state is observed through shifting of the $L^*_{2,3}$ molecular orbital splitting contributions towards the $L_{2,3}$ spin orbit coupling contribution. This is only observed in the amorphous state as opposed to the ‘partially damaged’ regions, suggesting this is intrinsic to the amorphisation transition. Furthermore, they report an orthorhombic to cubic phase transition within the partially damaged region, observed by the disappearance of electron diffraction reflections indicative of octahedral tilting.

The studies mentioned so far employed bulk *ex-situ* ion implantation, that is implantation of a bulk sample prior to characterisation. *In-situ* studies, most commonly in a TEM, have allowed real time observation of defect production and structural damage. For the purpose of this research, *in-situ* will refer to ion implantation experiments conducted *in-situ* in a TEM. Smith *et al* [97] employed *in-situ* 1 MeV Kr^+ implantation upon natural perovskite $(Ca_{1.02}[Ti_{0.98}Fe_{0.01}]_{0.98}O_3)$, and report an amorphisation dose of 2.2 dpa at room temperature. Conversions of fluence to dpa are made using the SRIM Monte Carlo code [98] by integrating the damage-depth profile over the thickness of the TEM sample (≈ 100 nm). Furthermore, 800 keV Kr^+ ion implantation was employed by Meldrum *et al* [8] on various perovskites, discussed fully in the following section, and report an amorphisation dose of 3.67×10^{14} ions cm^{-2} at 20 K (0.75 dpa), or 1.8 dpa at room temperature. These findings are in conflict with those reported by Davoisne *et al* [11], and the reported dose of 4 dpa using 2 MeV Kr^+ implantation. This is an example of common discrepancies between *in-situ* and *ex-situ* setups which have to be accounted for when comparing induced damage. For example, Meldrum *et al* [8] employed single crystal $CaTiO_3$, giving rise to a possible orientation specific response in comparison to the polycrystalline $CaTiO_3$ used by Davoisne *et al* [11]. When employing the use of thin films or crushed grain TEM samples, the < 100 nm thin sample can have unrepresentative effects on the strain/disorder induced, thermal effects and annealing, mobility of vacancies, grain boundary effects, sample orientation and the relaxation of the oxide lattice when compared to a bulk configuration. While useful when examining fundamental mechanisms and underlying properties, the caveats of *in-situ* must be considered when conducting such experiments.

3.2.2 Radiation Damage in A-site Deficient Perovskites

The focus of this research is the effect of A-site vacancies on the radiation damage response of perovskites. Studies to this effect are limited and have to-date been conducted *in-situ*. Smith *et al* [99], investigated the $Sr_{1-x}La_{2x/3}TiO_3$ A-site deficient solid-solution using 1 MeV Kr^+ ion implantation *in-situ* in a TEM to determine the T_c of amorphisation across the system. They report the phenomena of T_c dropping from 394 K for $SrTiO_3$, to 308 K at x = 0.15, to 275 K at x = 0.3, before rising to 379 K at x = 0.45. This is followed by further increases in T_c with increasing La^{3+} content, with the end member x = 1.0 having a T_c of 865 K. These values are presented graphically in figure 3.5. This initial drop in T_c up to x = 0.3 suggests an increase in damage tolerance at low La^{3+} doping levels. Smith *et al* [99] conclude this is unlikely as a result of compositional changes. Comparing temperature dependant critical fluences for amorphisation, the fluence at which no crystallinity is observed in electron diffraction patterns, would require cation displacement energies of the form E_d (x = 0.3) > E_d (x = 0.45) ≈ E_d (x = 0.1) > E_d (x = 0) ≈ E_d (x = 0.6) > E_d (x = 0.9) > E_d (x = 1.0). Whilst it seems feasible the x = 0 sample would have

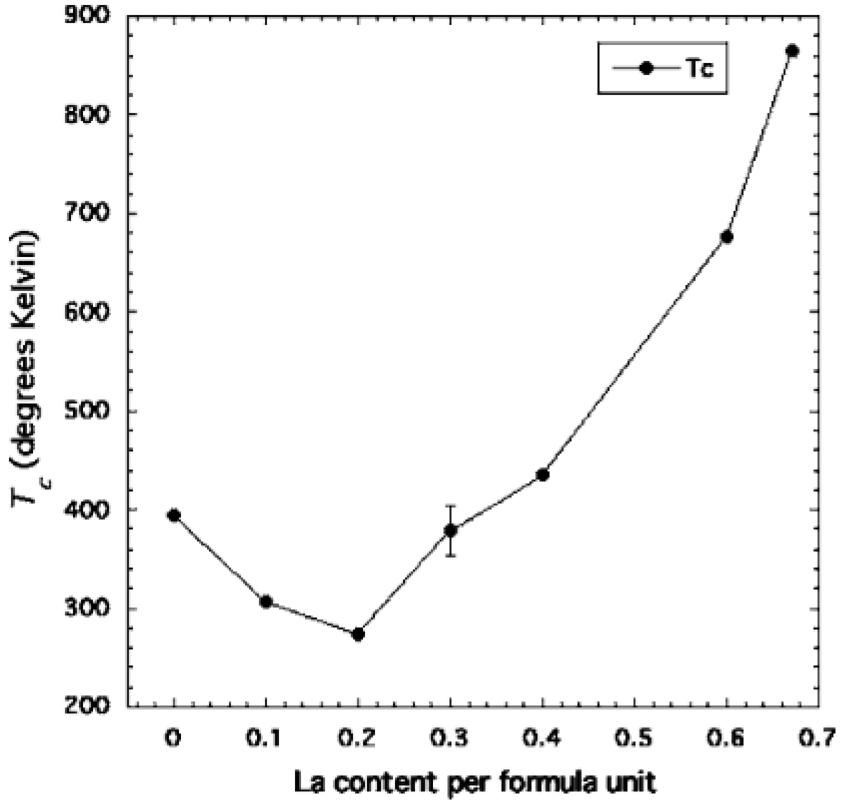

Figure 3.5 Critical temperature of amorphisation, T_c, versus La content for the $Sr_{1-x}La_{2x/3}TiO_3$ system. Reprinted Fig 8. from K. L. Smith, G. R. Lumpkin, M. G. Blackford, M. Colella and N. J. Zaluzec, "*In-situ* radiation damage studies of $La_xSr_{1-3x/2}TiO_3$" *Journal of Applied Physics* 103 (083531), p5, 2008 with permission from Elsevier 2019. Available: http://dx.doi.org/10.1016/j.actamat.2016.05.045

cation displacement energies exceeding x = 0.6, 0.9 and 1.0 due to the increasing number of oxygen vacancies in these heavily La^{3+} doped samples, the appearance of the x = 0.3 with the highest value for E_d seems unlikely based on compositional changes alone. Smith *et al* [99] further argue that based on previous studies by Smith *et al* [100], Cooper *et al* [101] and Thomas *et al* [102], showing oxygen E_d values of several compositional variations of perovskites, zirconolite and pyrochlores being within experimental error of one another (47 ± 11 eV). Furthermore, it is argued that as oxygen ions are fully bound within the $Sr_{1-x}La_{2x/3}TiO_3$ system, oxygen E_d values are unlikely to change significantly across the solid solution, and SRIM calculations rule out the effects of variations in stopping powers due to increasing density with La^{3+} content. They conclude that based on atomistic simulations of $SrTiO_3$ defects by Thomas *et al* [38], suggesting the most prominent damage recovery mechanism for $SrTiO_3$ is migration of O and Sr interstitials and oxygen vacancies, a vacancy-assisted recovery process dominates the damage response for < x = 0.45 driven by increasing A-site deficiency. It was further postulated that as these effects occur within the cubic regime of the system, the more complex landscape of the tetragonal and orthorhombic phases may lead to significant migration barriers due to distorted octahedra.

3.2.3 Radiation Damage in Related Perovskites

Studies have been conducted on various other perovskite samples, which can both aid in our understanding of the $Ca_{1-x}La_{2x/3}TiO_3$ response and offer a point of comparison as to the tolerance of the samples within the solid-solution. $BaTiO_3$ was investigated by Jiang *et al* [103] using 1 MeV Kr^+ implantation at 170 K and room temperature. In both temperature regimes, with full amorphisation of both the Ba and Ti sublattices at ≈ 0.5 dpa observed. This is about twice the *in-situ* dose required to amorphise $SrTiO_3$ [104] or $CaTiO_3$ [8], although less than the required 4 dpa reported by Davoisne *et al* [11] for bulk implanted $CaTiO_3$. Based on annealing studies, defect recovery is reported to occur between 420 K and 570 K, likely linked to T_c, before thermal epitaxial recrystallisation is observed between 720 K and 870 K. These values are in strong agreement with those reported by Meldrum *et al* [8] using *in-situ* measurements. Furthermore, bulk measurements of the *Pbnm* structured $CaZrO_3$ were undertaken by Lang *et al* [105] using X-ray diffraction after 940 MeV Au^+ swift heavy ion implantation. The damage in this instance is entirely due to electronic stopping, and the effects of nuclear stopping are not observed. This damage formulation is different to nuclear effects, consisting of long narrow ion tracks of damage. They observe full amorphisation at 1.5×10^{13} ions cm^{-2} in the sample, based on the reduction in XRD trace peak intensities. It is hard, from these results, to compare with studies that have focused on the nuclear stopping regimes expected in the nuclear environments perovskites will operate within. However, such differences are of interest in the context of the $Ca_{1-x}La_{2x/3}TiO_3$ system, and due to this reason two irradiation conditions in which nuclear and electronic stopping were dominant, respectively, were employed within this research. Geikielite, an ilmenite-group perovskite-like oxide in the form of $MgTiO_3$ has been investigated by Mitchell *et al* [106]. Bulk ion implantation upon single crystals with 200 keV Ar^+ and 400 keV Xe^+ was undertaken. Xe^+ implantation at 170 K required an amorphisation dose of 2×10^{15} ions cm^{-2} (5.4 dpa), increasing by a factor of three at 300 K (16.2 dpa), and to > 2.5×10^{16} ions cm^{-2} (> 67.5 dpa) at 470 K. A radiation induced phase is reported within the damage region, likely to lithium niobate or the orthorhombic perovskite structure. These mimic pressure/temperature induced phase transitions within ilmenite-structures. This is not the sole example of a radiation induced phase-transition within a perovskite, with Sabathier *et al* [107] reporting the transition of $SrTiO_3$ to Sr_2TiO_4 through XPS and XRD measurements after 320 keV Pb^+ implantation, likely due to the induced phase being more thermodynamically favourable when compared with $SrTiO_3$.

In-situ experiments conducted in a TEM have been employed on various perovskites. As mentioned, Meldrum *et al* [8] studied various perovskites with 800 keV Kr^+ ions ($CaTiO_3$, $SrTiO_3$, $BaTiO_3$, Nd doped $BaTiO_3$, $LiNbO_3$, $LiTaO_3$, $KNbO_3$, $KTaO_3$), 800 keV Xe^+ ($CaTiO_3$, $SrTiO_3$), 800 keV Ne^+ ($CaTiO_3$, $SrTiO_3$) and 280 keV Ne^+ ($KTaO_3$), and calculated room temperature amorphisation dosages and the T_c of amorphisation for each sample. For the Kr irradiated samples, T_c values descended in the order $KTaO_3$ (880 K) > $KNbO_3$ (770 K) > $LiTaO_3$ (650 K) > $LiNbO_3$ (600 K) > $BaTiO_3$:Nd (590 K) > $BaTiO_3$ (550 K) > $CaTiO_3$ (440 K) > $SrTiO_3$ (425 K). In terms of recovery, the titanates exhibit the greatest proficiency, requiring the least thermal energy to suppress amorphisation. This is mimicked when considering extrapolated amorphisation dosages at 20 K, with $CaTiO_3$ (0.75 dpa) and $SrTiO_3$ (0.93 dpa) requiring over twice the dose of the other perovskites irradiated. Furthermore, the $A^{2+}B^{4+}O^{-2}{}_3$ charge configuration appears superior compared with the $A^{1+}B^{5+}O^{-2}{}_3$ configured samples. For $CaTiO_3$ and $SrTiO_3$, Xe^+ irradiation yielded T_c values of 440 K and 420 K respectively, matching those calculated for Kr^+. Amorphisation of these samples could not be achieved using Ne^+ irradiation. This is due to the domination of electronic stopping in this regime when using light Ne ions. $CaTiO_3$, while still requiring a higher fluence, required a higher dose when considering dpa after irradiation with Xe^+, requiring 1.21 dpa compared to 0.97 dpa for $SrTiO_3$. Again, this likely due to changes in stopping mechanism, with the heavier Xe^+ ions tripling the nuclear stopping contribution compared to electronic. Recrystallisation temperatures, T_r were calculated by irradiating a sample with three times its specific critical dose, and observing the temperature at which crystallinity is recovered via electron diffraction. In all cases, $T_r \geq 800$ K, with the exception of $KTaO_3$, which did not recrystallise within the operating temperature range. For the titanates, T_r values are reported as $SrTiO_3$ (800 K) > $CaTiO_3$ (850 K) = $BaTiO_3$ = $BaTiO_3$:Nd, and all samples are reported to recrystallise epitaxially to form their initial single crystal orientations.

3.3 Helium Bubble Formation

A consequence of vacancy and void creation can be bubble formation. Inert gases have very low solubility within solid structures and in sufficient quantity gas accumulation within pores, voids or structural defects will occur. These bubbles can cause cracking, blistering and surface exfoliation. The study of bubble formation using ion implantation has typically been undertaken in elemental systems such as silicon [108-114], metals [115–120], SiC composites [121-123] and glasses [124]. Defect migration and formation plays a key role in the formation of inert-gas bubble formation. Vacancy defects can act as nucleation sites for helium bubble formation [121,125,126] and such bubbles can further limit defect migration once formed [127,128]. Furthermore, grain boundaries have been found to act as sinks for helium bubbles [120,129]. At room temperature, migrating helium will become trapped within such defects and the agglomeration and coalescence of bubbles will proceed within these vacancy pockets. The $Ca_{1-x}La_{2x/3}TiO_3$ system has significant potential in this regard, considering the intrinsic vacancy sites that exist within the structure. Matsunaga *et al* [130] conducted infusion studies in ZrO_2 doped with varying levels

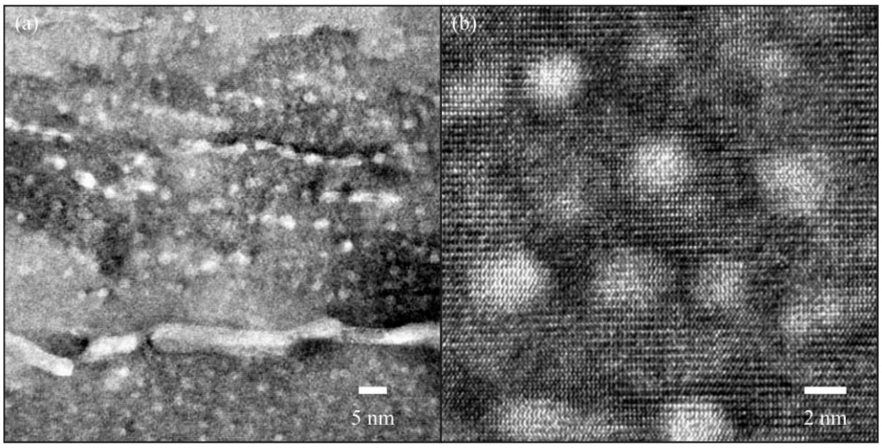

Figure 3.6 Helium bubbles observed in $LiNbO_3$ with 5 x 10^{15} 1 MeV He^+ ions. Reprinted Fig 2. with permission from A. Ofan, L. Zhang, O. Gaathon, S. Bakhru, H. Bakhru, Y. Zhu, D Welch and R. M. Osgood, Jr, *Physical Review B – Condensed Matter and Materials Physics* 82 (10), 2, 2010. Available: http://dx.doi.org/10.1103/PhysRevB.82.104113. Copyright 2019 by the American Physical Society.

of the reduction agent Fe^{3+}, forming oxygen vacancies to differing concentrations in the system $(Zr,Fe)O_{2-x}$. Helium was statically infused into precursor powders through hot isostatic pressing at 1273 K for 100 hours, using 91 MPa pressurisation in a He atmosphere. While bubble formation of diameter 0.5-10 nm was observed in all oxygen deficient samples, increasing Fe^{3+} had the effect of considerably increasing bubble densities. This increase continued until Fe^{3+} content reached a solubility limit in zirconia. While bubble size was not dependant on oxygen vacancy content, bubble density increases suggest vacancy content promotes bubble formation, offering increased formation sites for infused He.

Bubble formation can be significantly influenced by elevated temperatures. The increase in helium migration energy has the effect of both increasing the coalescence of bubbles, while also releasing helium trapped in vacancy defects when undertaking post implantation annealing [20,125,131–134]. This has the effect of lowering the fluence at which bubble formation is observed to occur, F_B. Hojo *et al* [135] report a decrease in the F_B value for 35 keV He^+ implanted yttria-stabilised zirconia from 1.8 x 10^{17} ions cm^{-2} at room temperature to 1.8 x 10^{16} ions cm^{-2} at 1273 K, and an increase in bubble dimeter from 2.8 nm to 3.3-5.6 nm. Such an effect is also observed by Sasajima *et al* [136] in spinel, with a decrease in F_B from 6 x 10^{16} ions cm^{-2} at room temperature to 6 x 10^{15} ions cm^{-2} at 650 K. Such behaviour is further reported for steels [118,127], Al_2O_3 [137] and $MgAlO_4$ [134].

Studies of helium bubble formation in perovskites are very limited. One of the few examples of He behaviour in a perovskite structure is that of $LiNbO_3$ reported by Ofan et al [138]. Implantation was undertaken with 1 MeV He^+ to 5 x 10^{16} ions cm^{-2} (2 at%). He bubble formation is observed, with bubbles exhibiting uniform spherical shape, with average diameter 1.3 ± 0.4 nm, as can be observed in figure 3.6. However, bubbles with radii < 0.9 nm are not observed to form, suggesting all the implanted He coalesced into these observed bubbles. In general, bubble mobility will reduce as He content increases, suggesting a bubble radius is reached after which coalescence is not feasible, leading to a maximum bubble radius. Furthermore, the bubbles exhibit a regular spacing of ≈ 4 nm, likely due to a strain effect introduced by neighbouring bubble interactions. Bubbles will attempt to minimise the total strain induced by neighbouring interactions, leading to a favourable arrangement in this manner. Annealing was undertaken to 350 °C, leading to the coalescence of large bubbles with radii ≈ 5 nm, and a threshold is observed for spherical bubble formulation, with bubbles of diameter > 3 nm forming oblate spheroids. Features such as straight edges and shaping facets are observed in these larger bubbles. The $Gd_2Ti_2O_7$ and $Gd_2Zr_2O_7$ structures have been studied by Taylor *et al* [89,139,140]. 200 keV He^+ ion implantation was undertaken on the structures, both in the pristine state and after 7 MeV Au^+ ion implantation in $Gd_2Zr_2O_7$ (8 dpa) and $Gd_2Ti_2O_7$ (6 dpa). Implantations are reported at fluences of 2 x 10^{15} and 2 x 10^{16}, with a third fluence of 2 x 10^{17} ions cm^{-2} using 65 keV He^+ ions. No bubble formation is observed in $Gd_2Zr_2O_7$ until 2 x 10^{17} ions cm^{-2} (a critical concentration of 4.6 at%) with bubble diameters in the range 1-3 nm. Bubble ‘chain’ formation was observed in lengths of 10-30 nm, as can

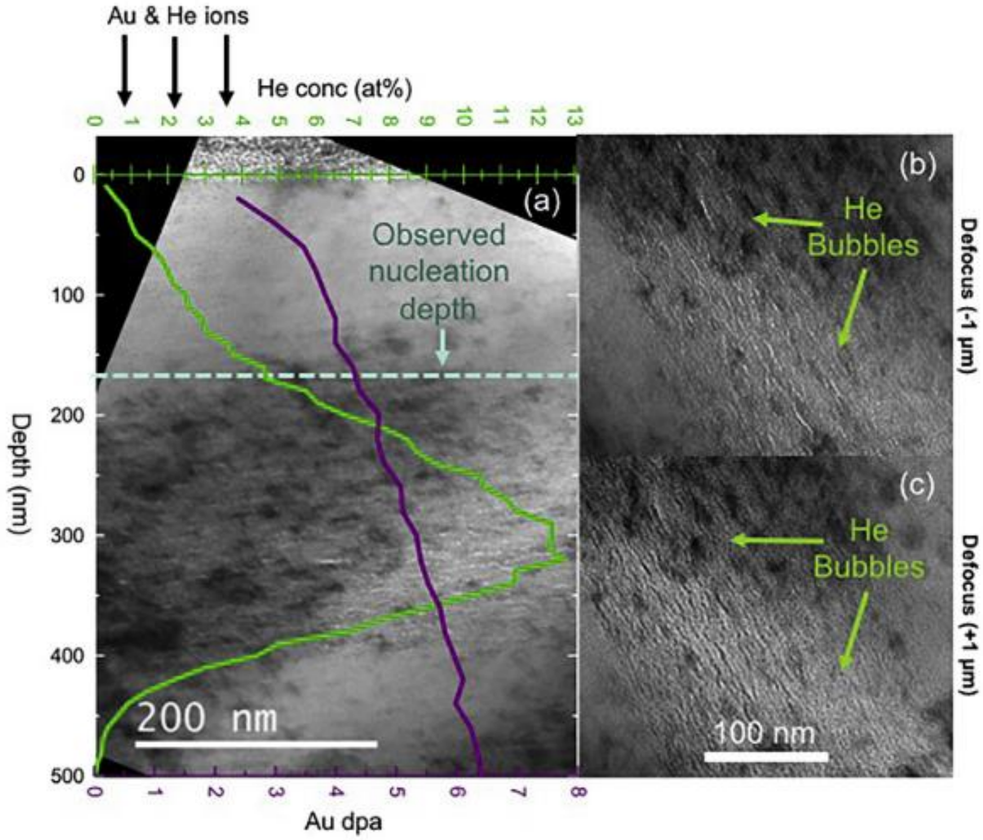

Figure 3.7 Helium bubble formation in $Gd_2Ti_2O_7$ pre-damaged with 7 MeV Au ions to a fluence of 2.2 x 10^{15} ions cm^{-2} and implanted with 65 keV He ions to 2 x 10^{17} ions cm^{-2}. Reprinted Fig 5. from C. A. Taylor, M. K. Patel, J. A. Aguiar, Y. Zhang, M. L. Crespillo, J Wen, H. Xue, Y. Wang, W. J. Weber, “Bubble formation and lattice parameter changes resulting from He irradiation of defect-fluorite Gd2Zr2O7” *Acta Materialia* 115, p118, 2016 with permission from Elsevier 2019. Available: http://dx.doi.org/10.1063/1.2901183

be observed in figure 3.7. Comparatively, $Gd_2Ti_2O_7$ is reported to have a critical concentration for bubble formation of 6 at%, with bubbles forming with an average diameter of 1.5 nm. Bubble formation is also reported in a pristine $Gd_2Ti_2O_7$ sample at this fluence, with bubble diameters averaging 2.1 nm and in higher density. A crystalline-amorphous transition was observed in the $Gd_2Ti_2O_7$ sample without pre-damage, suggesting a mechanism related to this transition that promotes bubble formation exists.

3.4 Closing Remarks and Research Aims

This chapter has discussed the various studies concerning radiation damage in perovskites and He bubble formation in several systems. A-site deficiency and its effect on radiation response and helium bubble formation is the central theme of this research and has received limited research interest as yet. The findings discussed pose several areas of research interest that were central to the work conducted within this thesis. Firstly, as this behaviour has only been observed with an A-site Sr parent cation, study of a system with a different A-site parent cation, namely the $Ca_{1-x}La_{2x/3}TiO_3$ system, was conducted to confirm this behaviour in another titanate system. Secondly, the effects of migration barriers brought on by distorted octahedral networks postulated by Smith *et al* [5] was investigated through the $Ca_{1-x}La_{2x/3}TiO_3$ titanate system. This offers a different structural landscape to $Sr_{1-x}La_{2x/3}TiO_3$. While the Sr sister system showed reductions in T_c in the cubic phase with minimal octahedral distortion, the $Ca_{1-x}La_{2x/3}TiO_3$ system maintains distorted octahedra in all three axes for $x \leq 0.5$, allowing for the role of octahedral distortions to be probed. The inverse is also applicable, whereby the increases in T_c with increased octahedral tilting can be tested as the $Ca_{1-x}La_{2x/3}TiO_3$ system reduces in distortion with La content. While T_c is a thermal *in-situ* measurement, this work has conducted *ex-situ* room temperature measurements. The caveats of *in-situ* studies have already been mentioned and such effects may have been due to this experimental set up. In order to test this possibility, *ex-situ* ion irradiation was employed within this study. Moreover, as these effects have only been observed for solely nuclear stopping regimes, an irradiation condition of 5 MeV Au^+ in which electronic stopping was dominant at the start of the damage track was also employed. This further allowed the effects of an ion other than Kr to be investigated. He bubble formation with regard to A-site vacancies has received no research interest, with the experiments of Matsunaga *et al* [130] offering evidence of enhanced bubble formation in oxygen deficient systems. Investigation of the $Ca_{1-x}La_{2x/3}TiO_3$ system allowed for the investigation of A-site deficient systems, while also probing the potential effects of enhanced and reduced resistance to amorphisation onset by A-site vacancies on helium bubble formation. The following four chapters present the results of investigations to elucidate these areas of interest by studying the $Ca_{1-x}La_{2x/3}TiO_3$ system.

4. Experimental Techniques

4.1 Introduction

The study of radiation effects within the $Ca_{1-x}La_{2x/3}TiO_3$ perovskite system has been undertaken using ion implantation, with various analytical techniques used to characterise the pre-and post-damaged states. Samples have been synthesised, characterised in the pristine state, bulk ion implanted and re-characterised to study induced radiation damage. Lastly, helium bubble formation has been observed using ion implantation *in-situ* in a TEM.

Synthesis was achieved via the solid-state route, with pristine structural characterisation undertaken using X-ray diffraction (XRD) and transmission electron microscopy (TEM), with grain size and elemental analysis undertaken using scanning electron microscopy/energy dispersive X-ray spectroscopy (SEM/EDS). These techniques ensured a high sample quality was achieved prior to ion implantation and clarified the structural characteristics of the system. Pristine characterisation further enabled comparison with the implanted samples and changes induced due to radiation damage.

Ion implantation has been used to induce the effects of radiation damage within the $Ca_{1-x}La_{2x/3}TiO_3$ system. This allows for the induction of damage without the use of radioactive material, requiring facilities for active handling and large timescales to allow observation of induced damaged, as was discussed within chapter 3. TEM and glancing-angle XRD (GAXRD) were the principle analytical tools used to characterise the effects of radiation damage induced by ion implantation. TEM provides high resolution imaging, allowing for the direct observation of structural damage and defect formation induced by ion implantation. The ion implantation conditions used produce damaged surface layers < 1 µm thick, and cross-sectional TEM (XTEM) has been employed to observe these regions. GAXRD studies, which provide depth selective structural analysis of the surface as an average, were further employed to probe induced radiation damage. The technique follows the same basic principles as XRD, but by decreasing the incident angle of the X-ray source, X-rays are attenuated more rapidly with respect to depth penetrated. This provides high-quality, quantifiable data to further study radiation damage, and has been used to examine radiation induced volume swelling and structural amorphisation. Lastly, *in-situ* ion implantation in a TEM using 6 keV He^+ ions was undertaken on compositions of the $Ca_{1-x}La_{2x/3}TiO_3$ system. This implantation condition allows for the retention of He within the TEM samples and observation of He agglomeration and bubble formation.

The following chapter outlines the theory behind and practical application of all the techniques described above to synthesise samples, induce the effects of radiation damage and characterise the system in the pristine and damaged state.

4.2 Sample Synthesis

4.2.1 Solid-state Synthesis

Synthesis of the relevant compounds was achieved using the dry, solid-state reaction route. This is the simplest of the available synthesis routes but achieves the required sample quality and, in the case of the perovskites within this thesis, > 95 %th sample density. Solid-state reaction is often referred to as the “shake n’ bake” method of sample synthesis [30], through its use of powder mixing, sieving, pressing and heat treating. Powdered reagents are dried to remove any accumulated water vapour and weighed into stoichiometric quantities based on the desired chemical composition. The weighed powders are then mixed, for example in a horizontal roller or planetary mill, using an aqueous medium such as isopropanol or ethanol to maximise the homogeneous spread of the suspended particles. The use of such solvents is preferred to high-purity water, as they are relatively non-polar, reducing the potential for heterogeneous agglomeration of particles. Milling media such as zirconia or silicon nitride beads can be employed to reduce the powder particle size and encourage homogenous mixing. This is followed by drying to remove the solvent mixing agent and sieving to an appropriate particle size. Pressing of the mixed reagents is often undertaken to produce a green body, acting to increase the high-temperature reaction rate and, if desired, increase the density of the final product. This can be achieved uniaxially or isostatically to maximise green body compression. High-temperature firing provides the thermal energy required to mix particle reagents on the atomic level, or to ‘react’ the reagents into the desired composition [30]. Often solid-state reaction will require multiple heat treatments, with intermittent grinding, mixing and pressing, until the final sample composition and density is achieved. Optimisation of these processing steps will ultimately lead to the best possible sample quality.

The solid-state synthesis route was used to produce dense samples of the $Ca_{1-x}La_{2x/3}TiO_3$ solid-solution (x = 0, 0.1, 0.2... 0.9). Stoichiometric amounts of La_2O_3 (Alfa Aesar 99.99 %), dried at 1073 K for 24 hours, TiO_2 (Sigma-Aldrich 99.9 % ≤) and $CaCO_3$ (Alfa Aesar 99.9 %), both dried at 453 K for 24 hours, were weighed and milled with isopropanol in a planetary ball-mill for 5 minutes each. The drying step allowed for all excess water vapour to be removed from these reagents, allowing for accurate weighing with a four-point balance. Once dried, milled powders were passed through a 212 µm sieve to increase the reactive surface area during heat treatments and compression when pressing. Sieving was followed by uniaxial pressing into 13 mm diameter green-body pellets to increase the reaction of fired powders. The green bodies were reacted at 1573 K in air for 48 hours, as by Zhang *et al* [72]. This process did not produce dense pellets, as is required for accurate SRIM modelling and GAXRD studies. A final sintering and densification step was employed, achieved by a final stage of grinding, sieving, pressing, and heating at 1673 K in air for 8 hours. This produced dense pellets (> 95 %th) of the $Ca_{1-x}La_{2x/3}TiO_3$ series, with density measurements presented in chapter 5. The process is shown graphically in figure 4.1.

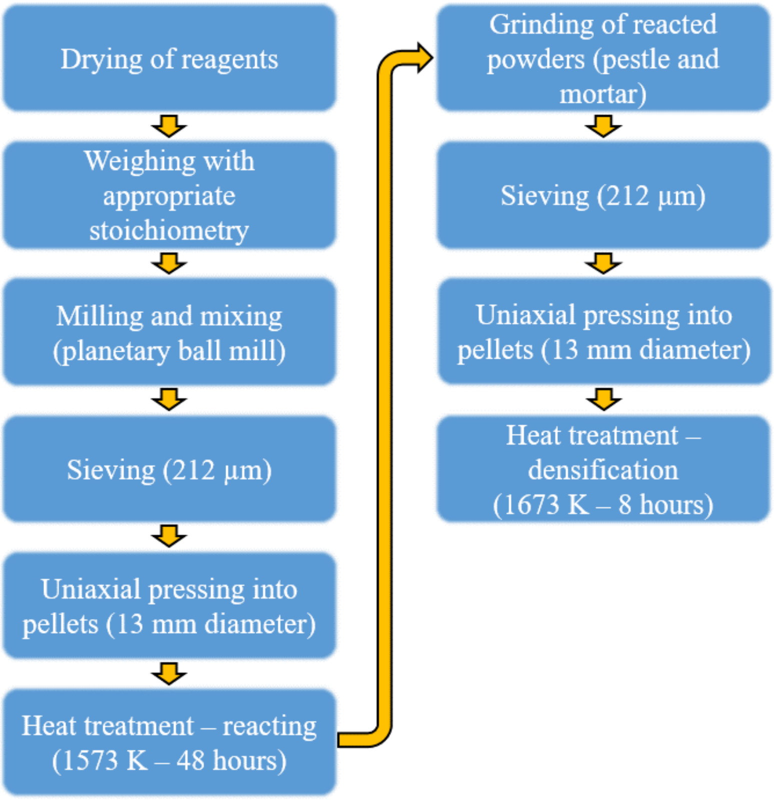

Figure 4.1 Flowchart of the synthesis route taken to produce samples of composition $Ca_{1-x}La_{2x/3}TiO_3$.

4.2.2 Grinding and Polishing

For ion implantation and various analytical techniques, sample surfaces required grinding and polishing to a high-grade finish (< 1 µm). This is due to the produced regions of damage, typically < 2 µm in depth. This was achieved via mechanically induced abrasive friction, using a vertical force automatic head-platen polishing unit (AutoMet, Buehler). This was combined with silicon carbide grinding papers and polishing cloths saturated with diamond crystals suspended in a water-based solution. Polishing was undertaken to a 0.25 µm finish for all samples within this thesis.

4.2.3 Density Measurement

Achieving a close to theoretical sample density is desirable when performing ion implantation to induce the effects of radiation damage. Porosity can lead to experimental errors when undertaking GAXRD analysis, as pores can expose non-implanted areas of the sample surface. Furthermore, an accurate measurement of density was required to estimate the damage-depth profile using the SRIM code [98] (see section 4.7) which requires an inputted value of density. This can be achieved via a simple measurement of volume and weight using callipers and high-accuracy scales, but is still limited by human error and the precision of the calliper used. For this reason, the Archimedes method was used, based on the principle that the apparent weight of an object suspended in a liquid will reduce by an amount equating to the weight of the liquid volume displaced. Measuring a samples weight first in air, and then suspended in water, sample density can be calculated as,

$$\rho = \rho_{\text{water}} \frac{m_1}{m_1 - m_2} \qquad (4.1)$$

where ρ is the sample density, ρ_{water} the density of water, m_1 is the weight of the sample in air, and m_2 the weight of the sample suspended in water. Within this work, all sample densities were measured five times and an average taken.

4.3 X-ray Diffraction

4.3.1 Bragg's law

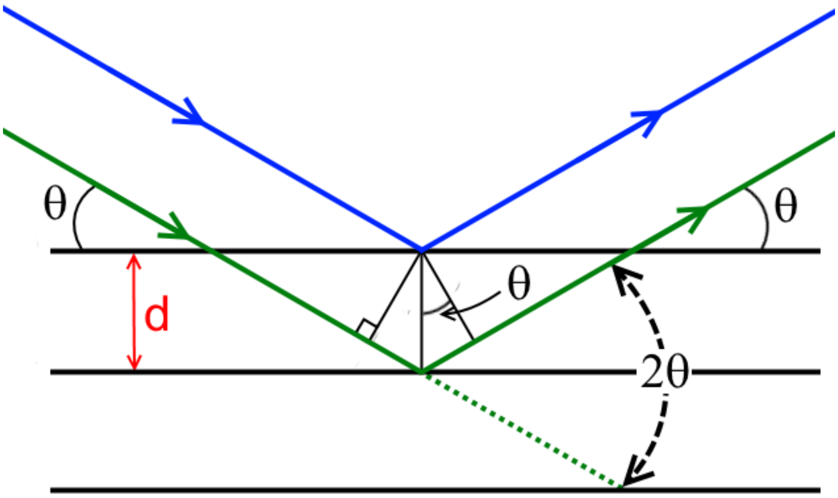

Figure 4.2 Diagram portraying the Bragg description of XRD. The incident X-rays are diffracted by two planes, with inter-planar spacing d, and reflect in-phase by an angle, θ, equal to the incident angle of the X-rays.

Structural analysis of synthesised samples was undertaken using XRD. This allowed for both phase identification and the calculation of structural unit parameters through non-destructive means. In reality, X-rays interact with matter through various scattering and absorption phenomena, but is most readily understood considering a uniform block of lattice planes separated by a distance d, as shown in figure 4.2. X-rays are scattered off a specific lattice plane in this example, and reflect at an angle equal to the incident angle of the beam. Two waves reflected with the same angle will present in-phase and interact constructively, leading to an increase in the detected intensity at that incident angle. Bragg's law defines the conditions for constructive interference to occur,

$$n\lambda = 2d\sin\theta\,, \tag{4.2}$$

where λ represents the X-ray wavelength, θ the scattering angle (the Bragg angle), d the inter-planar distance and n donates the requirement for the phase difference between reflected X-rays to equal a full wavelength for constructive interference. The planes available for constructive interference are structure dependant, planar reflections of which can be detected at different Bragg angles by changing the incident angle of the beam and detecting changes in intensity. Intensities are commonly reported with respect to 2θ, the angle between the incident and reflected beam, as this is what is experimentally detected. For the purpose of this research, measured values of 2θ were converted to d-spacing using equation 4.2, to allow for ease of observation with regard to ion implantation induced lattice expansion.

By focussing on a specific plane and corresponding d-spacing, unit cell sizes can be quantified. For the orthorhombic unit cell, in which all angles equal 90°, the lattice parameters a, b and c call be calculated as,

$$\frac{1}{d^2}=\frac{h^2}{a^2}+\frac{k^2}{b^2}+\frac{l^2}{c^2}, \qquad (4.3)$$

where h, k and l are miller indices of the reflecting plane.

In the present study, pristine X-ray diffraction was undertaken using a Philips PANalytical Powder X’pert3 diffractometer in reflection with Cu K_α (λ = 1.5418 Å). Samples were run between 10° and 100° with a step size of 0.02° and a step time of 1 s, with X-rays generated at 45 kV, 40 mA. An external silicon calibration was performed before measurements were commenced. Phase identification was undertaken using a combination of PDF4/Sieve+ software, comparison with the literature and by observing the appearance and diminishing of structure specific reflections. Lattice parameter calculations were undertaken using equation 4.3.

4.3.2 Glancing-Angle XRD

By reducing the X-ray angle incident upon the sample, the fraction of X-rays reflected within a surface region can be increased until only, for example, a damaged region is examined. Under a certain critical angle, Ω_c, an X-ray beam will be fully reflected by a depth on the order of < 50 nm. The critical angle can be calculated as

$$\Omega_c = 1.6 \times 10^{-3} \rho^{1/2} \lambda$$

where ρ denotes the sample density in g cm^{-3} and λ the incident X-ray wavelength in Å [141-145]. For $CaTiO_3$ (ρ = 3.996 g cm^{-3}, $\lambda_{CuK\alpha}$ = 1.5418 Å) this value is Ω_c = 0.282°. For $Ca_{0.1}La_{0.6}TiO_3$ (ρ = 5.102 g cm^{-3}, $\lambda_{CuK\alpha}$ = 1.5418 Å), Ω_c = 0.319°. If the incident angle employed is greater than this value, the X-ray will propagate into the sample and the linear absorption coefficient, μ, can be used to calculate the penetration depth, x. In this study, the lowest incident angle employed was $\Omega = 0.5°$ due to diffractometer limits, meaning $\Omega > \Omega_c$ always applied. The required angle to observe a region can be calculated using trigonometry, given by,

$$\Omega = \sin^{-1}\left(\frac{x}{3\mu}\right), \tag{4.4}$$

where Ω donates the angle of incidence, x the region thickness and μ the attenuation length of the compound. The attenuation length is defined as the length travelled before the X-ray intensity falls to 1/*e* of its original value, and an analysis depth of 3 μ is commonly assumed, leading to a > 95 % attenuation of incident X-rays in the defined thickness. The calculation of attenuation length for a compound is determined through addition of μ values of each individual element, multiplied by a weight fraction term for the specific unit cell, given by,

$$\mu = \sum_i w_i \mu_i,$$

Where w_i represents the weight fraction of the ith atom of the compound, and μ_i the attenuation legnth for the ith atom. Practically this has been achieved using the Hephaestus software package [146], which combines data from several databases and

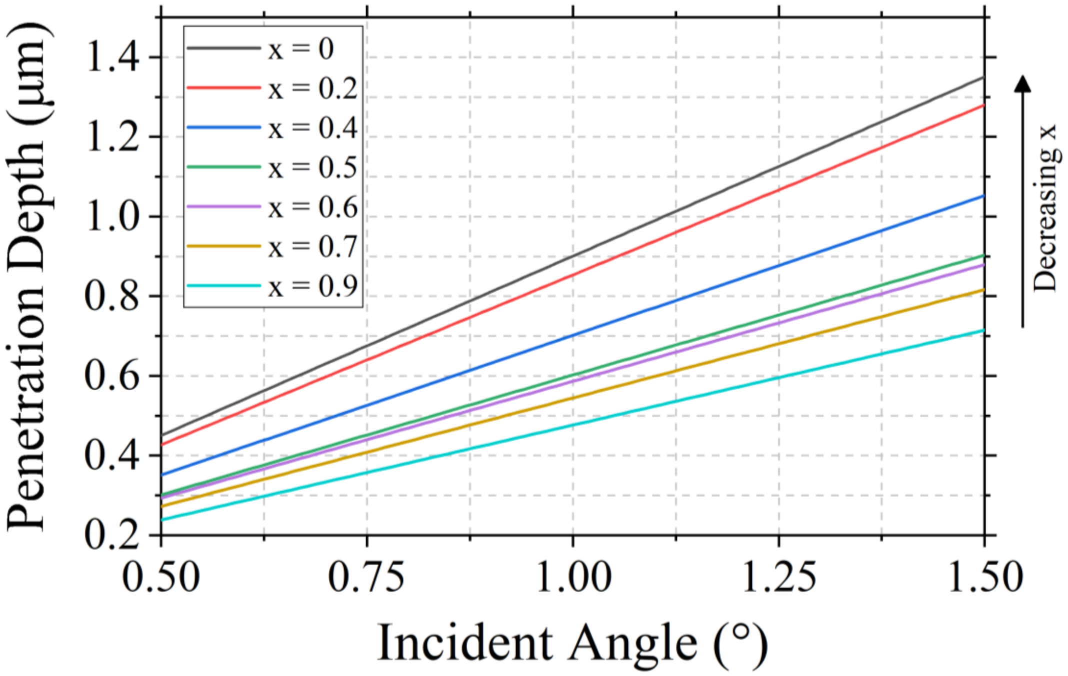

Figure 4.3 X-ray penetration depth with GAXRD incident angle for the x = 0, 0.2, 0.4, 0.5, 0.6, 0.7 and 0.9 samples.

user input values of composition, density and X-ray energy to calculate an attenuation length. Equation (4.4) was then employed to calculate the penetration depth at specific incident angles. Figure 4.3 shows the penetration depths of each sample with increasing incident angle, and penetration depths for each sample at Ω = 0.5° are reported throughout chapter 7.

The surface ion implanted regions of x = 0, 0.2, 0.4, 0.5, 0.6, 0.7 and 0.9 bulk ceramics were examined using a Philips PANalytical X'Pert^3 diffractometer in glancing-angle parallel beam configuration with Cu K_α (λ = 1.5418 Å). These samples were investigated to give a wide representation of the system, including La content and phase transitions. Incident angles of 0.5°, 1.0° and 1.5° were employed through a 2θ range of 20° - 60°, with a step size of 0.04° and a step time of 20s. Conversion to d-spacing was made using equation 4.2. A ¼° divergent slit and a 10 mm beam mask were employed, with both incident and detected beams passing through 0.04 rad Soller slits. The pellet of examination was placed within a 12 mm diameter circular cavity, machined into a silicon zero-background holder to ensure only response from the irradiated surface was received by the detector at low incident angles. X-ray penetration depths were calculated using X-ray attenuation theory as discussed and the Hephaestus software package [146].

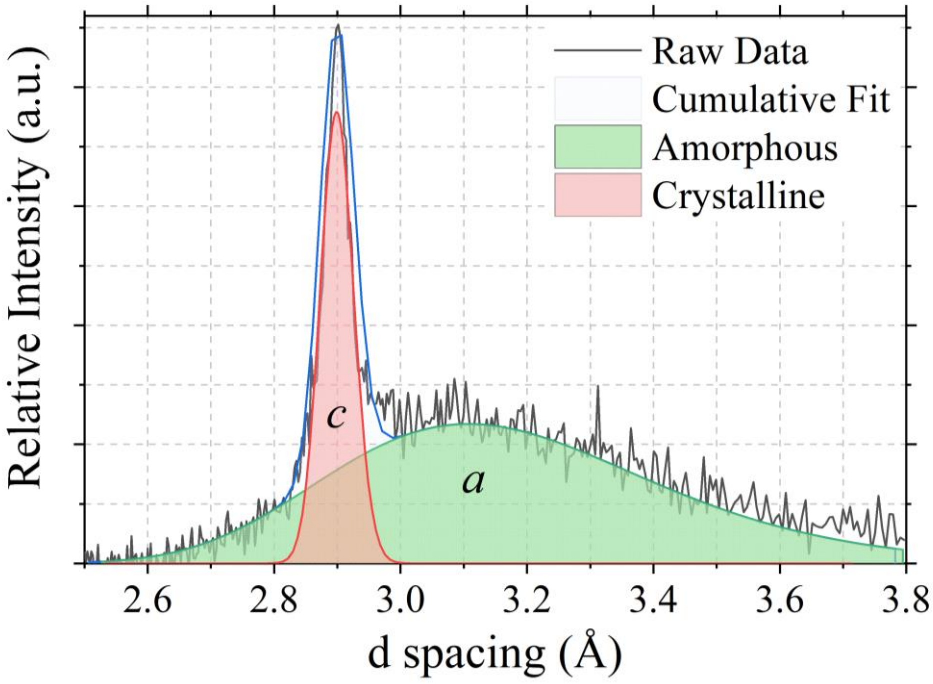

Figure 4.4 Example of a pseudo-Voigt fit of the 5 MeV Au$^+$ irradiated x = 0.5 $Ca_{1-x}La_{2x/3}TiO_3$ sample.

Amorphous fractions were calculated by fitting pseudo-Voigt peaks to the major lattice expanded $(101)_p$ reflection and diffuse scattering intensities, as has been employed by various studies [105,147,149], and taking a ratio of the amorphous area to the total area fitted. The $\Omega = 0.5°$ patterns were used to determine the amorphous fraction percentage, as this represents the damaged regions according to SRIM. An example of a sample of composition $x = 0.5$, showing both crystalline and amorphous components fitted with pseudo-Voigt peaks is shown in figure 4.4. For the $x = 0$ and $x = 0.5$ samples, only reflections related to radiation damage induced volume swelling were included in the calculations, as pristine reflections do not originate from the damaged region.

4.4 Scanning Electron Microscopy/Energy Dispersive Spectroscopy

Assessment of sample quality through grain size, porosity and elemental composition analysis was undertaken using SEM/EDS. The observable range of SEM stretches from < 10 μm to the nanoscale, operating in a reflection configuration using the phenomena exhibited by a specimen irradiated with a beam of electrons. Figure 4.5 presents a schematic of a basic SEM setup. An accelerated beam of electrons, in the order of < 30 keV, is focused using a series of electromagnetic lenses onto the surface of a specimen, leading to the near-surface emission of secondary electrons, back-scattered electrons and characteristic X-rays. Secondary electrons are emitted after being excited with sufficient energy by the incident electron beam to escape the sample surface. Emission is from < 10 nm from the sample surface, allowing for high-resolution imaging. Back-scattered electrons are beam electrons that are elastically scattered by lattice atoms < 1 μm deep and are ejected from the surface. They are more penetrating than secondary electrons, offering reduced image quality. However, they are intrinsically Z-sensitive as atoms with greater Z have a greater probability of elastic scattering. This provides elemental contrast within back-scattered electron images. A consequence of electron beam irradiation is the inevitable displacement of electrons from the inner shells of lattice atoms. Displacement leads to an electron in a higher energy state filling the now vacant shell, with energy being conserved through the emission of an X-ray characteristic to the emitting element. Such X-rays can be used to semi-quantitatively undertake elemental analysis through the produced spectra and allow for elemental mapping of the sample surface. This is known as energy dispersive spectroscopy (EDS).

In the present study, a Hitachi TM3030, operating in back-scatter electron configuration was used, with imaging undertaken using a 15 kV acceleration voltage in a partial vacuum. Pellets were mounted on aluminium stubs with 12mm adhesive carbon tabs (Leit, AGAR). EDS mapping was undertaken using a 10 kV acceleration voltage and a Quantax70 spectrometer with a 154 eV resolution silicon drift detector. Imaging and elemental mapping was undertaken at 2500x and 7000x magnification. Grain size analysis was undertaken by measuring the area of > 25 grains within SEM images using the ImageJ "analyze particles" function to produce a grain size distribution and an average range reported.

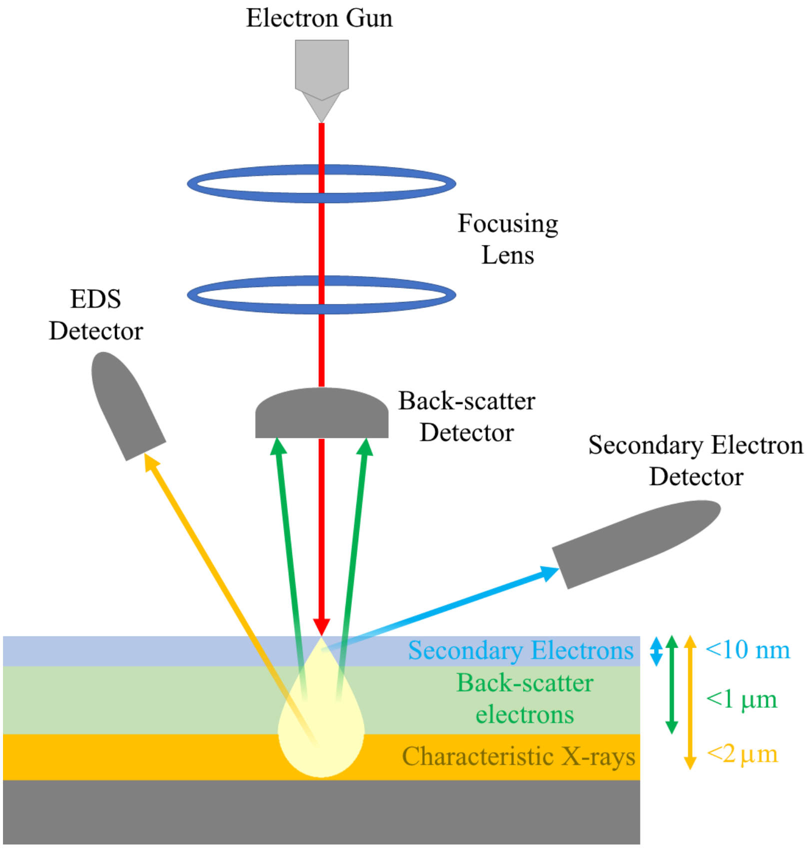

Figure 4.5 Basic schematic of an SEM setup, including escape depths for detectable secondary and back scattered electrons, and characteristic X-rays.

4.5 Transmission Electron Microscopy Sample Preparation

4.5.1 Cross-sectional and Plan-view Sample Preparation

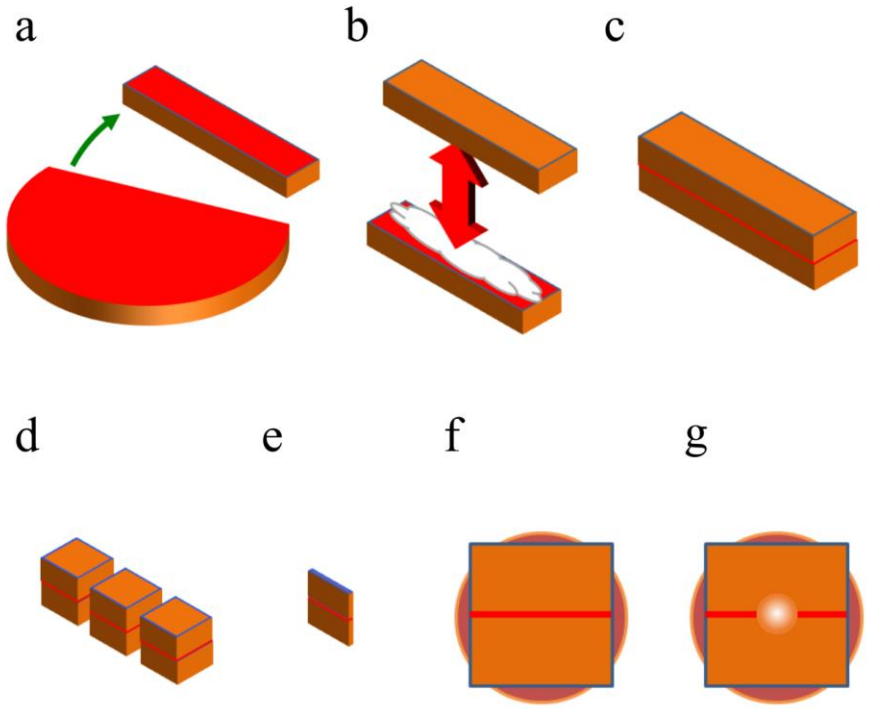

Figure 4.6 Schematic of XTEM samples preparation. In each case, red refers to the ion irradiated surface of the sample. (a) sectioning (b) gluing of two sections (c) glued cross-section (d) sectioned cross-section “sandwiches” (e) thinned cross-section (f) cross-section mounted on TEM grid (g) ion milled and mounted cross-section

In order for TEM analysis to be undertaken, sample preparation to achieve electron transparency was required. Characterisation of surface implanted samples requires location specific thinning, and easy identification of the sample surface. For this purpose, cross-sectional samples were produced. Plan-view samples were produced for *in-situ* ion implantation in a TEM, following the same process as the cross-sectional samples whilst omitting the cross-sectional sample preparation steps described.

The process of XTEM sample production is shown schematically in figure 4.6. Samples were sectioned into 2 x 2 x 1 mm dimensioned cuboids using a slowly rotating diamond edged circular blade with oil-based lubricant. Cross-sectional samples were produced as two implanted surfaces fixed to one another to create a surface-surface interface. A thin layer of Gatan G1 epoxy was applied to the implanted surface of a sectioned piece of material, with another implanted surface placed on top to create an interface. The resultant cross-section was clamped in a PTFE clamp and the epoxy set for 1 hour at 353 K to minimise thermal annealing of the implanted interface. This temperature will lead to minimal, if any, annealing of damage.

Initial thinning of samples was undertaken using mechanical polishing and grinding using a Buehler Ecomet 250 grind and polish unit. Samples were first mounted to an aluminium stub with CrystalBond (Gatan) and ground with silicon carbide grinding papers (Buehler), before polishing to a 0.25 µm finish with diamond suspension (MatPrep). After achieving this finish, the specimen was overturned and grinding was undertaken to reduce the sample to < 100 µm before polishing with diamond suspension to < 50 µm thickness.

Further mechanical thinning was undertaken using a Gatan dimple grinder unit. After mounting to a glass stub, the sample was rotated while a 1 mm thick copper wheel continuously grinds the sample with diamond suspension in a circular motion with a 0.2 N downward force. As the centre of the copper wheel is always in contact with the sample surface, a ‘dimple’ is created, with a thin centre and a thicker outer rim. Once < 20 µm thin, a felt wheel replaced the copper and 1 µm/0.25 µm diamond suspension thinned the sample close to perforation. Once dimple ground, the samples were mounted to Mo TEM slot grids (Agar) using G1 epoxy (Gatan).

4.5.2 Ion Beam Milling

Ion beam milling uses low energy ions to induce surface sputtering in a target sample until electron transparency is achieved. Sample rotation is employed to form a close to uniform ring of transparency. Duals beams are commonly employed, both to reduce milling times and increase transparency, whilst also removing any redeposited material sputtered onto the surface. This process is shown schematically in figure 4.7. Typically, angles have been employed < 30°, but improvements in ion beams have reduced milling times and angles ≤ 10° are now commonly used. The desire to minimise ion beam induced chemical or structural effects is achieved through the use of inert gases such as Argon with energies ≤ 10 keV. This provides a heavy enough ion to give reasonable sputtering rates, whilst light enough to reduce ion beam induced damage. The inert nature of Ar also minimises any risk of chemical contamination.

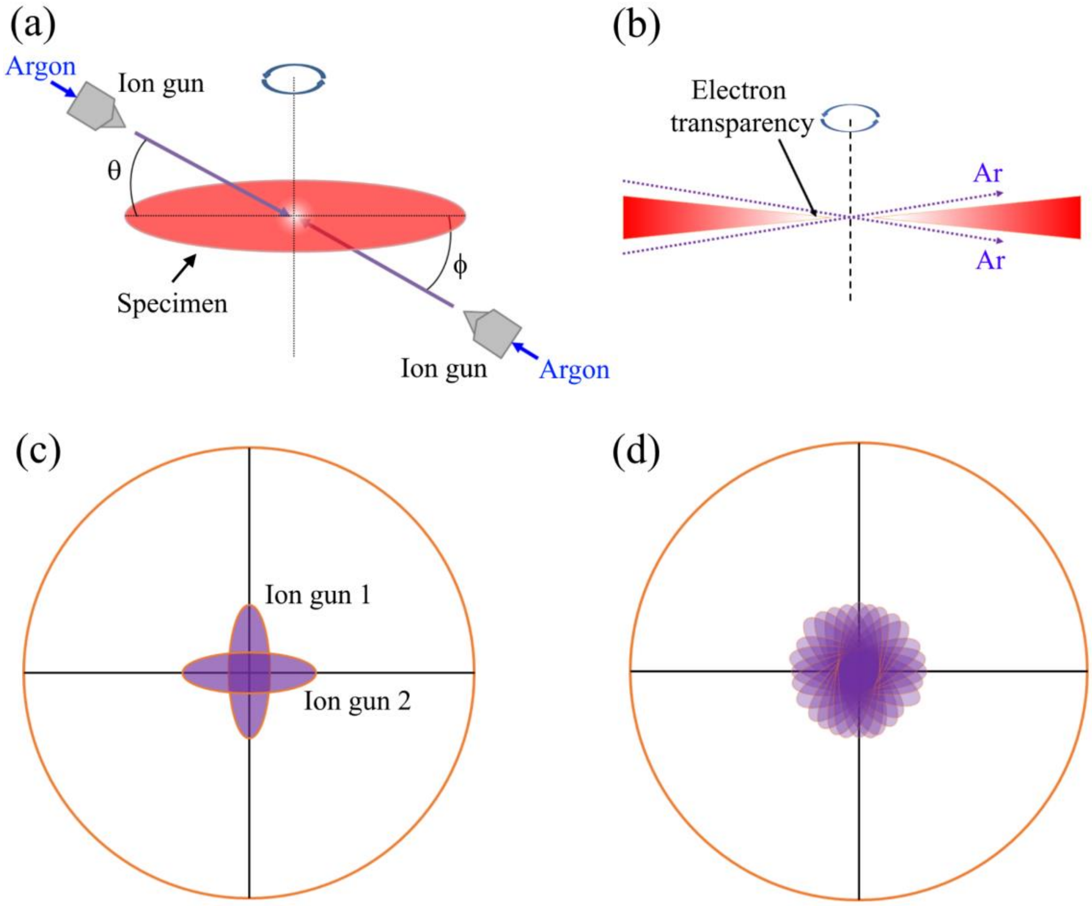

Figure 4.7 Diagrams of the ion milling process to produce electron transparent TEM samples. (a) Schematic of the ion milling process, (b) enlarged view of milling to transparency, (c) the cross-over achieved by dual beam ion guns and (d) the milling area induced by sample rotation.

Thin ion beam induced surface amorphous layers are the primary consequence of this thinning technique, and the strategies for damage reduction are widely reported in the literature [150–159]. This is most commonly attained through employing shallower incident milling angles and lower energy incident ions, consequently leading to increased milling times. A regime of higher energy and angle thinning, followed by reduced energy and angle thinning is employed as a compromise. A further consequence of using energetic ion milling is the transfer of kinetic energy from the ions to the sample, with specimen heating potentially induced as a result. Samples are susceptible to heating of < 437 K [151], although this is material dependant [160,161].

For the purpose of this research, a Gatan PIPS II was used to prepare samples by ion beam milling. After initial mechanical thinning using polishing wheels and dimple grinding, samples were thinned to near perforation using an 8° angle, 4 keV Ar+ ion beam, followed by further thinning to perforation using a 6° angle, 2 keV Ar+ ion beam, with final thinning using a 4° angle, 0.5 keV Ar^+ ion beam. This procedure was developed to prevent surface modification observed within the $Ca_{1-x}La_{2x/3}TiO_3$ system, as is outlined in chapter 6 of this thesis. The samples presented in chapter 6 underwent various different milling recipes, including different energies and milling temperatures, and these are identified within the chapter. All milling was undertaken using a Gatan PIPS II, and the same initial grinding procedure prior to ion milling was employed.

4.5.3 Crushed Grain Sample Preparation

Samples were also prepared using finely ground synthesised powders. Materials can be prepared for TEM analysis using this technique, providing grains of thickness that allow for electron transparency. This preparation route involves no mechanical polishing or ion beam milling, and observed regions of electron transparency should be unaltered from the pristine state. Whilst minimising the potential for sample alteration, samples prepared via this route do not allow for observation of surface implanted regions or grain boundaries, as with the cross-sectional or plan-view techniques.

Preparation of crushed grain samples was performed by rapidly hand grinding a small amount of powdered material in a pestle and mortar with isopropanol for 5 minutes, with the fine particulates then allowed to settle. Liquid was syphoned from the very top of the solvent line and pipetted onto a 300 µm copper mesh grid lined with carbon holey support film and allowed to dry.

4.6 Transmission Electron Microscopy

Within this research, TEM has been used extensively. An accelerated electron beam, in the keV to MeV regime, allows for observations to be made on the length-scale of defects and structural damage induced by radiation damage. Whereas SEM operates in a reflection geometry, TEM relies on the transmission of electrons through a specimen. Depending on the material, the electrons will be variously scattered, and thereafter are directed onto a fluorescent screen or CCD camera. Furthermore, diffraction phenomena that occur through electron wave-particle duality allow for detailed levels of structural characterisation, including space group analysis, unit cell quantification and, when considering radiation damage, investigation of crystalline-amorphous phase transitions.

Various TEMs have been employed within this research to examine bulk irradiated TEM samples, prepared as outlined previously. Imaging was undertaken using either a FEI Tecnai F20 operating at 200 keV or a JEOL 3010 operating at 200 keV. In each instance, imaging and diffraction was undertaken using a CCD camera. All images have been taken in bright-field mode with conventional electron diffraction employed to study structural effects.

Electron diffraction patterns were analysed through a combination of the Single Crystal software package and comparison with the literature. Analysis of polycrystalline diffraction was undertaken by taking 15 individual line-scans of a concentric rings pattern in the ImageJ software package. This produces a greyscale intensity diffractogram, which was converted to d-spacing using the camera length when capturing the diffract pattern. The line-scans were calibrated to the central spot of the diffraction pattern before normalisation to the highest intensity peak and addition of the patterns to create an average. Images of the line-scans and averaging procedure are given in appendix 2.

4.7 Ion Implantation

4.7.1 Bulk Ion Implantation and SRIM

A description of the physics of radiation damage was given in section 2.2, and practically this is achieved used large ion accelerators. Three ion implanters were used within this research, two *ex-situ* and an *in-situ* setup described in section 4.7.2. In order to configure the implantation conditions, the SRIM software package was employed [98]. Whilst the software package allows for calculations of various stopping power and energy loss values, the Monte Carlo code within the software allows for estimates of ion implantation range, vacancy/displacement quantification and dpa calculations. These values are calculated using a defined implantation species and energy, based on displacement values for the inputed atomic compound species and sample density. For the purpose of this research, the ‘Detailed Calculation with Full Damage Cascades’ option (SRIM 2008) was operated, with 99,999 ions run for all calculations. As mentioned in chapter 2, various displacement energies are reported for Ca, La, Ti and

O, so each atomic component was set with a displacement energy of 50 eV with density inputs based on those reported in section 5.2.

The Australian National University operates a National Electrostatics Corporation 5SDH 1.7 MV pelletron accelerator [162]. A negative ion beam is produced at the ion source, after which ions are accelerated to 20-30 keV before passing into the pelletron. This is a tandem accelerator, as ions pass through a dual stage acceleration tube of alternating metal and ceramic rings. Stage one involves negatively charged ions being accelerated toward a positively charged high voltage terminal. Ions are then stripped of ≥ 2 electrons to achieve a positive charge before entering the second stage and acceleration away from the positive terminal. This process is capable of achieving ions with MeV energy levels. Similarly, the University of Surrey operates a 2 MV Tandetron ion implanter capable of MeV ion acceleration [163]. A heavy ion negative sputter source is employed to produce ions from almost all of the periodic table, after which ions are accelerated through acceleration tubes using a Cockroft-Walton type high voltage power supply.

In the present study, 1 MeV Kr^+ ion implantation was undertaken at the University of Surrey, using a 2 MV high energy Tandetron ion implanter at room temperature, to a total fluence 1 x 10^{15} ions cm^{-2} with a flux of 8 x 10^{11} ions cm^{-2} s^{-1}. 5 MeV Au^+ ion implantation was undertaken at the Australian National University (Canberra), using a National Electrostatics Corporation 5SDH 1.7 MV tandem accelerator at room temperature to a total fluence of 5 x 10^{14} ions cm^{-2} with a flux of 6 x 10^{11} ions cm^{-2} s^{-1}.

4.7.2 In-situ – MIAMI I and II

Implantations have been undertaken using *in-situ* implantation in a TEM to investigate helium bubble formation in $Ca_{1-x}La_{2x/3}TiO_3$ ceramics. Various facilities exist to this end, but for the purpose of this work the MIAMI I and II facilities at the University of Huddersfield have been employed [164]. The MIAMI I system employs a Colutron G-2 ion source, allowing for the acceleration of various ions in the energy range of 0.5-10 keV. Due to the mechanics of the TEM column it is not possible to

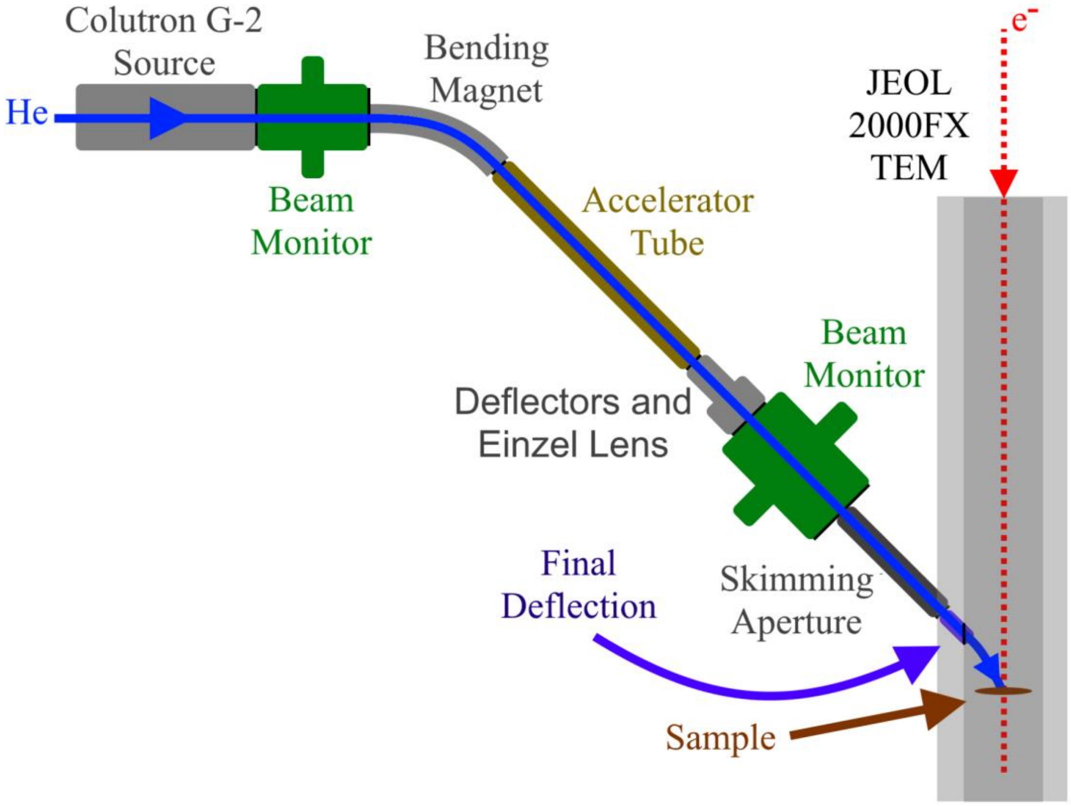

Figure 4.8 Basic schematic of the MIAMI I *in-situ* ion accelerator, adapted from [164].

implant at a normal to the sample surface, so accelerated ions are magnetically bent through a 53° profile to allow for a steep angle of entry into the column. Post-acceleration is available after the bending magnet allowing for acceleration < 100 keV. Ions are focussed using an Einzel lens and dual electrostatic deflectors, before a final deflection gives an implantation angle of 30° to the sample normal. The ion beam enters a JOEL 2000FX 200 keV TEM, with various heating/cooling stages available and imaging undertaken using an ORIUS SC200 CCD camera. Throughout implantation, the ion beam is monitored at several stages. Initial monitoring is undertaken using two National Electrostatic Corporation profile monitors, consisting of helical wires that detect ion beam generated secondary electrons which are collected as a current. These are placed directly after the ion source and on the beamline chamber, giving a dual-axis beam profile. A skimming diaphragm ensures the ion beam enters the final deflection stage at zero-potential between the deflection plates, whilst also allowing for a beam current reading as it is struck. Finally, a current meter rod is employed to enter the TEM column where the sample will sit, and provides a current reading after the final deflection. Calibration between the skimming diaphragm and the current reading allows for the current/flux to be monitored throughout an experiment. This set up is shown in figure 4.8. The MIAMI II facility was also employed, in this instance to investigate helium bubble formation in grain boundaries. The system operates with a higher ion beam accelerator voltage of < 350 keV, however as with MIAMI I it operates a < 20 keV Colutron source, with post acceleration possible if required. The beam enters a 300 keV Hitachi H-9500 TEM at 18.6° from the electron beam, with images captured using a Gatan OneView CCD camera. The effects of this change in angle are discussed in chapter 8.

Samples of the compositions x = 0, 0.1, 0.2, 0.4, 0.6, 0.7 and 0.9 were prepared for TEM observation using both the crushed grain and ion milling methods described in section 4.5. An extra sample of composition x = 0.2 was also prepared via the crushed grain route using Mo (400-mesh) carbon holey grids (Agar) to allow for high-temperature implantation. Based on SRIM calculations, 6 keV He^+ ions were used to maximise helium retention in the samples. These SRIM calculations are presented in chapter 8 and discussed in detail. The flux in all cases was 4.2×10^{13} ions cm^{-2} s^{-1}, with each sample implanted to total fluence of 1×10^{17} ions cm^{-2} (2.1 at% at 40 nm predicted by SRIM). In order to avoid dual-beam effects such as electron beam damage and recovery, ion implantation was undertaken in 2-minute intervals, during which the electron beam was turned off and after which the ion beam was disabled to allow for imaging and selective area electron diffraction patterns to be taken. TEM *in-situ* observation was undertaken at an operating voltage of 200 keV, with images and diffraction patterns captured using the CCD camera. Imaging was undertaken through-focal-series, with the objective lens ≈ 500 nm under, in and ≈ 500 nm over focus to allow for accurate identification of bubbles. The same procedure was repeated for samples of composition x = 0, 0.2, 0.4, 0.6, 0.7 and 0.9 using the MIAMI II system, however samples were prepared as PVTEM samples. The TEM was operated at 200 keV and a flux of 4.2×10^{13} cm^{-2} s^{-1} was maintained. Identification of helium bubble formation required the through-focal-series method. This is a systematic procedure that was employed. An under-focus electron beam will focus electrons below the TEM image plane, while an over-focus beam will focus electrons above the TEM image plane [151]. This has the effect of producing Fresnel fringes, which can be used to identify lattice defects such as helium bubbles. Helium bubbles will present as light regions with a dark fringe in under-focus images and as dark regions with light fringes in over-focus images. To practically achieve this, the TEM was focused ≈ 500 nm under- and over-focus, with images taken in both conditions. Comparison of through-focal-series images allowed for the identification of helium bubbles by aligning the observed Fresnel fringes. An example of the contrasting under-focus and over-focus images can be observed in figure 4.9. Bubble diameters were measured using the ImageJ program, an example of which can be observed in figure 4.9. Linescans were taken of bubbles formed in both grain boundaries and in the bulk and scaled depending on the magnification of the image. In each case, > 50 bubbles were measured for each sample. This process was undertaken on both under- and over-focused micrographs to minimise any bias induced using a particular focal series. An average bubble diameter was then determined by grouping bubble diameters into ± 0.2 nm groups to form a bubble distribution, as observed in figure 4.10. A pseudo-Voigt fit was then performed using the OriginLab 2018 software package to give the average bubble diameter and associated error. All bubble diameter analysis was undertaken on samples ion implanted to a fluence of 1 x 10^{17} ions cm^{-2}. This process has been commonly employed in the literature to produce average bubble diameters [118,120,124,129,138–140].

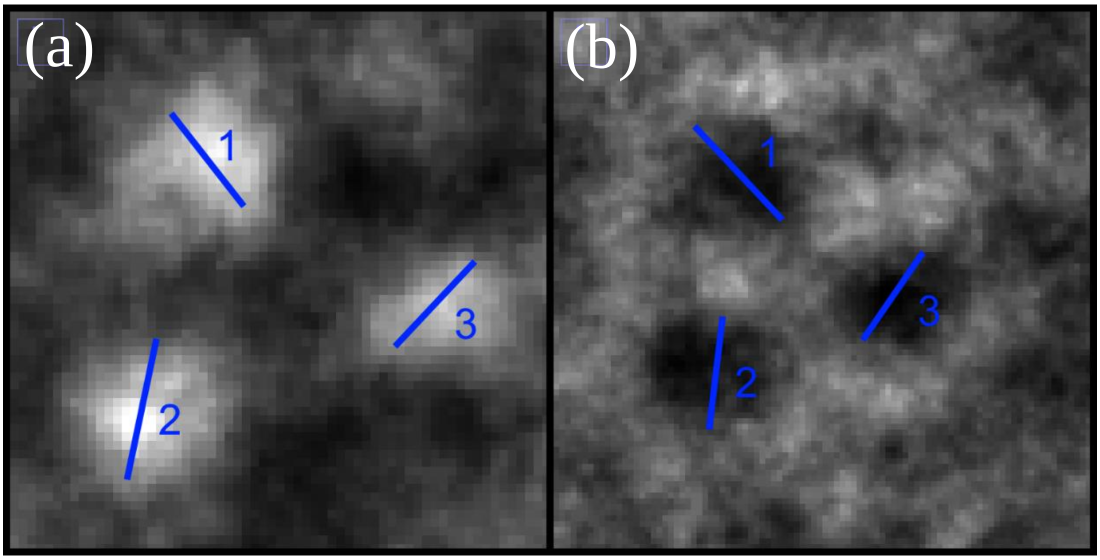

Figure 4.9 Graphical representation of various bubble diameter measurements taken using ImageJ for (a) under-focus and (b) over-focus micrographs.

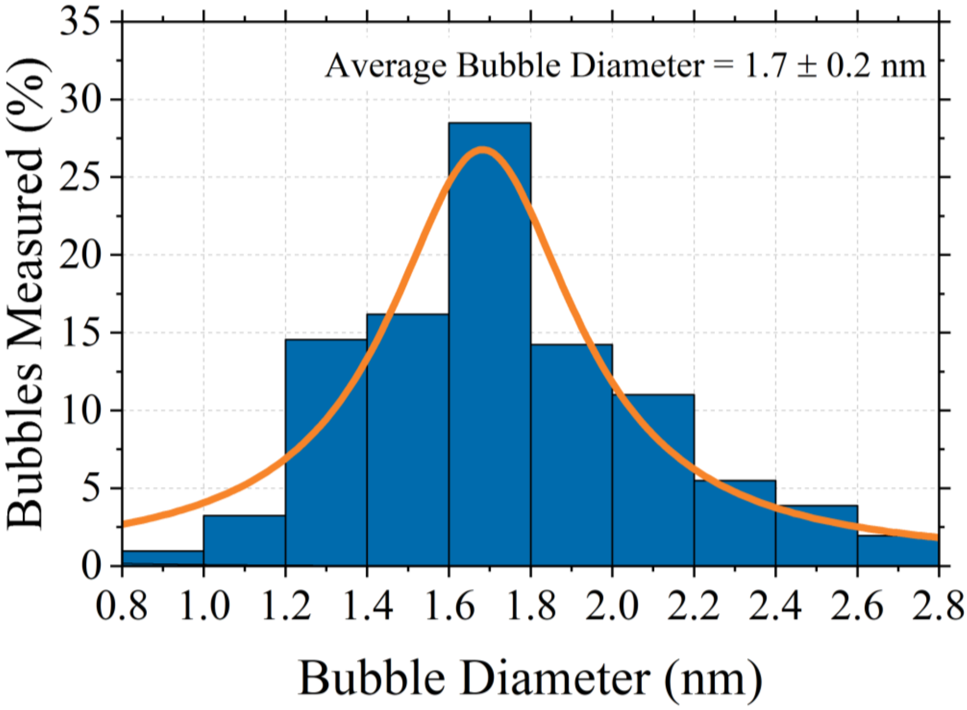

Figure 4.10 Bubble size distribution for the crushed grain x = 0 sample ion implanted with 6 keV He^+ to a fluence of 1 x 10^{17} ions cm^{-2}.

5. The Pristine $Ca_{1-x}La_{2x/3}TiO_3$ System

5.1 Introduction

Prior to radiation damage investigations, the $Ca_{1-x}La_{2x/3}TiO_3$ system was fully characterised in the pristine state using XRD, SEM, and TEM. This allowed for initial structural characterisation, including identification of phase transitions and induced structural changes, validation of sample integrity prior to undertaking ion implantation experiments and for comparison of the pre- and post-implanted states.

Sample density requires accurate quantification, having a significant impact on X-ray penetration depth when undertaking GAXRD studies, and is a variable in the calculation of damage profiles using the SRIM Monte Carlo software package. Furthermore, compositional purity, in particular when examining < 1 µm thin damaged surface regions using GAXRD and XTEM, was essential to ensure observed damage formation was representative. The crystal structures of pristine samples were indexed and confirmed prior to irradiation of a specimen using XRD and electron diffraction pattern analysis, to allow direct comparison with implanted samples to determine any damage-induced structural modifications. The following chapter presents pristine sample characterisation to this end, prior to undertaking irradiations.

5.2 Sample Density

Sample density measurements were undertaken using the Archimedes method. In each case, 5 measurements were conducted and an average taken, presented in table 5.1. Sample 1 refers to that used for 1 MeV Kr^+ implantation, and sample 2 for 5 MeV Au^+ implantation. Theoretical values were based on unit cell sizes reported in the literature [2,44,48] and composition. All samples, with the exception of the $x = 0.1$ sample, had theoretical density in excess of 95 %th, and for this reason the $x = 0.1$ sample was not used for ion implantation experiments. Densities of > 95 %th are commonly sufficient for ion implantation [11,139,140,165], accurate damage estimations using SRIM [98], and reliable GAXRD analysis.

Table 5.1 Calculated densities of samples in the system $Ca_{1-x}La_{2x/3}TiO_3$, and associated theoretical densities, for both samples used in *ex-situ* ion implantations.

x	**Sample 1 ϱ (g cm^{-3}) ± 0.01**	**Sample 2 ϱ (g cm^{-3}) ± 0.01**	**Theoretical ϱ (g cm^{-3}) ± 0.01**	**Sample 1 %Th ± 0.01**	**Sample 2 %Th ± 0.01**
0	3.996	3.983	4.039	98.94	98.61
0.1	3.757	3.801	4.101	91.61	92.69
0.2	4.100	4.081	4.163	98.49	98.03
0.3	4.221	4.208	4.366	96.68	96.38
0.4	4.360	4.394	4.589	95.01	95.75
0.5	4.533	4.567	4.741	95.61	96.33
0.6	4.660	4.647	4.830	96.48	96.21
0.7	4.776	4.705	4.948	96.52	95.09
0.8	4.873	4.795	5.085	95.83	95.30
0.9	5.102	5.153	5.233	97.50	98.47

5.3 Scanning Electron Microscopy (SEM)

Sample grain size and composition was investigated using SEM/EDS. Figure 5.1 shows back-scattered electron images of the x = 0, 0.2, 0.4, 0.5, 0.6, 0.7 and 0.9 pristine samples, as these samples were investigated after ion implantation. Limited porosity is observed within each sample, which was expected due to the highly dense nature of the samples. In all samples the grains exhibit non-uniform shapes. Grain sizes increase with La content: $CaTiO_3$ exhibits a typical grain size of 5 – 30 µm, the x = 0.2 and 0.4 samples comprise grains ranging in sizes from 10 – 30 µm, and for x ≥ 0.5 grain sizes are exhibited of < 50 µm. The increase in grain size was highly related to La content, and this is likely due to increased diffusion induced by increases in vacancy content.

Figure 5.2 shows an EDS map of the x = 0.2 sample, with oxygen counts shown in blue, titanium in orange, calcium in green and lanthanum in red. The EDS

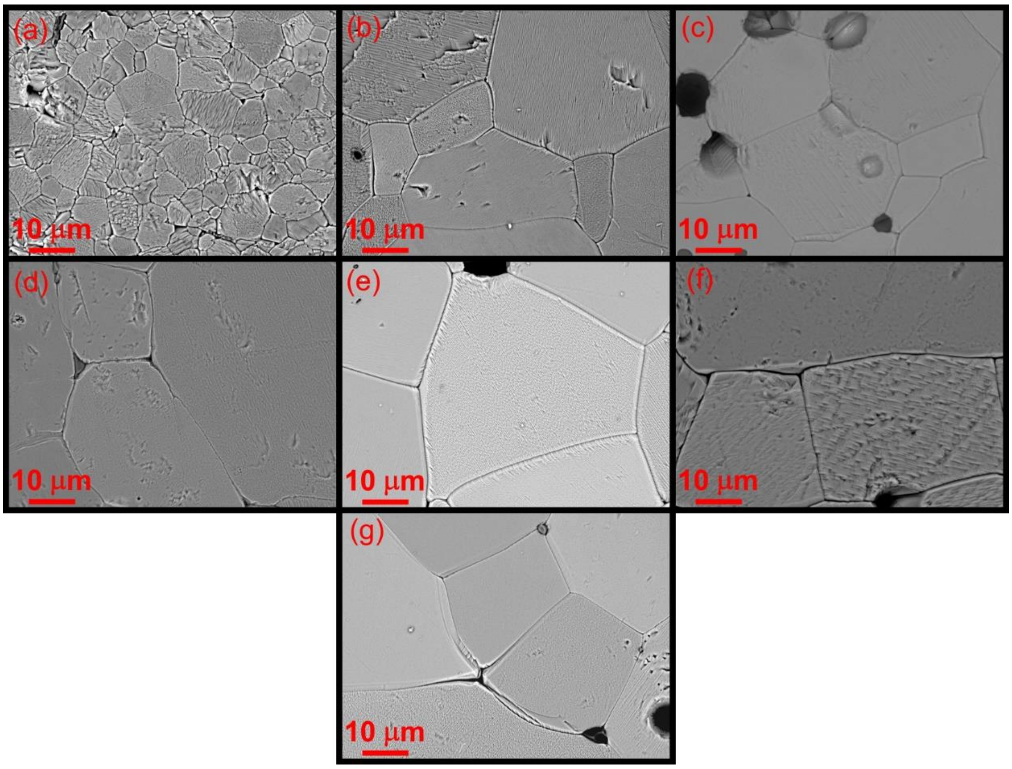

Figure 5.1 Back-scatter electron images taken at 2500x magnification for (a) x = 0, (b) x = 0.2, (c) x = 0.4, (d) x = 0.5, (e) x = 0.6, (f) x = 0.7 and (g) x = 0.9

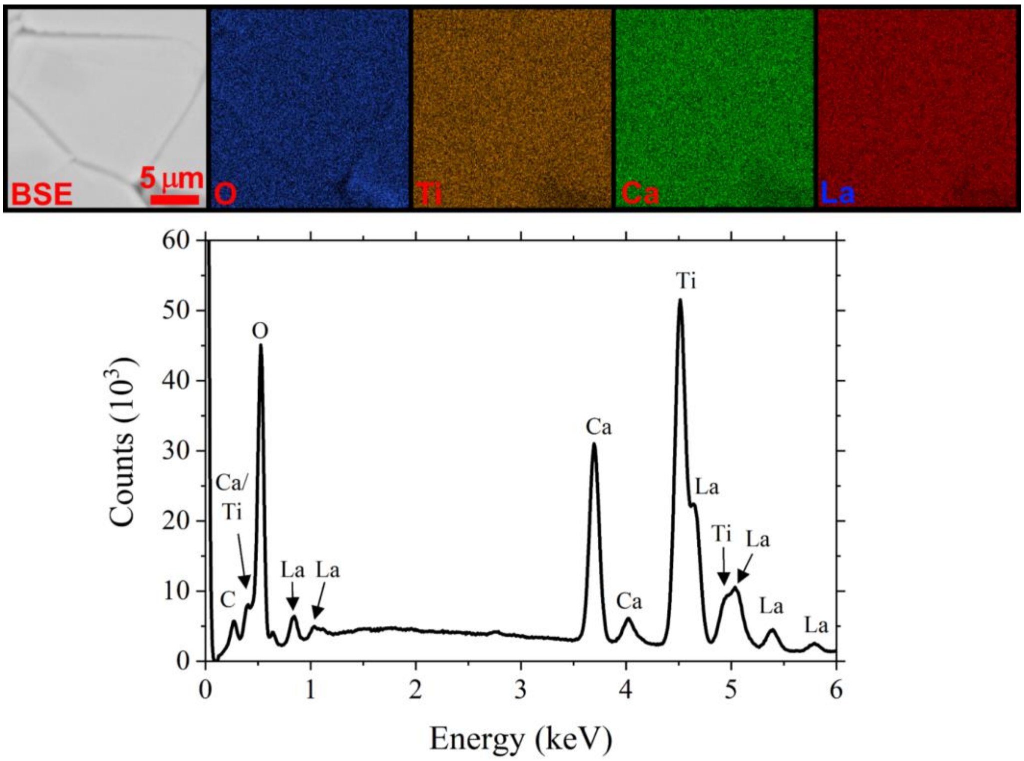

Figure 5.2 SEM micrograph and EDS map for the x = 0.2 sample, with oxygen, titanium, calcium and lanthanum denoted in blue, yellow, green and red, respectively. The EDS spectrum for the sample is also presented, with peaks indexed and labelled with the corresponding chemical symbol.

spectrum is also presented. Further compositions of the ion implanted sample range are shown in appendix 1 figures A1.1-A1.6. Across the sample range, the EDS maps show a uniform distribution of the target elements, with no areas rich in reagents such as TiO_2, La_2O_3, $CaCO_3$, calcined CaO, or any unintended phases. The evidence of sample homogeneity offered by SEM/EDS allowed for ion implantation and GAXRD studies to be conducted with confidence, along with any data analysis.

5.4 X-ray Diffraction

Recorded XRD patterns for the $Ca_{1-x}La_{2x/3}TiO_3$ system in the d-spacing regions $1 Å \leq d \leq 1.5 Å$, $1.5 Å \leq d \leq 2.5 Å$ and $2.5 Å \leq d \leq 4 Å$ are presented in figures 5.3a, 5.3b and 5.4, respectively. Reflections are indexed with relation to the aristotype perovskite unit cell. Phase transitions are shown through colour coding, with *Pbnm* shown in red, *Ibmm* in blue, *I4/mcm* in green, mixed phase *I4/mcm-Cmmm* in orange and *Cmmm* in black. Each pattern is normalised to the $(101)_p$ pseudo-cubic perovskite reflection, representing the most intense reflection in each sample. Reflections are further indexed based on their origin. Those not marked arise from the aristotype unit cell, '+' arise from in-phase octahedral rotation, '–' from anti-phase rotation, and '*' arising from concert reflections or A-site cation/vacancy ordering [26,72]. Samples in the regime $0 \leq x \leq 0.5$ are indexed to the *Pbnm* orthorhombic structure, through the appearance of in-phase, anti-phase and concert reflections, indicative of the mixed tilt $a^-a^-c^+$ system.

5.4.1 The *Pbnm* → *Ibmm* Transition

Reflections indicative of in-phase tilting, such as $½(310)_p$ and $½(312)_p$, are lost at $x = 0.6$, and a magnification of the $½(310)_p$ reflection is shown in figure 5.5a showing the diminishment of this reflection. This provides evidence of a phase transition from *Pbnm*, albeit the intensity present in the $x = 0.5$ sample is not definitive. For this reason, electron diffraction was used to clarify this phase transition, reported in section 5.5. As is reported by Zhang *et al* [72], based on Glazer's rigid octahedron model [24,25], the disappearance of these reflections allows for both the *Ibmm* and *I4/mcm* phase, and it is argued that the similarity of the $x = 0.6$ pattern with the *Pbnm* phase suggests the transition to *Ibmm* is continuous, making *Ibmm* the only possible phase.

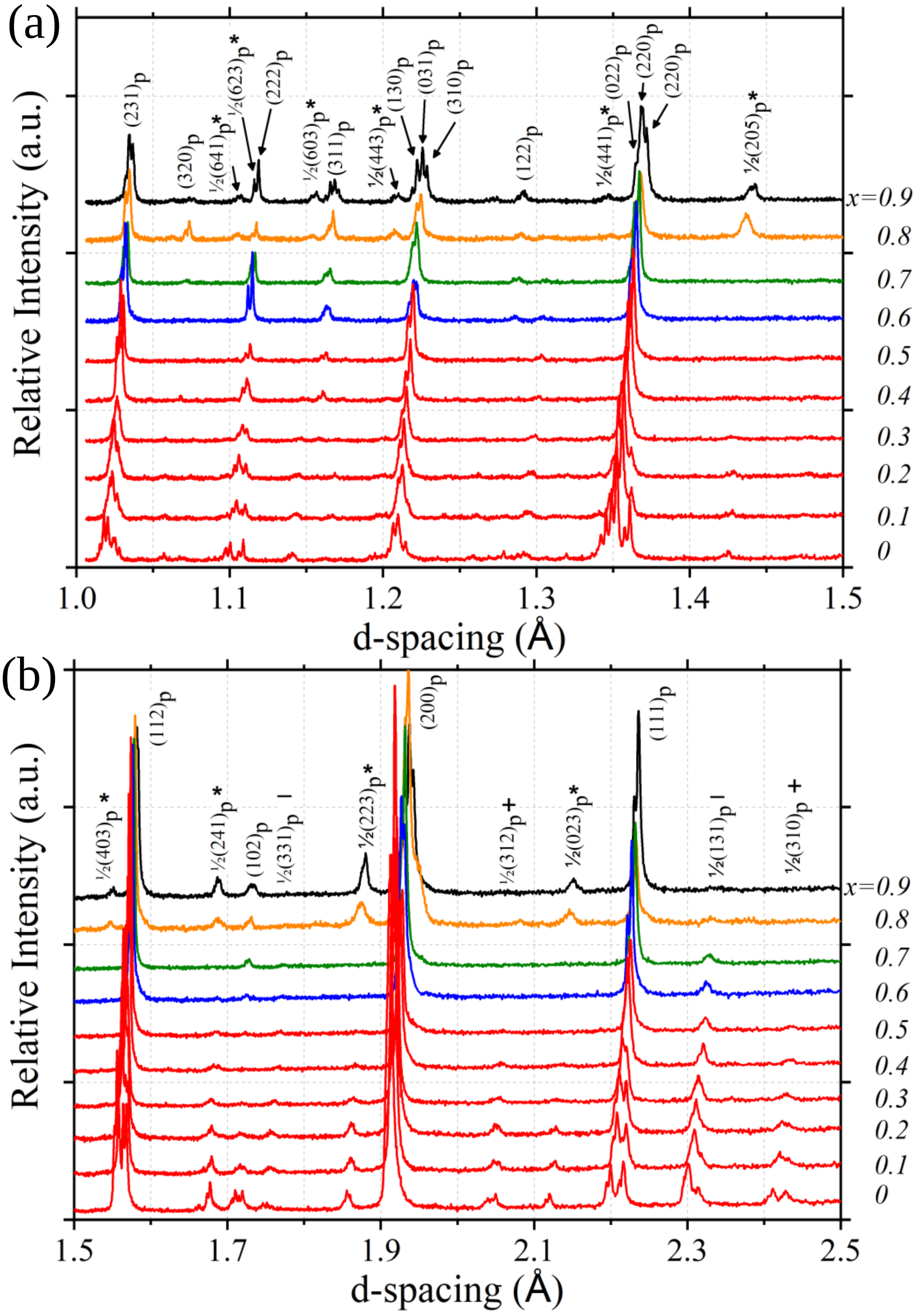

Figure 5.3 Observed X-ray diffraction patterns of the $Ca_{1-x}La_{2x/3}TiO_3$, system in the range (a) 1 Å ≤ d ≤ 1.5 Å and (b) 1.5 Å ≤ d ≤ 2.5 Å. Major reflections are indexed to the perovskite aristotype unit cell, with peaks related to in-phase octahedral tilting denoted by '+', anti-phase by '–', concert and cation/vacancy ordering by '*', and those not denoted related to the aristotype perovskite unit cell. Colour coding is denoted with red indicating *Pbnm*, blue *Ibmm*, green *I4/mcm*, orange mixed phase *Cmmm I4/mcm* and black *Cmmm*.

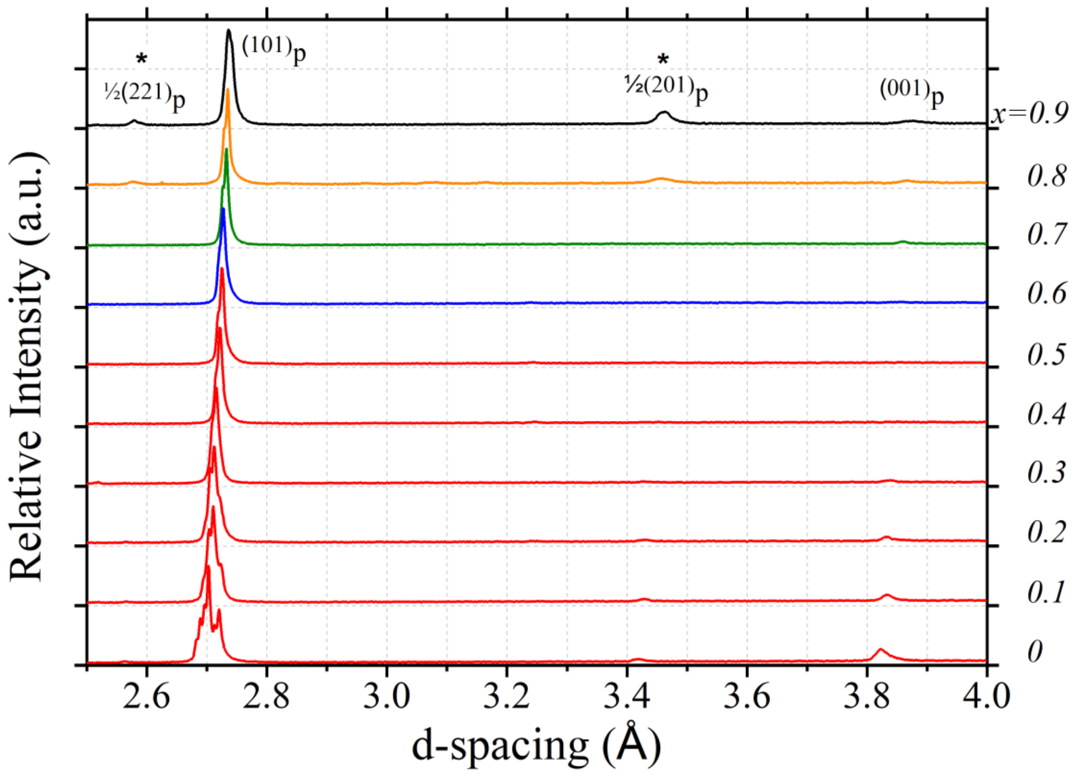

Figure 5.4 Observed X-ray diffraction patterns of the $Ca_{1-x}La_{2x/3}TiO_3$, system in the range 2.5 Å ≤ d ≤ 4 Å. Major reflections are indexed to the perovskite aristotype unit cell, with reflections related to concert and cation/vacancy ordering by ‘*’ and those not denoted related to the aristotype perovskite unit cell. Colour coding is denoted with red indicating *Pbnm*, blue *Ibmm*, green *I4/mcm*, orange mixed phase *Cmmm I4/mcm* and black *Cmmm*.

Furthermore, observation of the $(200)_p$ reflection, shown in figure 5.5b, shows a doublet has formed within the x = 0.6 pattern. Lattice parameter analysis suggests that in this instance the pseudo-cubic lattice parameter $b_p > a_p$, satisfying the *Ibmm* orthorhombic requirement for $a_p \neq b_p$ while the tetragonal symmetry requires $a_p = b_p$.

5.4.2 The *Ibmm* → *I4/mcm* Transition

The pattern for the x = 0.7 sample is similar to x = 0.6. The $(200)_p$ reflection collapses from a doublet to a singlet, making the *I4/mcm* and *Ibmm* phases both possible. Both Vashook *et al* [2] and Zhang *et al* [72] tentatively index this phase as *I4/mcm*, based on extrapolations of high-temperature phase diagram measurements and the positioning of the $½(131)_p$ anti-phase tilt reflection. The $(100)_p$ reflection, presented in figure 5.5c, increased the validity of this conclusion. While theoretically the $(100)_p$ reflection is present within the *Ibmm* phase, the intensity is unlikely visible using lab-

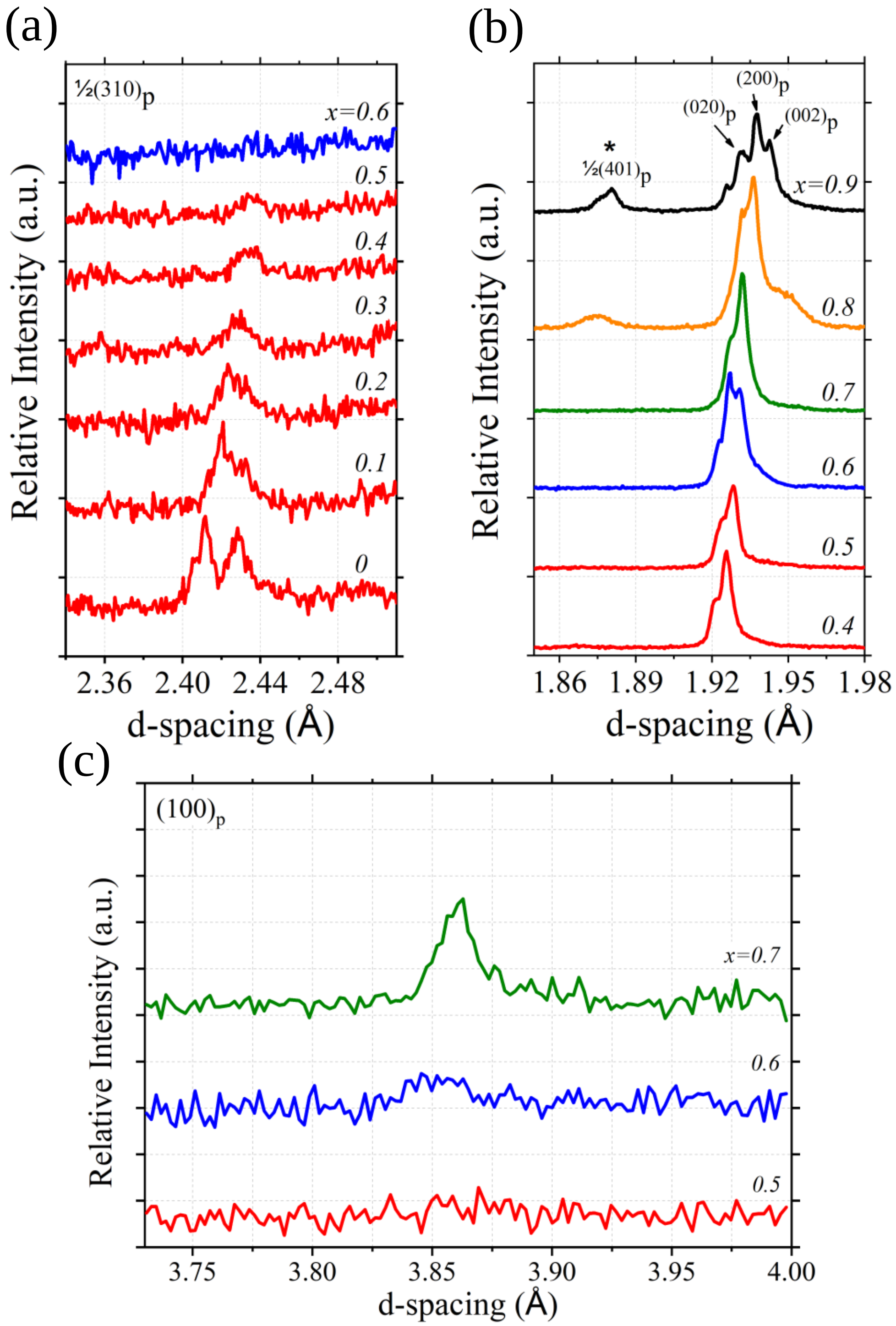

Figure 5.5 Magnifications of X-ray diffraction patterns of the $Ca_{1-x}La_{2x/3}TiO_3$ system in the range (a) 2.34 Å ≤ d ≤ 2.51 Å showing the evolution of the $½(310)_p$ reflection, (b) 1.85 Å ≤ d ≤ 1.98 Å showing the evolution of the $(200)_p$ reflection and (c) 3.72 Å ≤ d ≤ 4.00 Å showing the evolution of the $(100)_p$ reflection. Colour coding is denoted with red indicating *Pbnm*, blue *Ibmm*, green *I4/mcm*, orange mixed phase *Cmmm I4/mcm* and black *Cmmm*.

scale XRD for this phase. The observed intensity of this reflection within the x = 0.7 sample suggested the phase can be indexed as *I4/mcm*.

5.4.3 The *I4/mcm* → *Cmmm* Transition

For the x = 0.8 and 0.9 samples, several reflections are present that arise from concert reflections due to mixed tilt systems or A-site cation/vacancy ordering. The patterns observed suggested a mixed phase system may exist for the x = 0.8 sample, with the $\frac{1}{2}(221)_p$ reflection present in figure 5.4 indicative of the *Cmmm* phase. Peak splitting was also not observed in major aristotype perovskite peaks that would suggest the *I4/mcm* phase was formed. The x = 0.8 sample was indexed as *Cmmm* by Vashook *et al* [1,2], however Zhang *et al* [72] negate the mixed tilt/ordering reflections from their refinements as they argue these are the result of A-site cation ordering, and index the phase as *I4/mcm.* It is likely the phase boundary for this transition either lies very close the x = 0.8 boundary, or a small mixed-phase region exists. For this reason, the x = 0.8 sample was not used for ion implantation experiments in chapter 7, to ensure two competing damage responses were not characterised. The x = 0.9 sample presented in the *Cmmm* space group. Superlattice reflections were present due to the doubling of the unit cell parameter and the splitting of aristotype perovskite peaks were observed due to the orthorhombic transition, as shown in figure 5.5b for the $(200)_p$ reflection. Further reflections denoted as mixed tilt reflections originated from the ordering of A-site cations/vacancies [1,2,10,44], also present within the sister $Sr_{0.1}La_{0.6}TiO_3$ composition [48].

5.4.4 Lattice Parameters

The development of lattice parameters within the $Ca_{1-x}La_{2x/3}TiO_3$ system with increasing La^{3+} content is shown in figure 5.6a. The conversion from the real unit cell to pseudo-cubic was achieved through the following conversions,

(a) *Pbnm*: a/√2, b/√2, c/2
(b) *Ibmm*: a/√2, b/√2, c/2
(c) *I4/mcm*: a/√2, c/2
(d) *Cmmm*: a/2, b/2, c/2.

The shift of reflections toward higher d-spacings was attributed to the radii of the La^{3+} cation (1.36 Å) when substituted for the smaller A-site Ca^{2+} cation (1.34 Å). This

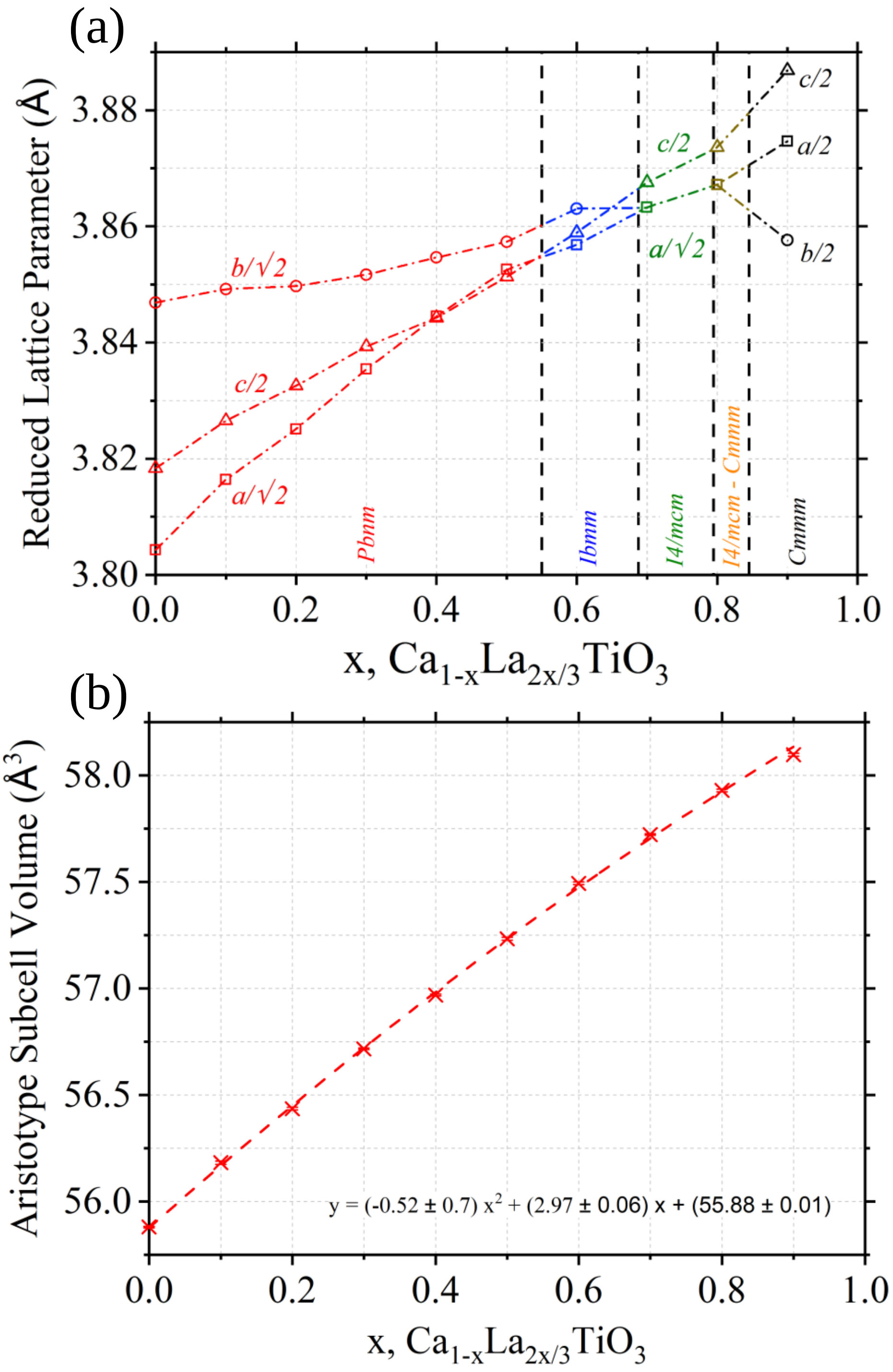

Figure 5.6 (a) aristotype perovskite unit cell lattice parameter development for the $Ca_{1-x}La_{2x/3}TiO_3$ system and (b) aristotype perovskite unit cell volume development. The lines presented act as a guide for the eye. For (a) squares represent the *a* parameter, circles the *b* parameter and triangles the *c* parameter. Colour coding is denoted with red indicating *Pbnm*, blue *Ibmm*, green *I4/mcm*, orange mixed phase *Cmmm I4/mcm* and black *Cmmm*.

led to the lattice parameter development observed, and the quadratic increase in pseudo-cubic unit cell volume observed in figure 5.6b. This data is similar to that observed by Vashook *et al* [2] and Zhang *et al* [72], with the x = 0.8 sample indexed using the *I4/mcm* phase to allow for ease of comparison.

5.5 Electron Diffraction

Electron diffraction was used to further clarify the structural transitions observed using XRD in section 5.4. Electron diffraction patterns were taken from the crushed grain samples used for *in-situ* ion implantation conducted in chapter 8. As with XRD patterns, all electron diffraction patterns were indexed with respect to the aristotype perovskite unit cell. As Woodward and Reaney report [26], multiple scattering, or dynamic diffraction, is usually present when conducting electron diffraction experiments. This limits the use of systematic absences when indexing the tilt systems associated with perovskites structures. A series of rules have been developed by Woodward and Reaney [26] that allow for the identification of anti-phase, in-phase and mixed-phase tilting, and the indexing of structures on this basis. These rules were discussed in chapter 2 in detail.

5.5.1 *Pbnm* Phase

Down-zone selected area electron diffraction patterns of x = 0 sample are shown in figure 5.7. Figure 5.7a presents the [001] zone axis, with kinematically forbidden ½(*ooe*) reflections by denoted pink circles. These reflections were indicative of in-phase tilting, which was confirmed by the additional reflections identified in the [111] zone axis in figure 5.7d. Furthermore, additional ½(*ooo*) reflections identified in the [110] zone axis, indicated in figure 5.7b with green circles, were indicative of anti-phase tilting suggesting the x = 0 sample is a mixed-tilt system. This was confirmed through the presence of ½(*oee*) reflections in the [101] zone axis pattern presented in figure 5.7c and indicated with blue arrows. These ‘concert’ reflections occur through combined diffraction from in-phase and anti-phase tilting, indicative of a mixed-tilt system. This confirmed the *Pbnm* system was present, as indexed by XRD.

This structure was also confirmed for the x = 0.2 sample, and SAEDPs of the x = 0.2 sample are shown in figure 5.8. Additional ½(*ooe*) reflections were present in the [001] zone axis shown in figure 5.8a, confirming the presence of c^+ tilting. Concert

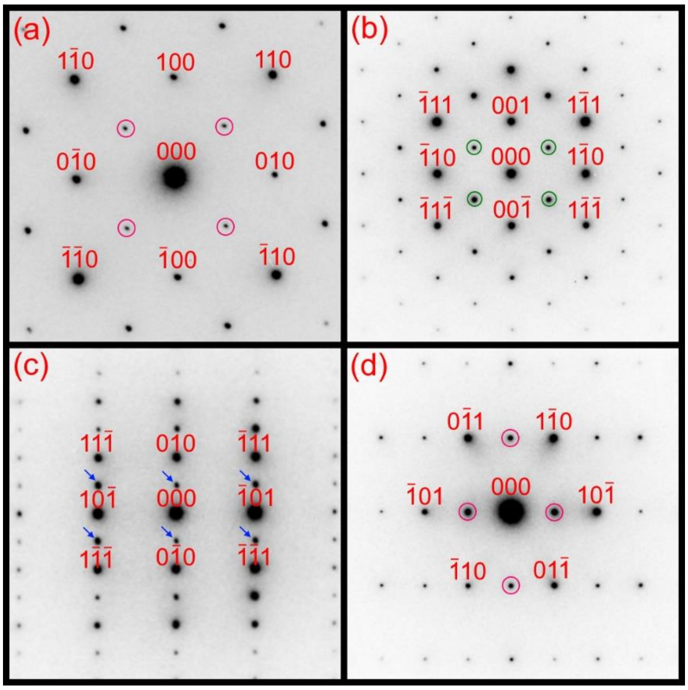

Figure 5.7 SAEDPs of the x = 0 sample, indexed with relation to the zone axes (a) [001], (b) [110], (c) [101] and (d) [111]. Anti-phase tilt reflections are donated by green circles, in-phase tilt reflections with pink circles, and concert reflections by blue arrows.

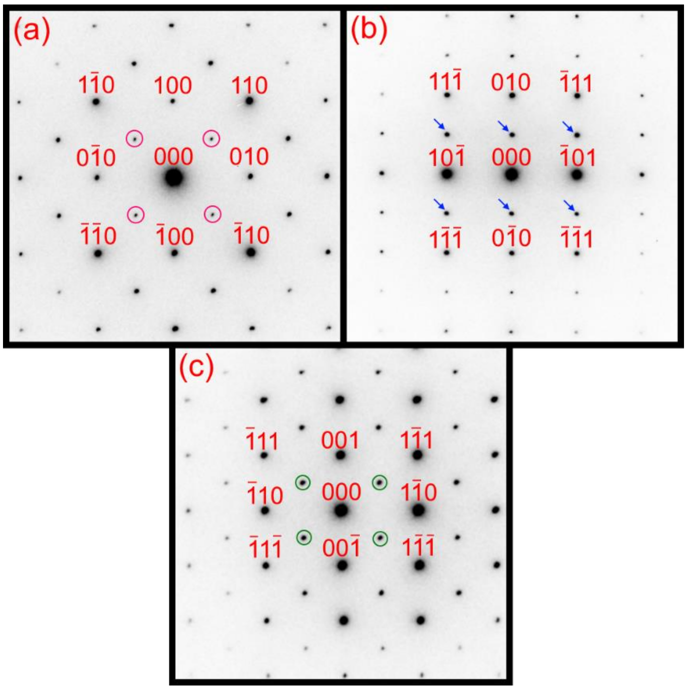

Figure 5.8 SAEDPs of the x = 0.2 sample, indexed with relation to the zone axes (a) [001], (b) [101] and (c) [110]. Anti-phase tilt reflections are donated by green circles, in-phase tilt reflections with pink circles, and concert reflections by blue arrows.

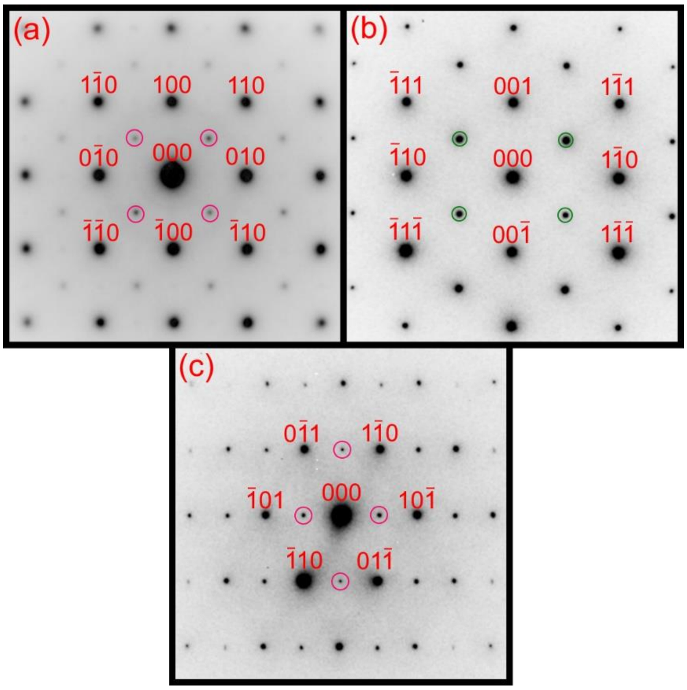

Figure 5.9 SAEDPs of the x = 0.5 sample, indexed with relation to the zone axes (a) [001], (b) [110] and (c) [111]. Anti-phase tilt reflections are donated by green circles, in-phase tilt reflections with pink circles.

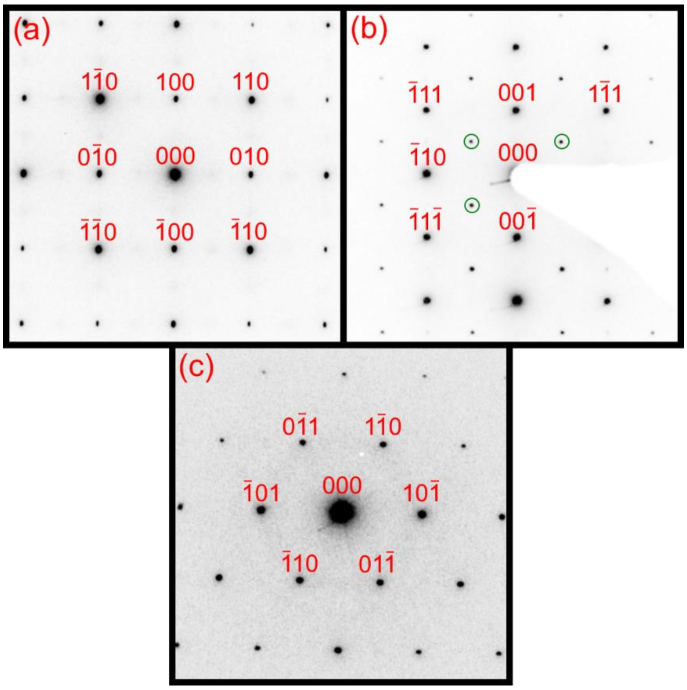

Figure 5.10 SAEDPs of the x = 0.6 sample, indexed with relation to the zone axes (a) [001], (b) [110] and (c) [111]. Anti-phase tilt reflections are donated by green circles.

reflections were present in the [101] zone axis presented in figure 5.8b, providing evidence of a mixed-tilt system, with evidence of a^- tilting shown through the presence of ½(*ooo*) reflections in the [110] zone axis pattern shown in figure 5.8c. This confirmed the $a^-a^-c^+$ tilt system and the corresponding *Pbnm* space group, as was indexed by XRD.

5.5.2 *Pbnm* → *Ibmm* Transition

The transition from *Pbnm* to *Ibmm* was tentatively confirmed using XRD, however this transition was not wholly conclusive. SAEDPs of the x = 0.5 sample are shown in figure 5.9. As with the x = 0 sample, the [001] and [111] zone axes, presented in figures 5.9a and 5.9c, respectively, showed additional reflections of the form ½(*ooe*), These reflections were indicative of in-phase tilting. Anti-phase tilting was confirmed through the presence of ½(*ooo*) reflections in the [110] zone axis, shown in figure 5.9b. This confirmed the x = 0.5 sample is a mixed-tilt system, and further confirmed the $a^-a^-c^+$ tilt system with space group *Pbnm*. The transition to *Ibmm* was found by XRD to occur at x = 0.6. The *Ibmm* space group has tilt system $a^-a^-c^0$, and in-phase/mixed tilt reflections should not be present if the x = 0.6 sample has this structure. The x = 0.6 sample [001] and [111] zone axes, shown in figures 5.10a and 5.10c, showed reflections originating from the aristotype perovskite structure and no evidence of in-phase tilting was found. Furthermore, the [110] zone axis pattern for the x = 0.6 sample, shown in figure 5.10b, contained ½(*ooo*) reflections confirming anti-phase tilting. This allowed for confirmation of the transition to *Ibmm* with tilt system $a^-a^-c^0$ at x = 0.6.

5.5.3 *Ibmm* → *I4/mcm* Transition

The transition from x = 0.6 to 0.7 was more subtle, having been indexed tentatively as *I4/mcm* with tilt system $a^0a^0c^-$. Figure 5.11 presents SAEDPs of the x = 0.7 sample. The [110] zone axis (figure 5.11a) contained ½(*ooo*) reflections indicative of antiphase tilting, and ½(*oee*) reflections were present within the same SAEDP. SAEDPs taken from a sample of $Ca_{0.5}Sr_{0.5}TiO_3$ by Woodward *et al* [75] showed similar reflections and was indexed as the $P2_1/m$ structure. However, the [111] SAEDP taken from the same $Ca_{0.5}Sr_{0.5}TiO_3$ sample shows ½(*ooe*) reflections indicative of in-phase tilting. No evidence of ½(*ooe*) reflections were observed down the [111] zone-axis for x = 0.7 in figure 5.11b, a prerequisite for in-phase tilting. It is likely these reflections were due to ordering of A-site vacancies within the structure or due to antiparallel displacement of the A-site cations. A-site cation ordering has been reported for the x = 0.7 sample [72], and it is likely this contributed to the observed diffraction pattern. Furthermore these additional reflections have been observed in various system exhibiting cation vacancy ordering [81,166–168]. Once again it was difficult to distinguish between the *I4/mcm* and *Ibmm* space groups as the additional ½(*oee*) reflections were the only observed differences between the obtained diffraction patterns.

5.5.4 *I4/mcm* → *Cmmm* Transition

SAEDPs of the x = 0.9 sample are shown in figure 5.12. No reflections indicative of in-phase tilting were observed within the [001] or [111] zone axes. The [110] axis contained ½(*ooo*) reflections as would be expected from the $a^-b^0c^0$ tilt series, however additional ½(*oee*) and ½(*ooe*) reflections were also present. As with x = 0.7, the ½(*oee*) reflections were likely related to a combination of long-range ordering and antiparallel cation displacement, however this did not offer an explanation for the appearance of ½(*ooe*) reflections that would indicate in-phase tilting. However, as was observed by Lu *et al* [167] in the $Sr_{1-x}La_{2x/3}TiO_3$ system, the presence of a layered structure with ordered A-site vacancies produces double diffraction routes for ½(*oee*) reflections. Such reflections are forbidden in [111] zone axis diffraction patterns [26], and figure 5.12c confirms such reflections were not present for x = 0.9. Therefore, it was concluded that these reflections were not indicative of in-phase tilting but the result of A-site vacancy ordering. In combination with the observed XRD patterns in section 5.4 the $a^-b^0c^0$ tilt configuration was confirmed.

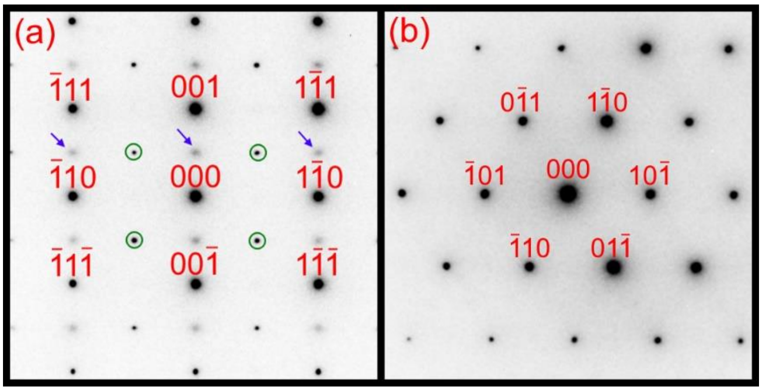

Figure 5.11 SAEDPs of the x = 0.7 sample, indexed with relation to the zone axes (a) [110] and (b) [111]. Anti-phase tilt reflections are donated by green circles, with ½(*oee*) reflections donated by purple arrows.

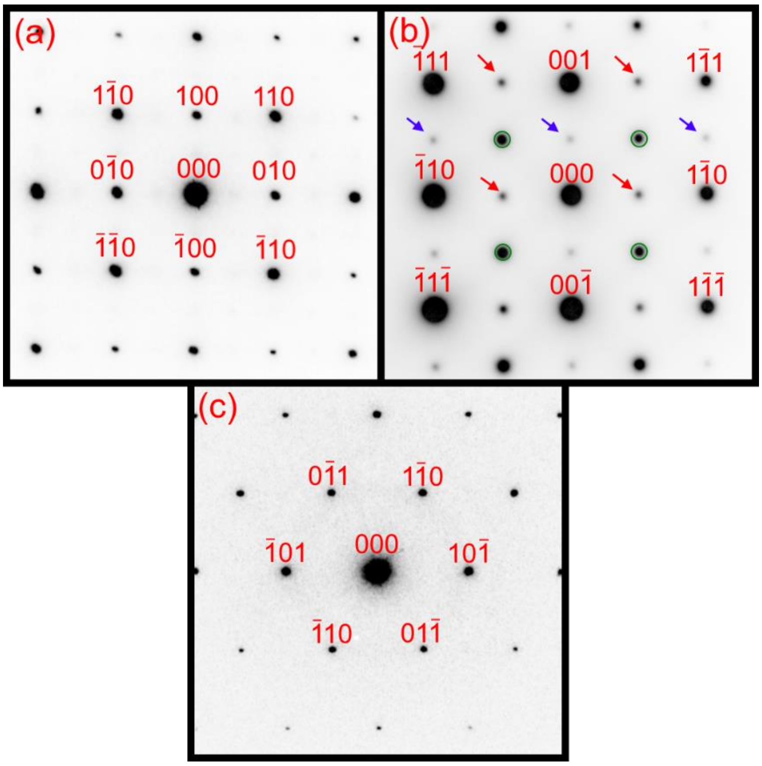

Figure 5.12 SAEDPs of the x = 0.9 sample, indexed with relation to the zone axes (a) [001], (b) [110], and (c) [111]. Anti-phase tilt reflections are donated by green circles, with ½(*ooe*) reflections donated by purple arrows and ½ (*eeo*) reflections by red arrows.

5.6 Conclusions

The $Ca_{1-x}La_{2x/3}TiO_3$ system has been synthesised as a series of dense pellets, and has been characterised by XRD, SEM and TEM. With the exception of the x = 0.1 sample, all samples had density of 95 %th, sufficient for ion implantation investigations laid out in chapter 7 of this thesis. SEM/EDS characterisation showed the synthesis of dense samples was achieved with compositional homogeneity, and grain sizes as synthesised have been reported. Structural characterisation of the system through XRD and electron diffraction indexed the system as *Pbnm* with tilt system $a^-a^-c^+$ for $0 \leq x \leq 0.5$, *Ibmm* with $a^-a^-c^0$ for x = 0.6, *I4/mcm* with $a^0a^0c^-$ for x = 0.7 and *Cmmm* with $a^-b^0c^0$ for x = 0.9, while a single-phase product in the case of the x = 0.8 sample could not be confirmed. The appearance of ½(*oee*) reflections within electron diffraction patterns for x = 0.7 and x = 0.9 specimens confirmed the presence of A-site vacancy ordering within these samples.

Pristine characterisation of the synthesised samples allowed for ion implantation experiments to be undertaken and for comparison with the post-implanted state. Before XTEM analysis could be undertaken, however, any structural or chemical modifications induced by ion milling of the samples had to be clarified. Pristine XTEM sample preparation and the effects upon the $Ca_{1-x}La_{2x/3}TiO_3$ samples are presented in the following chapter.

6. Effect of Argon Ion Milling on $Ca_{1-x}La_{2x/3}TiO_3$ samples prepared for Transmission Electron Microscopy

6.1 Introduction

The process of TEM sample preparation can lead to significant sample modification from the pristine state, as was discussed in chapter 4. This involves mechanical polishing followed by ion milling with energetic Ar^+ ions, with the full process described in section 4.5. Initial investigations of pristine samples were performed to determine the impact of TEM sample preparation on sample micro and nanostructures. All samples were investigated using TEM imaging and electron diffraction analysis. These results were used to ensure the reported radiation damage induced in ion implanted $Ca_{1-x}La_{2x/3}TiO_3$ samples was representative and not due to TEM sample preparation.

6.2 Results

6.2.1 SRIM Calculations

Prior to ion milling taking place, SRIM calculations were run using the “Monolayer Collision Steps/Surface Sputtering” program to give an indication of the sputtering yields at different Ar^+ ion milling energies. These values are presented in table 6.1. In each case Ti is the most resistant to sputtering, while La sputters to a greater extent than Ca. The sputtering ratio of O to each lattice cation is greater by a factor of 4.8 – 6 for Ca, 13 – 15 for Ti and 3 – 5 for La. The effect of these sputtering yields on the ion milled samples is discussed in more detail in section 6.3.

Table 6.1 Sputtering yields, as estimated by SRIM, for each elemental constituent of the x = 0.6 sample, using input ion implantation values of 2, 4 and 6 keV Ar^+.

Element	**Sputtering Yield (atoms/ion)** **6 keV Ar^+**	**Sputtering Yield (atoms/ion)** **4 keV Ar^+**	**Sputtering Yield (atoms/ion)** **2 keV Ar^+**
Ca	1.86	1.47	0.973
Ti	0.795	0.658	0.381
La	2.37	2.89	1.18
O	10.82	8.85	5.75

6.2.2 Ar^+ Milling of the x = 0 sample

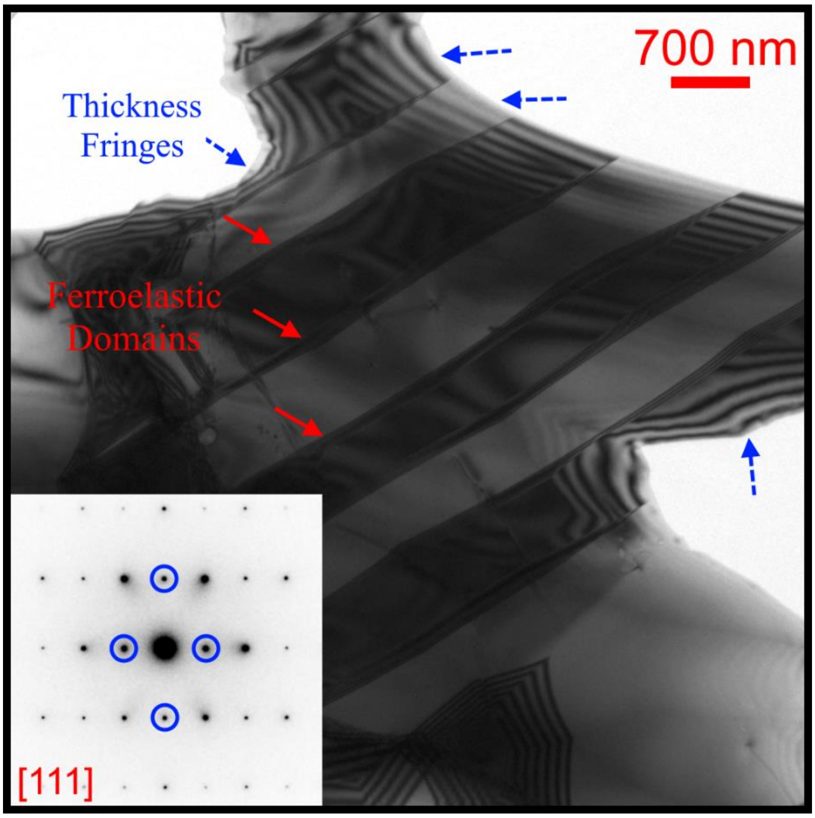

Figure 6.1 Bright field TEM micrograph of 4 keV Ar^+ ion milled x = 0 sample. An electron diffraction pattern taken down the [111] zone axis is presented inset. Thickness fringes donated by dashed blue arrows, while ferroelastic domains are donated with solid red arrows.

Firstly, the end member $CaTiO_3$ was examined using 4 keV Ar^+ ion with no sample cooling and milling undertaken at 4° from the sample surface. A bright field TEM micrograph of the 4 keV Ar^+ ion milled x = 0 sample is presented in figure 6.1. The micrograph was taken down-zone as exhibited by the crystalline reflections in the electron diffraction pattern in the same figure, confirming the samples crystallinity. The thicker band structure shown in figure 6.1 appears as alternating layers of bright and dark contrast, denoted by red arrows, indicative of ferroelastic domains as described by various authors [33,40,46]. In this instance, the sample surface appeared unaltered by ion milling, as can observed through the [111] zone axis electron diffraction pattern in figure 6.1. Only crystalline reflections were visible, including in-phase ½(*ooe*) reflections as expected from the *Pbnm* ($a^-a^-c^+$) structure.

6.2.3 Ar^+ Milling of $0.2 \leq x \leq 0.9$ samples

Bright field TEM micrographs of the x = 0.2, 0.4, 0.6, 0.7 and 0.9 samples are shown in figures 6.2a, 6.2b, 6.2c, 6.2d and 6.2e, respectively. In each instance, 4 keV Ar^+ ion milling was undertaken at an angle of 4°. Small regions of dark contrast ≈ 10 nm in diameter were observed to have formed in each sample, surrounded by light regions of contrast. Comparison with the x = 0 sample would suggest these samples underwent a process of structural modification, and the x = 0.6 sample was used to investigate these effects further.

A higher magnification bright field TEM image of the x = 0.6 sample ion milled with 4 keV Ar^+ at 4° is presented in figure 6.3a. The regions of high contrast were observed to have a diameter of ≈ 5 nm. Moiré fringes were visible in the grains indicated by red arrows, confirming that the regions of high contrast were crystalline, and will from hence forth be referred to as nano-crystallites. Furthermore, these fringes are the result of overlapping crystals with similar interatomic spacing. This suggests the nano-crystallites formed a surface layer on top of an unmodified bulk, or further nanocrystallites formed below the visible surface. The electron diffraction pattern shown in figure 6.3b was taken from the region shown in figure 6.3a. Two contributions were observed. Firstly, single crystal diffraction reflections were observed, indicative of electron diffraction from an isolated grain. Secondly, a

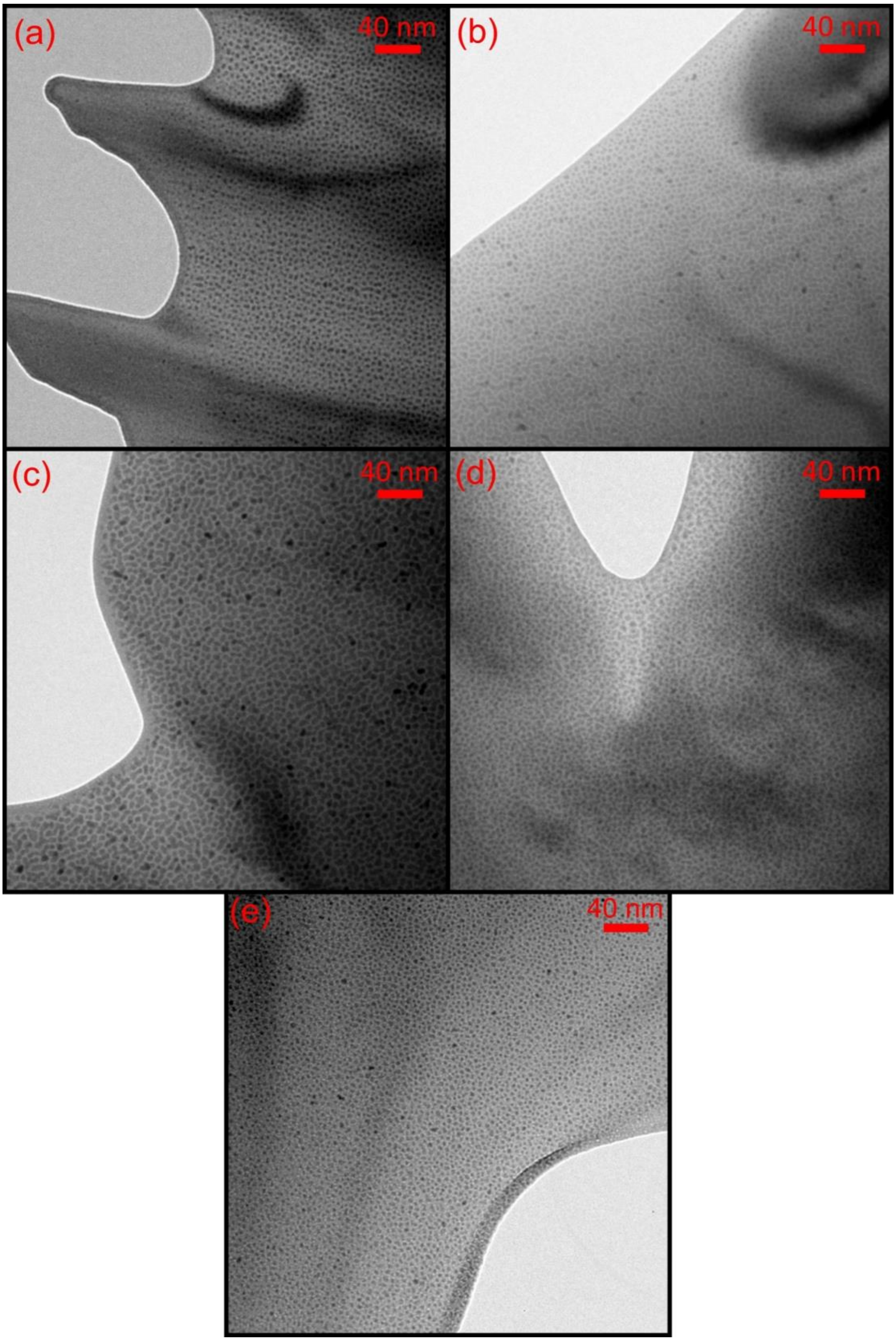

Figure 6.2 Bright field TEM micrographs of 4 keV Ar^+ ion milled samples (a) x = 0.2, (b) x = 0.4, (c) x =0.6, (d) x = 0. 7 and (e) x = 0.9.

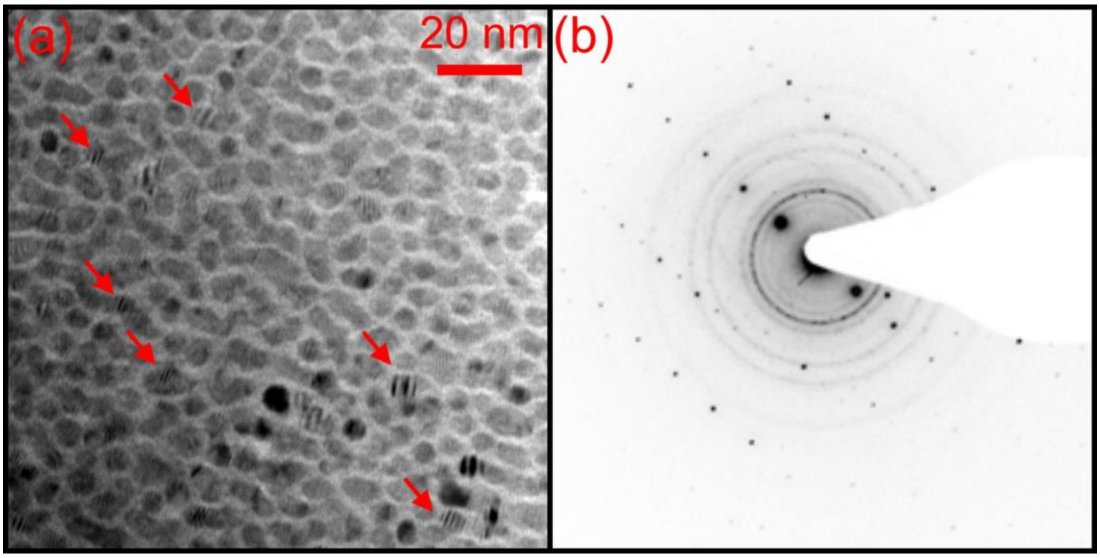

Figure 6.3 Bright field TEM micrograph of the ion milled x = 0.6 sample at (a) 150,000x magnification and (b) an SAEDP taken from the sample. Moiré fringes are indicated by red arrows.

polycrystalline contribution was present as concentric rings. The polycrystalline contribution was likely as a result of the nano-crystallites, each with an individual orientation that leads to the formation of the concentric ring patterns.

Figure 6.4 presents a lower magnification bright field TEM micrograph of the 4 keV Ar^+ ion milled x = 0.6 sample at room temperature. Small regions of high contrast were still visible at this resolution, confirming the presence of nano-crystallites. Electron diffractions patterns from the circled areas a, b and c are presented in figures 6.4a, 6.4b and 6.4c, respectively. Figure 6.4c was taken from the sample edge, and both polycrystalline diffraction rings and single crystal diffraction maxima were observed. Figure 6.4b was taken with the selective area aperture centred 600 nm from the sample edge, and in this instance polycrystalline diffraction rings were observable but with reduced intensity when compared with figure 6.4c. Figure 6.4a was taken with the aperture centred 1100 nm from the sample edge, and in this instance only single crystal maxima were observed. Below the diffraction patterns in figure 6.4 is a schematic showing the decreasing thickness of the sample as the aperture moves closer to the sample edge. Considering this schematic, electrons diffracting from the thinner

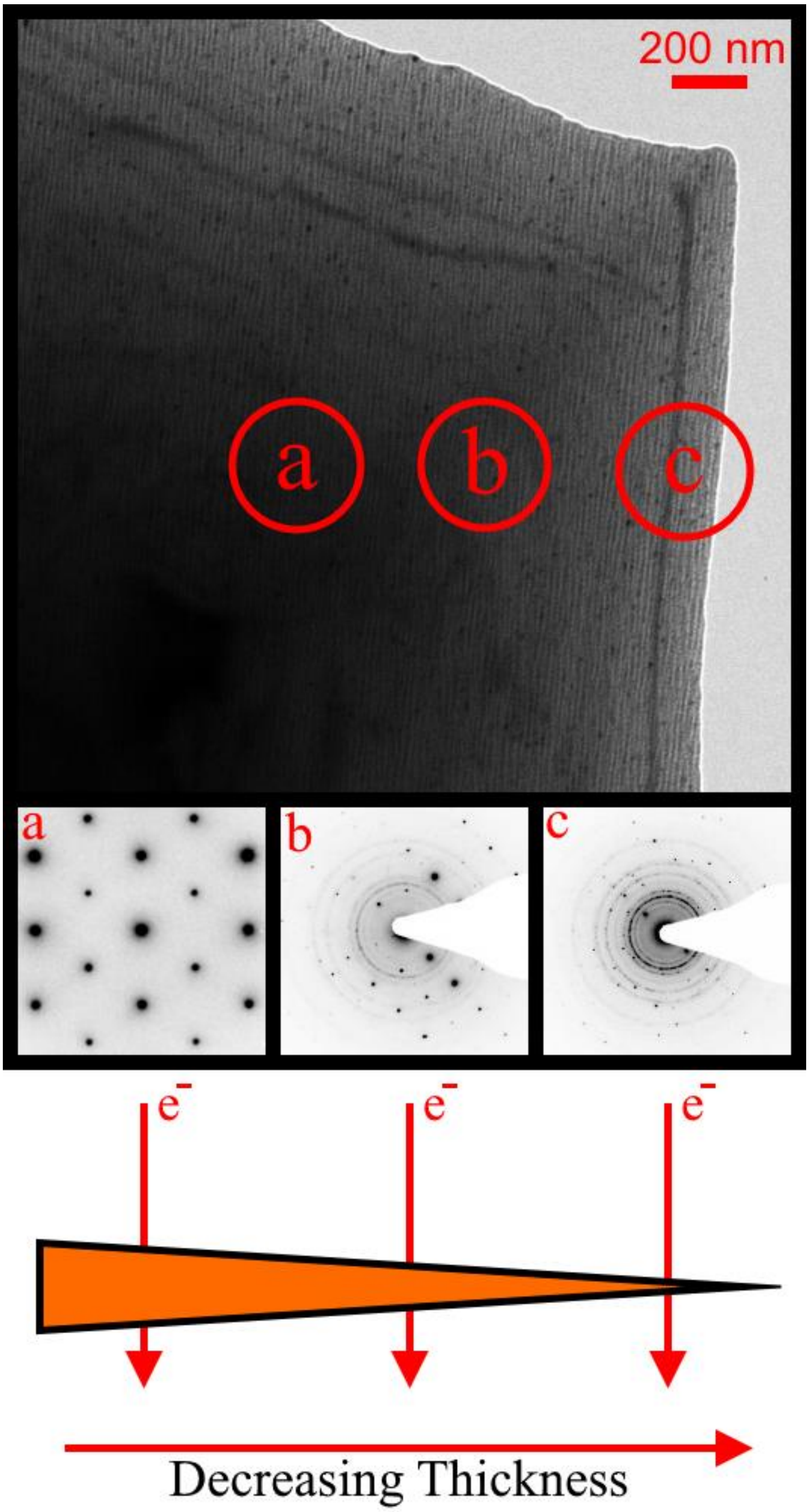

Figure 6.4 Bright field TEM micrograph taken from an x = 0.6 sample ion milled with 4 keV Ar^+ at room temperature SAEDPs taken from the circled regions (a), (b) and (c) where indicated. A schematic of the decreasing thickness of the sample from edge inwards is presented below.

sample edge will receive a higher contribution from any surface modified layer. Taking a diffraction pattern from the thicker regions further from the sample edge will lead to the electrons receiving a greater contribution from the underlying unmodified sample bulk. This was evidenced by the diffraction patterns observed in figure 6.4, as a greater polycrystalline contribution was evidenced by a greater intensity of concentric rings when the selective area aperture was located closer to the sample edge. Therefore, it was concluded that a thin modified surface layer is induced by 4 keV Ar^+ ion milling of the x = 0.6 sample.

To better understand the processes behind the surface modifications observed, the electron diffraction pattern in figure 6.4c was further studied. Polycrystalline diffraction concentric rings were converted to a 1D diffraction pattern by taking 15 line-scans of the obtained pattern. To ensure each line-scan passed through the centre of the electron diffraction pattern, lines were drawn between several symmetrical diffraction maxima and the centre point identified. This process is

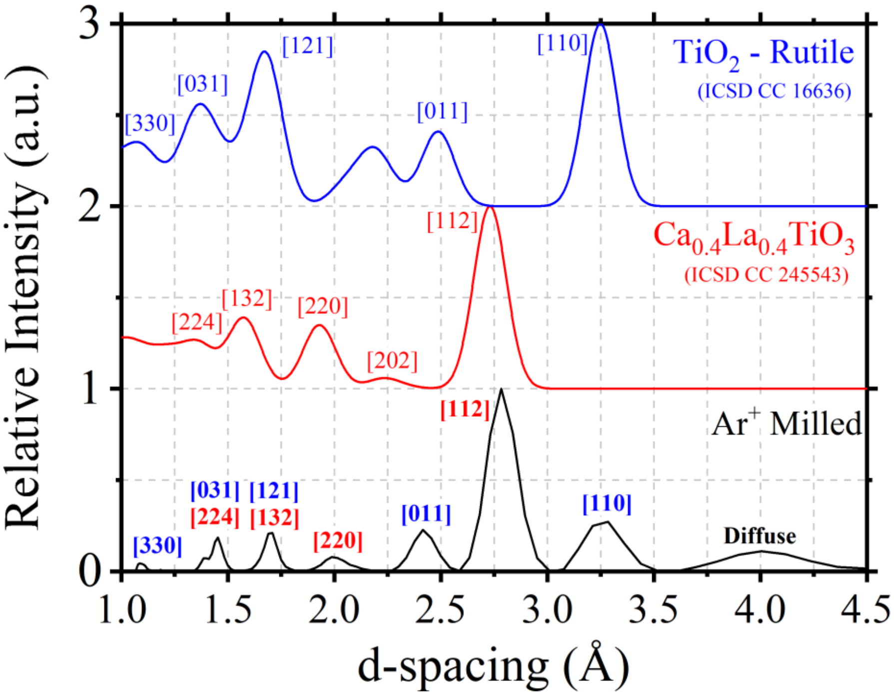

Figure 6.5 1D diffraction pattern obtained from the electron diffraction pattern in figure 6.4c shown in black, with theoretical 1D electron diffraction patterns for the $Ca_{0.4}La_{0.4}TiO_3$ (ICSD CC 245543) and TiO_2 (ICSD CC 16636) phases generated using the CrystalDiffract software package and the ICSD database. All peaks are normalised to the maximum intensity peak of that respective pattern.

exhibited in appendix figure A2.1. Line scans were then taken using ImageJ, as exhibited in appendix figure A2.2, and the “Plot Profile” function used to give intensity as a grey scale plot. All images were calibrated to the observed maximum intensity peak, and combined to produce an average composite of each line-scan. The background intensity was then fitted and major peaks identified using the Origin 2018 software and the “Peaks and Baseline” function, as shown in appendix figure A2.3. This background was then subtracted. The centre point of the two mirrored composite diffraction patterns was then identified as the centre point between the two maximum intensity peaks (0.94079 Å^{-1}) as shown in appendix figure A2.4. All values were then subtracted by 0.94079 Å^{-1} and a y-axis reflection operation undertaken for the now negative valued portion of the 1D pattern. Both patterns were then combined and converted to d-spacing by inverting each Å^{-1} value, producing the composite 1D diffraction pattern presented in figure 6.5. Indexing of the pattern was then undertaken using the CrystalDiffract software package [169] and International Crystal Structure Database (ICSD) [170] files for comparison. Two patterns found to give the best match with the obtained 1D pattern are shown for reference in figure 6.5, TiO_2 rutile and $Ca_{0.4}La_{0.4}TiO_3$, the x = 0.6 composition. The 1D pattern for the 4 keV Ar^+ milled x = 0.6 sample is shifted to higher d-spacings in the case of the theoretical x = 0.6 pattern. The possible mechanisms for this formation are discussed in section 6.3.

As this technique was to be employed for XTEM and *in-situ* PVTEM sample preparation in chapters 7 and 8, respectively, a series of ion milling conditions were attempted to minimise the surface modification observed. Figure 6.6 presents a series of bright field TEM micrographs with associated SAEDPs for a matrix of ion milling conditions utilised on the x = 0.6 sample. The sample ion milled with 6 keV Ar^+ is presented in figure 6.6a, 4 keV Ar^+ milled at liquid nitrogen temperatures in figure 6.6b, 2 keV Ar^+ at liquid nitrogen temperatures in figure 6.6c, and 2 keV Ar^+ at room temperature in figure 6.6d. All samples were milled at an angle of 4°. Firstly, the 6 keV Ar^+ milled x = 0.6 sample shown in figure 6.6a contains nano-crystallites as evidenced by image contrast, however they are larger than those induced by 4 keV Ar^+ milling and < 30 nm in diameter. Furthermore, single crystal maxima reflections have reduced in intensity, suggesting the increased penetration depth of the higher energy 6 keV Ar^+ ions increased the thickness of the modified surface layer. Secondly,

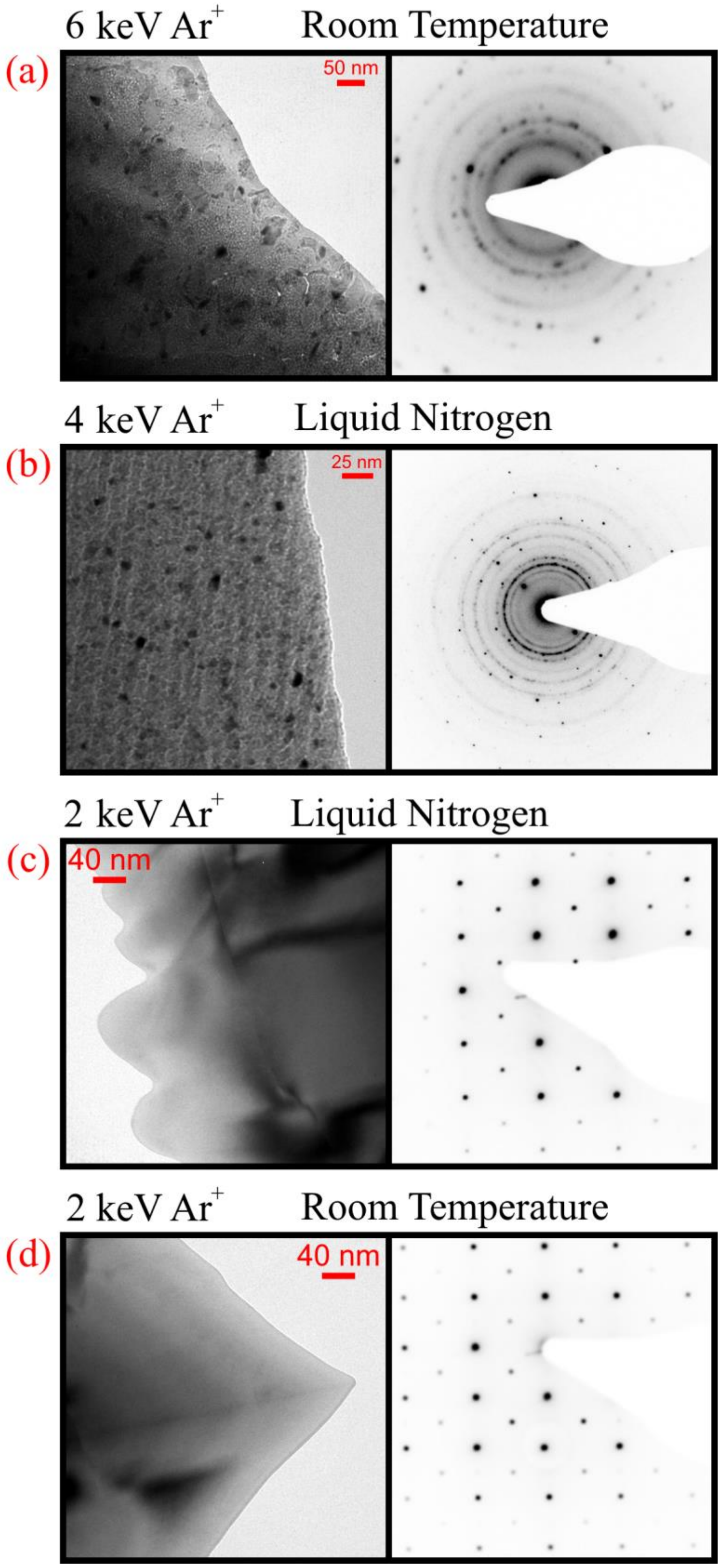

Figure 6.6 Bright field TEM micrographs and electron diffraction patterns from x = 0.6 samples ion milled with (a) 6 keV Ar^+ at room temperature (b) 4 keV Ar^+ with liquid nitrogen cooling (c) 2 keV Ar^+ with liquid nitrogen cooling and (d) 2 keV Ar^+ at room temperature.

nano-crystallites are present within the sample milled with 4 keV Ar^+ at liquid nitrogen temperatures, as exhibited by the ≈ 10 nm regions of high contrast shown in figure 6.4b. The associated diffraction pattern in figure 6.6b contains both single crystal and polycrystalline diffraction, and it can be concluded that liquid nitrogen temperatures did not prevent the induction of a surface modified layer. The two samples ion milled with 2 keV Ar^+ are presented at liquid nitrogen temperatures in figure 6.6c and at room temperature in figure 6.6d. Both samples show an absence of nano-sized regions of high contrast, and in both cases only single crystal diffraction from the isolated grains is observed. This suggests that surface modification was prevented under both conditions, and a pristine sample produced of a microstructure similar to that of the $x = 0$ sample presented in figure 6.1. Considering both these samples were milled with 2 keV Ar^+, it can be concluded surface modification is a consequence of incident ion energy during milling, rather than milling temperature.

6.3 Discussion

Several explanations could account for the observed behaviour of $Ca_{1-x}La_{2x/3}TiO_3$ ceramics after ion milling. Before these are considered, it should be noted that the end member $x = 0$ sample did not show a tendency for surface modification when ion implanted with 4 keV Ar^+. For $x = 0$, several examples of the samples preparation are exhibited in the literature and no surface modification has been reported.

Ion beam milling and ion implantation has been reported to produce nanocrystalline material. Recrystallisation of metallic glasses has been observed using 4.4 keV Ar^+ by Sun *et al* [171], although the nanoregions of crystallinity in this instance are of the < 100 nm in size. Similarly, nanocrystalline regions in the $Cu_{50}Zr_{45}Ti_5$ metallic glass were observed using 3 keV ≤ Ar^+ ion milling by Fu *et al* [172], in this instance of ≈ 3 nm in size. However, these were mechanisms of recrystallisation of an amorphous material, while the $Ca_{1-x}La_{2x/3}TiO_3$ system is inherently crystalline. Furthermore, Meldrum *et al* [173] provide an overview of the use of ion implantation to form nanoceramics, but this work considered the use of non-inert implantation to form nanocomposites, while the present study has used inert Ar^+ milling. Rao *et al* [154] report similar nanocrystallite formation due to focused ion beam (FIB) milling in GaAs and report nanocrystallite formation as a common artefact of ion milling, although the process behind this behaviour is not discussed. None of these examples account for the mechanism of nanocrystallite formation within $Ca_{1-x}La_{2x/3}TiO_3$ ceramics nor the rutile component identified within the 1D diffraction pattern obtained.

Considering the nanocrystallite formation mechanism in the La-doped samples, the possibility that the samples were synthesised with an intrinsic nanocrystalline structure was first ruled out. Several reports of nanocrystalline perovskites are found in the literature synthesised via various routes [174–176]. It has been reported that a two-step sintering process in $BaTiO_3$ can produce nanograins of a similar size and geometry to those induced in this study [177–180]. This process involves an initial sintering stage, followed by a reduced temperature sinter that suppresses grain growth while the sample is densified. Within the present study, samples were fired at 1150 °C and 1300 °C, followed by a final sinter at 1400 °C. Furthermore, grain size analysis showed the samples to have grains < 30 µm, and the use of 2 keV Ar^+ appears to prevent nano-crystallite formation. Analysis of bright field TEM micrographs of samples prepared via the crushed grain route also exhibit no evidence of nanocrystallite formation, as can be observed in chapter 8. This suggests the material synthesis route employed did not lead to nano-crystallite formation.

Secondly, the potential for sample contamination was considered. Contamination can occur from redeposition of sputtered material, hydrocarbons from solvents during sample preparation and the sputtering of metal particles from TEM grids during ion milling [150,152,154,159]. This can be further ruled out, as the size and uniformity of the nano-crystallites does not lend itself to contamination in comparison with the literature, nor do the polycrystalline diffraction patterns obtained index with any metal or hydrocarbon contamination. Thirdly, the induction of localised temperature increases may lead to such effects [181]. Several reports have been made regarding the effects of ion beam induced heating, in particular for ceramics, for which low thermal conductivity leads to localised temperature increases [150–152]. However, these effects were minimised by conducting liquid nitrogen cooled ion milling, and modification was still observed using 4 keV Ar^+ ions. Furthermore, the use of 2 keV Ar^+ under both room temperature and liquid nitrogen cooled temperatures prevented any surface modifications, suggesting such modification is not a temperature-based phenomena.

The last explanation to be considered is the effect of preferential sputtering of lattice ions at the surface, with sputtering yield values presented in table 6.1. Considering the proficiency for O sputtering when compared with other lattice constituents, the possibility of Ti reduction within the perovskite systems should be considered, whilst the higher levels of A-site sputtering when compared with B-site Ti cations also may play a role in nanocrystallite formation. The 1D diffraction pattern presented in figure 6.5 was indexed as a combination of TiO_2 and $Ca_{0.4}La_{0.4}TiO_3$, with the additional rutile phase not present within the 2 keV Ar^+ ion milled samples or the crushed grain prepared equivalent. The d-spacings of the *Ibmm* structure are shifted slightly higher than in the pristine state, suggesting that reduction from Ti^{4+} to Ti^{3+} may occur, with the increased size of the Ti^{3+} radii (0.67 Å) compared to Ti^{4+} (0.605 Å) leading to this shift. The reduction behaviour of A-site deficient perovskites has been studied by Neagu *et al* [182,183], including the $Sr_{0.4}La_{0.4}TiO_3$ sister composition to the x = 0.6 sample. In these studies, reduction was induced by sintering samples under reducing conditions and shifts to higher d-spacings are reported in XRD patterns post-reduction. The appearance of micron sized TiO_2 particles is also reported, as TiO_2 was forced out of solution (exsolution) through the reducing conditions. On the loss of oxygen from the structure, an oxygen deficiency limit is breached whereby the A-site deficient structure can no longer accommodate further oxygen loss. To compensate, the associated B-site oxide, in this case TiO_2, goes into exsolution, which is most easily understood by considering the system as being in a state of B-site excess, rather than A-site deficiency. Neagu *et al* formulate this as

$$\mathrm{A_{0.8}TiO_3} \xrightarrow{\text{reduction}} \mathrm{A_{0.8}TiO_{3-\delta limit}} \xrightarrow{\text{reduction}} \mathrm{A_{0.8}Ti_{1-\mathit{y}}O_{3-\delta limit-yn}} + \mathrm{yTiO_n},$$

whereby the $yTiO_n$ term compensates for the inability to accommodate further reduction. The results of this study preliminarily suggest that Ti^{4+} reduction has been induced through ion beam milling as opposed to temperature-based reduction in the $Ca_{0.4}La_{0.4}TiO_3$ sample. Based on the diffraction contrast observed, it is theorised that a nanocrystalline structure of a reduced $Ca_{0.4}L_{0.4}TiO_3$ has formed surrounded by TiO_2 that has undergone exsolution. The "grain boundary" regions between nanocrystallites have lower contrast, and it could be hypothesised that this is due to the lower Z-number of TiO_2 compared with $Ca_{0.4}La_{0.4}TiO_3$, suggesting this "grain boundary" material is the indexed rutile phase. However, a high-resolution or energy-filtered study would be required to conclusively determine the composition of this phase. Of further interest is the lack of nanocrystallite formation when using 2 keV Ar^+, suggesting that a threshold energy limit is required for the phenomena to be induced.

These findings should be considered preliminary, and as this thesis prioritises the production of unmodified TEM samples ion beam effects were not the main focus of this study. To conclusively confirm this mechanism of nanocrystallite formation, a full and comprehensive EFTEM/EELS study would be required, in particular observing any microstructural alterations using low energy Ar^+ implantation on a pristine TEM sample *in-situ* in TEM.

There are many potential applications for dispersed nanostructured layers/particles, including as tailored functional ceramics and catalytic nanoparticles [183]. The benefit of reducing A-site deficient perovskites in this manner is the microstructure produced can be highly tuned, to a greater extent than conventional methods of dispersing nanoparticles on materials [184–191]. However, thermal reduction of materials using temperatures ≤ 1400 °C in reducing atmospheres is an expensive process. The use of an inert ion beam milling process, as has been reported here, has the potential to produce similar microstructures and nanoparticles at a greatly reduced cost if the exact nature of the surface modifications can be established.

Moreover, the focus of this study was achieved. The production of unmodified TEM samples is achieved through the use of 2 keV Ar^+ milling across all samples, allowing for reliable observation of both bulk implanted samples and those produced for *in-situ* irradiations.

6.4 Conclusions

Ion milling using low energy Ar^+ was found to induce nanoregions of crystallinity in the $Ca_{1-x}La_{2x/3}TiO_3$ system for compositions x = 0.2. 0.4, 0.6, 0.7 and 0.9. Such crystallites form ≈ 5 nm in diameter and are surrounded by a light contrast “grain boundary” like material. Electron diffraction analysis showed the nanocrystallites formed as a surface modified layer on the pristine sample bulk. Analysis of polycrystalline electron diffraction patterns taken from the x = 0.6 sample provided evidence of Ti^{4+} reduction, through shifts of reflections to higher d-spacings. The nanocrystallites could be further indexed to both TiO_2 rutile and a reduced $Ca_{0.4}La_{0.4}TiO_3$ structure. Ion milling with 2 keV Ar^+ prevented such nanocrystallite formation in all samples, allowing for the production of TEM samples for radiation damage studies presented in chapters 7 and 8.

7. Bulk Ion Implantation of the $Ca_{1-x}La_{2x/3}TiO_3$ System

7.1 Introduction

In chapter 5, the characterisation of the $Ca_{1-x}La_{2x/3}TiO_3$ system in its pristine state was reported in preparation for radiation damage studies, including the structural changes associated with La doping and the onset of A-site deficiency. This chapter outlines the effects of radiation damage, induced using ion implantation, on samples of the A-site deficient $Ca_{1-x}La_{2x/3}TiO_3$ system. Post-implantation, the samples were investigated using glancing-angle X-ray diffraction (GAXRD) to qualitatively calculate the amorphous/crystalline components of the samples and quantify lattice parameters. Cross-sectional transmission electron microscopy was used to complement GAXRD patterns and directly observe the damage induced by ion implantation.

7.2 SRIM Calculations

The two ion implantation conditions of 1 MeV Kr^+ implantation to a fluence of 1×10^{15} ions cm^{-2} and 5 MeV Au^+ to a fluence of 5×10^{14} ions cm^{-2} were first estimated with SRIM. These two conditions were used to investigate two irradiation conditions with varying electronic-nuclear stopping (ENSP) ratios and different irradiating ions. Figure 7.1 presents SRIM calculations of both implantation conditions on $CaTiO_3$ and $Ca_{0.1}La_{0.6}TiO_3$, and table 7.1 presents values of the peak implantation depth, R_p, the peak damage depth, R_d, the nuclear stopping power, dE/dx_n, the electronic stopping power, dE/dx_e, the electronic-nuclear stopping power ratio, ENSP, and the peak damage in dpa for the implanted x = 0, 0.2, 0.4, 0.5, 0.6, 0.7 and 0.9 samples for both conditions. The peak dpa levels remained between 1.34 dpa and 1.42 dpa for 1 MeV Kr^+, and between 1.37 dpa and 1.48 dpa for 5 MeV Au^+, or within 8% for both conditions. The peak damage depths ranged from 310 nm to 300 nm for 1 MeV Kr^+ and 640 nm and 600 nm for 5 MeV Au^+. The ENSP for 1 MeV Kr^+ implantation was 0.7681 for $CaTiO_3$, increasing by a maximum of 3.8% to 0.7979 for $Ca_{0.1}L_{0.6}TiO_3$, with all compositions in the nuclear stopping regime. For 5 MeV Au^+, the ENSP increased for $CaTiO_3$ to 1.222 in the electronic stopping regime and decreased by 2.9% to 1.186 for $Ca_{0.1}La_{0.6}TiO_3$.

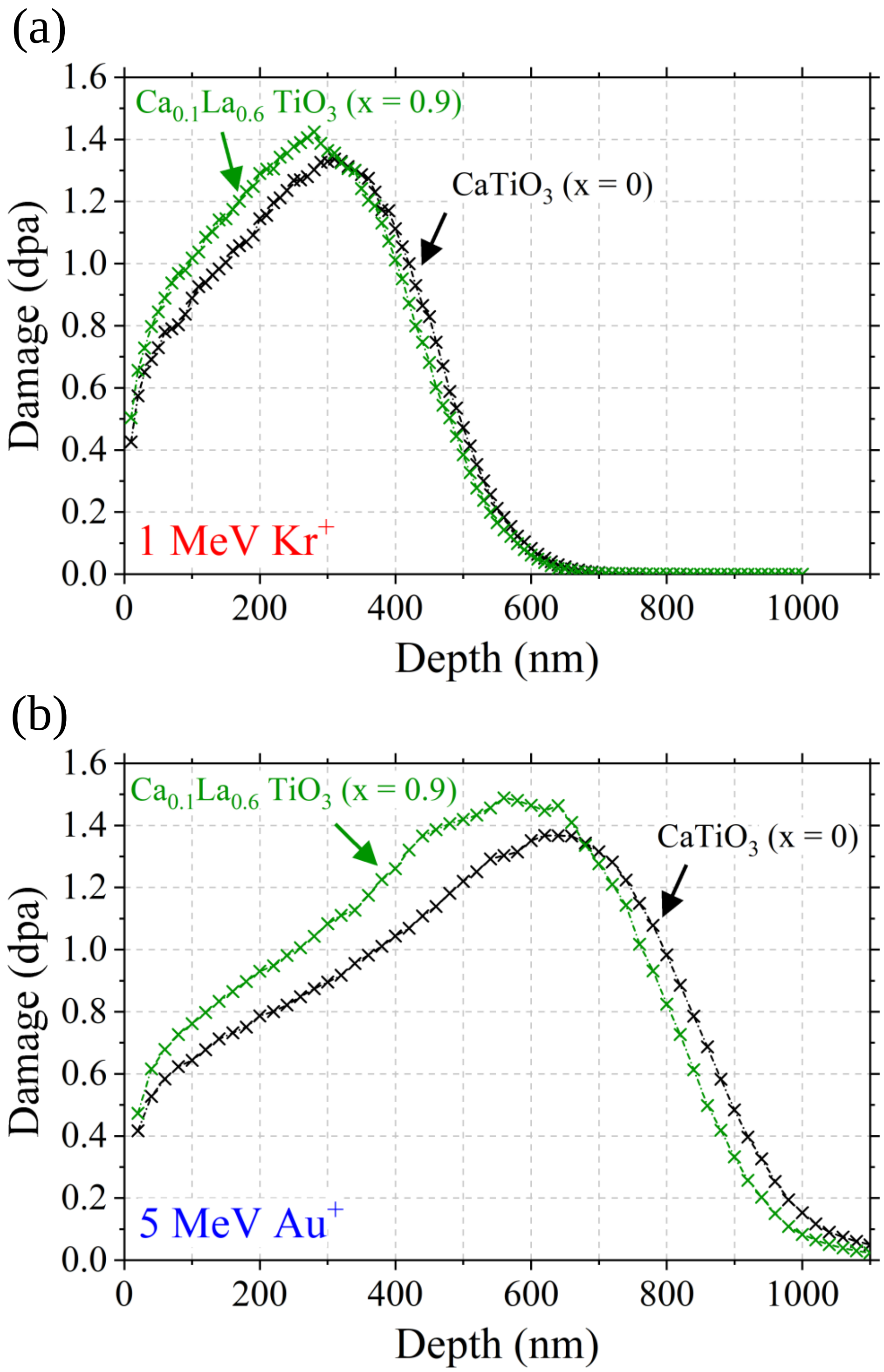

Figure 7.1 SRIM calculated damage-depth profiles for (a) 1 MeV Kr^+ irradiated (a) $CaTiO_3$ and $Ca_{0.1}La_{0.6}TiO_3$ and (b) 5 MeV Au^+ irradiated $CaTiO_3$ and $Ca_{0.1}La_{0.6}TiO_3$ to fluences of 5×10^{14} ions cm^2.

Table 7.1 Values calculated by SRIM for the maximum damage depth, R_d, peak damage depth, R_{peak}, nuclear stopping power dE/dx_n, electronic stopping power, dE/dx_e, electronic to nuclear stopping power ratio, ENSP and peak damage in dpa.

Sample	**R_d (nm)**	**R_{peak} (nm)**	**dE/dx_n eV nm^{-1}**	**dE/dx_e eV nm^{-1}**	**ENSP**	**dpa**
1 MeV Kr$^+$						
x = 0	600	310	1228	942.7	0.7676	1.34
x = 0.2	600	310	1181	915.0	0.7748	1.35
x = 0.4	600	300	1180	922.6	0.7819	1.37
x = 0.5	600	300	1194	937.3	0.7850	1.37
x = 0.6	600	300	1193	940.3	0.7882	1.38
x = 0.7	600	300	1190	942.2	0.7918	1.40
x = 0.9	600	300	1209	964.9	0.7981	1.42
5 MeV Au$^+$						
$CaTiO_3$	1000	640	2823	3450	1.2221	1.37
x = 0.2	1000	640	2744	3330	1.2136	1.38
x = 0.4	1000	630	2809	3385	1.2051	1.41
x = 0.5	1000	630	2856	3431	1.2013	1.43
x = 0.6	1000	620	2840	3400	1.1972	1.45
x = 0.7	1000	610	2815	3358	1.1929	1.46
x = 0.9	1000	600	2963	3512	1.1853	1.48

7.3 Glancing-Angle XRD

7.3.1 $CaTiO_3$, $Ca_{0.8}La_{0.13}TiO_3$ and $Ca_{0.6}La_{0.267}TiO_3$ (x = 0, 0.2 and 0.4)

In the first instance, the x = 0, 0.2 and 0.4 samples ion implanted with 1 MeV Kr^+ to a fluence of 1 x 10^{15} ion cm^{-2} were investigated using GAXRD. For the case of $\Omega = 0.5°$, the X-ray penetration depth for x = 0 was 450 nm, and the corresponding damage region for 1 MeV Kr^+ implantation was 425 nm with peak damage at 310 nm by SRIM. A lower incident angle would have been desirable but was unavailable due to the limitations of the diffractometer used. As was described in section 7.2, the peak and most penetrating damage depths remained fairly constant, while X-ray penetration depths will be reported through this section. Penetration depths decrease to 420 nm and 360 nm for the x = 0.2 and 0.4 samples. GAXRD patterns for the x = 0, 0.2 and 0.4 samples implanted with 1 MeV Kr^+ are presented in figures 7.2a, 7.2b and 7.2c, respectively. In all cases, lattice expansion to higher d-spacings was observed, indicative of radiation damage induced lattice expansion by ion implantation. Diffuse scattering was observed within the x = 0 sample, but the x = 0.2 and 0.4 samples remained fully crystalline by GAXRD. The crystalline response was significant, and the $(101)_p$, $(200)_p$ and $(112)_p$ reflections had sufficient intensity in both the pristine and damaged state to be indexed. The ‘damaged’ reflection was distinguished by a shift to higher d-spacings, a direct result of lattice expansion onset by ion implantation. As Ω increased, and therefore penetration depth, a greater volume of pristine material below the implanted surface was penetrated, leading the ratio of damaged to crystalline material decreasing. For the x = 0 sample, significant underlying pristine material was observed in the $\Omega = 0.5°$ pattern, as the penetration depth was greater than the induced damage region. This was not the case for the x = 0.2 and 0.4 samples, and only slight shoulder peaks in the $(101)_p$ peaks index to the pristine structure. The highly crystalline response of the x = 0.2 and 0.4 samples at $\Omega = 0.5°$ provides evidence of increased damage tolerance in these sample when compared with x = 0. It was possible to distinguish the lattice expanded ½$(131)_p$ and ½$(241)_p$ reflections in both the x = 0.2 and 0.4 patterns. These corresponded to anti-phase tilting and mixed-tilt concert reflections, respectively, confirming the samples remain in the *Pbnm* structure with tilt series $a^-a^-c^+$. It was not

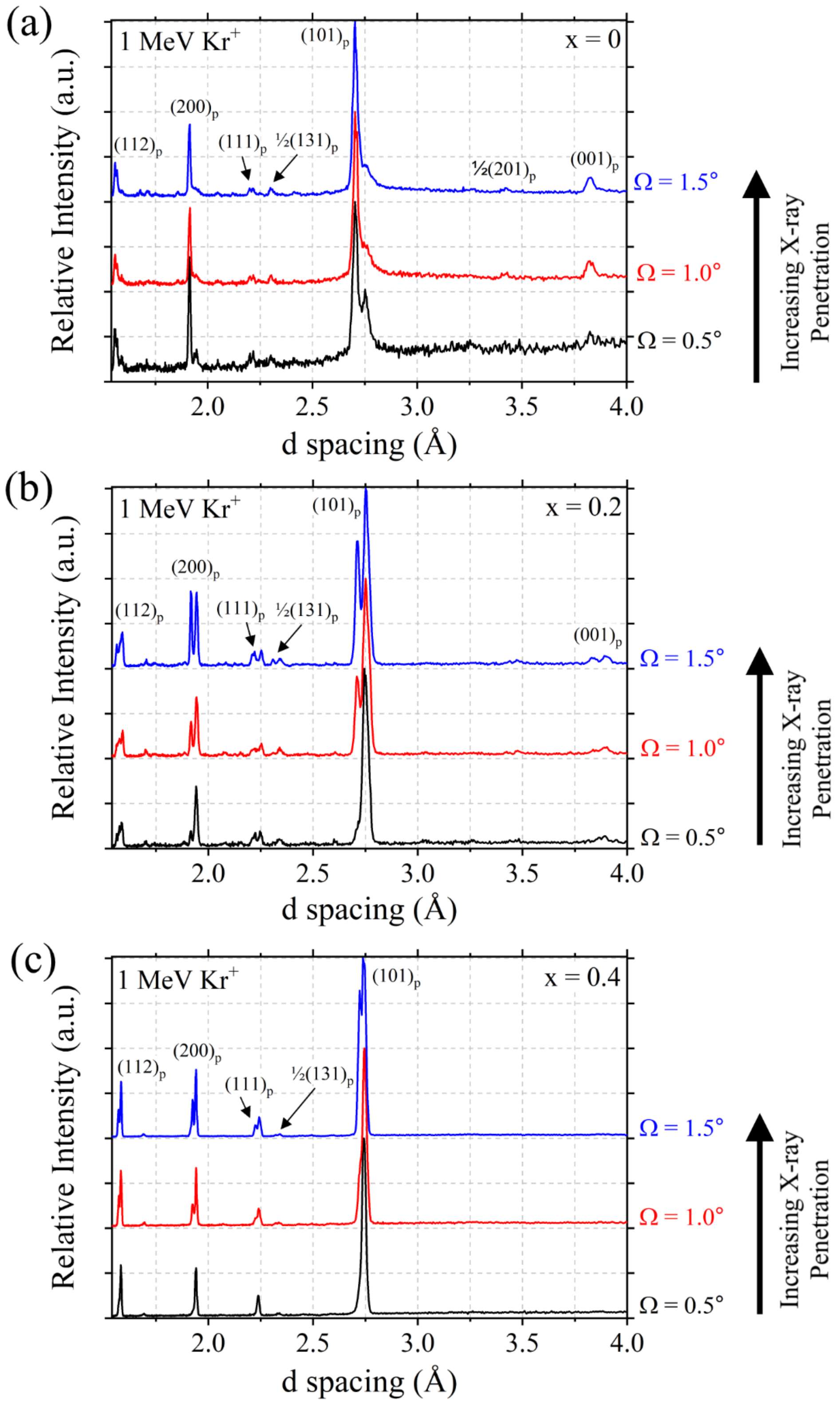

Figure 7.2 GAXRD patterns for (a) x = 0, (b) x = 0.2 and (c) x = 0.4 samples irradiated with 1 MeV Kr$^+$ to a fluence of 1 x 10^{15} ions cm^{-2}. Observed peaks are indexed with regard to the aristotype perovskite structure. Three incident angles are presented with Ω = 0.5° in black, Ω = 1.0° in red and Ω = 1.5° in blue.

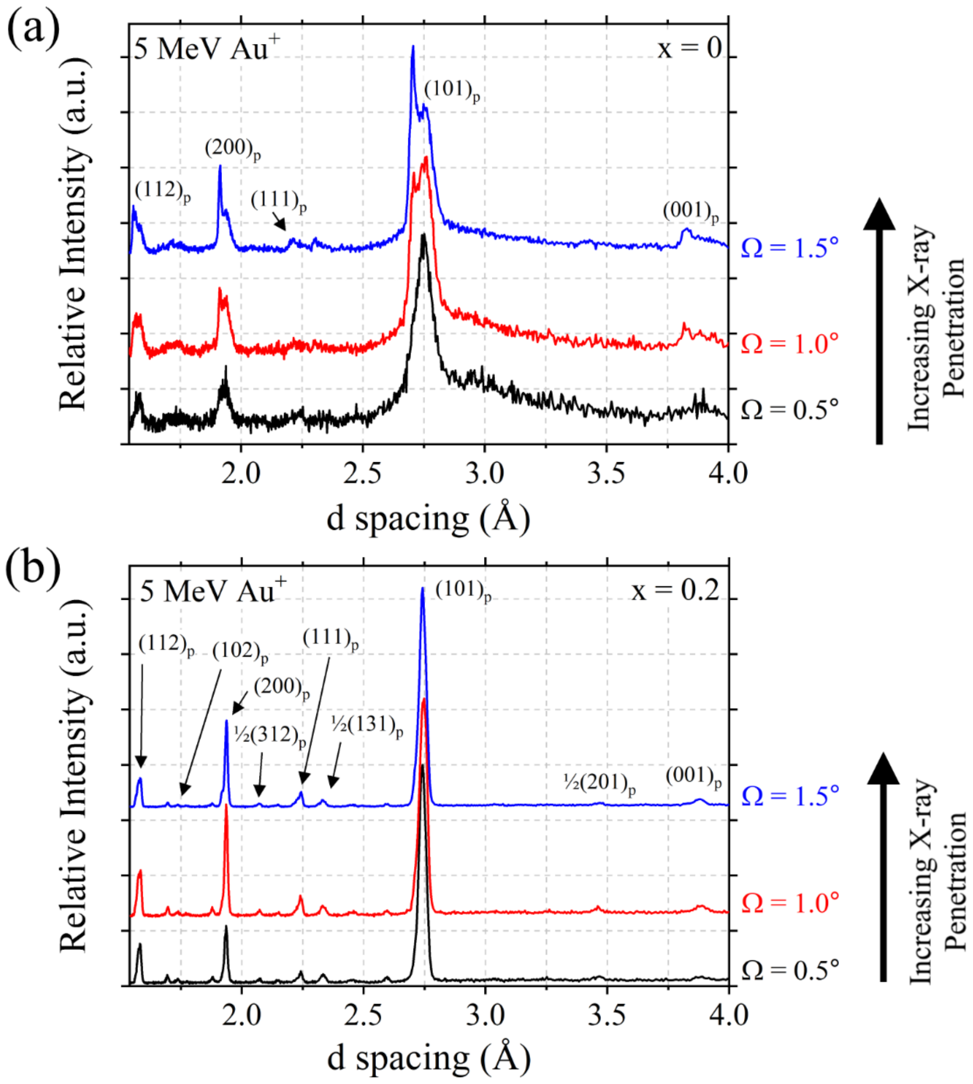

Figure 7.3 GAXRD patterns for (a) x = 0 and (b) x = 0.2 samples irradiated with 5 MeV Au^{+} to a fluence of 5 x 10^{14} ions cm^{-2}. Three incident angles are presented with Ω = 0.5° in black, Ω = 1.0° in red and Ω = 1.5° in blue.

possible to distinguish these reflections in the x = 0 patterns, although this is likely due to the high noise contribution. For this reason, SAED was used to confirm the structure of this sample in section 7.4.

The x = 0 and 0.2 samples were further investigated using GAXRD after ion implantation with 5 MeV Au^{+} to a fluence of 5 x 10^{14} ions cm^{-2}. The x = 0.4 sample fell off the mounting stage during 5 MeV Au^{+} implantations resulting in an unknown final fluence, so this sample was not employed for analysis. For x = 0 and 0.2, a damage region is produced of 1000 nm by SRIM, with peak damage at 640 nm. GAXRD patterns for the x = 0 and 0.2 samples are presented in figures 7.3a and 7.3b, respectively. For x = 0, the Ω = 0.5° trace exhibits no presence of pristine reflections, and all crystallinity present had undergone damage induced lattice expansion. A significant increase in diffuse scattering and broadening of crystalline reflections was observed when compared with the 1 MeV Kr^+ implanted sample, indicating an increase in induced damage. As with figure 7.2a, only peaks related to the aristotype perovskite structure were identified, but this did not provide conclusive evidence of a transition from the *Pbnm* structure due to the high background contribution within the pattern. Such background was a result of the low-incident angle used and the reduced signal received from highly damaged material compared to a crystalline response. For x = 0.2, the patterns indicated the sample remained highly crystalline, as was observed under the 1 MeV Kr^+ implantation condition in figure 7.2b. All the reflections within the sample underwent radiation damage induced volume swelling, and only slight shoulder peaks in the $(101)_p$ and $(200)_p$ reflections were observed within the $\Omega = 1.5°$ pattern. This corresponded to an X-ray penetration depth of 1.2 µm, or almost double the peak damage depth. As with the 1 MeV Kr^+ data, this suggested the x = 0.2 sample had increased resistance to amorphisation compared to the x = 0 sample. Furthermore, the structure was confirmed as *Pbnm* with tilt series $a^-a^-c^+$ after ion implantation through the identification of lattice expanded ½$(131)_p$, ½$(241)_p$ and ½$(312)_p$ reflections, corresponding to anti-phase tilting, mixed-phase tilting and in-phase tilting, respectively.

In all cases, it was possible to quantify the induced lattice expansions by observing shifts in d-spacing values. Lattice parameters as calculated for the 1 MeV Kr^+ implanted x = 0, 0.2 and 0.4 samples and for the 5 MeV Au^+ ion implanted x = 0 and 0.2 samples are presented in table 7.2. For x = 0, both ion implantation conditions led to a lattice volume expansion of 4.8 ± 0.1 % from the pristine. Considering the increased damage induced under the 5 MeV Au^+ implantation condition, this provided evidence of a saturation of lattice expansion prior to amorphisation. As shown in table 7.2, the scaled *b* parameter was found to saturate at 1.2 ± 0.1 % across both conditions, with the *a* and *c* parameters saturating with expansions of 1.5 ± 0.1 % and 2.2 ± 0.1 %, respectively. Therefore, it was concluded the lattice expansion in the x = 0 sample is anisotropic under Kr^+ and Au^+ ion implantation. Lattice expansion for the x = 0.2 sample was 2.1 ± 0.1 % and 1.7 ± 0.1 % for the 1 MeV Kr^+ and 5 MeV Au^+ conditions, respectively. This suggests a saturation point for lattice expansion had not been reached, and further expansion would be induced by a higher

Table 7.2 Calculated lattice parameters for the x = 0, 0.2 and x = 0.4 samples after 1 MeV Kr^+ and 5 MeV Au^+ implantation, with pristine values presented for comparison.

	Pristine	1 MeV Kr^+	5 MeV Au^+
Dose		1×10^{15} ions cm^{-2}	5×10^{14} ions cm^{-2}
$CaTiO_3$ (x = 0)			
Volume Expansion (%)	-	4.81 (5)	4.78 (7)
a (Å)	3.8043 (2)	3.863 (5)	3.861 (3)
b (Å)	3.8469 (2)	3.892 (6)	3.891 (5)
c (Å)	3.81835 (3)	3.904 (3)	3.903 (4)
$Ca_{0.8}La_{0.13}TiO_3$ (x = 0.2)			
Volume Expansion (%)		2.11 (8)	1.72 (6)
a (Å)	3.8251 (4)	3.846 (5)	3.841 (7)
b (Å)	3.8497 (3)	3.859 (7)	3.856 (9)
c (Å)	3.8326 (5)	3.884 (5)	3.876 (4)
$Ca_{0.6}La_{0.267}TiO_3$ (x = 0.4)			
Volume Expansion (%)		1.90 (3)	-
a (Å)	3.8445 (1)	3.874 (6)	-
b (Å)	3.8573 (2)	3.864 (3)	-
c (Å)	3.8513 (5)	3.879 (5)	-

ion implantation fluence. However, expansion of the *b* parameter was 0.25 ± 0.03 % and 0.17 ± 0.02 % for the 1 MeV Kr^+ and 5 MeV Au^+ conditions respectively, compared with 0.54 ± 0.02 % and 0.42 ± 0.02 % for the *a* parameters, and 1.32 ± 0.12 % and 1.12 ± 0.09% for the *c* parameters. As with the x = 0 sample, the *b* parameter expanded to a lesser extent than the *c* and *a* parameters, and this trend continued for the x = 0.4 sample implanted with 1 MeV Kr^+, with a *b* parameter expansion of 0.25 ± 0.04 %, and *a* and *c* expansions of 0.75 ± 0.05 % and 0.90 ± 0.06 %, respectively.

7.3.2 $Ca_{0.5}La_{0.33}TiO_3$, $Ca_{0.4}La_{0.4}TiO_3$ and $Ca_{0.3}La_{0.467}TiO_3$ (x = 0.5, 0.6 and 0.7)

In the previous section, it was observed that doping $CaTiO_3$ (x = 0) with La was found to increase the resistance to amorphisation of the x = 0.2 and 0.4 samples, relative to x = 0. On increasing the La content further, the increases in resistance to amorphisation were seen to diminish. Incident angles of $\Omega = 0.5°$ gave X-ray penetration depths of 310nm, 300 nm and 280 nm for the x = 0.5, 0.6 and 0.7 samples, respectively. GAXRD patterns for the x = 0.5, 0.6 and 0.7 samples, ion implanted with 1 MeV Kr^+ are shown in figures 7.4a, 7.4b and 7.4c, respectively. For the x = 0.5 sample, both lattice expanded and pristine material was observable in the $(101)_p$, $(111)_p$, $(200)_p$ and $(112)_p$ reflections. Diffuse scattering was also evident for the x = 0.5 patterns, suggesting a reduction in damage tolerance when compared with the x = 0.2 and 0.4 samples. Furthermore, a doping limit was reached whereby increased damage tolerance was no longer observed. It was not possible to clarify the *Pbnm* structure for the x = 0.5 sample implanted with 1 MeV Kr^+, as only reflections indexed to the aristotype perovskite structure were observable. This was likely due to limitations of the GAXRD configuration, which does not provide the resolution of conventional XRD. An observable increase in diffuse scattering was found for the x = 0.6 and 0.7 samples when compared with x = 0.5, suggesting a further decrease in damage tolerance. The difficulties in distinguishing between the *Ibmm* and *I4/mcm* phases have already been discussed and by investigating highly damaged material in a GAXRD configuration these were further enhanced due to the reduced volume of material probed. A low intensity ½$(131)_p$ reflection can be observed in both samples, suggesting anti-phase tilting is still present, although the high background contributions brought on by diffuse scattering made these reflections difficult to conclusively identify. While

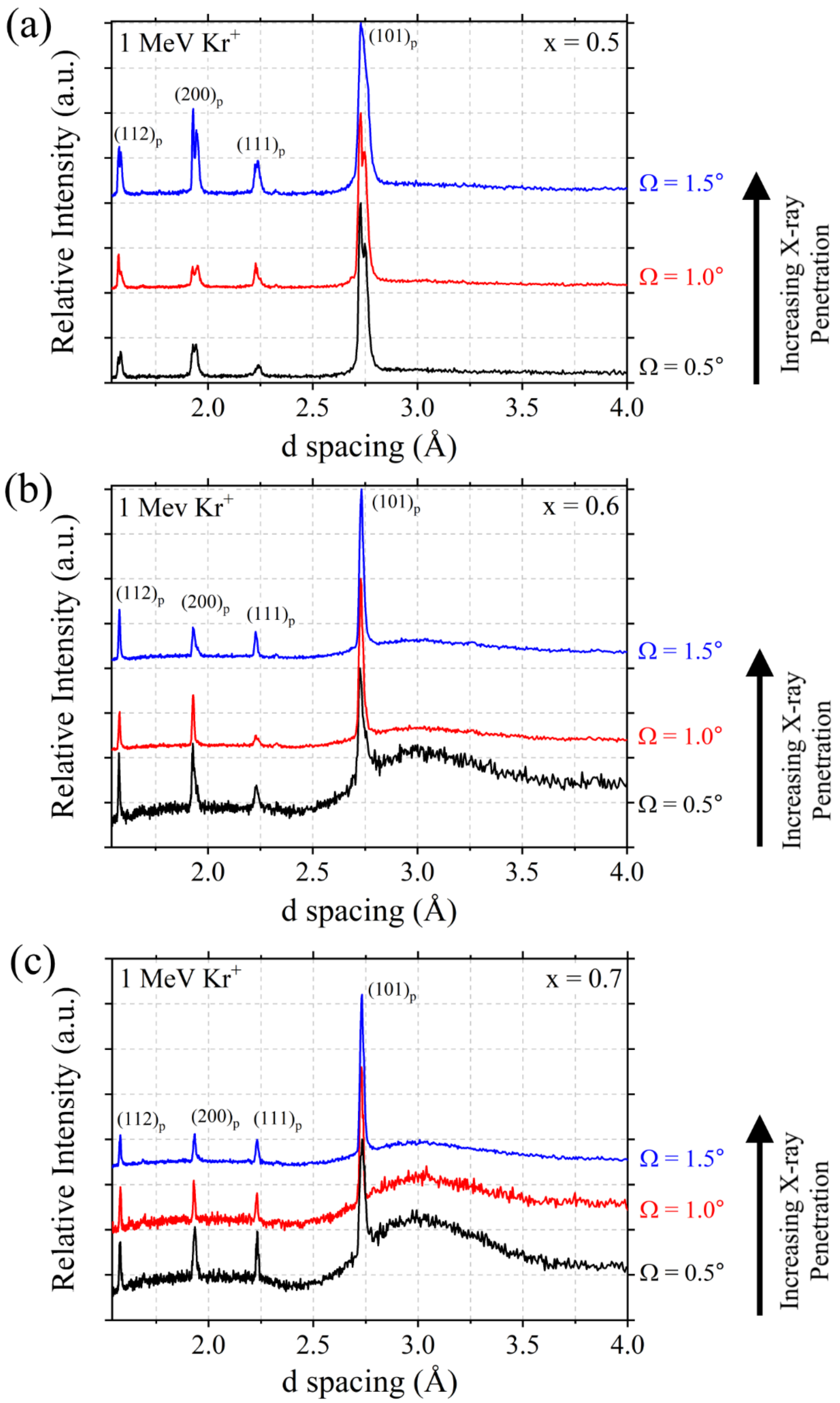

Figure 7.4 GAXRD patterns for (a) x = 0.5, (b) x = 0.6 and (c) x = 0.7 samples irradiated with 1 MeV Kr^+ to a fluence of 1 x 10^{15} ions cm^{-2}. Three incident angles are presented with Ω = 0.5° in black, Ω = 1.0° in red and Ω = 1.5° in blue.

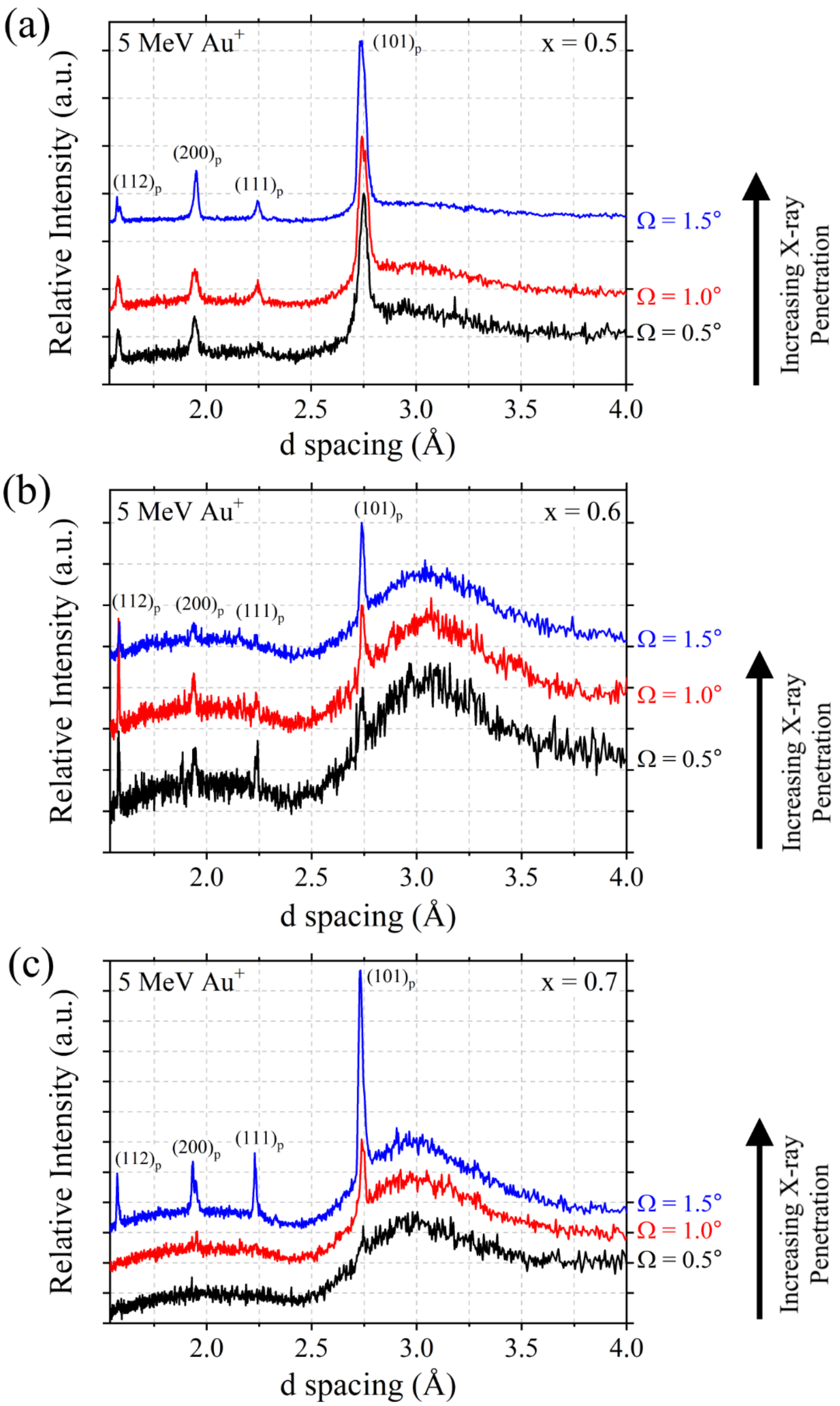

Figure 7.5 GAXRD patterns for (a) x = 0.5, (b) x = 0.6 and (c) x = 0.7 samples irradiated with 5 MeV Au$^+$ to a fluence of 5 x 10^{14} ions cm^{-2}. Three incident angles are presented with Ω = 0.5° in black, Ω = 1.0° in red and Ω = 1.5° in blue.

lattice expansion was evident in the x = 0.5 sample, no lattice expansion was observed within the crystalline phases observed in the x = 0.6 and 0.7 patterns.

GAXRD patterns for the 5 MeV Au^+ ion implanted x = 0.5, 0.6 and 0.7 samples are presented in figures 7.5a, 7.5b and 7.5c. A further increase in diffuse scattering was observed for the x = 0.5 sample when compared with the 1 MeV Kr^+ implantation condition, suggesting an increase in the induced damage using the 5 MeV Au^+ condition. Only lattice expanded reflections were observable within the sample, a consequence of the deeper penetration of the 5 MeV Au^+ ions. As with 1 MeV Kr^+, no peaks other than those related to the aristotype perovskite structure were identified, but this did not provide evidence of any phase changes due to the high background contribution potentially hiding non-aristotype reflections. The x = 0.6 and 0.7 patterns after 5 MeV Au^+ ion implantation had a large diffuse component, the x = 0.6 patterns exhibiting some residual crystallinity and the x = 0.7 sample presented with only a slight $(101)_P$ peak. As with the 1 MeV Kr^+ implanted patterns, no lattice expansion was observed. Once more, this represented a further drop in damage tolerance from x = 0.5, and an increase in the induced damage from the 5 MeV Au^+ condition when compared with 1 MeV Kr^+.

While it was not possible to distinguish any lattice expansion in the x = 0.6 or 0.7 samples under either implantation condition, lattice expansion in the x = 0.5 sample was quantified. Expanded lattice parameters for the x = 0.5 sample under both conditions are shown in table 7.3. Comparison of the overall lattice expansion values for the 1 MeV Kr^+ and 5 MeV Au^+ conditions suggested a saturation point, as with the x = 0 sample, had been reached of 1.8 ± 0.1 %. Furthermore, lattice expansion with regard to the *b* parameter was again observed to occur to a lesser extent than the *a* and *c* parameters, with expansion under the 1 MeV Kr^+ and 5 MeV Au^+ conditions of 0.14 ± 0.3 % and 0.13 % ± 0.02, respectively, 0.54 ± 0.07 % and 0.73 ± 0.06 % for the *a* parameters, and 1.03 ± 0.08 % and 1.00 ± 0.06 % for the *c* parameters, respectively. If expansion had reached a saturation point, this represents a 2.6 – 2.8 factor decrease in the lattice expansion that the x = 0.5 sample can accommodate when compared with the x = 0 sample.

Table 7.3 Calculated lattice parameters for the x = 0.5 sample after 1 MeV Kr^+ and 5 MeV Au^+ implantation, with pristine values presented for comparison.

	Pristine	1 MeV Kr^+	5 MeV Au^+
Dose	-	1×10^{15} ions cm^{-2}	5×10^{14} ions cm^{-2}
Volume Expansion (%)	-	1.71 (7)	1.85 (4)
a (Å)	3.8526 (6)	3.873 (6)	3.881 (4)
b (Å)	3.8573 (3)	3.863 (5)	3.862 (3)
c (Å)	3.8513 (3)	3.891 (3)	3.890 (2)

7.3.3 $Ca_{0.1}La_{0.6}TiO_3$ (x = 0.9)

Finally, the x = 0.9 end member was studied by GAXRD. An incident angle of $\Omega = 0.5°$ gave an X-ray penetration depth of 250 nm. GAXRD patterns for the x = 0.9 sample implanted with 1 MeV Kr^+ and 5 MeV Au^+ are presented in figures 7.6a and 7.6b, respectively. For the 1 MeV Kr^+ condition, the $\Omega = 0.5°$ pattern consisted of high levels of diffuse scattering, with a small amount of residual crystallinity, suggesting the sample was highly damaged. When compared with the x = 0.6 and 0.7 samples, this represented the most highly damaged of the 1 MeV Kr^+ implanted samples. Furthermore, the $\Omega = 0.5°$ pattern for the 5 MeV Au^+ implanted x = 0.9 sample contained no crystallinity, containing only diffuse scattering as the sample had amorphised. Again, this provides evidence that the x = 0.9 sample is the least damage tolerant of the samples within the $Ca_{1-x}La_{2x/3}TiO_3$ under these conditions. The lack of lattice expansion is in agreement with the x = 0.6 and 0.7 samples, although this statement is not conclusive due to the lack of crystalline reflections observed in the $\Omega = 0.5°$ patterns. Considering the peak damage depth of 640 nm in the 5 MeV Au^+ condition, the X-ray penetration depth of 560 nm at $\Omega = 1.0°$ was expected to also consist solely of diffuse scattering. It is likely that the decreased density of the amorphised damaged layer led to an increased X-ray penetration depth, not considered by the GAXRD penetration calculations.

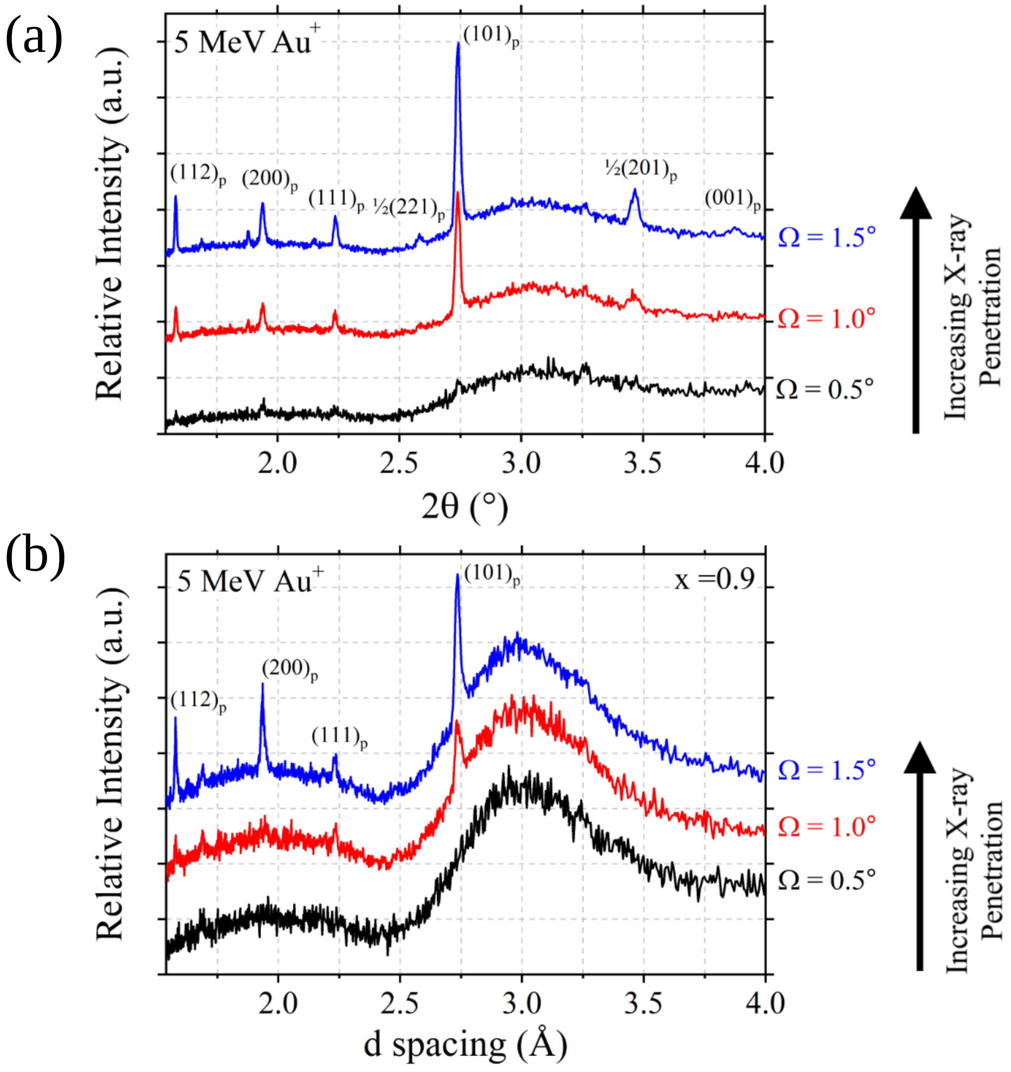

Figure 7.6 GAXRD patterns for the x = 0.9 sample ion implanted with (a) 1 MeV Kr$^+$ to a fluence of 1 x 10^{15} ions cm^{-2} and (b) 5 MeV Au$^+$ to a fluence of 5 x 10^{14} ions cm^{-2}. Three incident angles are presented with **Ω** = 0.5° in black, **Ω** = 1.0° in red and **Ω** = 1.5° in blue.

7.3.4 Amorphous Fractions

This chapter has given a qualitative assessment of diffuse scattering and damage induced, while lattice expansion has been quantified. The amorphous fraction of the implanted surface regions was quantified using the GAXRD patterns obtained, as is described in section 4.3.2. This was achieved through fitting pseudo-Voigt peaks to the $(101)_p$ reflection and diffuse scattering intensities, as has been employed by various studies [105,147–149] and taking a ratio of the amorphous area to the total area fitted. The **Ω** = 0.5° patterns were used to determine the amorphous fraction percentage

Table 7.4 Calculated Amorphous fractions for the $Ca_{1-x}La_{2x/3}TiO_3$ system under both 1 MeV Kr^+ and 5 MeV Au^+ conditions.

x, $Ca_{1-x}La_{2x/3}TiO_3$	1 MeV Kr^+ Amorphous Fraction (%)	5 MeV Au^+ Amorphous Fraction (%)
0	60 (2)	75 (3)
0.2	0 (0)	0 (0)
0.4	0 (0)	-
0.5	52 (12)	76 (2)
0.6	89 (2)	97 (2)
0.7	91 (2)	98 (2)
0.9	98 (2)	100 (0)

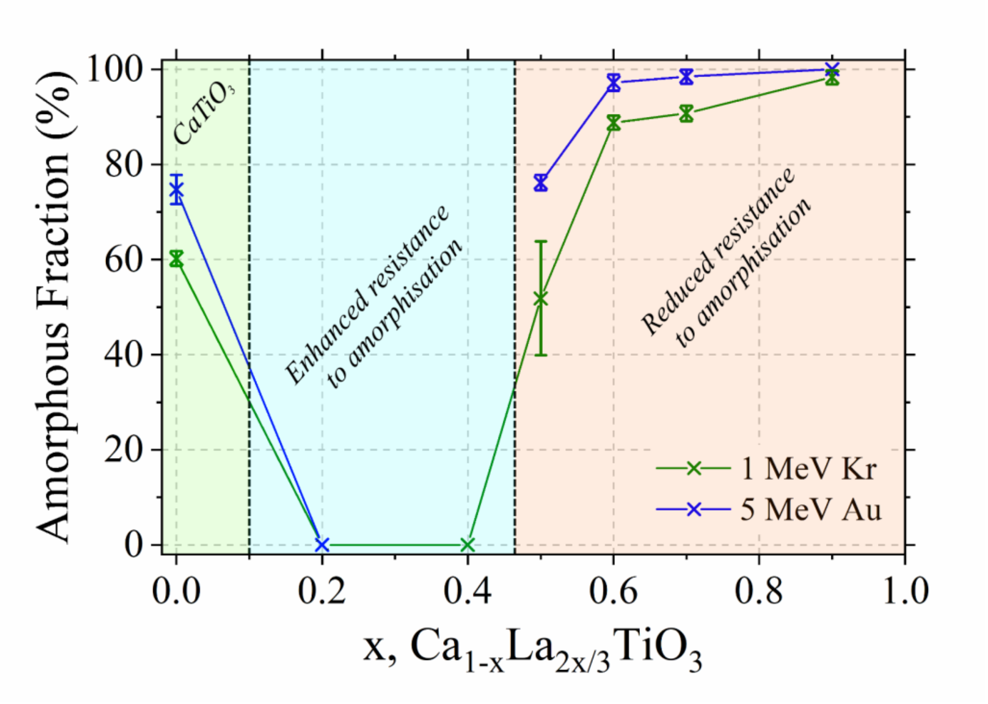

Figure 7.7 Amorphous fractions of samples in the $Ca_{1-x}La_{2x/3}TiO_3$ system. Fractions as calculated for 1 MeV Kr^+ implanted samples are presented in green, and 5 MeV Au^+ in blue. Three regions were identified with $CaTiO_3$ in light green enhanced/reduced resistance to amorphisation in blue and orange, respectively.

for both ion implantation conditions presented in table 7.4, and these data are presented graphically in figure 7.7. The use of this angle over both conditions cannot provide a precise quantification of the amorphous fraction within the damaged region, as the depth-damage profile are not identical for 1 MeV Kr^+ and 5 MeV Au^+. However, under both conditions maximum damage was observed at $\Omega = 0.5^\circ$, providing the best estimation of damage tolerance of each sample. The amorphous fractions, as calculated, allowed for the resistance to amorphisation of the samples to be ordered, with (x =) 0.2 = 0.4 > 0 = 0.5 > 0.6 > 0.7 > 0.9.

7.4 Cross-sectional Transmission Electron Microscopy

7.4.1 1 MeV Kr^+ Implanted $CaTiO_3$ (x = 0)

Confirmation of the effects of induced radiation damage was undertaken using XTEM to clarify samples in the enhanced and reduced damage tolerance regimes. Specifically, the x = 0, 0.2 and 0.9 samples implanted with 1 MeV Kr^+ were examined. Figure 7.8a shows a bright field XTEM micrograph of the x = 0 sample implanted with 1 MeV Kr^+ ions. Electron diffraction patterns taken from regions marked i and ii are shown in figures 7.8ai and 7.8aii, respectively. The damage profile calculated by SRIM is overlaid on the XTEM micrograph. In the XTEM micrograph, the dark mottled contrast located between about 450 nm and 600 nm was attributed to interstitial-type defect clusters, the lighter region located around the peak of the SRIM profile was attributed to amorphous material, and the regions of dark contrast between the surface and 450 nm were attributed to nano-crystallites within highly-damaged material. This was confirmed by the electron diffraction pattern taken at point i, which comprised a diffuse ring indicative of amorphous material and diffraction spots from crystalline material. According to the SRIM profile, the maximum depth of damage was ≈ 600 nm, with the peak damage depth at 310 nm. This is in good agreement with the XTEM results, and the electron diffraction pattern taken at point ii 800 nm from the implanted surface is indicative of undamaged, crystalline material. Figure 7.9 showed a magnified XTEM image of the nano-crystallites. Moiré fringes were visible where some of the nano-crystallites overlap, confirming the dark contrast was from overlapping crystalline material with the same or similar interatomic spacing. Such nano-crystallites were ≈ 10 nm in diameter and observed across the implanted region.

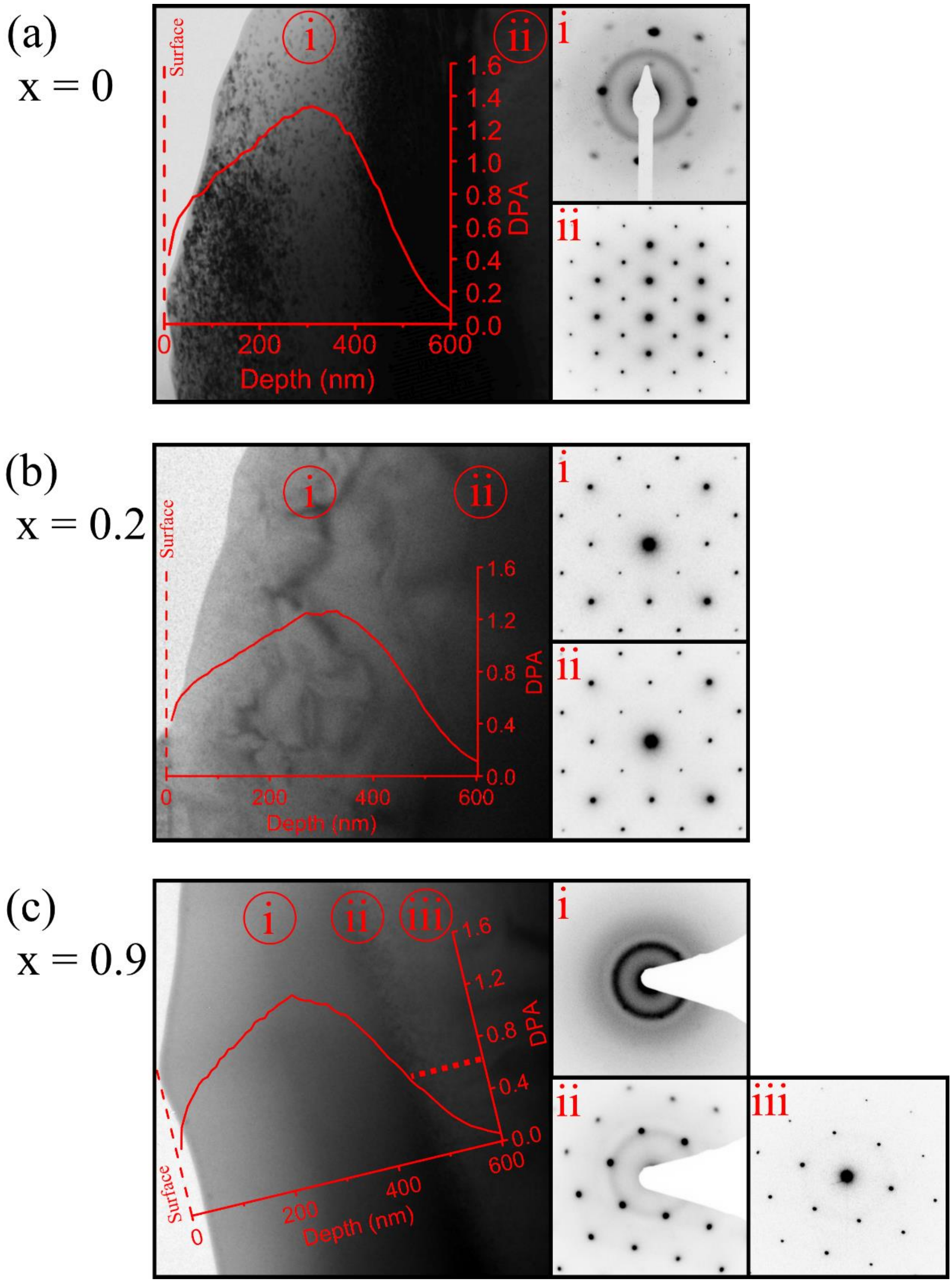

Figure 7.8 Bright-field XTEM micrographs of the (a) x = 0, (b) x = 0.2 and (c) x = 0.9 samples, all ion implanted with 1 MeV Kr^+ to a fluence of 1 x 10^{15} ions cm^{-2}. SAEDPs are presented for each sample from the damaged regions and in the pristine bulk, and are labelled according to their origin with an i, ii or iii on each micrograph. Calculated SRIM profiles for each sample are superimposed to scale.

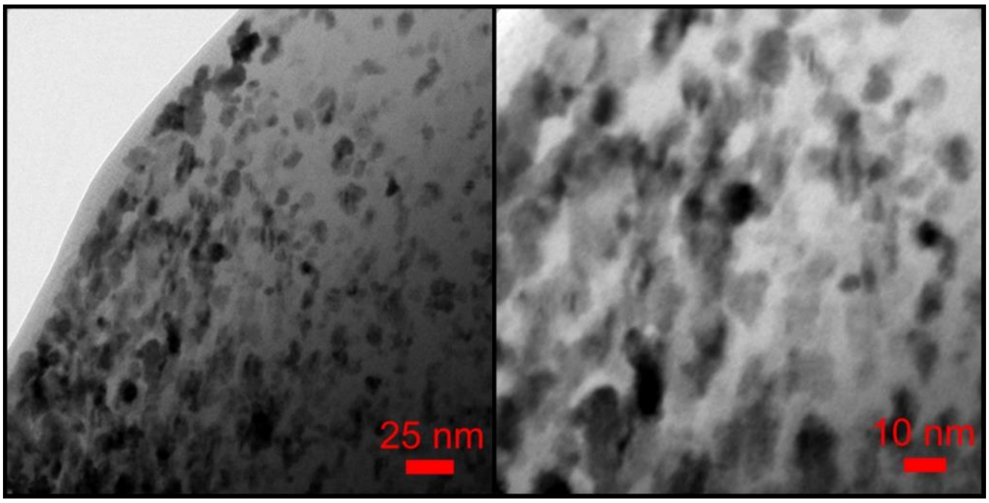

Figure 7.9 Bright-field TEM micrographs of the x = 0 sample. Areas of mottled dark contrast show crystallite formation among highly damaged material. Moiré fringes are also visible, confirming the crystalline nature of these regions.

The crystallite concentration decreased with increasing dpa, suggesting the formation was directly related to the damage dose, as opposed to recrystallisation from induced amorphous material. As was discussed in chapter 6 of this thesis, ion milling has been shown to produce crystallites such as these within the A-site deficient samples. However, non-implanted areas of the implanted x = 0 sample showed no indication of crystallite formation, and crystallite formation was unique to the implanted region. It was concluded that 1 MeV Kr^+ ion implantation to this fluence in the x = 0 sample leads to the formation of a partially damaged layer and full amorphisation of the structure is not observed at any depth. This was confirmed through the SAEDP presented in figure 7.8ai. This SAEDP represents the [110] zone axis, and the presence of ½(*ooo*) reflections provides evidence of the $a^-a^-c^+$ tilt system and the *Pbnm*. GAXRD was unable to resolve the structure within the damaged region, and this SAEDP offered evidence that the structure *Pbnm* structure was maintained.

7.4.2 1 MeV Kr^+ Implanted $Ca_{0.8}La_{0.13}TiO_3$ (x = 0.2)

A bright field XTEM micrograph of the x = 0.2 sample implanted with 1 MeV Kr^+ is presented in figure 7.8b. No crystallite formation was observed as with the x = 0 end member, as small regions of darker contrast were not observed and Moiré fringes were absent. The SAEDP presented in figure 7.8bi taken from the peak damage depth at 310 nm on the superimposed SRIM calculated was crystalline with no diffuse rings present. The sample maintained its *Pbnm* structure, as can be observed through the presence of ½(*ooe*) reflections within the [001] zone axis SAEDP, presented in figure 7.8i, indicative of in-phase tilting within the $a^-a^-c^+$ configuration. Kinked bands of darker contrast were present within the damaged region, and these likely originated either from strain fields within the sample onset by radiation damage or thickness contrast inherent in the prepared sample. Diffraction contrast across the 600 nm damage region further suggested the sample is fully crystalline across the superimposed SRIM damage profile, suggesting the fluence required for amorphisation, or even partial damage of the structure, was greater than the 1.3 dpa induced using 1 MeV Kr^+ irradiation. This represented a significant increase in damage tolerance when compared with the x = 0 sample, onset by the 13 mol% La^{3+} doping used, and unrelated to structural changes. This offered confirmation of the increased damage tolerance of the sample observed via GAXRD.

7.4.3 1 MeV Kr^+ Implanted $Ca_{0.1}La_{0.6}TiO_3$ (x = 0.9)

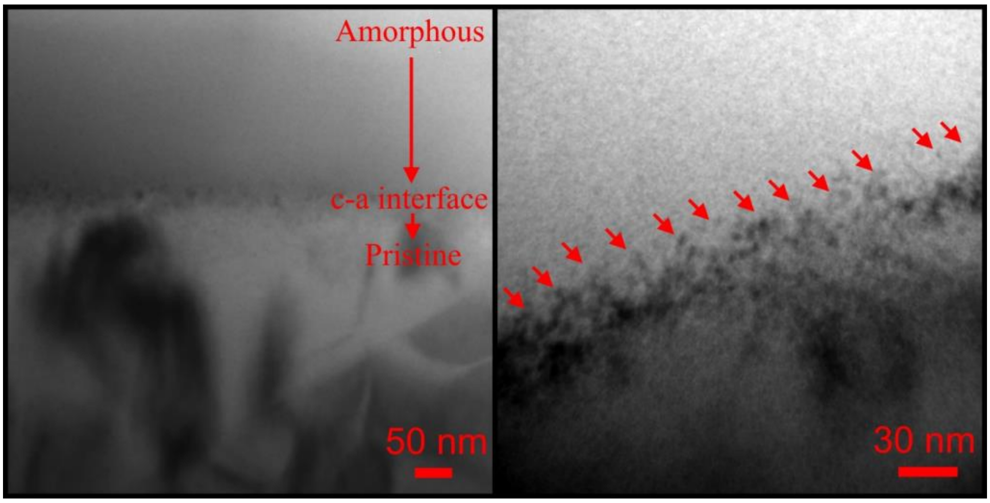

Figure 7.10 Crystalline to amorphous (c-a) interface for the x = 0.9 sample, with end of track defects present as small regions of high contrast, indicated by red arrows.

The final sample investigated using XTEM was the x = 0.9 end member. A bright field XTEM micrograph of the sample ion implanted with 1 MeV Kr^+ is presented in figure 7.8c, with the calculated SRIM profile superimposed. Light contrast across the SRIM profile to a depth of ≈ 450 nm was indicative of amorphous material. This was confirmed through the SAEDP taken from the peak damage region at 300 nm, presented in figure 7.8ci, in which no crystalline reflections were observed and only diffuse rings present. At 450 nm, dark regions of mottled contrast were visible and attributed to interstitial-type end of damage track defects. This is the crystalline-amorphous (c-a) interface whereby the implanting ions have transferred energy to the point whereby they have insufficient energy to induce amorphisation. This interface and the darker regions of contrast are shown in figure 7.10 and indicated by red arrows. The c-a interface was used quantify the dose required to amorphise the x = 0.9 sample using the SRIM profile overlaid as $F_C = 0.61 \pm 0.2$ dpa. The partially damaged nature of the c-a interface was confirmed through the SAEDP taken from the region and presented in figure 7.8cii, in which a diffuse ring was observed among crystalline reflections. 500 nm from the implanted surface the sample was fully crystalline as undamaged material was observed, shown through the SAEDP in figure 7.8iii in which only crystalline reflections were present.

7.5 Discussion

7.5.1 Phase Stability

The use of GAXRD allowed for the structural changes induced by the 1 MeV Kr^+ and 5 MeV Au^+ ion implantation conditions, while XTEM allows for the direct observation of such effects and confirmation of the GAXRD findings. First, let us consider the x = 0 end member and the lesser La doped x = 0.2 and 0.4 samples. Reports of an orthorhombic to cubic transition has been observed prior to amorphisation by various groups [6,11,192], however this was ruled out for the 1 MeV Kr^+ implanted x = 0 sample though the presence of ½(*ooo*) reflections in the [110] zone axis SAEDP presented in figure 7.8ai, indicative of anti-phase tilting and forbidden by cubic symmetry. This is likely due to the level of damaged induced, and a higher-dose is likely needed to induce the orthorhombic-cubic transition in $CaTiO_3$. No phase transitions were observed for the x = 0.2 and 0.4 samples, through the presence of the anti-phase tilting $½(131)_p$ and mixed phase tilting $½(241)_p$ reflections, indicative of the mixed tilt system $a^-a^-c^+$ as was observed in pristine XRD and electron diffraction in chapter 5. This was observed in both ion implanted conditions, although a phase transition in the 5 MeV Au^+ implanted x = 0 sample cannot be conclusively ruled out due to a lack of resolution.

7.5.2 Lattice Expansion

Characterisation of the x = 0, 0.5, 0.6, 0.7 and 0.7 samples under both ion implantation conditions provided evidence of a higher induced damage level through 5 MeV Au^+ ion implantation, as exhibited by the increased amorphous fractions under this condition. It is very likely the SRIM code underestimated the induced damage using this condition, and would agree with previous studies suggesting that SRIM can overestimate the electronic stopping powers of heavy ions implanting into compounds containing light atoms [89,193,194]. Considering this proviso in the context of the x = 0 sample, lattice expansion was found to be equivalent within error for both implantation conditions, while a higher proportion of diffuse scattering was observed for the 5 MeV Au^+ condition. This suggests a saturation point for lattice expansion is reached prior to amorphisation of the structure. This finding is in agreement with Ball *et al* [90], in which a saturation value of 3.8 % is reported, with the discrepancy likely due to the use of neutron irradiation as opposed to heavy ion implantation. Ball *et al* [90] also report the anisotropic nature of lattice expansion within $CaTiO_3$, with the *b* parameter saturating at a lower value than the *a* and *c* parameters, and this can be further confirmed within this work. Increasing the La^{3+} content was shown in chapter 5 to increase the unit cell parameters of the $Ca_{1-x}La_{2x/3}TiO_3$ system. However, such increases occur to a greater extent in the *a* and *c* parameters as the anti-phase and in-phase octahedral tilt angle decrease. The increase in the *a* parameter, for example, is 0.048 ± 0.001 Å from x = 0 to x = 0.5, while the *b* parameter increases by 0.012 ± 0.001 Å. It is likely a similar mechanism exists within the context of radiation induced lattice expansion. Saturation of lattice expansion was also observed for the x = 0.5 sample at 1.8 ± 0.1 %, while the *b* parameter was similarly found to saturation at a lower value than the *a* and *c* parameters. Such effects were not observed for the x = 0.2 and 0.4 samples, but this is likely due to the highly crystalline nature of the samples, and a higher fluence was likely required for a saturation point for lattice expansion to be observed. Furthermore, while saturation of lattice expansion was not observed for the x = 0.6, 0.7 or 0.9 samples, it is likely these structures are unable to accommodate significant lattice expansion prior to amorphisation for this to be resolvable using GAXRD.

7.5.3 Damage Comparison

The x = 0 end member sample was partially damaged under both ion implantation conditions, with amorphous fractions of 60 % and 72 % for the induced 1.34 and

1.37 dpa induced, as calculated by SRIM, respectively. *In-situ* studies conducted using 400 keV Kr^+ ion implantation by Meldrum *et al* [8] report a room temperature amorphisation dose of 1.8 dpa for $CaTiO_3$, while Smith *et al* [97] report an amorphisation dose of 2.2 dpa. These values agree with this study based on the partially damaged nature of the x = 0 sample under both conditions at 1.34 and 1.37 dpa. Direct comparison with other amorphisation studies, such as those conducted using neutron irradiation [90] or actinide doping [86,192,195], is difficult due to the requirement for dpa conversion. However, the most accurate comparison can be made with the 2 MeV Kr^+ bulk ion implantation on a Nd-doped $CaTiO_3$ sample reported by Davoisne *et al* [11]. The amorphisation dose is reported as 4 dpa, while the sample reported in this work is partially damaged by ≈ 1.3 dpa. Considering the level of damage observed in the bright field TEM micrograph of the x = 0 sample in figure 7.8a, and the 60 % amorphous fraction induced across the damage region, it seems unlikely that a 3-fold increase in dpa would be required for amorphisation of the structure. This study would suggest that the dpa required for amorphisation is closer to the level reported by Meldrum *et al* [8] of 1.8 dpa. As has been observed through the calculated amorphous fractions under both implantation conditions, the x = 0.2 and 0.4 samples remain crystalline, suggesting an increased damage tolerance when compared with the x = 0 end member. Increasing La content to $x \geq 0.5$ leads to a progressive drop in radiation damage tolerance when compared with the x = 0.4 sample, allowing an enhanced damage tolerance regime of $0.2 \leq x \leq 0.4$. The most directly comparable compositions to the $Ca_{1-x}La_{2x/3}TiO_3$ system are the sister compositions of the $Sr_{1-x}La_{2x/3}TiO_3$ system. With regard to the x = 0.2 and 0.4 samples, the most directly comparable compositions are the $Sr_{0.85}La_{0.2}TiO_3$ and $Sr_{0.55}La_{0.3}TiO_3$ samples. Smith *et al* [99] do not report room temperature amorphisation doses but applying their report values to equation 2.9 allows for room temperature values to be estimated. In both cases, the required fluence for amorphisation are room temperature is $2.5 \pm 0.2 \times 10^{15}$ ions cm^{-2}, which considering the implantation fluences employed in this study, would suggest agreement with the increased tolerance for radiation damage observed within the $0.2 \leq x \leq 0.4$ regime. Secondly, let us consider $CaTiO_3$, and the bulk studies conducted by Davoisne *et al* [11]. As has been discussed, this sample required an amorphisation dosage of 4 dpa, and at ≈ 3.5 dpa even partial damage is hard to identify. However, this study used Nd^{3+}-doping to 10 mol% on the A-site, compensated by 10 mol% Al^{3+} on the B-site. Semi-quantitative EDS composition analysis was undertaken by Davoisne *et al* [11] and this could suggest a level of A-site deficiency was induced, but this method is unable to quantify vacancy defects and considers the average composition of atoms present. It is likely, based on the observations of this study that a similar mechanism enhancing radiation damage tolerance was induced as with the x = 0.2 sample within this study, onset by A-site deficiency. This provides replicability of the results observed for the x = 0.2 and x = 0.4 samples within bulk titanate perovskites and suggests the amorphisation fluence for these samples may prove to be greater than 4 dpa.

Considering the x = 0.5, 0.6 and 0.7 samples, comparison can be made with the $Sr_{0.55}La_{0.3}TiO_3$ and $Sr_{0.4}La_{0.4}TiO_3$ samples, reported by Smith *et al* [99] as having amorphisation dosages of 2.7 x 10^{15} ions cm^{-2} and 1.1 x 10^{15} ions cm^{-2}, respectively. The data reported in this study would suggest a similar amorphisation dosage is required, with the $Sr_{0.55}La_{0.3}TiO_3$ sample implanted by Smith *et al* [99] not amorphised. This can be related to a possible $Ca_{1-x}La_{2x/3}TiO_3$ composition of the form x = 0.45, lying between the highly damage resistant x = 0.4 sample and the partially damaged x = 0.5 sample. The x = 0.6 sample remains highly damaged with some residual crystallinity amorphisation, whilst the x = 0.7 is more susceptible to amorphisation, requiring a reduced fluence based on GAXRD results presented. This would agree with the 1.1 x 10^{15} ions cm^{-2} implantation conducted by Smith *et al* [99] on the $Sr_{0.4}La_{0.4}TiO_3$ sample, as the radiation damage tolerance of the samples reduces with increasing lanthanum content for x > 0.4.

The x = 0.9 end member was quantified as having an amorphisation dosage of 0.61 ± 0.2 dpa using 1 MeV Kr^+ ion implantation. This represents a 3 fold decrease in the value for $CaTiO_3$ reported by Meldrum *et al* [8], and a 6.67 factor decrease when compared with the sample reported by Davoisne *et al* [11]. Comparison can be made with the compositionally similar La_2Ti_2O, $La_{0.67}TiO_3$, $LaAlO_3$, La_2TiO_5 [53] and the sister composition $Sr_{0.1}La_{0.67}TiO_3$ [99] using equation 2.9 and statistics inputted from the relevant literature. This converts to amorphisation fluence values for $La_2Ti_2O_7$ (2.16 x 10^{14} ions cm^{-2}), $La_{0.67}TiO_3$ (2.57 x 10^{14} ions cm^{-2}), $LaAlO_3$ (3.7 x 10^{14} ions cm^{-2}), La_2TiO_5 (1.92 x 10^{14} ions cm^{-2}) and $Sr_{0.1}La_{0.6}TiO_3$ (3.47 x 10^{14} ions cm^{-2}). The value of F_c = 0.61 ± 0.2 dpa for $Ca_{0.1}La_{0.6}TiO_3$ converts by SRIM to 4.3 x 10^{14} ions cm^{-2}, suggesting that the x = 0.9 sample is more damage tolerant than those samples reported. Considering the value for $La_{0.67}TiO_3$ reported by

Whittle *et al* [53], the decreasing damage tolerance continues post x = 0.9, and a region for enhanced amorphisation onset by increasing La content and A-site deficiency can be deduced for $0.5 \leq x \leq 1.0$ for the $Ca_{1-x}La_{2x/3}TiO_3$ system.

7.5.4 Enhanced Resistance to Amorphisation 0.1 < x < 0.5

Amorphous fraction calculations for the x = 0.2 and 0.4 samples presented in table 7.4 provide evidence of a region of enhanced resistance to amorphisation that exists within the $Ca_{1-x}La_{2x/3}TiO_3$ for $0.2 \leq x \leq 0.4$. In previous chapters the system has been considered with regard to its intrinsic A-site deficiency, however several explanations could give rise to the behaviours observed across the solid solution that are not linked to the A-site deficiency of the samples. These include changes in displacement energies through La doping, cation ordering, structural changes such as phase transitions and recovery effects. These effects will now be considered in detail. In the first instance, the $0.2 \leq x \leq 0.4$ enhanced damage tolerance regime will be discussed. Cation ordering can be ruled out as a possibility out as no ordering has been reported within this regime, as has been confirmed in the x = 0.2 sample by Danaie *et al* [10] and for x < 0.7 by Zhang *et al* [72] and Vashook *et al* [2]. Secondly, no structural changes are induced within the $0 \leq x \leq 0.5$ regime, with all samples shown to maintain the *Pbnm* structure and $a^-a^-c^+$ tilt system in chapter 5. Harder to deduce is the effect of threshold displacement energy, E_d, values, with no values across the $Ca_{1-x}La_{2x/3}TiO_3$ system reported. Values have been calculated for $CaTiO_3$ using high angular resolution electron channelling X-ray spectroscopy by Smith *et al* [34], giving E_d values for Ca of 82 ± 11 eV and 69 ± 9 eV for Ti, and a value for La in the $LaPO_4$ system is reported by Yaqi *et al* [196] of 56 eV. Considering these values for Ca and La, and the constant mol% of Ti, a proportional change in damage tolerance would be expected as La content increases, assuming E_d values do not change dramatically. In fact, the lower E_d of La when replacing Ca would suggest damage tolerance would reduce, and this is not observed experimentally in the x = 0.2 or 0.4 samples. Smith *et al* [5] gave consideration to the effect of oxygen vacancies, and data from various oxides have been reported including metal oxides, perovskites and pyrochlores [100,101]. In each case, the E_d value for oxygen remains in the region 47 ± 13 eV, and there is no evidence to suggest a significant change would be observed within the $Ca_{1-x}La_{2x/3}TiO_3$ solid solution. Again, this suggests changes to oxygen E_d values cannot explain the enhanced damage tolerance regime.

Now the variations in E_d have been considered, let us consider the possibility that radiation damage recovery could lead to such a damage response. In general, the rate of damage recovery is intrinsically linked to the mobility of defects within the atomic structure, and the increase in efficiency of recovery mechanisms such as interstitial-vacancy recombination this provides. It is possible to compare estimations of the energy required for the activation of recovery, calculated using equation 2.10. Unfortunately, *in-situ* data values for $Ca_{1-x}L_{2x/3}TiO_3$ are not currently available, however Smith *et al* [99] do report calculations based on the sister $Sr_{1-x}La_{2x/3}TiO_3$ system. Values for the activation energy for dynamic recovery reduce from 0.228 eV for $SrTiO_3$ to 0.192 eV and 0.168 eV for the x = 0.15 and 0.3 samples, respectively. However, the dynamic component is within error of $SrTiO_3$ for the x = 0.45 and 0.6 samples. Activation energies for the thermal component of recovery show a reduction from 0.931 eV for $SrTiO_3$ to 0.742 e V and 0.669 eV for the x = 0.1 and 0.3 samples, with the x = 0.45 sample within error of $SrTiO_3$. However, the x = 0.6 sample increases to 1.015 eV, requiring an increased level of thermal energy to activate thermal recovery. When compared with the current study, and assuming this trend translates to the $Ca_{1-x}La_{2x/3}TiO_3$ sister system, it can be postulated that both effects play a significant role. Conducting this study at room temperature does allow for the assertion that these effects are not directly related to varying temperature, and samples within the $0.2 \leq x \leq 0.4$ regime are intrinsically more damage tolerant than the x = 0 end members. Considering the enhanced recovery regime within the $Sr_{1-x}La_{2x/3}TiO_3$ system maintains the cubic *Pm-3m* structure and values for T_c were calculated *in-situ*, evidence has been presented that the enhanced recovery mechanism is not related the degree of structural ordering, the effects are not unique to the $Sr_{1-x}La_{2x/3}TiO_3$ system, the effects are present without varied temperature, and the effects occur within a bulk solid solution. Furthermore, as two different structures and A-site end member constituents within titanate systems exhibit enhanced recovery, increased damage tolerance appears to be directly linked to the induction of A-site vacancies, and as has been discussed, the apparent reductions in the activation energies required for both dynamic and thermal recovery. When considering the discussion in section 7.5.3 concerning the work of Davoisne *et al* [11] and the effects of Nd-doping on $CaTiO_3$, it appears this process is not specific to La doping, and in fact may be applicable to various lanthanides and other A-site dopants.

7.5.5 Reduced Resistance to Amorphisation $0.5 \leq x \leq 0.9$

In the $x \geq 0.5$ regime, increasing A-site deficiency leads to a decrease in resistance to amorphisation, and the factors leading to enhanced damage tolerance for $0.2 \leq x \leq 0.4$ are either supressed by or insufficiently prominent to overcome factors that lead to decreased damage tolerance. The first explanation could be a shift in crystal structure from *Pbnm* to *Ibmm* at $x = 0.6$, *I4/mcm* at $x = 0.7$ and *Cmmm* at 0.9. Considering the reduction in damage tolerance first occurs at $x = 0.5$, still with the *Pbnm* structure, this process cannot solely be structure driven, however the effects of crystal structure could impact defect migration. This is raised by Smith *et al* [99] in relation to the $Sr_{1-x}La_{2x/3}TiO_3$ system, however in this instance they suggest migration barriers for the tetragonal and orthorhombic phases, as opposed to the cubic phase for $x \leq 0.3$ in this system, are induced by the distorted octahedra. This is clearly not the case for $Ca_{1-x}La_{2x/3}TiO_3$, in which enhanced damage tolerance is observed within the *Pbnm* phase with the most highly tilted octahedra. Alternatively, in the $Ca_{1-x}La_{2x/3}TiO_3$ system, decreasing octahedral tilt angles for $x \geq 0.5$ leads to a decrease in damage tolerance. A combination of these two data sets would suggest structure does not play a role in the reduced damage tolerance observed, and furthermore is also not a factor in the enhanced damage tolerance regime $0.2 \leq x \leq 0.4$. For the $x \geq 0.7$ regime, ordering of vacancies further increases the ordered nature of these samples and, as with the $Sr_{1-x}La_{2x/3}TiO_3$ system, samples exhibiting A-site vacancy ordering show reduced radiation damage tolerance when compared with $CaTiO_3$. It could be argued that the ordered nature of these vacancy sites in fact promotes amorphisation, as the structure is unable to accommodate randomly induced vacancies through ion implantation. Conducted such studies on similarly ordered systems could add weight to this argument, or through a detailed high-resolution TEM study of such samples irradiated to varying fluences. This may explain the marked decrease in damage tolerance in the $x = 0.7$ and 0.9 samples, but for $x \geq 0.5$ it is likely the decrease in damage tolerance is directly related to A-site vacancy content, and an underlying mechanism promoting amorphisation.

7.6 Conclusions

The $Ca_{1-x}La_{2x/3}TiO_3$ has been bulk ion implanted with 1 MeV Kr^+ and 5 MeV Au^+, to fluences of 1×10^{15} ions cm^{-2} and 5×10^{14} ions cm^{-2}, respectively. Characterisation with XTEM has shown that ion implantation leads to the formation of crystallites within the $x = 0$ sample, with a decrease in crystallite density with increasing fluence prior to amorphisation. These results agree with those reported by Meldrum *et al* [8], but conflict is found with Davoisne *et al* [11], and the possible effects of A-site deficiency have been discussed in this regard. Volume expansion is observed for $x \leq 0.5$, with a decreasing tolerance for lattice expansion observed with increasing A-site doping. Furthermore, the expansion is found to be anisotropic, with the *b* parameter found to be less accommodating to lattice expansion than the *a* and *c* parameters. Within the system as a whole, several conclusions have been reached.

a) Samples in the $0.2 \leq x \leq 0.4$ regime exhibit enhanced damage tolerance when compared with $x = 0$.
b) For $x \geq 0.5$, A-site deficiency inhibits damage tolerance.
c) Both mechanisms are not related to structure.
d) Both mechanisms are observed in bulk ceramics for the first time, using *ex-situ* methods, and are present at constant room temperature.
e) Enhanced damage tolerance has been observed within a second perovskite system, the first being observed by Smith *et al* [99] in the $Sr_{1-x}La_{2x/3}TiO_3$.
f) Amorphous fractions, when compared with the reported amorphisation dosages for Nd-doped $CaTiO_3$, suggest the study by Davoisne *et al* [11] inadvertently induced A-site deficiency enhanced radiation damage tolerance.

8. Helium Bubble Formation in the $Ca_{1-x}La_{2x/3}TiO_3$ System

8.1 Introduction

In chapter 7, the effects of A-site deficiency upon the radiation damage tolerance of the $Ca_{1-x}La_{2x/3}TiO_3$ system were investigated using bulk ion implantation. These effects were discussed in detail, with a regime of enhanced damage tolerance confirmed for $0.2 \leq x \leq 0.4$ with respect to $CaTiO_3$, and decreased damage tolerance for $x \geq 0.5$.

While the effects of bulk ion implantation have received limited interest within the literature, the effects of A-site deficiency upon helium bubble formation are currently unknown. Furthermore, while studies have been reported investigating helium bubble formation within various metals, metal oxides and complex ceramics, few studies have specifically investigated perovskite structured compounds. However, considering the proficiency for He bubbles to nucleate on existing or induced defect sites, the effects of inherent A-site deficiency upon He bubble formation are of key interest. This is compounded by the phenomena observed within chapter 7 and the effect of enhanced damage tolerance upon the formation of helium bubbles.

This chapter outlines *in-situ* ion implantation experiments conducted in a TEM using 6 keV He^+ ions. Initial investigations were conducted using crushed grain TEM samples, allowing for quantification of the fluence required for observable bubble formation. An elevated temperature experiment was further conducted on the $x = 0.2$ sample, allowing for investigation of thermally driven effects related to helium bubble formation. Secondly, plan-view TEM (PVTEM), or ion milled, samples were ion implanted using the same conditions to allow for the investigation of helium bubble formation within grain boundaries and the surrounding grains, in particular the effect upon the fluences required for observable bubble formation and bubble migration to grain boundaries.

8.2 Results

8.2.1 SRIM Calculations

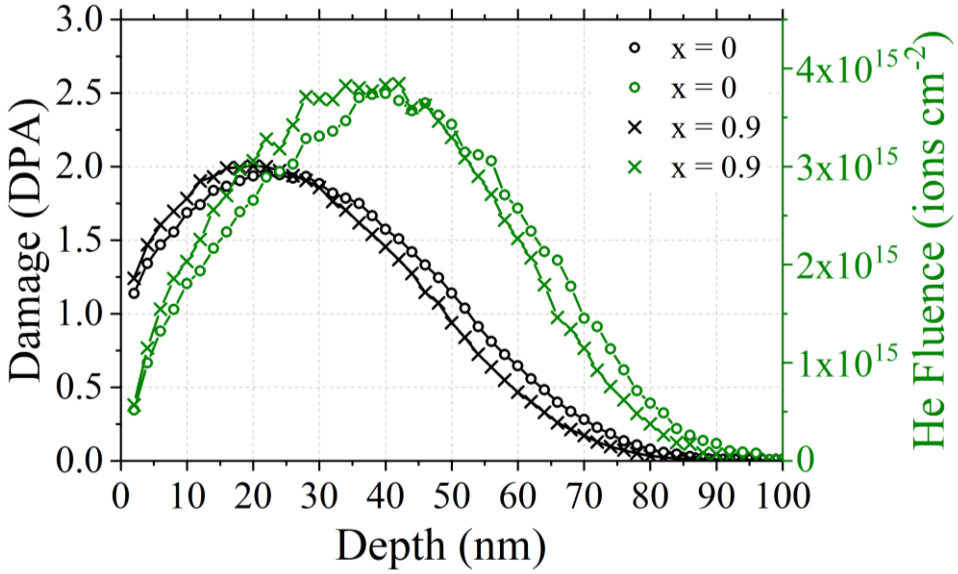

Figure 8.1 SRIM calculations of the 6 keV He$^+$ ion implantation-depth profiles for the x = 0 and x = 0.9 samples at 30° from the sample surface, representing the implantation angle for MIAMI I. In both instances, the maximum implantation depth is ~40 nm, and all He is retained up to a depth of ~100 nm.

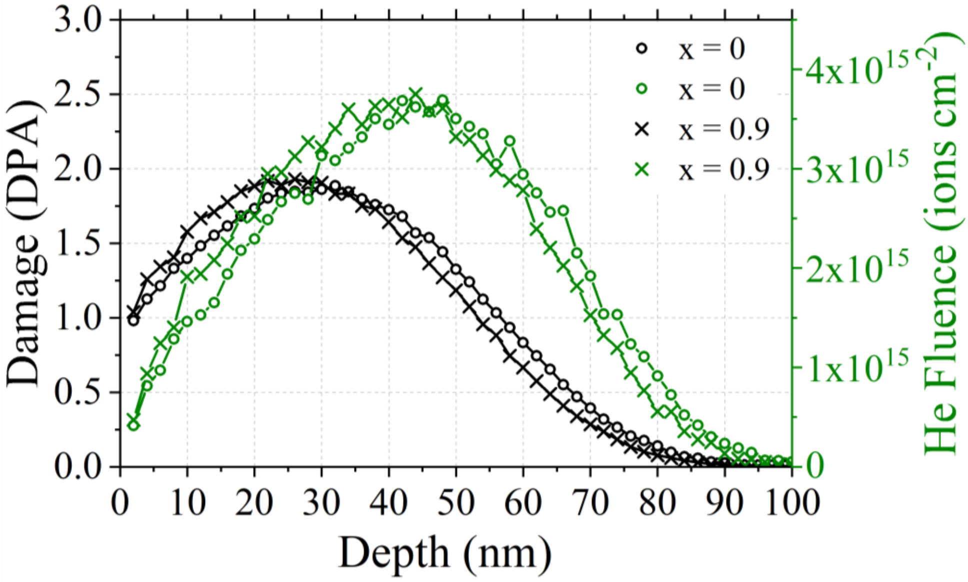

Figure 8.2 SRIM calculations of the 6 keV He$^+$ ion implantation-depth profiles for the x = 0 and x = 0.9 samples at 18.6° from the sample surface, representing the implantation angle for MIAMI II. In both instances, the maximum implantation depth is ~45 nm, and all He is retained up to a depth of ~100 nm.

Two *in-situ* ion implanters were used to investigate helium bubble formation in the $Ca_{1-x}La_{2x/3}TiO_3$ system in this research. The same 6 keV He^+ ion implantation condition was used over both experimental setups, with flux remaining constant at 4.2 x 10^{13} ions cm^{-2} s^{-1} and the maximum implantation fluence at 1 x 10^{17} ions cm^{-2}. However, the MIAMI I implanter uses an implantation angle of 30° from the sample normal, while MIAMI II employs an 18.6° implantation angle from the sample normal. SRIM estimated damage-depth profiles are presented for the $x = 0$ and $x = 0.9$ end members implanted with 6 keV He^+ to a fluence 1 x 10^{17} ions cm^2 with an implantation angle of 30° in figure 8.1, and with an implantation angle of 18.6° in figure 8.2. For both samples, the maximum induced damage was ≈ 2 dpa under at both angles, with the maximum damage depth increasing from 20 nm at 30° to 30 nm at 18.6°. The peak implantation depth increased for both samples from 40 nm at 30° to 45 nm at 18.6°, while all helium ions are retained within a 100 nm implantation depth for both samples at both angles. Considering the < 100 nm thickness of a TEM sample, this confirmed the change in implantation angle should have had minimal effect on the observation of helium bubbles and the imparted damage across the system. Furthermore, the use of 6 keV He^+ was justified across both *in-situ* setups. Converting from fluence to at.% using SRIM gives an 18 at.% He content at maximum implantation for $CaTiO_3$ and 19 at.% for the $x = 0.9$ end member.

8.2.2 Crushed Grain Prepared Samples

Bright field TEM micrographs of the crushed grain sample of the $x = 0$ sample are shown in figure 783. As was described in chapter 4, samples were irradiated with a constant flux, with imaging undertaken at regular 2-minute intervals. Both under-focus and over-focus (both by ≈ 500 nm) images are presented in figure 8.3 as designated. In the under-focus images, bubbles appear as light regions with a dark fringe, and the in the over-focus images, bubbles appear as dark regions with a light fringe. Bright field TEM micrographs of the sample irradiated are presented from the region indicated in red on the pristine sample micrographs to allow for identification of helium bubble formation. This style of presentation is consistent throughout all the bubble formation figures presented within this chapter. Helium bubble formation was first observed at a fluence, F_B, of 4.8 ± 0.3 x 10^{16} ions cm^{-2}, as indicated by the light regions observed and indicated with red arrows within figure 8.3. Large regions of dark contrast are also observable in both under- and over-focused images at all

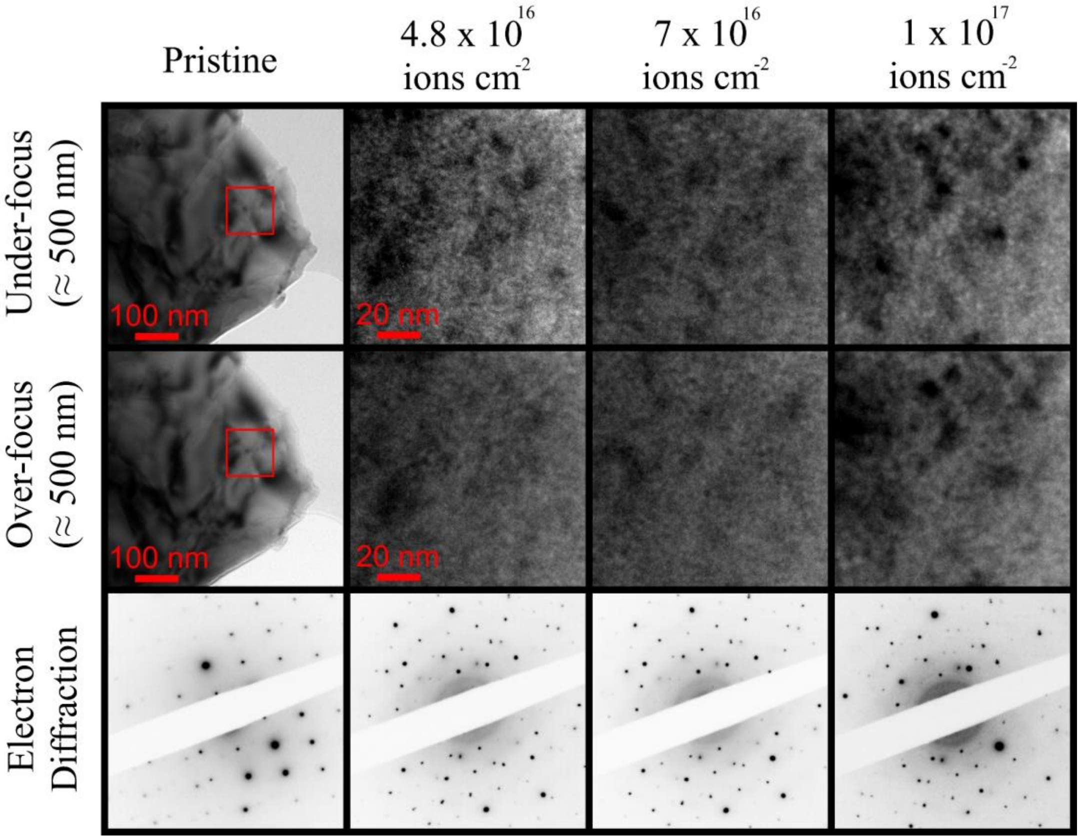

Figure 8.3 Bright field TEM micrographs and SAEDPs of the crushed grain x = 0 sample in the pristine and ion implanted at room temperature with 6 keV He^+ to fluences of 4.8 x 10^{16}, 7 x 10^{16} and 1 x 10^{17} ions cm^{-2}. Under- and over-focus images are defocused by ≈ 500 nm, respectively. Ion implanted micrographs are presented as magnifications of the region identified by the red box in the pristine micrographs to ease identification of bubble formation.

fluences that are not related to helium bubble formation. These regions were likely related to dislocation loop and interstitial-type defects. The resolution of the images was insufficient to allow for bubble-size analysis to be undertaken, however in all cases the bubble sizes remained < 2 nm in diameter. SAEDPs are presented within figure 8.3 taken at each of the indicated fluences. No diffuse scattering was observed in the pristine state, confirming the crystallinity of the material prior to implantation. While crystalline diffraction reflections were observed at all fluences, diffuse scattering was observed to increase with fluence.

Bright field TEM micrographs of the x = 0, 0.2, 0.4, 0.6, 0.7 and 0.9 samples are presented in figure 8.4. Within this figure, under-focus micrographs are presented in the pristine, at the F_B fluence, and at the maximum implantation fluence of

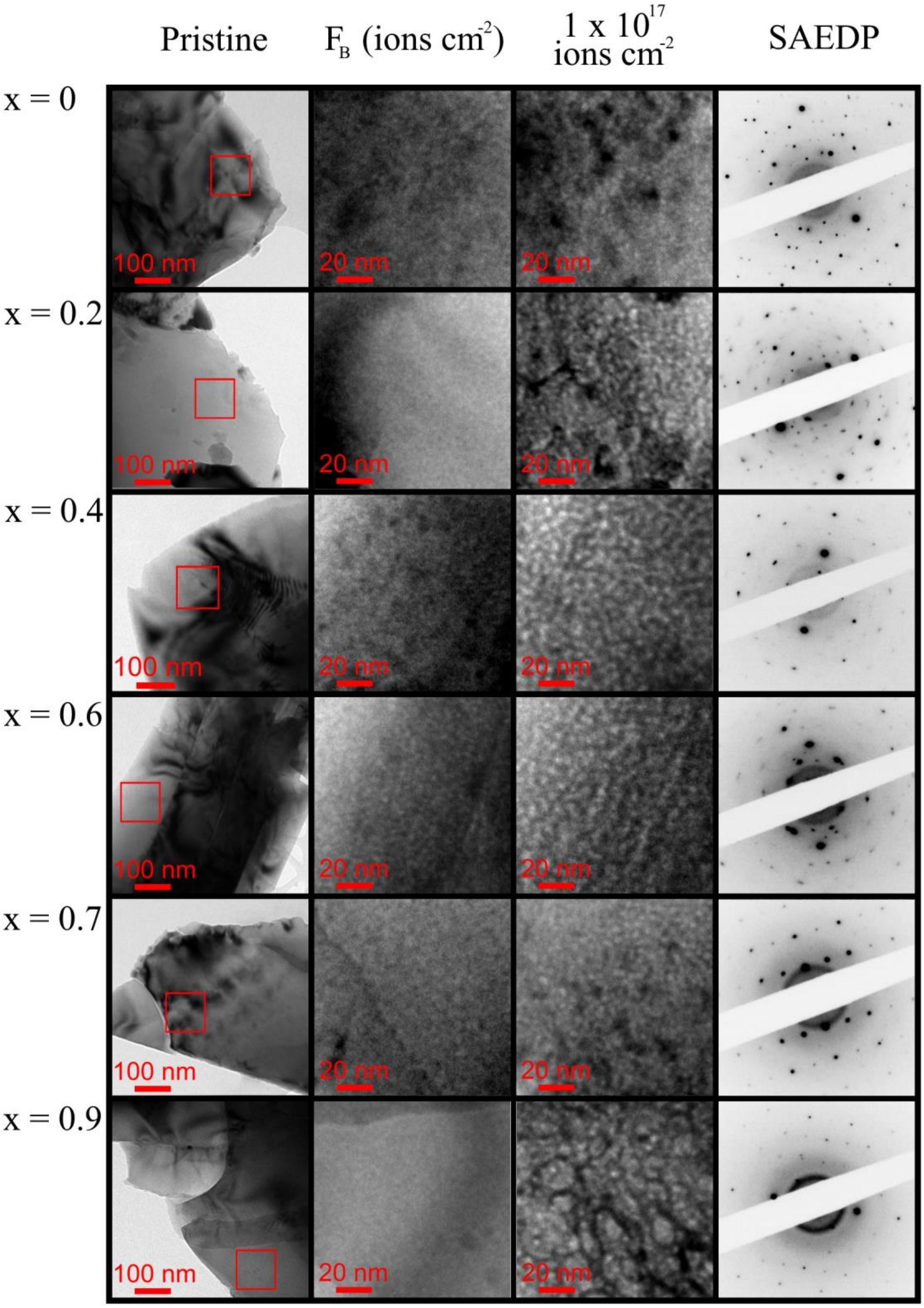

Figure 8.4 Bright field TEM micrographs and SAEDPs of the x = 0, 0.2, 0.4, 0.6, 0.7 and 0.9 samples in the pristine and ion implanted at room temperature to the F_B fluence and 1 x 10^{17} ions cm^{-2} with 6 keV He$^+$. All micrographs are under-focus by ≈ 500 nm. Ion implanted micrographs are presented as magnifications of the region identified by the red box in the pristine micrographs to ease identification of bubble formation.

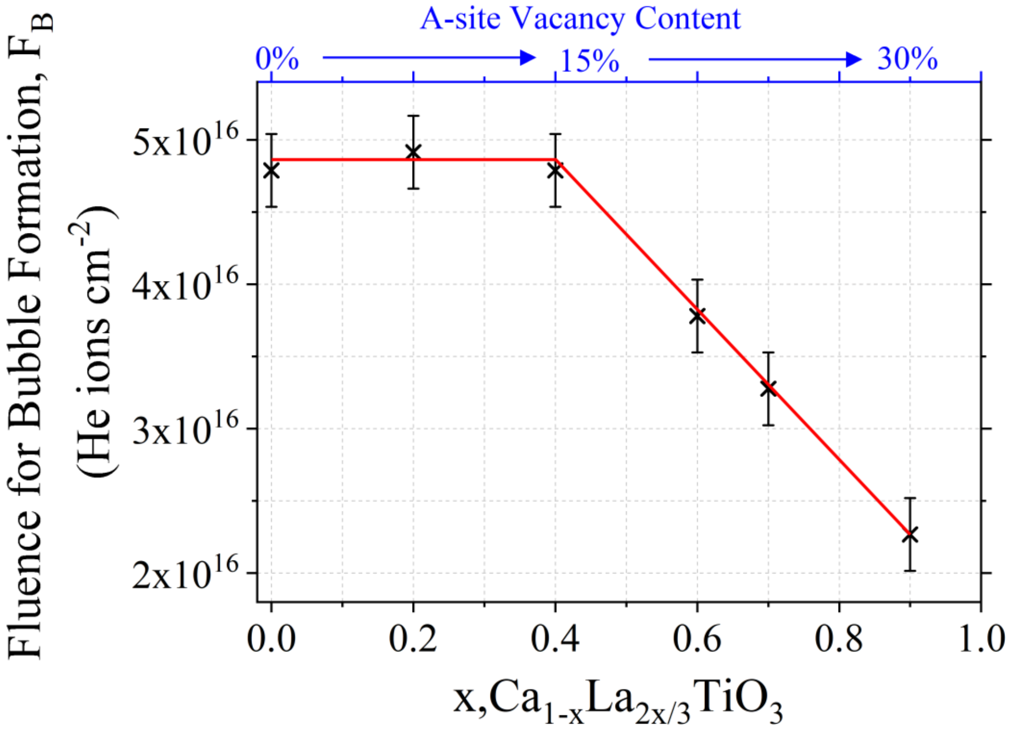

Figure 8.5 Crushed grain fluences for bubble formation, F_B, plotted against formula unit values, x, for the $Ca_{1-x}La_{2x/3}TiO_3$ system. The red curve is presented as an aide for the reader. A-site vacancy content (mol.%) is shown in blue.

1 x 10^{17} ions cm^{-2}. Micrographs of the implanted specimens are presented as magnified regions indicated by the red boxes superimposed on the pristine sample micrographs. The SAEDPs presented were taken from the magnified regions at fluences of 1 x 10^{17} ions cm^{-2}. In each instance, helium bubble formation was observed as exemplified in figure 8.4. For reference, under- and over-focus micrographs and SAEDPs of the x = 0.2, 0.4, 0.6, 0.7 and 0.9 samples in the pristine, at the F_B fluence and at fluences of 7 x 10^{16} ions cm^{-2} and 1 x 10^{17} ions cm^{-2} are presented in appendix 3 figures A3.1, A3.2, A3.3, A3.4 and A3.5, respectively. Values of F_B are tabled in section 8.2.3, with the crushed grain F_B values presented graphically in figure 8.5. The values of F_B for the x = 0, 0.2 and 0.4 samples remain within error with $F_B = 4.8 \pm 0.4$ ions cm^{-2}. A linear decrease with increasing x was observed for $x \geq 0.4$ with a minimum F_B value observed for the x = 0.9 sample of 2.3 ± 0.3 ions cm^{-2}. At the maximum fluence of 1 x 10^{17} ions cm^{-2}, the light contrast indicative of bubble formation increased in intensity and size. This was indicative of helium bubble growth and agglomeration with increasing helium fluence. It was not possible to accurately determine the size of the formed bubbles within these images due to the resolution of

samples prepared via the crushed grain route. This sample preparation route commonly produced lower resolution images due to the non-uniform thickness of the grains observed. However, bubbles were observed of ≈ 2 nm diameter for all samples at 1 x 10^{17} ions cm^{-2} and not exceeding 3 nm. SAEDPs taken at 1 x 10^{17} ions cm^{-2} all show the presence of both crystalline reflections and diffuse scattering. The diffuse scattering intensity was most prominent in the x = 0.6, 0.7 and 0.9 samples, with the x = 0.9 sample exhibiting the least intense crystalline reflections. Furthermore, the x = 0 sample exhibited reduced diffuse scattering intensity compared with the x ≥ 0.6 samples, with the x = 0.2 and 0.4 samples exhibiting the least intense diffuse rings.

8.2.3 6 keV He^+ implantation of $Ca_{0.8}La_{0.13}TiO_3$ (x = 0.2) at 823 K

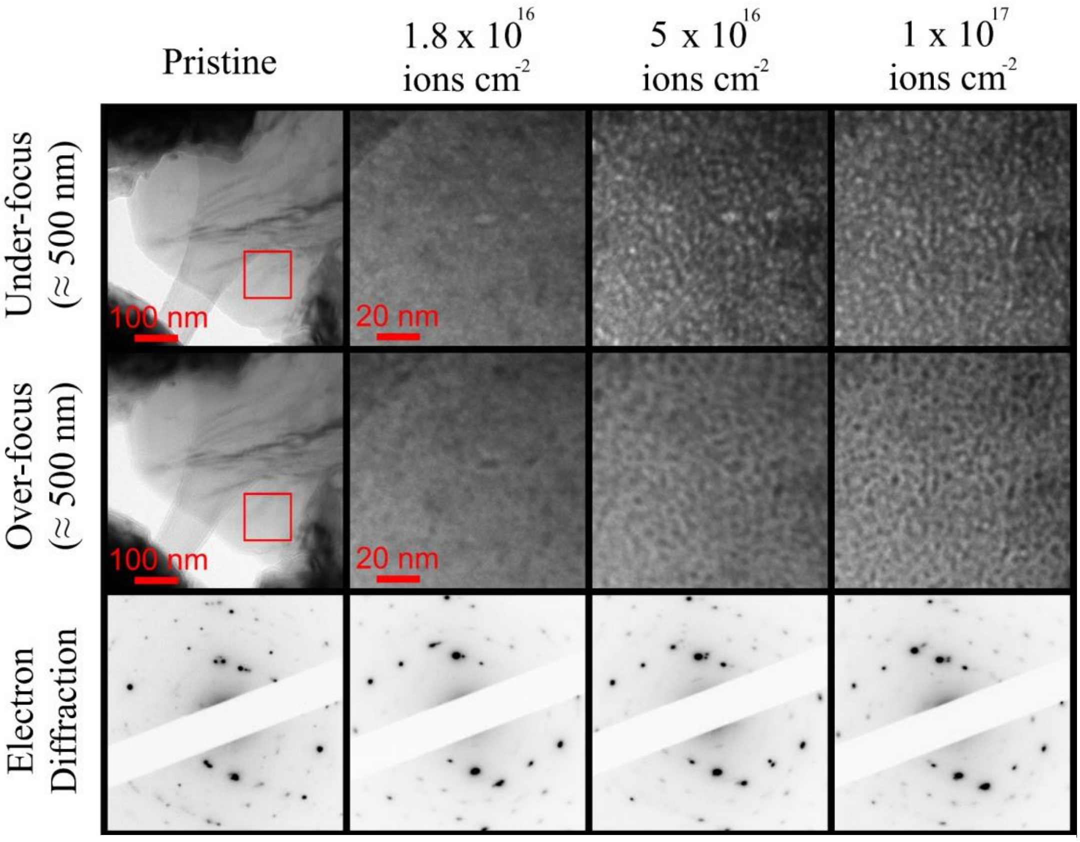

Figure 8.6 Bright field TEM micrographs and SAEDPs of the crushed grain x = 0.2 sample in the pristine and ion implanted with 6 keV He^+ to fluences of 1.8 x 10^{16}, 5 x 10^{16} and 1 x 10^{17} ions cm^{-2} at 823 K. Under- and over-focus images are defocused by ≈ 500 nm, respectively. Ion implanted micrographs are presented as magnifications of the region identified by the red box in the pristine micrographs in order to ease identification of bubble formation. Bubble formation was first observed at 1.8 x 10^{16} ions cm^{-2}.

The x = 0.2 sample was further investigated at an elevated temperature of 823 K. Under- and over-focus bright field TEM micrographs of this sample in the pristine and implanted at the F_B fluence of 1.8 x 10^{16} ions cm^{-2} and fluences of 5 x 10^{16} and 1 x 10^{17} ions cm^{-2} are presented in figure 8.6. The value of F_B in this instance was determined as F_B = 1.8 ± 0.3 x 10^{16} ions cm^{-2}, representing a 2.7 factor decrease from the same sample implanted at room temperature. With increasing fluence the light contrast in under-focus images and dark contrast in over-focus images grew in intensity, as with the samples implanted at room temperature. However, bubbles sizes did not exceed 2 nm in diameter and no bubble growth was distinguished for fluences > 5 x 10^{16} ions cm^{-2}. SAEDPs taken at each implantation fluence showed no evidence of diffuse scattering, suggesting the sample remained crystalline at all fluences when implanted at 823 K.

8.2.4 Ion Milled Samples

8.2.4.1 Fluence for Bubble Formation, F_B

Further investigations were undertaken on ion milled PVTEM samples to investigate the effect of grain boundaries on helium bubble formation mechanisms. Under- and over-focus bright field TEM micrographs of an ion milled x = 0 sample ion implanted with 6 keV He^+ ions are presented in figure 8.7, with associated SAEDPs. The pristine micrographs show the enlarged area identified by a red box was centred on a grain boundary, which can be identified through the two neighbouring regions of differing contrast. In this instance, helium bubble formation is observed in both the bulk and the grain boundary of the sample at 4.8 ± 0.3 x 10^{16} ions cm^{-2} using the through-focal-series method. Observation of the over-focus image at 4.8 x 10^{16} ions cm^{-2} showed darker regions of contrast within the grain boundary than the neighbouring bulk. Furthermore, these regions had a greater qualitative areal density (2D density) than the bulk and at the maximum implantation fluence of 1 x 10^{17} ions cm^{-2} the grain boundary becomes hard to distinguish as the bubble contrast became too intense. Analysis of the SAEDPs present in figure 8.8 for the x = 0 sample showed a combination of diffuse scattering and crystalline reflections after ion implantation in a similar nature to the crushed grain sample presented in figure 8.3. Diffuse scattering was first observed at the F_B fluence but the intensity of the diffuse rings did not increase with fluence to 1 x 10^{17} ions cm^{-2}.

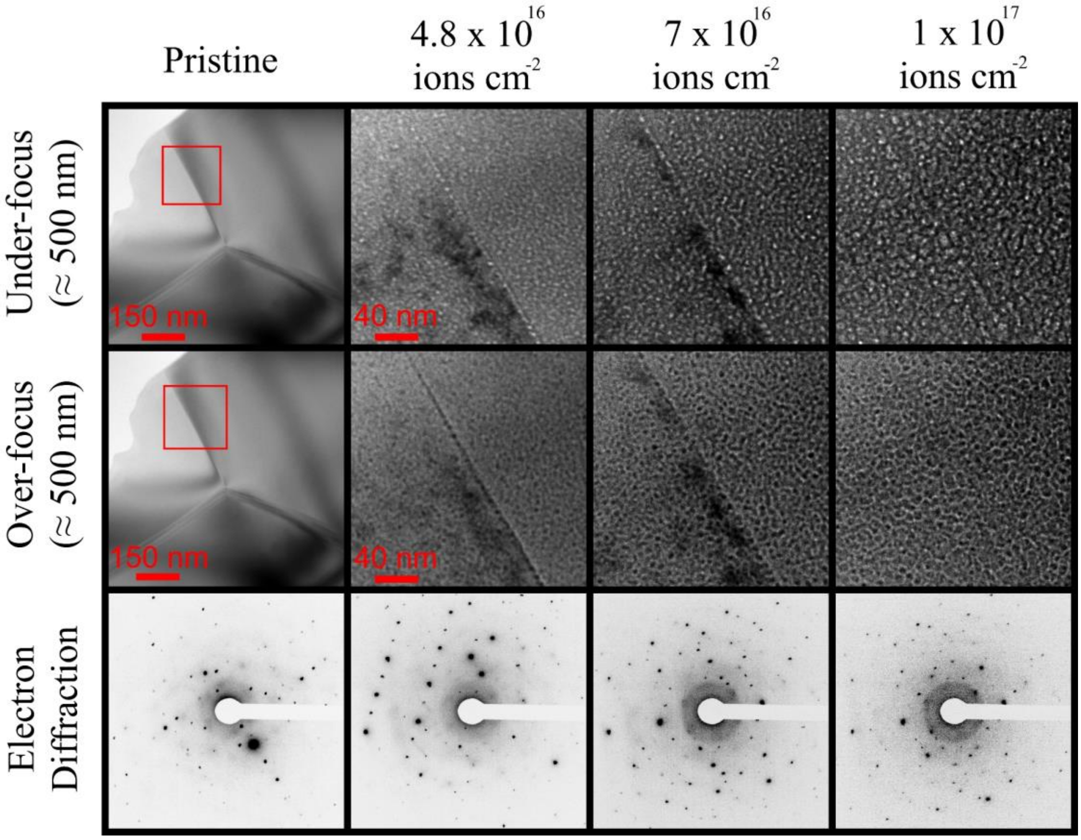

Figure 8.7 Bright field TEM micrographs and SAEDPs of the ion milled x = 0 sample in the pristine and ion implanted with 6 keV He^+ to fluences of 4.8 x 10^{16}, 7 x 10^{16} and 1 x 10^{17} ions cm^{-2}. Under- and over-focus images are defocused by ≈ 500 nm, respectively. Ion implanted micrographs are presented as magnifications of the region identified by the red box in the pristine micrographs to ease identification of bubble formation.

Under-focus bright field TEM micrographs and SAEDPs of the 6 keV He^+ ion implanted x = 0, 0.2, 0.4, 0.6, 0.7 and 0.9 samples are presented in figure 8.8. In these figures, micrographs are presented at F_B values at the grain boundary, F_B in the bulk and at the 1 x 10^{17} ions cm^{-2} fluence are presented. SAEDPs at the maximum 1 x 10^{17} ions cm^{-2} fluence are also presented. For reference, under- and over-focus micrographs and SAEDPs of the x = 0.2, 0.4, 0.6, 0.7 and 0.9 samples in the pristine, at F_B fluences in the bulk and grain boundary and at 1 x 10^{17} ions cm^{-2} are presented in appendix 3 figures A3.6, A3.7, A3.8, A3.9 and A3.10, respectively. In all samples, helium bubble formation was observed as regions of light contrast, with dark regions present through the advent of dislocation loop and interstitial-type defects. For the x = 0.2 sample, the F_B value remained within error in the bulk and grain boundary, as was observed for the x = 0 sample. For samples in the x ≥ 0.4 regime, bubble formation

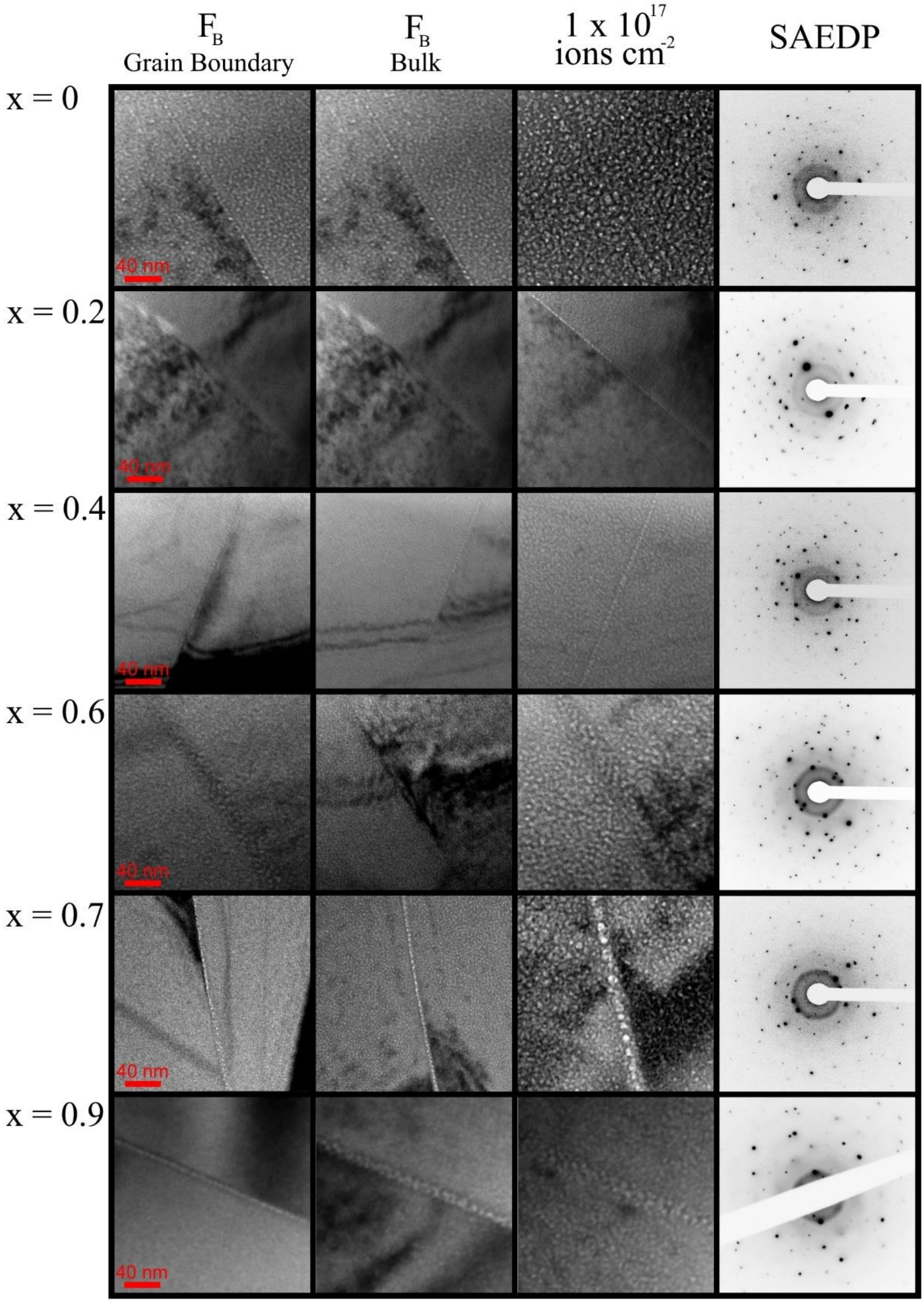

Figure 8.8 Bright field TEM micrographs and SAEDPs of the ion milled x = 0, 0.2, 0.4, 0.6, 0.7 and 0.9 samples ion implanted with 6 keV He^+ at room temperature to the F_B fluences in the grain boundary, bulk and at 1×10^{17} ions cm^{-2}. All micrographs are under-focus by ≈ 500 nm. Ion implanted micrographs are presented as magnifications of the region identified by the red box in the pristine micrographs to ease identification of bubble formation.

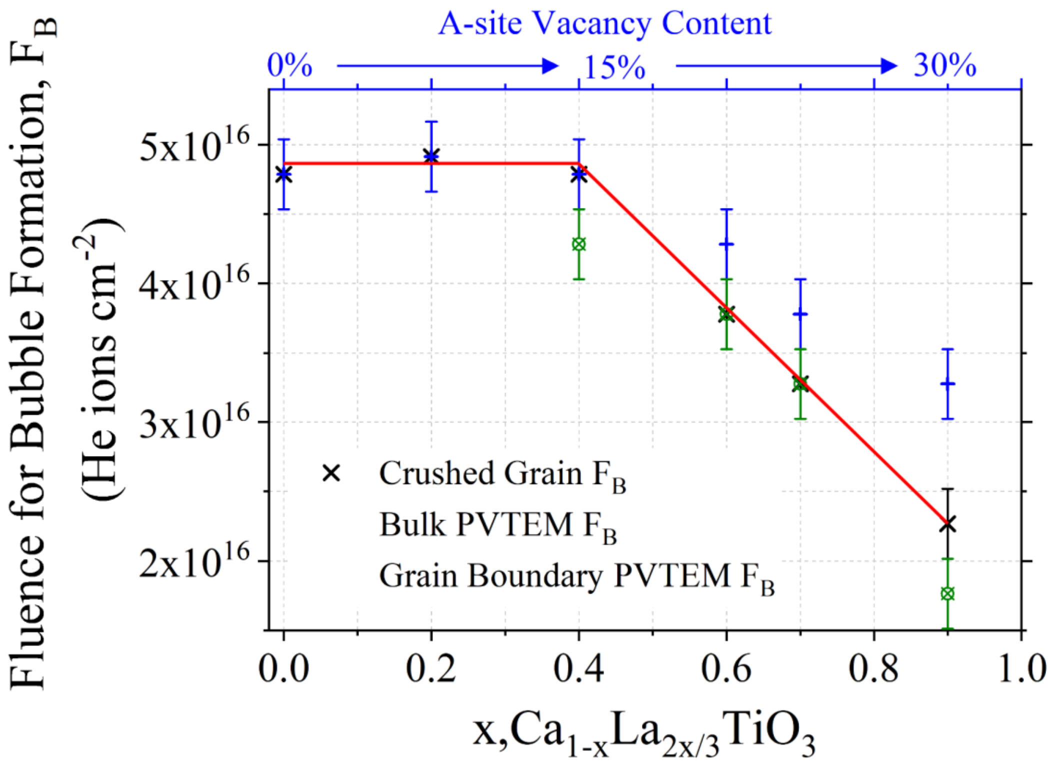

Figure 8.9 Crushed grain and ion milled fluences for bubble formation, F_B, plotted against formula unit values, x, for the $Ca_{1-x}La_{2x/3}TiO_3$ system. F_B values are presented for both the grain boundary and bulk for ion milled specimens. The red curve is a cubic fit of the crushed grain F_B values, presented as an aide for the reader. A-site vacancy content (mol.%) is shown in blue.

was observed in the grain boundary prior to formation in the bulk. This was identified using the through-focal-series method as can be observed in the full-series appendix figures presented. Values for F_B determined using ion milled samples in both the bulk and grain boundary are reported in table 8.1 with crushed grain F_B values. These values are presented graphically in figure 8.9. The bulk F_B value for the x = 0.4 sample remained constant across the crushed grain and ion milled preparation techniques at $4.8 \pm 0.3 \times 10^{16}$ ions cm^{-2}, while grain boundary bubble formation occured at $4.3 \pm 0.3 \times 10^{16}$ ions cm^{-2}. Increasing the La content, and by association the A-site vacancy content, led to differing behaviour. In the x = 0.6 and 0.7 samples, the grain boundary F_B values were consistent with bulk crushed grain F_B values of $3.8 \pm 0.3 \times 10^{16}$ ions cm^{-2} and $3.3 \pm 0.3 \times 10^{16}$ ions cm^{-2}, respectively. Bulk F_B values for the x = 0.6 and 0.7 samples were observed of $4.3 \pm 0.3 \times 10^{16}$ ions cm^{-2} and $3.8 \pm 0.3 \times 10^{16}$ ions cm^{-2}, respectively. Lastly, the x = 0.9 sample showed grain boundary bubble formation at an F_B value of $1.8 \pm 0.3 \times 10^{16}$ ions cm^{-2} and a bulk

F_B value of 3.3 ± 0.3 x 10^{16} ions cm^{-2}. These values are discussed in detail within the discussion section of this chapter.

Table 8.1 F_B values for the x = 0, 0.2, 0.4, 0.6, 0.7 and 0.9 samples of the $Ca_{1-x}La_{2x/3}TiO_3$ system. Values presented are for observed bubble formation in samples prepared via crushed grain, and in the bulk and grain boundary of ion milled TEM samples.

x, $Ca_{1-x}La_{2x/3}TiO_3$	**F_B, Crushed Grain Bulk (± 0.3 x 10^{16} ions cm^{-2}) [at.%]**	**F_B, Ion Milled Bulk (± 0.3 x 10^{16} ions cm^{-2}) [at.%]**	**F_B, Ion Milled Grain Boundary (± 0.3 ions x 10^{16} cm^{-2}) [at.%]**
0	4.8 [9.0]	4.8 [9]	4.8 [9]
0.2	4.9 [9.3]	4.9 [9.3]	4.9 [9.3]
0.4	4.8 [9.1]	4.8 [9.1]	4.3 [8]
0.6	3.8 [7]	4.3 [8]	3.8 [7]
0.7	3.3 [6.2]	3.8 [7.2]	3.3 [6.2]
0.9	2.3 [4]	3.3 [6]	1.8 [3.3]

8.2.4.2 Bubble Size Analysis

The experimental procedure for determining average bubble diameters was provided in chapter 4. Bubbles formed were close to circular in nature. Calculated average bubble diameters in both the bulk and grain boundary at 1 x 10^{17} ions cm^{-2} are presented in figure 8.10. This fluence was chosen to provide a constant fluence for comparison, with bubbles at maximum contrast at this fluence. For the x = 0 sample, the grain boundary and bulk bubble diameter remains within error at 1.7 ± 0.2 nm. For the rest of the $Ca_{1-x}La_{2x/3}TiO_3$ system, grain boundary bubble diameters were greater than in bulk, although values for grain boundary and bulk diameters are within error for the x = 0.2 and 0.4 samples. A reduction bubble diameter was observed from x = 0 to x = 0.2, with diameters calculated as 1.1 ± 0.2 nm in the bulk and 1.2 ± 0.2 nm in the grain boundary. For $x \geq 0.2$, bubble diameter increased with La content in both the bulk and grain boundary, with maximum diameters for the x = 0.9 sample calculated as 2.6 ± 0.2 nm and 3.0 ± 0.2 nm in bulk and grain boundary, respectively.

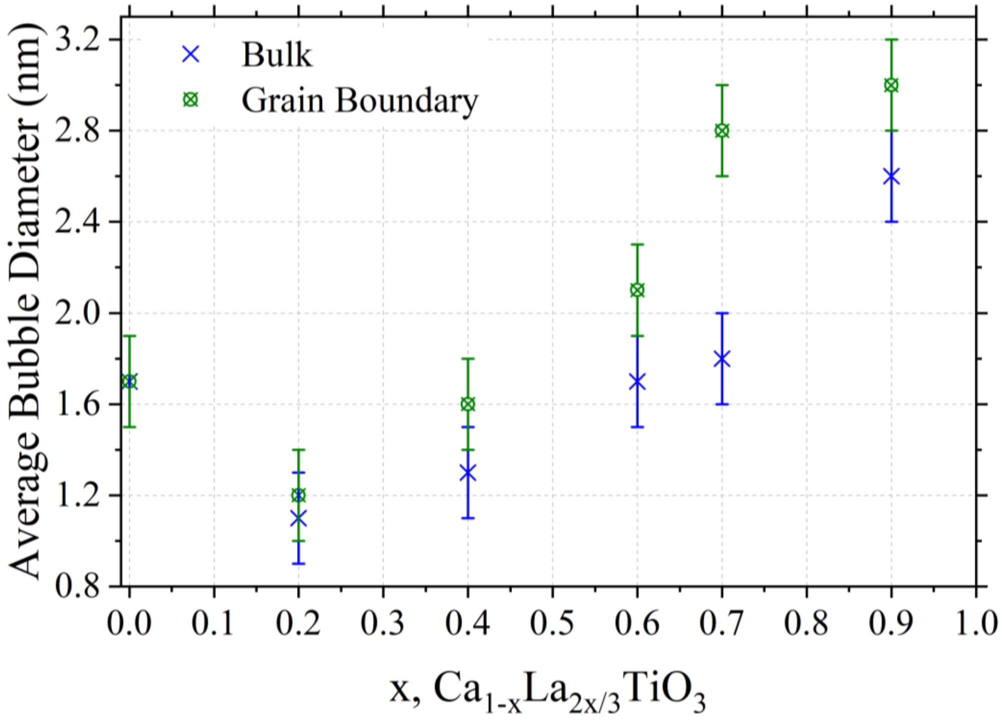

Figure 8.10 Average bubble diameters for the ion milled samples in the $Ca_{1-x}La_{2x/3}TiO_3$ system at 1 x 10^{17} ions cm^{-2}. Values are presented for both the grain boundary and bulk.

8.3 Discussion

8.3.1 Defect Migration and A-site Vacancies

The relationships observed for the $Ca_{1-x}La_{2x/3}TiO_3$ system with regard to F_B suggested a mechanism exists that inhibits bubble formation in the x = 0.2 and 0.4 samples. Vacancy defects have been shown to act as nucleation sites for helium bubble formation in various systems, in which helium is trapped at room temperature [121,125,126,130]. Matsunaga *et al* [130] conducted infusion helium studies in ZrO_2 doped with Fe^{3+} to promote the induction of oxygen vacancies and report increased density of formed helium bubbles with increasing oxygen vacancy content. Furthermore, long-range defect migration is unlikely at room temperature in insulating ceramics such as $CaTiO_3$, and short-range migration and localised strain effects are reported mechanisms leading to room temperature bubble formation [137]. Within the

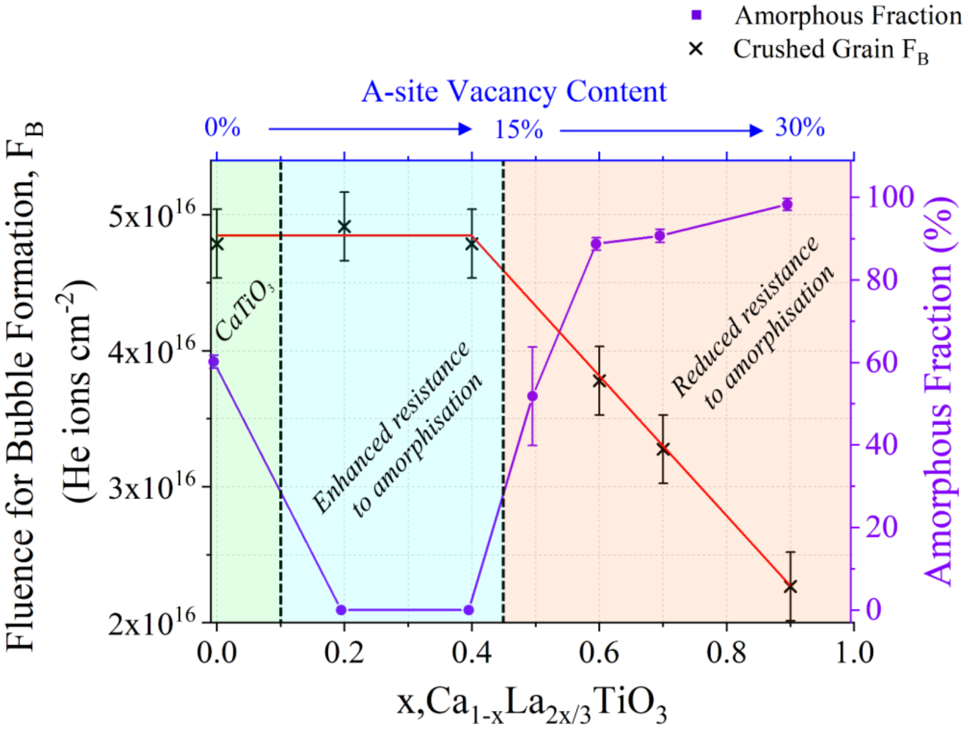

Figure 8.11 Crushed grain fluences for bubble formation, F_B, and amorphous fractions calculated from GAXRD patterns for 1 MeV Kr^+ ion implanted samples with formula unit value, x, for the $Ca_{1-x}La_{2x/3}TiO_3$ system. The three damage regions are identified with $CaTiO_3$ in light green and the regions of enhanced/reduced resistance to amorphisation in blue and orange, respectively, to aid comparison.

$Ca_{1-x}La_{2x/3}TiO_3$, the addition of La on the A-site of the structure inevitably led to A-site vacancy induction. Considering the intrinsic local sites this offers for bubble nucleation, in particular considering the lack of long-range defect migration at room temperature, it was expected that the fluence required for observable bubble formation would decrease with A-site vacancy content. However, values of F_B observed for crushed grain $x = 0.2$ and 0.4 samples were within error of the $x = 0$ counterpart. Enhanced resistance to amorphisation was reported in chapter 7 of this study for the $x = 0.2$ and 0.4 samples ion implanted with 1 MeV Kr^+ when compared with the $x = 0$ sample. It is proposed that the damage tolerance of these samples led to the fluence required for observable bubble formation remaining within error for the $x = 0$, 0.2 and 0.4 samples. Reduced proficiency for defect formation, induced by the implanted ion, likely led to a reduction in the number of produced sites available for helium bubble nucleation. This process, in combination with the intrinsically available A-site vacancies leads to F_B values in error of the $x = 0$ sample, which while less damage tolerant has less initial sites for helium bubble formation. Considering samples in regime $x \geq 0.6$, a combination of decreased damage tolerance and the greatly increased number of A-site vacancies available intrinsically for bubble formation leads to a progressive drop in value required for F_B. F_B values for the crushed grain samples of the $Ca_{1-x}La_{2x/3}TiO_3$ system are presented in figure 8.11 with the amorphous fractions calculated for the $Ca_{1-x}La_{2x/.3}TiO_3$ system ion implanted with 1 MeV Kr^+ to a fluence of 1 x 10^{15} ions cm^{-2}. Comparison of the two curves shows the described relationship between F_B and the induced amorphous fractions graphically, with a correlation observed between increased and decreased resistance to amorphisation with increased and decreased F_B, respectively.

A further mechanism related to enhanced damage tolerance may also have led to such a relationship. In all samples, the F_B fluence coincided with the fluence at which partial damage of the structure was observed. This was not the case for the elevated temperature sample, although helium bubble formation in this instance is likely dominated by thermal effects increasing helium migration. The SRIM curves presented in figures 8.1 and 8.2 show the maximum damage region remained between 20 and 30 nm, and it is likely that the majority of the diffuse scattering came from this region, with lesser damaged material also present within the TEM specimen. It was therefore not possible to determine if the sample had been amorphised at specific depths, however it is apparent that a trend was exhibited between the observation of diffuse scattering and values for F_B. Taylor *et al* [89,140] employed bulk 7 MeV He^+ ion implantation on both crystalline and pre-amorphised $Gd_2Ti_2O_7$ and report bubbles forming larger in size and higher in density in the crystalline state. A crystalline to amorphous phase transformation is reported for the crystalline sample, and considering the observations of this study, it may be that the crystalline to amorphous transition is key to the bubble formation mechanism and may promote bubble nucleation and growth. It is possible these observations are coincidental and these findings should not be constituted as hard evidence of a link between the c-a transition and helium bubble formation. One observation that can be made is the increased intensity of the diffuse scattering in SAEDPs taken from the x = 0.6, 0.7 and 0.9 samples at 1 x 10^{17} ions cm^{-2} prepared by both methods when compared with x = 0, 0.2 and 0.4. Furthermore, the x = 0 sample exhibited increased diffuse scattering intensity compared to the x = 0.2 and 0.4 counterparts. This provideed further confirmation of the damage phenomena reported in chapter 7. Reports have suggested that helium bubbles can limit the mobility of defects within ceramic structures, and specifically the mobility vacancy defects [127,197]. Moreover, defect mobility is central to damage tolerance through the promotion of damage recovery processes, and the activation energies for recovery in the $Sr_{1-x}La_{2x/3}TiO_3$ system [5] suggest recovery processes will be central to the phenomena observed in the x = 0.2 and 0.4 samples. This raises the possibility that helium bubble formation can inhibit the processes leading to enhanced damage tolerance and reducing the fluences required to damage the structure. However, in this instance the damage phenomena observed did not appear to be compromised by helium bubble formation.

Comparison can be made with similar structures. The $LiNbO_3$ perovskite structure is reported by Ofan *et al* [132], whom report bubble formation at 5×10^{16} ions cm^{-2} (2 at.%). Considering nuclear waste forms, room temperature bubble formation is reported in pyrochlore $Gd_2Ti_2O_7$ at 6 at.% [140] and $Gd_2Zr_2O_7$ at 4.6 at% [139], bubble formation in nuclear glasses is reported at 3 at.% [124]. Furthermore, bubble formation in Al_2O_3 is reported at 4.5 at.% and $MgAl_2O_4$ at 3.8 at.% [137]. This is compared to the F_B value for $CaTiO_3$ in at.% of 9 at.%, the maximum value in the x = 0.2 sample of 9.3 at.%, and the minimum value of F_B for the x = 0.9 sample of 4 at.%.

8.3.2 Elevated Temperature

Implantation of the x = 0.2 sample prepared via the crushed grain route at 823 K lowered the required F_B from $4.9 \pm 0.3 \times 10^{16}$ ions cm^{-2} to $1.8 \pm 0.3 \times 10^{16}$ ions cm^{-2}, a 2.7 factor decrease. Various examples of this behaviour are found in the literature [118,127,134–137,198,199], and the observed drop in F_B is due to increased migration energies for defects and helium atoms to migrate and agglomerate. No damage to the crystal structure of the x = 0.2 sample was observed when implanted at 823 K to 1×10^{17} ions cm^{-2}. Room temperature experiments on the same sample showed partial damage in both the crushed grain and ion milled TEM samples. Considering the reported T_c value for $Sr_{0.85}La_{0.1}TiO_3$ is reported as 308 K, implantation at 823 K is likely above the T_c value for the x = 0.2 sample, and therefore damage is not observed [99]. However, bubble formation is still prominent and, as discussed, the F_B value decreases.

8.3.3 Grain Boundary Bubble Formation

So far, only the effects within crushed grain samples have been discussed. Considering the enhanced contrast observed at grain boundaries in the ion milled samples, it is likely implanted helium ions migrate to grain boundaries whereby agglomeration and coalescence of bubbles can occur. A consequence of this process is observed in the F_B values for the ion milled samples. For $x \geq 0.4$, helium bubble formation was observed in the grain boundary prior to the bulk. This process was not observed for $x \leq 0.2$, although this cannot be ruled out considering the ± 0.3 x 10^{16} ions cm^{-2} error in the F_B measurements. Figure 8.9 shows two linear fits for the crushed grain F_B values. Grain boundary F_B values for the $x \leq 0.4$ samples remained below or equal to the second linear fit, while bulk values remain above this value. While in both the crushed grain and ion milled prepared samples this trend is followed, the presence of grain boundaries pushes the required F_B value to higher fluences. Helium bubble migration to grain boundaries was expected and has been reported in the literature [120,129]. It is therefore postulated that by the grain boundary acting as a helium sink in which helium is trapped, a reduced percentage of implanted helium was available for bubble formation within the bulk. Therefore, higher fluences were required for bulk helium bubble formation when grain boundaries were present, compared to the grain boundary free crushed grain samples. The only anomaly to this rule was the $x = 0.4$ sample, in which bulk F_B values were consistent across TEM specimens, although the ± 0.3 x 10^{16} ions cm^{-2} makes it likely this process fell within the two-minute implantation interval. This may also be the case for the $x = 0$ and 0.2 samples. However, this also raises the possibility that increasing A-site vacancy content reduced the barriers to migration for implanted helium atoms, which found easier migration routes to the grain boundary for higher La content.

The resolution of the ion milled samples allowed for accurate quantification of the average bubble diameters within the bulk and grain boundaries of samples. Within crushed grain samples, the resolution required for such measurements is not tenable. However, bubbles were not observed of diameters exceeding 3 nm, which agreed with ion milled measurements. Within the ion milled samples, measurements were taken from the 1 x 10^{17} ions cm^{-2} at maximum fluence and are presented graphically in figure 8.10. These values followed a roughly inverse trend to the obtained F_B values. This is due to the constant flux employed. If helium bubble formation occured at a lower F_B value, a constant flux will lead to a constant growth rate if the mechanisms governing bubble formation do not prevent further bubble growth. In this manner, the inverse relationship with F_B is observed. These bubble sizes are comparable with other ceramic systems [137–140].

8.4 Conclusions

Helium bubble formation within the $Ca_{1-x}La_{2x/3}TiO_3$ perovskite system was observed using 6 keV He^+ ion implantation *in-situ* in a TEM. Ion implantation on samples prepared via both the crushed grain and ion milling routes was undertaken. The fluence at which helium bubble formation was first observed, F_B, was observed to remain within error in the $0 \leq x \leq 0.4$ regime for samples prepared via the crushed grain route, before decreasing for $x \geq 0.4$. These findings have been discussed in relation to the enhanced damage tolerance phenomena observed in chapter 7, with enhanced damage tolerance postulated to supress the fluence at which He bubbles are observed to form. Bubble diameters remained < 3 nm for all samples prepared via the crushed grain route. For PVTEM samples, bubble formation was observed at lower fluences within grain boundaries for $x \geq 0.4$ than in neighbouring bulk grains, likely due to the migration of bubbles and defects to grain boundaries acting as sinks. This further decreased the available helium for bubble formation in the bulk, increasing the bulk F_B value in the presence of grain boundaries when compared with a crushed grain sample. Bubble diameters were found to be greater in the grain boundary than the neighbouring bulk. Electron diffraction analysis of samples implanted using both preparation routes in the $0 \leq x \leq 0.4$ regime showed a greater tolerance for radiation damage when compared with $x \geq 0.4$, in agreement with the findings of chapter 7. Ion implantation of the $x = 0.2$ prepared using the crushed grain method at 823 K led to a decrease in F_B, as has been previously observed in the literature. Furthermore, no diffuse scattering was observed in this sample, and comparison with similar compositions would suggest this temperature was above the critical temperature of amorphisation, T_c, for this composition. This also provided evidence that the mechanisms that lead to enhanced bubble formation at elevated temperature do not affect the enhanced damage tolerance of this sample.

9. Summary and Conclusions

Synthesis of the $Ca_{1-x}La_{2x/3}TiO_3$ system was achieved via the solid state route with a 48-hour heat treatment at 1573 K, with bulk pellets of density > 95 th% achieved through an additional sintering step for 8 hours at 1673 K. The production of high quality samples was essential in this study to ensure radiation damage studies were representative of the $Ca_{1-x}La_{2x/3}TiO_3$ system. SEM characterisation of sample grain sizes showed an increase in average grain size, from < 15 µm for $x = 0$, < 30 µm for $0.1 \leq x \leq 0.4$ and < 50 µm for $0.5 \leq x \leq 0.9$. The increase in grain size with La content was attributed to the associated increase in A-site vacancies leading to increased atomic diffusion that promoted grain growth. EDS characterisation provided evidence of the compositional homogeneity of the samples, with no trace reagents or additional secondary phases identified. Structural characterisation was undertaken using XRD and electron diffraction, with phase transitions identified through the diminishment and appearance of reflections as *Pbnm* in tilt system $a^-a^-c^+$ for $0 \leq x \leq 0.5$, *Ibmm* with $a^-a^-c^0$ for $x = 0.6$, *I4/mcm* with $a^0a^0c^-$ for $x = 0.7$ and *Cmmm* with $a^-b^0c^0$ for $x = 0.9$. A single-phase product could not be confirmed for $x = 0.8$ due to the appearance of concert reflections likely brought on by cation vacancy ordering. The appearance of non-aristotype ½(*eeo*) reflections in captured electron diffraction patterns confirmed the presence of A-site vacancy ordering within the $x = 0.7$ and 0.9 samples.

Ion milling of A-site deficient $x = 0.2$, 0.4, 0.6, 0.7 and 0.9 samples led to the formation of nano-regions of crystallinity ≈ 5 nm in diameter. This investigation was not intended, but the production of unaltered TEM samples was essential to the completion of this study, and therefore a study of this alteration was conducted. Electron diffraction analysis provided evidence of nanocrystallite formation as a surfaced modified layer on the pristine sample bulk. Polycrystalline electron diffraction of the $x = 0.6$ sample provided evidence of Ti reduction, while nanocrystallites were indexed to both the TiO_2 and $Ca_{0.4}La_{0.4}TiO_3$ structures. Exsolution of the TiO_2 was attributed to the reduction of TiO_2, as has been observed in previous heat treatments of A-site deficient perovskites in reducing atmospheres. Ion milling with 2 keV Ar^+ was found to prevent the formation of nanocrystallites, providing evidence of a threshold energy for surface modification and phase segregation.

GAXRD and XTEM analysis of $Ca_{1-x}La_{2x/3}TiO_3$ samples bulk ion implanted with 1 MeV Kr^+ and 5 MeV Au^+ to fluences of 1 x 10^{15} ions cm^{-2} and 5 x 10^{14} ions cm^{-2}, respectively, has been conducted. Enhanced resistance to amorphisation has been observed for the $0.2 \leq x \leq 0.4$ formula unit region when compared with the $x = 0$ sample, and this behaviour has been discussed with regard to A-site vacancy content. It has been concluded that these process are likely due to reduced barriers to defect migration enhanced the recovery of induced damage in these samples. This is the second A-site deficient perovskite system in which these effects have been observed, and the first time in a bulk ion implanted sample. This was followed by reduced resistance to amorphisation for $x \geq 0.5$, and this process has been discussed with regard to the reduced tolerance for disorder in this region. This includes through ordering of A-site cations/vacancies. Comparison with previous literature suggests these mechanisms are not related to structural transitions, and the next steps should include investigating non-titanate perovskites and different rare-earth dopants.

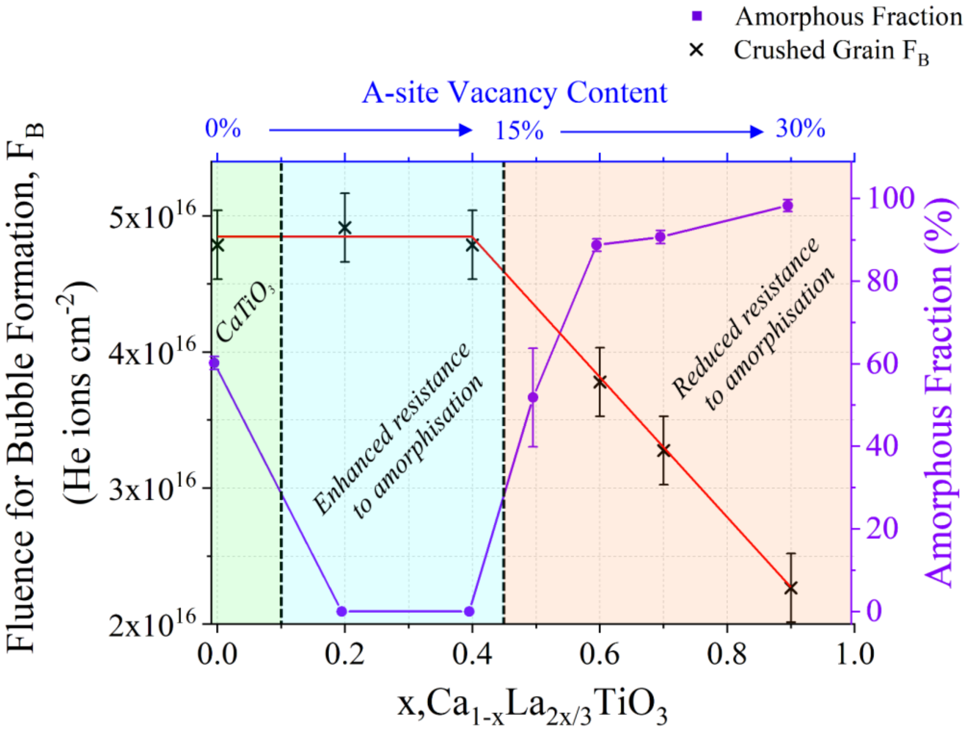

Figure 8.11 Crushed grain fluences for bubble formation, F_B, and amorphous fractions calculated from GAXRD patterns for 1 MeV Kr^+ ion implanted samples with formula unit value, x, for the $Ca_{1-x}La_{2x/3}TiO_3$ system. The three damage regions are identified with $CaTiO_3$ in light green and the regions of enhanced/reduced resistance to amorphisation in blue and orange, respectively, to aid comparison.

Ion implantation *in-situ* in a TEM with 6 keV He^+ showed the fluence required for bubble formation was within error for the $x = 0$, 0.2 and 0.4 samples. This was true for both crushed grain and ion milled TEM samples. It was expected that the increased A-site vacancy content in the $x = 0.2$ and 0.4 samples would reduce this required fluence due to the increased number of sites available for helium bubble formation. It was concluded that bubble formation was supressed by the enhanced resistance to amorphisation for these samples reported in chapter 7. For $x < 0.4$, the fluence required for bubble formation decreased linearly with La content, suggesting the reduced resistance to amorphisation in these samples promoted bubble formation. These effects can be seen in figure 8.11, reprinted from chapter 8 within this section. Furthermore, electron diffraction showed the radiation damage tolerance effects observed with bulk ion implantation were also observed with 6 keV He^+ ion implantation. Contrast from diffuse scattering for the $x = 0.6$, 0.7 and 0.9 samples at the maximum implantation fluence of 1×10^{17} ions cm^{-2} was greater than for the $x = 0$, 0.2 and 0.4 samples, suggesting these effects are also present for low-mass ion implantation as well as the heavier Kr^+ and Au^+ ions. Furthermore, preferential formation was observed within grain boundaries, increasing the fluence required for bulk helium bubble formation in the $Ca_{1-x}La_{2x/3}TiO_3$ ceramics.

While this thesis has presented several conclusions to meet the initial research goals set out, several questions remain and are raised by this work. In the following chapter, a selection of potential future work into the $Ca_{1-x}La_{2x/3}TiO_3$ system, other perovskite systems and the effects of A-site deficiency are presented.

10. Future Work

Several areas of interest could be pursued to elucidate further characteristics of the $Ca_{1-x}La_{2x/3}TiO_3$ system. In the pristine, the *Ibmm* to *I4/mcm* transition could be definitively confirmed by observing all [110] zone axes and determining the x = 0.7 space group through identification of ½(*ooo*) anti-phase tilting reflections. A full EELS/ELNES study to identify the oxidation state of Ti in ion milled A-site deficient samples could be undertaken, while energy-filtered TEM would allow for elemental mapping of the sample surface to confirm the identified phase-segregation discussed in chapter 6. Furthermore, conducting ion milling on other A-site deficient perovskites such as the $Sr_{1-x}La_{2x/3}TiO_3$ and those identified by Neagu *et al* [182,183] would allow for confirmation of the reduction process in further systems.

The underlying mechanisms of radiation damage in the $Ca_{1-x}La_{2x/3}TiO_3$ system would benefit from a full *in-situ* study using 1 MeV Kr^+ ion implantation in a TEM. In this manner, the activation energies for recovery and T_c values for the system could be quantified to aid in the understanding of the bulk irradiations. Considering the effects of A-site deficiency on radiation damage, the potential for investigating other systems is wide ranging. Several systems have been synthesised within the literature, and exploring which systems show the greatest proficiency for enhanced radiation tolerance would aid understanding of the underlying mechanisms that govern A-site deficiency enhanced tolerance.

With regard to He bubble formation, conducting bulk helium ion implantation would allow for confirmation of the observed phenomena, whereby A-site deficiency shows the potential to suppress the fluence at which bubbles are observed. Furthermore, investigation of other A-site deficient perovskites would once again help with determining the mechanisms that govern enhanced damage tolerance.

Considering ceramics for applications within the nuclear sector, cation deficient zirconolites have been reported. Zirconolite is a candidate for the immobilisation of plutonium, the mixed valance state of which is likely to promote cation deficiency. If cation deficiency enhanced damage tolerance within zirconolites is observed, the effect upon dissolution would be of keen interest, and would enhanced the safety case for this disposal route.

References

[1] V Vashook *et al.*, *A-site deficient perovskite-type compounds in the ternary CaTiO3-LaCrO3-La2/3TiO3 system*, J. Alloys Compd. 419, (**1**–**2**), 271–280, 2006

[2] V Vashook, L Vasylechko, M Knapp, H Ullmann, and U Guth, *Lanthanum doped calcium titanates: synthesis, crystal structure, thermal expansion and transport properties*, J. Alloys Compd. 354, 13–23, 2003

[3] E Salje and H Zhang, *Domain boundary engineering*, Phase Transitions 82 (**6**), 452–469, 2009

[4] I-S Kim, W-H Jung, Y Inaguma, T Nakamure, and M Itoh, *Dielectric Properties of A-Site Deficient Peroskite-Type Lanthanum-Calcium-Titanium Oxide Solid Solution System*, Mater. Res. Bull. 30 (**3**), 307–316, 1995

[5] KL Smith, GR Lumpkin, MG Blackford, M Colella, and NJ Zaluzec, *In situ radiation damage studies of La(x)Sr(1-3x/2)TiO(3) perovskites*, J. Appl. Phys. 103 (**8**), 083531, 2008

[6] AE Ringwood *et al.*, *Immobilization of high-level nuclear reactor wastes in SYNROC: A current appraisal*, Nucl. Chem. Waste Manag. 2 (**4**), 287–305, 1981

[7] W Sinclair and AE Ringwood, *Alpha-recoil damage in natural zirconolite and perovskite*, 15, 229–243, 1981

[8] A Meldrum, LA Boatner, WJ Weber, and RC Ewing, *Amorphization and recrystallization of the ABO3 oxides*, J. Nucl. Mater. 300, 242–254, 2002

[9] GR Lumpkin, M Colella, KL Smith, RH Mitchell, and AO Larsen, *Chemical Composition, Geochecmial Alteration, and Radiation Damage Effects in Natural Perovskite*, MRS Proc. 506, 207–214, 1998

[10] M Danaie *et al.*, *Characterization of Ordering in A-Site Deficient Perovskite* $Ca_{1-x}La_{2x/3}TiO_3$ *Using STEM/EELS*, Inorg. Chem. 55, 9937–9948, 2016

[11] C Davoisne, MC Stennett, NC Hyatt, N Peng, C Jeynes, and WE Lee, *Krypton irradiation damage in Nd-doped zirconolite and perovskite*, J. Nucl. Mater. 415, 67–73, 2011

[12] Nuclear Decommissioning Authority, *Radioactive Wastes in the UK: UK Radioactive Waste Inventory Report*. 2017

[13] NC Hyatt, *Plutonium management policy in the United Kingdom: The need for a dual track strategy*, Energy Policy 101, 303–309, 2017

[14] SE Kesson, *The Synroc strategy for HLW management*, 58, 458–459, 1993

[15] JP Evans, KA Boult, EL Paige, and JAC Marples, *The preparation of fully active Synroc and its radiation stability - Progress Report*, Harwell, UK, 1986

[16] JL Kloosterman and PMG Damen, *Reactor physics aspects of plutonium burning in inert matrix fuels*, J. Nucl. Mater. 274 (**1**–**2**), 112–119, 1999

[17] C Lombardi and A Mazzola, *Exploiting the Plutonium Stockpiles in PWRs by using Inert Martix Fuels*, Ann. Nucl. Energy 23 (**14**), 1117–1126, 1996

[18] IAEA, *Viability of inert matrix fuel in reducing plutonium amounts in reactors*, Vienna, 2006

[19] RC Ewing, WJ Weber, and FW Clinard, *Radiation effects in nuclear waste forms for high-level radioactive waste*, Prog. Nucl. Energy 29 (**2**), 63–127, 1995

[20] SJ Zinkle, *Effect of H and He irradiation on cavity formation and blistering in ceramics*, Nucl. Inst. Methods Phys. Res. B 268, 4–19, 2012

[21] VM Goldschmidt, *Die Gesetze der Krystallochemie*, Naturwissenschaften 14, 477–485, 1926

[22] MH Roger, *Perovskites: Modern and Ancient*. Thunder Bay: Almaz Press Inc., 2002

[23] IM Reaney, EL Colla, and N Setter, *Dielectric and structural characteristics of perovskites and related materials as a function of tolerance factor*, Jpn. J. Appl. Phys. 33, 3984–3990, 1994

[24] AM Glazer, *The classification of tilted octahedra in perovskites*, Acta Crystallogr. Sect. B 28 (**11**), 3384–3392, 1972

[25] AM Glazer, *Simple ways of determining perovskite structures*, Acta Crystallogr. Sect. A 31 (**6**), 756–762, 1975

[26] DI Woodward and IM Reaney, *Electron diffraction of tilted perovskites*, Acta Crystallogr. Sect. B Struct. Sci. 61, 387–399, 2005

[27] DI Woodward, IM Reaney, RE Eitel, and CA Randall, *Crystal and domain structure of the BiFeO3–PbTiO3 solid solution*, J. Appl. Phys. 94 (**5**), 3313–3318, 2003

[28] LW Hobbs, FW Clinard, SJ Zinkle, and RC Ewing, *Radiation effects in ceramics*, J. Nucl. Mater. 216, 291–321, 1994

[29] K Reeve and J Woolfrey, *Accelerated irradiation testing of Synroc using fast neutrons - First results on barium hollandite, perovskite and synroc B*, J. Austrialian Ceram. Soc. 16 (**1**), 1980

[30] AR West, *Solid State Chemistry and its Applications (2nd Edition)*. Chichester: John Wiley, 2014

[31] M Nastasi and JW Mayer, *Ion Implantation and Synthesis of Materials*. New York: Springer, 2006

[32] GH Kinchin and RS Pease, *The Displacement of Atoms in Solids by Radiation*, 1955

[33] MJ Norgett, MT Robinson, and IM Torrens, *A proposed method of calculating displacement dose rates*, Nucl. Eng. Des. 33, 50–54, 1975

[34] KL Smith and NJ Zaluzec, *The displacement energies of cations in perovskite (CaTiO3)*, J. Nucl. Mater. 336 (**2**–**3**), 261–266, 2005

[35] KL Smith, M Colella, R Cooper, and ER Vance, *Measured displacement energies of oxygen ions in titanates and zirconates*, J. Nucl. Mater. 321 (**1**), 19–28, 2003

[36] M Robinson, N a. Marks, KR Whittle, and GR Lumpkin, *Systematic calculation of threshold displacement energies: Case study in rutile*, Phys. Rev. B - Condens. Matter Mater. Phys. 85 (**10**), 1–11, 2012

[37] GP Pells, *The temperature dependence of the threshold displacement energy in MgO*, Radiat. Eff. Defects Solids 64 (**1**), 71–75, 1982

[38] BS Thomas, N a. Marks, and BD Begg, *Defects and threshold displacement energies in SrTiO3 perovskite using atomistic computer simulations*, Nucl. Instruments Methods Phys. Res. Sect. B Beam Interact. with Mater. Atoms 254 (**2**), 211–218, 2007

[39] KR Whittle, *Nuclear Materials Science*. Bristol, UK: IOP Publishing Ltd, 2016

[40] W. Weber, *Models and mechanisms of irradiation-induced amorphization in ceramics*, Nucl. Instruments Methods Phys. Res. Sect. B Beam Interact. with Mater. Atoms 166–167, 98–106, 2000

[41] WJ Weber, RC Ewing, and LM Wang, *The radiation-induced crystalline-to-amorphous transition in zircon*, J. Mater. Res. 9 (**3**), 688–698, 1994

[42] FF Morehead and BL Crowder, *A model for the formation of amorphous Si by ion bombardment*, Radiat. Eff. 6 (**1**), 27–32, 1970

[43] LM Wang and WJ Weber, *Transmission electron microscopy study of ion-beam-induced amorphization of Ca2La8(SiO4)6O2*, Philos. Mag. A 79 (**1**), 237–253, 1999

[44] A Meldrum, CW White, V Keppens, LA Boatner, and RC Ewing, *Irradiation-induced amorphization of Cd2Nb2O7 pyrochlore*, Phys. Rev. B 63 (**10**), 104109, 2001

[45] A Meldrum, LA Boatner, and RC Ewing, *Size effects in the irradiation-induced crystalline-to-amorphous transformation*, Nucl. Instruments Methods Phys. Res. Sect. B Beam Interact. with Mater. Atoms 207 (**1**), 28–35, 2003

[46] J Lian, X Zu, K Kutty, J Chen, L Wang, and R Ewing, *Ion-irradiation-induced amorphization of La2Zr2O7 pyrochlore*, Phys. Rev. B 66 (**5**), 054108, 2002

[47] LL Snead, SJ Zinkle, JC Hay, and MC Osborne, *Amorphization of SiC under ion and neutron irradiation*, Nucl. Instruments Methods Phys. Res. Sect. B Beam Interact. with Mater. Atoms 141 (**1**–**4**), 123–132, 1998

[48] CJ Howard, GR Lumpkin, RI Smith, and Z Zhang, *Crystal structures and phase transition in the system SrTiO3–La2/3TiO3*, J. Solid State Chem. 177 (**8**), 2726–2732, 2004

[49] Y Zhang, CM Wang, MH Engelhard, and WJ Weber, *Irradiation behavior of SrTiO[sub 3] at temperatures close to the critical temperature for amorphization*, J. Appl. Phys. 100 (**11**), 113533, 2006

[50] GR Lumpkin *et al.*, *Ion Irradiation of Ternary Pyrochlore Oxides*, Chem. Mater. 21 (**13**), 2746–2754, 2009

[51] RD Aughterson *et al.*, *The influence of crystal structure on ion-irradiation tolerance in the Sm(x)Yb(2-x)TiO5 series*, J. Nucl. Mater. 471, 17–24, 2016

[52] MG Blackford *et al.*, *Structure Versus Radiation Damage Response in LaXSr(1-3X/2)TiO3 Perovskites*, Microsc. Microanal. 10 (**S02**), 596–597, 2004

[53] KR Whittle, GR Lumpkin, MG Blackford, RD Aughterson, KL Smith, and NJ Zaluzec, *Ion-beam irradiation of lanthanum compounds in the systems La 2O3Al2O3 and La2O 3TiO2*, J. Solid State Chem. 183 (**10**), 2416–2420, 2010

[54] A Meldrum, SJ Zinkle, and LA Boatner, *Heavy-ion irradiation effects in the AB O 4 orthosilicates : recrystallization Decomposition , amorphization , and*, 59 (**6**), 3981–3992, 1999

[55] WJ Weber and LM Wang, *The temperature dependence of ion-beam-induced amorphisation in B-SiC*, Nucl. Instruments Methods Phys. Res. Sect. B Beam Interact. with Mater. Atoms 106, 298–302, 1995

[56] A Meldrum, LM Wang, and RC Ewing, *Ion beam induced amorphisation of monazite*, Nucl. Instruments Methods Phys. Res. Sect. B Beam Interact. with Mater. Atoms 116, 220–224, 1996

[57] Y Zhang, WJ Wber, W Jiang, CM Wang, V Shutthanandan, and A Hallén, *Effects of implantation temperature on damage accumulation in Al-implanted 4H–SiC*, J. Appl. Phys. 95 (**8**), 4012, 2004

[58] GR Lumpkin, KL Smith, and MG Blackford, *Heavy ion irradiation studies of columbite, brannerite, and pyrochlore structure types*, J. Nucl. Mater. 289 (**1**–**2**), 177–187, 2001

[59] K Smith, M Blackford, G Lumpkin, K Whittle, and N Zaluzec, *Radiation Tolerance of A2B2O7 Compounds at the Cubic-Monclinic Boundary*, Microsc. Microanal. 12 (**S02**), 1094–1095, 2006

[60] SX Wang, LM Wang, RC Ewing, and RH Doremus, *Ion beam-induced amorphization in MgO-Al2-O3-SiO2. I . Experimental and theoretical basis*, J. Non. Cryst. Solids 238, 198–213, 1998

[61] FA Kröger and HJ Vink, *Relations between the Concentrations of Imperfections in Crystalline Solids*, Solid State Phys. 3, 307–435, 1956

[62] H Zheng, IM Reaney, and CDC Csete de Gyorgyfalva, *Raman spectroscopy of* $CaTiO_3$*-based perovskite*, J. Mater. Res. 19 (**2**), 488–495, 2004

[63] P Mcmillan and N Ross, *The Raman Spectra of Several Orthorhombic Calcium Oxide Perovskites ~ CoTiO d o*, Phys. Chem. Miner. 16, 21–28, 1988

[64] Z Zhang, MG Blackford, GR Lumpkin, KL Smith, and ER Vance, *Aqueous Dissolution of Perovskite (*$CaTiO_3$*): Effects of Surface Damage and [*Ca^{2+}*] in the Leachant*, J. Mater. Res. 20 (**9**), 2462–2473, 2005

[65] T Hirata, K Ishioka, and M Kitajima, *Vibrational Spectroscopy and X-Ray Diffraction of Perovskite Compounds* $Sr_{1-x}M_xTiO_3(M= Ca, Mg; 0 \leq x \leq 1)$, J. Solid State Chem. 124 (**2**), 353–359, 1996

[66] M Bassoli *et al.*, *Defect chemistry and dielectric properties of* $Yb^{3+}: CaTiO_3$ *perovskite*, J. Appl. Phys. 103 (**2008**), 14104, 2008

[67] DSL Pontes *et al.*, *Effects of strontium and calcium simultaneous substitution on electrical and structural properties of Pb1−x−y Ca x Sr y TiO3 thin films*, Appl. Phys. A 96 (**3**), 731–740, 2009

[68] Y Ni, Z Zhang, D Wang, Y Wang, and X Ren, *The effect of point defects on ferroelastic phase transition of lanthanum-doped calcium titanate ceramics*, J. Alloys Compd. 577, S468–S471, 2013

[69] M Sindhu, N Ahlawat, S Sanghi, A Agarwal, R Dahiya, and N Ahlawat, *Rietveld refinement and impedance spectroscopy of calcium titanate*, Curr. Appl. Phys. 12 (**6**), 1429–1435, 2012

[70] U Balachandran and NG Eror, *Laser-induced raman scattering in calcium titanate*, Solid State Commun. 44 (**6**), 815–818, 1982

[71] MA Carpenter, CJ Howard, KS Knight, and Z Zhang, *Structural Relationships and a Phase Diagram for (Ca,Sr)*TiO_3 *Perovskites*, J. Phys. Condens. Matter 18, 10725–10749, 2006

[72] Z Zhang, GR Lumpkin, CJ Howard, KS Knight, KR Whittle, and K Osaka, *Structures and phase diagram for the system* $CaTiO_3$-$La_{2/3}TiO_3$, J. Solid State Chem. 180 (**3**), 1083–1092, 2007

[73] S Van Aert, S Turner, R Delville, D Schryvers, G Van Tendeloo, and EKH Salje, *Direct observation of ferrielectricity at ferroelastic domain boundaries in* $CaTiO_3$ *by electron microscopy*, Adv. Mater. 24 (**4**), 523–527, 2012

[74] IM Reaney, *Tem observations of domains in ferroelectric and nonferroelectric perovskites*, Ferroelectrics 172 (**1**), 115–125, 1995

[75] DI Woodward, PL Wise, WE Lee, and IM Reaney, *Space group symmetry of* $(Ca_xSr_{1-x})TiO_3$ *determined using electron diffraction*, J. Phys. Condens. Matter 18 (**8**), 2401–2408, 2006

[76] LS Cavalcante *et al.*, *Synthesis, structural refinement and optical behavior of* $CaTiO_3$ *powders: A comparative study of processing in different furnaces*, Chem. Eng. J. 143 (**1**–**3**), 299–307, 2008

[77] S Qin, X Wu, F Seifert, and AI Becerro, *Micro-Raman study of perovskites in the* $CaTiO_3$-$SrTiO_3$ *system*, J. Chem. Soc. Dalt. Trans. (**19**), 3751–3755, 2002

[78] V Železný *et al.*, *Temperature dependence of infrared-active phonons in* $CaTiO_3$*: A combined spectroscopic and first-principles study*, Phys. Rev. B 66 (**22**), 224303, 2002

[79] H Zheng *et al.*, *Raman spectroscopy of B-site order–disorder in* $CaTiO_3$*-based microwave ceramics*, J. Eur. Ceram. Soc. 23 (**14**), 2653–2659, 2003

[80] H Yokota *et al.*, *Direct evidence of polar nature of ferroelastic twin boundaries in* $CaTiO_3$ *obtained by second harmonic generation microscope*, Phys. Rev. B - Condens. Matter Mater. Phys. 89 (**14**), 1–9, 2014

[81] R Ali and M Yashima, *Space group and crystal structure of the Perovskite* $CaTiO_3$ *from 296 to 1720 K*, J. Solid State Chem. 178, 2867–2872, 2005

[82] M Abe and K Uchino, *X-ray study of the deficient perovskite* $La_{2/3}TiO_3$, Mater. Res. Bull. 9 (**2**), 147–155, 1974

[83] HJ Lee, HM Park, YK Cho, and S Nahm, *Microstructure Characterization of the* $(1-x)La_{2/3}TiO_3$-$xLaAlO_3$ *System*, J. Am. Ceram. Soc. 86 (**8**), 1395–1400, 2003

[84] JB MacChesney and HA Sauer, *The System La2O3— TiO5; Phase Equilibria and Electrical Properties,* J. Am. Ceram. Soc. 45 (**9**), 416–422, 1962

[85] G King and PM Woodward, *Cation ordering in perovskites*, J. Mat. Chem. 20, 5785–5796, 2010

[86] W Sinclair and AE Ringwood, *Alpha-recoil damage in natural zirconoite and perovskite*, Geochem. J. 15, 229–243, 1981

[87] GR Lumpkin, *Alpha-decay damage and aqueous durability of actinide host phases in natural systems,* J. Nucl. Mater. 289 (**1**–**2**), 136–166, 2001

[88] JL Woolfrey, DJ Reeve, and KD Cassidy, *Accelerated Irradiation Testing of SYNROC and its Constituent Minearls Using Fast Neutrons*, 108/109, 739–747, 1982

[89] CA Taylor, *Helium Diffusion and Accumulation in Gd2Ti2O7 and Gd2Zr2O7*, 2016

[90] CJ Ball, RG Blake, DJ Cassidy, and JL Woolfrey, *Neutron irradiations effects in perovskite (CaTiO3),* J. Nucl. Mater. 151, 151–161, 1988

[91] MD Strachan *et al.*, *Radiation Damage Effects in Candidate Ceramics for Plutonium Immobilization : Final Report*, 2004

[92] WJ Weber, RC Ewing, and L-M Wang, *The radiation-induced crystalline-to-amorphous transition in zircon,* J. Mater. Res. 9 (**03**), 688–698, 2011

[93] FG Karioris, L Cartz, K Appaji, and JC Labbe, *Damage cross-sections of heavy ions in crystal structures,* J. Nucl. Mater. 108–9, 748–750, 1982

[94] CW White *et al.*, *Ion Implantation and Annealing of Crystalline Oxides and Ceramic Materials*, Nucl. Instr. Meth. Phys. Res. B 32, 11–22, 1988

[95] CW White, CJ McHargue, PS Sklad, LA Boatner, and GC Farlow, *Ion implantation and annealing of crystalline oxides*, Mater. Sci. Reports 4, 41–146, 1989

[96] J Rankin, LW Hobbs, LA Boatner, and CW White, *An in situ annealing study of lead implanted single crystal calcium titanate*, Nucl. Inst. Methods Phys. Res. B 32 (**1**–**4**), 28–31, 1988

[97] KL Smith, NJ Zaluzec, and GR Lumpkin, *In situ studies of ion irradiated zirconolite, pyrochlore and perovskite*, J. Nucl. Mater. 250 (**1**), 36–52, 1997

[98] JF Ziegler, MD Ziegler, and JP Biersack, *SRIM - The stopping and range of ions in matter (2010)*, Nucl. Instruments Methods Phys. Res. Sect. B Beam Interact. with Mater. Atoms 268 (**11**–**12**), 1818–1823, 2010

[99] KL Smith, GR Lumpkin, MG Blackford, M Colella, and NJ Zaluzec, *In situ radiation damage studies of* $La_xSr_{1-3x/2}TiO_3$ *perovskites*, J. Appl. Phys. 103 (**8**), 083531, 2008

[100] KL Smith, M Colella, R Cooper, and ER Vance, *Measured displacement energies of oxygen ions in titanates and zirconates*, J. Nucl. Mater. 321 (**1**), 19–28, 2003

[101] R Cooper, KL Smith, M Colella, ER Vance, and M Phillips, *Optical emission due to ionic displacements in alkaline earth titanates*, J. Nucl. Mater. 289 (**1**–**2**), 199–203, 2001

[102] BS Thomas, N a. Marks, and BD Begg, *Defects and threshold displacement energies in* $SrTiO_3$ *perovskite using atomistic computer simulations*, Nucl. Instruments Methods Phys. Res. Sect. B Beam Interact. with Mater. Atoms 254, 211–218, 2007

[103] W Jiang, W. Weber, and S Thevuthasan, *Damage accumulation and recovery in gold-ion-irradiated barium titanate*, Nucl. Instruments Methods Phys. Res. Sect. B Beam Interact. with Mater. Atoms 175–177, 610–614, 2001

[104] WJ Weber, W Jiang, S Thevuthasan, RE Williford, A Meldrum, and LA

Boatner, *Ion-Beam-Induced Defects and Defect Interactions in Perovskite-Structure Titanates*, 1998

[105] M Lang *et al.*, *Swift heavy ion-induced amorphization of $CaZrO_3$ perovskite*, Nucl. Instruments Methods Phys. Res. Sect. B Beam Interact. with Mater. Atoms 286 271–276, 2012

[106] JN Mitchell, N Yu, KE Sickafus, M a Nastasi, and KJ McClellan, *Ion irradiation damage in geikielite ($MgTiO_3$)*, Philos. Mag. A-Physics Condens. Matter Struct. Defects Mech. Prop. 78 (**3**), 713–725, 1998

[107] C Sabathier, J Chaumont, S Rouzière, and A Traverse, *Characterisation of Ti and Sr atomic environments in $SrTiO_3$ before and after ion beam irradiation by X-ray absorption spectroscopy*, Nucl. Instr. Meth. Phys. Res. B 234 (**4**), 509–519, 2005

[108] Y Yamauchi, *Bubble formation on silicon by helium ion bombardment*, Appl. Surf. Sci. 169–170 (**1**–**2**), 626–630, 2001

[109] V Raineri, S Coffa, E Szilágyi, J Gyulai, and E Rimini, *He-vacancy interactions in Si and their influence on bubble formation and evolution*, Phys. Rev. B 61 (**2**), 937–945, 2000

[110] M Maekawa and A Kawasuso, *Characterization of helium bubbles in Si by slow positron beam*, J. Phys. Conf. Ser. 225 2010

[111] B Pivac *et al.*, *Early stages of bubble formation in helium-implanted (100) silicon*, Phys. status solidi 198 (**1**), 29–37,

[112] KJ Abrams *et al.*, *Helium irradiation effects in polycrystalline Si, silica, and single crystal Si*, J. Appl. Phys. 111 (**8**), 083527 (1-6), 2012

[113] SE Donnelly, JA Hinks, CJ Pawley, KJ Abrams, and JA van den Berg, *An* in-situ *TEM study of the effects of 6 keV He ion irradiation on Si and SiO_2*, J. Phys. Conf. Ser. 371, 012045, 2012

[114] AS Gandy, *A Transmission Electron Microscopy Study of the Interaction between Defects in Amorphous Silicon and a Moving Crystalline / Amorphous Interface Amy S Gandy Institute of Materials Research (IMR) University of Salford , Salford , UK Faculté des Sciences F*, 2008

[115] B Glasgow, A Si-Ahmed, WG Wolfer, and F Garner, *Helium Bubble Formation and Swelling in Metals*, J. Nucl. Mater. 103 & 104, 981–986, 1981

[116] W Wilson, M Baskes, and C Bisson, *Atomistics of helium bubble formation in a face-centered-cubic metal*, Phys. Rev. B 13 (**6**), 2470–2478, 1976

[117] PD Edmondson, CM Parish, Y Zhang, A Hallén, and MK Miller, *Helium entrapment in a nanostructured ferritic alloy*, Scr. Mater. 65 (**8**), 731–734, 2011

[118] B Kaiser *et al.*, *TEM study and modeling of bubble formation in dual-beam* He_{+}/Fe_{3+} *ion irradiated EUROFER97*, J. Nucl. Mater. 484, 59–67, 2017

[119] Q Li, CM Parish, KA Powers, and MK Miller, *Helium solubility and bubble formation in a nanostructured ferritic alloy*, J. Nucl. Mater. 445 (**1**–**3**), 165–174, 2014

[120] O El-atwani, K Hattar, JA Hinks, G Greaves, SS Harilal, and A Hassanein, *Helium bubble formation in ultrafine and nanocrystalline tungsten under different extreme conditions*, J. Nucl. Mater. 458, 216–223, 2015

[121] R Li *et al.*, *He-vacancy interaction and multiple He trapping in small void of silicon carbide*, J. Nucl. Mater. 457, 36–41, 2015

[122] Q Shen, G Ran, J Hinks, SE Donnelly, L Wang, and N Li, *In situ Observation of Microstructure Evolution in 4H-SiC under 3.5keV* He^+ *Irradiation*, J. Nucl. Mater. 2016

[123] A Hasegawa, M Saito, S Nogami, K Abe, RH Jones, and H Takahashi, *Helium-bubble formation behavior of SiCf / SiC composites after helium implantation*, J. Nucl. Mater. 264, 355–358, 1999

[124] G Gutierrez *et al.*, *Helium bubble formation in nuclear glass by in-situ TEM ion implantation*, J. Nucl. Mater. 452 (**1**–**3**), 565–568, 2014

[125] PMG Damen, A Van Veen, F Labohm, H Schut, and MA Van Huis, *Thermal annealing behaviour and defect evolution of helium in fully stabilised zirconia*, J. Nucl. Mater. 319, 65–73, 2003

[126] WR Allen and SJ Zinkle, *Lattice location and clustering of helium in ceramic oxides*, J. Nucl. Mater. 191–194, 625–629, 1992

[127] H Ullmaier, *Helium in fusion materials: High temperature embrittlement*, J. Nucl. Mater. 133–134, 100–104, 1985

[128] DM Stewart, YN Osetsky, RE Stoller, SI Golubov, T Seletskaia, and PJ Kamenski, *Atomistic studies of helium defect properties in bcc iron: Comparison of He–Fe potentials*, Philos. Mag. 90 (**7**–**8**), 935–944, 2010

[129] O El-Atwani *et al.*, *In-situ TEM observation of the response of ultrafine- and nanocrystalline-grained tungsten to extreme irradiation environments*, Sci. Rep. 4, 4–10, 2014

[130] J Matsunaga, K Sakamoto, H Muta, and S Yamanaka, *Dependence of vacancy concentration on morphology of helium bubbles in oxide ceramics*, J. Nucl. Sci. Technol. 51 (**10**), 1231–1240, 2014

[131] MA van Huis *et al.*, *Formation, growth and dissociation of He bubbles in* Al_2O_3, Nucl. Instruments Methods Phys. Res. Sect. B 216, 149–155, 2004

[132] A Ofan *et al.*, *Twinning and dislocation pileups in heavily implanted* $LiNbO_3$, Phys. Rev. B - Condens. Matter Mater. Phys. 83 (**6**), 1–8, 2011

[133] G Velisa, A Debelle, L Vincent, L Thomé, A Declémy, and D Pantelica, *He implantation in cubic zirconia: Deleterious effect of thermal annealing*, J. Nucl. Mater. 402 (**1**), 87–92, 2010

[134] S Furuno *et al.*, *Ion Irradiation and Annealing Effects in Al2O3 and MgAlO4*, Nucl. Instr. Meth. Phys. Res. B 127/128, 181–185, 1997

[135] T Hojo *et al.*, *Radiation effects on yttria-stabilized zirconia irradiated with He or Xe ions at high temperature*, Nucl. Instruments Methods Phys. Res. Sect. B Beam Interact. with Mater. Atoms 241 (**1**–**4**), 536–542, 2005

[136] N Sasajima, T Matsui, S Furuno, T Shiratori, and K Hojou, *Radiation effects on MgAl2O4-stabilized ZrO2 composite material under He+ or Xe2+ ion irradiation*, Nucl. Instruments Methods Phys. Res. Sect. B Beam Interact. with Mater. Atoms 166, 250–257, 2000

[137] SJ Zinkle, *Effect of H and He irradiation on cavity formation and blistering in ceramics*, Nucl. Instruments Methods Phys. Res. Sect. B Beam Interact. with Mater. Atoms 286, 4–19, 2012

[138] A Ofan *et al.*, *Spherical solid He nanometer bubbles in an anisotropic complex oxide*, Phys. Rev. B - Condens. Matter Mater. Phys. 82 (**10**), 1–8, 2010

[139] CA Taylor *et al.*, *Bubble formation and lattice parameter changes resulting from He irradiation of defect-fluorite Gd2Zr2O7*, Acta Mater. 115 (**225**), 115–122, 2016

[140] CA Taylor *et al.*, *Combined effects of radiation damage and He accumulation on bubble nucleation in Gd2Ti2O7*, J. Nucl. Mater. 479, 542–547, 2016

[141] Y-H Li, C-P Xu, C Gao, and Z-G Wang, *Ne2+ Ion Irradiation Induced Swelling Effects in Pyrochlore Ho2Ti2O7 by Using a GIXRD Technique*, Chinese Phys. Lett. 28 (**6**), 066102, 2011

[142] J Als-Nielsen and D McMorrow, *Elements of Modern X-ray Physics*. 2011

[143] G Lim, W Parrish, C Ortiz, M Bellotto, and M Hart, *Grazing incidence synchrotron x-ray diffraction method for analyzing thin films*, J. Mater. Res. 2 (**04**), 471–477, 1987

[144] S Rugel, H Metzger, G Wallner, and J Peisl, *Grazing incidence X-ray diffraction on silicon after ion implantation and thermal annealing*, Appl. Surf. Sci. 54, 507–510, 1992

[145] S Wang, M Tang, L Zhang, G Xiao, KS Brinkman, and F Chen, *Irradiation effect on the structure change for Sr2Fe1.5Mo0.5O6−δ perovskite ceramic*, J. Alloys Compd. 57,8 170–175, 2013

[146] B Ravel and M Newville, *ATHENA, ARTEMIS, HEPHAESTUS: Data analysis for X-ray absorption spectroscopy using IFEFFIT*, J. Synchrotron Radiat. 12 (**4**), 537–541, 2005

[147] DY Yang *et al.*, *Structure and radiation effect of Er-stuffed pyrochlore Er2(Ti2-xErx)O7-x/2 (x=0–0.667),* Nucl. Inst. Methods Phys. Res. B 357, 69–74, 2015

[148] M Gupta, PK Kulriya, R Shukla, RS Dhaka, R Kumar, and SS Ghumman, *Reduction and structural modification of zirconolite on He+ ion irradiation,* Nucl. Instruments Methods Phys. Res. Sect. B Beam Interact. with Mater. Atoms 379, 119–125, 2016

[149] S Park *et al.*, *Response of Gd2Ti2O7 and La2Ti2O7 to swift-heavy ion irradiation and annealing*, Acta Mater. 93, 1–11, 2015

[150] E Eberg, Å F Monsen, T Tybell, ATJ Van Helvoort, and R Holmestad, *Comparison of TEM specimen preparation of perovskite thin films by tripod polishing and conventional ion milling*, J. Electron Microsc. (Tokyo). 57 (**6**), 175–179, 2008

[151] DB Williams and CB Carter, *Transmission Electron Microscopy: A Textbook for Materials Science*, 1–4. 2009

[152] J Ayache, L Beaunier, J Boumendil, G Ehret, and D Laub, *Sample Preparation Handbook for Transmission Electron Microscopy methodology*. 2010

[153] A Strecker *et al.*, *Optimization of TEM specimen preparation by double-sided ion beam thinning under low angles*, J. Electron Microsc. (Tokyo). 48 (**3**), 235–244, 1999

[154] DVS Rao, K Muraleedharan, and CJ Humphreys, *TEM specimen preparation techniques*, Microsc. Sci. Technol. Appl. Educ. 320, 1232–1244, 2010

[155] LA Giannuzzi and FA Stevie, *A review of focused ion beam milling techniques for TEM specimen preparation*, Micron 30 (**3**), 197–204, 1999

[156] T Mehrtens, S Bley, P Venkata Satyam, and A Rosenauer, *Optimization of the preparation of GaN-based specimens with low-energy ion milling for (S)TEM,* Micron 43 (**8**), 902–909, 2012

[157] A Aitkaliyeva, JW Madden, BD Miller, JI Cole, and J Gan, *Comparison of preparation techniques for nuclear materials for transmission electron microscopy (TEM)*, J. Nucl. Mater. 459, 241–246, 2015

[158] MJ Süess, E Mueller, and R Wepf, *Minimization of amorphous layer in Ar+ion milling for UHR-EM*, Ultramicroscopy 111 (**8**), 1224–1232, 2011

[159] L Dieterle, B Butz, and E Müller, *Optimized Ar+-ion milling procedure for TEM cross-section sample preparation*, Ultramicroscopy 111 (**11**), 1636–1644, 2011

[160] D Bahnck and R Hull, *Experimental Measurement of Transmission Electron Microscope Specimen Temperature during Ion Milling*, MRS Proc. 199, 253, 1990

[161] MJ Kim and RW Carpenter, *Tem specimen heating during ion beam thinning: Microstructural instability,* Ultramicroscopy 21 (**4**), 327–334, 1987

[162] National Electrostatics Corp., *Instruction Manual No. 2AT051510 for Operation and Service of 5SDH Pelletron Accelerator*,. Middleton, WI, 2009

[163] DJW Mous, R Koudijs, P Dubbelman, and HAP van Oosterhout, *The HVEE Tandetron Line; new developments and design considerations*, Nucl. Inst. Methods Phys. Res. B 62 (**3**), 421–424, 1992

[164] JA Hinks, JA van den Berg, and SE Donnelly, *MIAMI: Microscope and ion accelerator for materials investigations*, J. Vac. Sci. Technol. A Vacuum, Surfaces, Film. 29 (**2**), 021003, 2011

[165] M Gilbert *et al.*, *Krypton and helium irradiation damage in neodymium-zirconolite*, J. Nucl. Mater. 416 (**1**–**2**), 221–224, 2011

[166] S Schmid and RL Withers, *A-site deficient perovskites in the SrO-ZrO2-Nb2O5system: Composition dependent structures from neutron powder diffraction data*, J. Solid State Chem. 191, 63–70, 2012

[167] Z Lu, H Zhang, W Lei, DC Sinclair, and IM Reaney, *High-Figure-of-Merit Thermoelectric La-Doped A-Site-Deficient SrTiO3 Ceramics*, Chem. Mater. 28 (**3**), 925–935, 2016

[168] J Sloan, *A-site cation-vacancy ordering in* $Sr_{1-3x/2}La_xTiO_3$ *: A study by HRTEM*, J. Sol. Stat. Chem. 149. 360-369, 2000

[169] CrystalMaker Software Ltd, *CrystalDiffract*,. Begbrooke, UK, 2018

[170] G Bergerhoff and ID Brown, *ICSD, Crystallographic Databases*. Chester, 1987

[171] BB Sun *et al.*, *Artifacts induced in metallic glasses during TEM sample preparation*, Scr. Mater. 53 (**7**), 805–809, 2005

[172] EG Fu *et al.*, *Ar-ion-milling-induced structural changes of Cu50Zr45Ti5metallic glass*, Nucl. Instruments Methods Phys. Res. Sect. B

Beam Interact. with Mater. Atoms 268 (**6**), 545–549, 2010

[173] A Meldrum, RF Haglund, LA Boatner, and CW White, *Nanocomposite materials formed by ion implantation*, Adv. Mater. 13 (**19**), 1431–1444, 2001

[174] M Ghasdi and H Alamdari, *Highly Sensitive Pure and Pd-Doped LaFeO3 Nanocrystalline Perovskite-Based Sensor Prepared by High Energy Ball Milling*, in *THERMEC 2011 Supplement*, 2012, 409, 486–491,

[175] OB Pavlovska, LO Vasylechko, I V. Lutsyuk, NM Koval, YA Zhydachevskii, and A Pieniążek, *Structure Peculiarities of Micro- and Nanocrystalline Perovskite Ferrites La1−xSmxFeO3*, Nanoscale Res. Lett. 12 (**1**), 2017

[176] U Chandra *et al.*, *High-pressure Mössbauer measurements on nanocrystalline perovskite (La,Sr)(Mn,Fe)O3*, Hyperfine Interact. 163 (**1**–**4**), 129–141, 2005

[177] XH Wang, IW Chen, XY Deng, YD Wang, and LT Li, *New progress in development of ferroelectric and piezoelectric nanoceramics*, J. Adv. Ceram. 4 (**1**), 1–21, 2015

[178] Z Zhao *et al.*, *Grain-size effects on the ferroelectric behavior of dense nanocrystalline BaTiO3 ceramics*, Phys. Rev. B 70 (**2**), 24107, 2004

[179] MT Buscaglia *et al.*, *High dielectric constant and frozen macroscopic polarization in dense nanocrystalline* $BaTiO_3$ *ceramics*, Phys. Rev. B 73 (**6**), 64114, 2006

[180] X Wang, X Deng, H Wen, and L Li, *Phase transition and high dielectric constant of bulk dense nanograin barium titanate ceramics*, Appl. Phys. Lett. 89 (**16**), 1–4, 2006

[181] B Viguier and A Mortensen, *Heating of TEM specimens during ion milling*, Ultramicroscopy 87 (**3**), 123–133, 2001

[182] D Neagu and JTS Irvine, *Structure and properties of La0.4Sr0.4TiO3 Ceramics for use as anode materials in solid oxide fuel cells*, Chem. Mater. 22 (**17**), 5042–5053, 2010

[183] D Neagu, G Tsekouras, DN Miller, H Menard, and JT Irvine, *In situ growth of nanoparticles through control of non-stoichiometry*, Nat Chem 5 (**11**), 916–923, 2013

[184] JT Yates and CT Campbell, *Key to control and advance myriad technologies*, Proc. Natl. Acad. Sci. 108 (**3**), 911–916, 2011

[185] J-S Kim *et al.*, *Highly Active and Thermally Stable Core-Shell Catalysts for Solid Oxide Fuel Cells,* J. Electrochem. Soc. 158 (**6**), B596, 2011

[186] PI Cowin, CTG Petit, R Lan, JTS Irvine, and S Tao, *Recent Progress in the Development of Anode Materials for Solid Oxide Fuel Cells*, Adv. Energy Mater. 1 (**3**), 314–332, 2011

[187] RJ Gorte and JM Vohs, *Nanostructured anodes for solid oxide fuel cells*, Curr. Opin. Colloid Interface Sci. 14 (**4**), 236–244, 2009

[188] SP Jiang, *Nanoscale and nano-structured electrodes of solid oxide fuel cells by infiltration: Advances and challenges*, Int. J. Hydrogen Energy 37 (**1**), 449–470, 2012

[189] P Holtappels, U Vogt, and T Graule, *Ceramic materials for advanced solid oxide fuel cells*, Adv. Eng. Mater. 7 (**5**), 292–302, 2005

[190] EO Oh *et al.*, *Extremely thin bilayer electrolyte for solid oxide fuel cells (SOFCs) fabricated by chemical solution deposition (CSD),* Adv. Mater. 24 (**25**), 3373–3377, 2012

[191] TZ Sholklapper, CP Jacobson, SJ Visco, and LC Dejonghe, *Synthesis of dispersed and contiguous nanoparticles in solid oxide fuel cell electrodes*, Fuel Cells 8 (**5**), 303–312, 2008

[192] TJ White, H Mitamura, and T Tsuboi, *Rietveld Analysis of Phase Separation in Annealed and Leach Tested Cm-Doped Perovskite*, MRS Proc. 353, 871–878, 1995

[193] K Jin *et al.*, *Electronic stopping powers for heavy ions in SiC and SiO2*, J. Appl. Phys. 115 (**4**), 2014

[194] Y Zhang *et al.*, *Damage profile and ion distribution of slow heavy ions in compounds*, J. Appl. Phys. 105 (**10**), 2009

[195] H Mitamura, S Matsumoto, T Tsuboi, ER Vance, BD Begg, and KP Hart, *Alpha-decay Damage of Cm-Doped Perovskite*, MRS Proc. 353, 1405–1412, 1995

[196] Y Ji, PM Kowalski, S Neumeier, G Deissmann, PK Kulriya, and JD Gale, *Nuclear Instruments and Methods in Physics Research B Atomistic modeling and experimental studies of radiation damage in monazite-type* $LaPO_4$ *ceramics*, 393, 54–58, 2017

[197] DM Stewart, YN Osetsky, RE Stoller, SI Golubov, T Seletskaia, and PJ Kamenski, *Atomistic studies of helium defect properties in bcc iron: Comparison of He–Fe potentials*, Philos. Mag. 90 (**7**–**8**), 935–944, 2010

[198] N Sasajima, T Matsui, S Furuno, K Hojou, and H Otsu, *Damage accumulation in Al2O3 during H2+ or He+ ion irradiation*, Nucl. Instruments Methods Phys. Res. Sect. B Beam Interact. with Mater. Atoms 148 (**1**–**4**), 745–751, 1999

[199] LL Bonilla, A Carpio, JC Neu, and WG Wolfer, *Kinetics of helium bubble formation in nuclear materials*, Phys. D Nonlinear Phenom. 222 (**1**–**2**), 131–140, 2006

Appendix 1

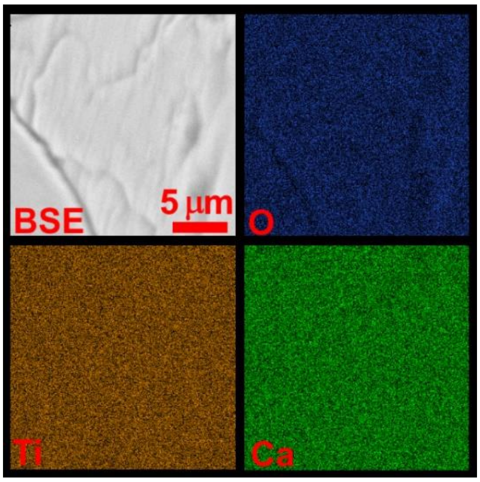

Figure A1.1 SEM micrograph and EDS map for the x = 0 sample, with oxygen, titanium and calcium donated in blue, yellow and green, respectively.

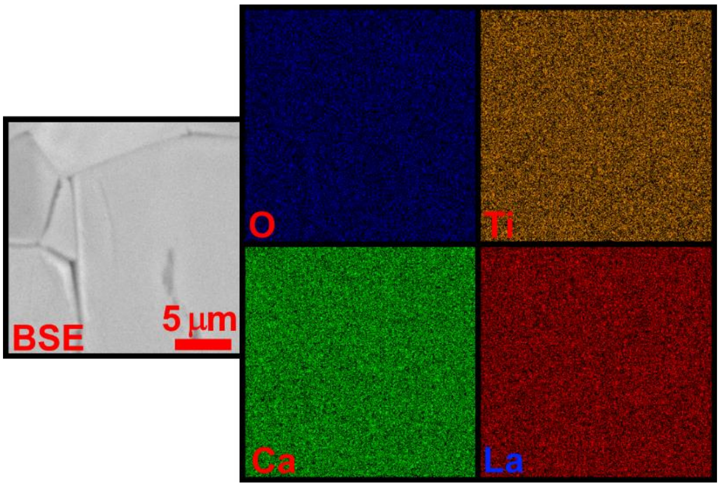

Figure A1.2 SEM micrograph and EDS map for the x = 0.4 sample, with oxygen, titanium, calcium and lanthanum donated in blue, yellow, green and red, respectively.

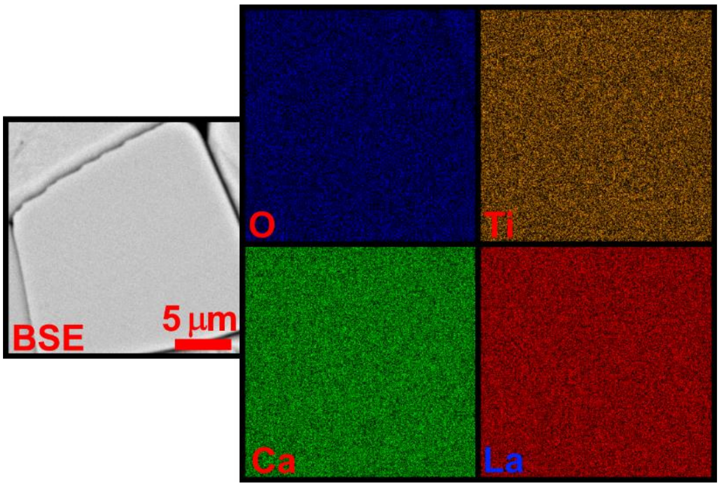

Figure A1.3 SEM micrograph and EDS map for the x = 0.2 sample, with oxygen, titanium, calcium and lanthanum donated in blue, yellow, green and red, respectively.

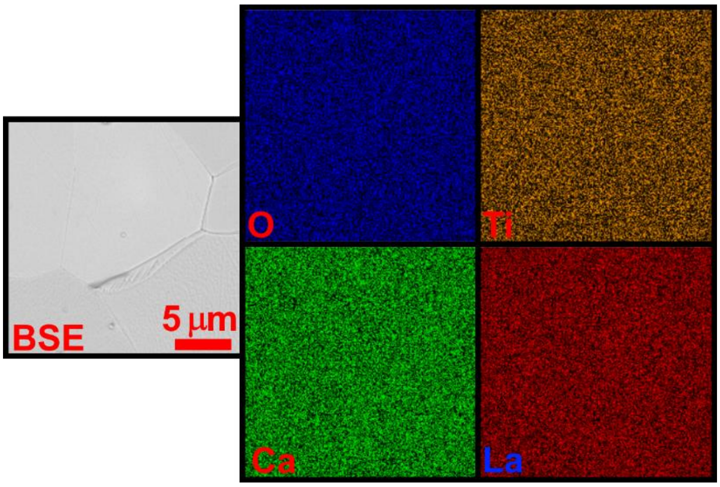

Figure A1.4 SEM micrograph and EDS map for the x = 0.6 sample, with oxygen, titanium, calcium and lanthanum donated in blue, yellow, green and red, respectively.

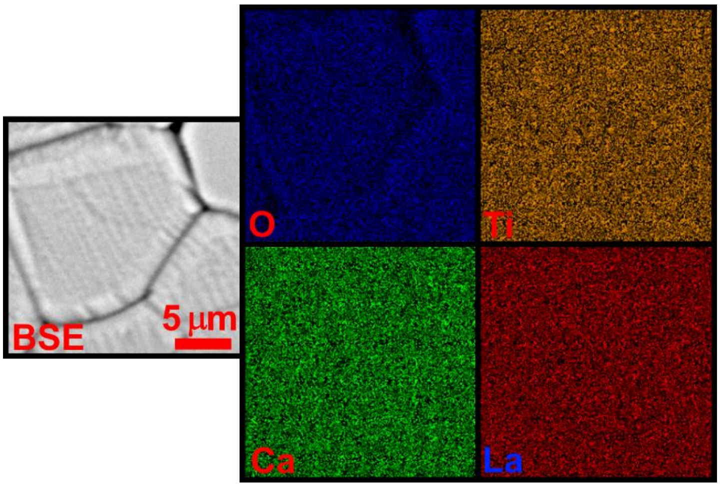

Figure A1.5 SEM micrograph and EDS map for the x = 0.7 sample, with oxygen, titanium, calcium and lanthanum donated in blue, yellow, green and red, respectively.

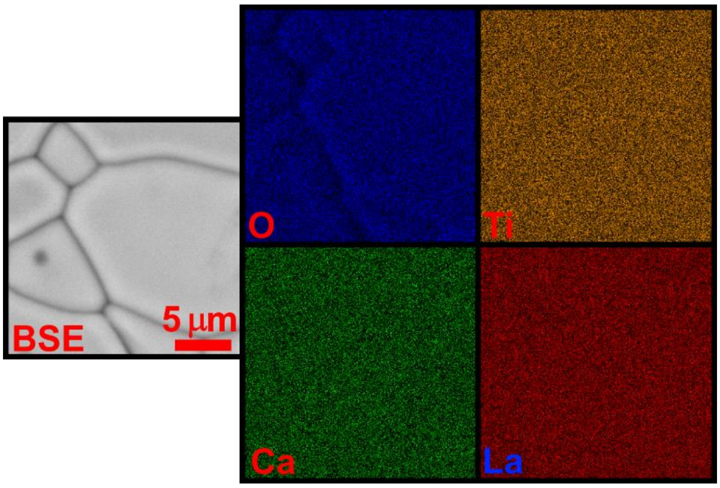

Figure A1.6 SEM micrograph and EDS map for the x = 0.9 sample, with oxygen, titanium, calcium and lanthanum donated in blue, yellow, green and red, respectively.

Appendix 2

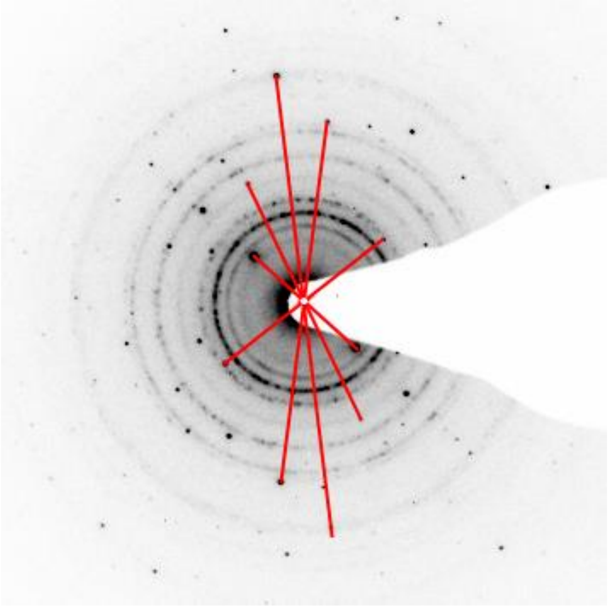

Figure A2.1 Identification of the centre point of the diffraction pattern taken from the x = 0.6 sample, shown in figure 6.4c.

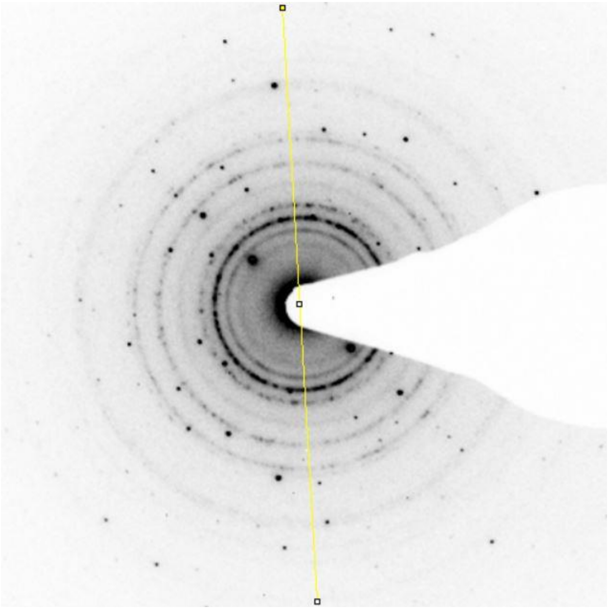

Figure A2.2 Example of a single linescan, preformed using the ImageJ software package, taken from the diffraction pattern from the x = 0.6 sample shown in figure 6.4c.

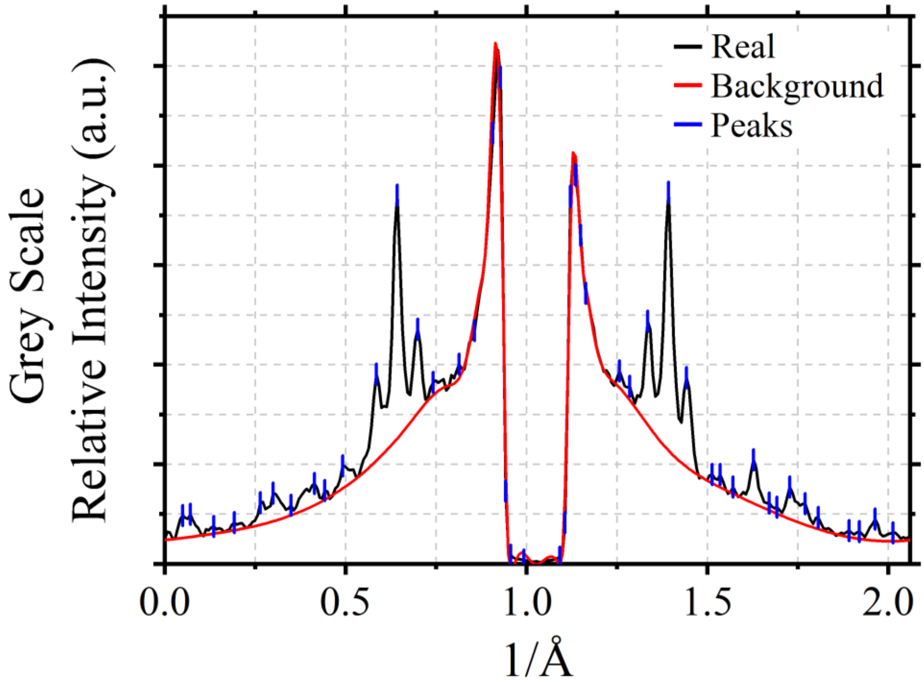

Figure A2.3 Background removal and peak identification of the combined linescan profiles taken from the x = 0.6 sample in figure 6.4c.

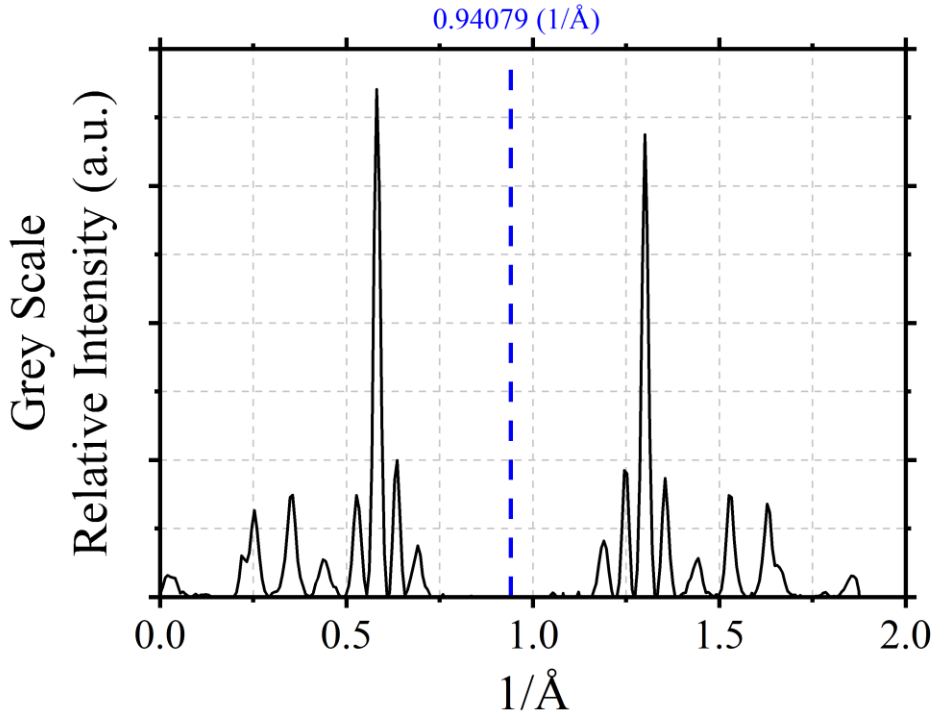

Figure A2.4 Identification of the centre point of the combined linescan profiles taken from the x = 0.6 sample in figure 6.4c.

Appendix 3

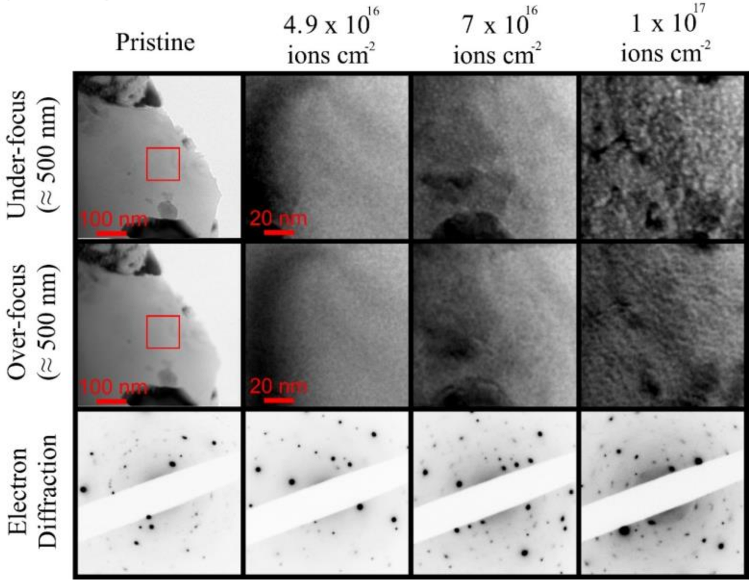

Figure A3.1 Bright field TEM micrographs and SAEDPs of the crushed grain x = 0.2 sample in the pristine and ion implanted at room temperature with 6 keV He^+ to fluences of 4.9 x 10^{16}, 7 x 10^{16} and 1 x 10^{17} ions cm^{-2}. Under- and over-focus images are defocused by ≈ 500 nm, respectively. Ion implanted micrographs are presented as magnifications of the region identified by the red box in the pristine micrographs to ease identification of bubble formation.

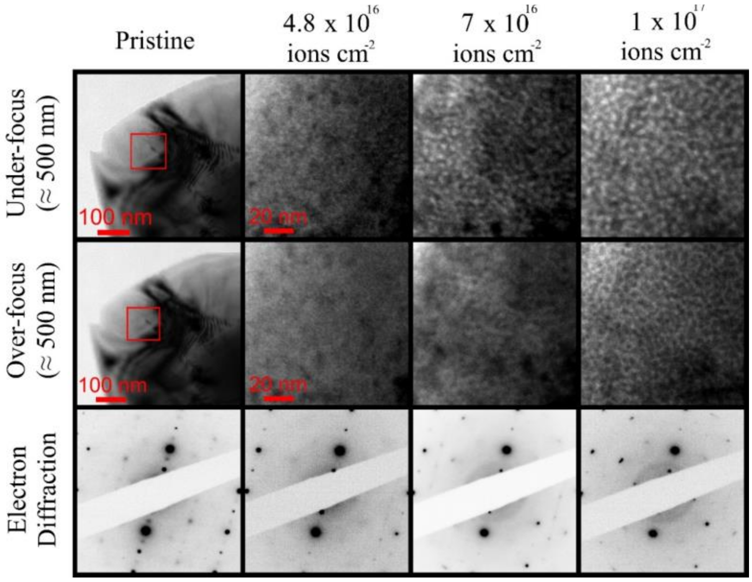

Figure A3.2 Bright field TEM micrographs and SAEDPs of the crushed grain x = 0.4 sample in the pristine and ion implanted at room temperature with 6 keV He^+ to fluences of 4.8 x 10^{16}, 7 x 10^{16} and 1 x 10^{17} ions cm^{-2}. Under- and over-focus images are defocused by ≈ 500 nm, respectively. Ion implanted micrographs are presented as magnifications of the region identified by the red box in the pristine micrographs to ease identification of bubble formation.

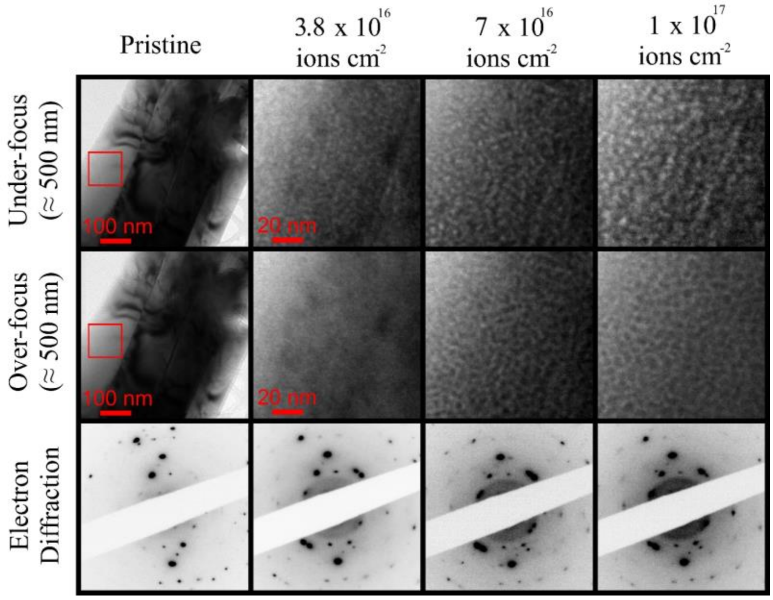

Figure A3.3 Bright field TEM micrographs and SAEDPs of the crushed grain x = 0.6 sample in the pristine and ion implanted at room temperature with 6 keV He$^+$ to fluences of 3.8 x 10^{16}, 7 x 10^{16} and 1 x 10^{17} ions cm^{-2}. Under- and over-focus images are defocused by ≈ 500 nm, respectively. Ion implanted micrographs are presented as magnifications of the region identified by the red box in the pristine micrographs to ease identification of bubble formation.

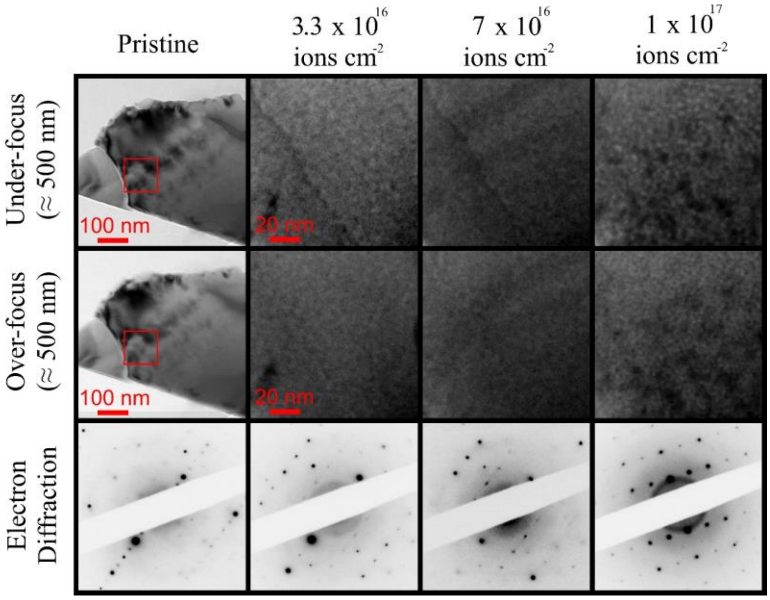

Figure A3.4 Bright field TEM micrographs and SAEDPs of the crushed grain x = 0.7 sample in the pristine and ion implanted at room temperature with 6 keV He$^+$ to fluences of 3.3 x 10^{16}, 7 x 10^{16} and 1 x 10^{17} ions cm^{-2}. Under- and over-focus images are defocused by ≈ 500 nm, respectively. Ion implanted micrographs are presented as magnifications of the region identified by the red box in the pristine micrographs to ease identification of bubble formation.

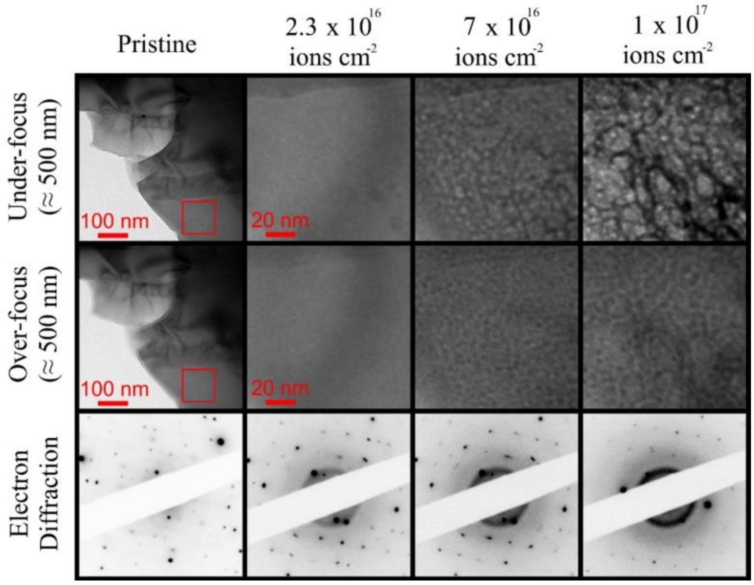

Figure A3.5 Bright field TEM micrographs and SAEDPs of the ion milled x = 0.2 sample in the pristine and ion implanted at room temperature with 6 keV He$^+$ to fluences of 4.9 x 10^{16}, 7 x 10^{16} and 1 x 10^{17} ions cm^{-2}. Under- and over-focus images are defocused by ≈ 500 nm, respectively. Ion implanted micrographs are presented as magnifications of the region identified by the red box in the pristine micrographs to ease identification of bubble formation.

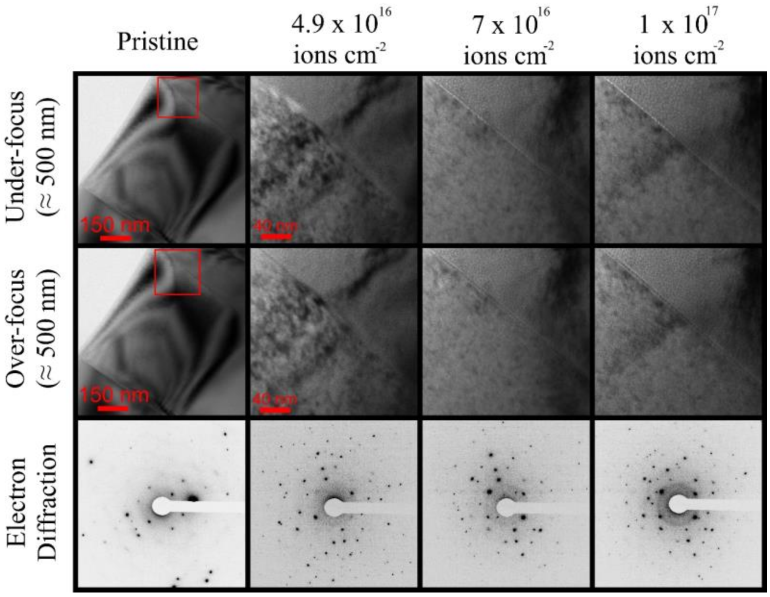

Figure A3.6 Bright field TEM micrographs and SAEDPs of the ion milled x = 0.2 sample in the pristine and ion implanted at room temperature with 6 keV He$^+$ to fluences of 4.9 x 10^{16}, 7 x 10^{16} and 1 x 10^{17} ions cm^{-2}. Under- and over-focus images are defocused by ≈ 500 nm, respectively. Ion implanted micrographs are presented as magnifications of the region identified by the red box in the pristine micrographs to ease identification of bubble formation.

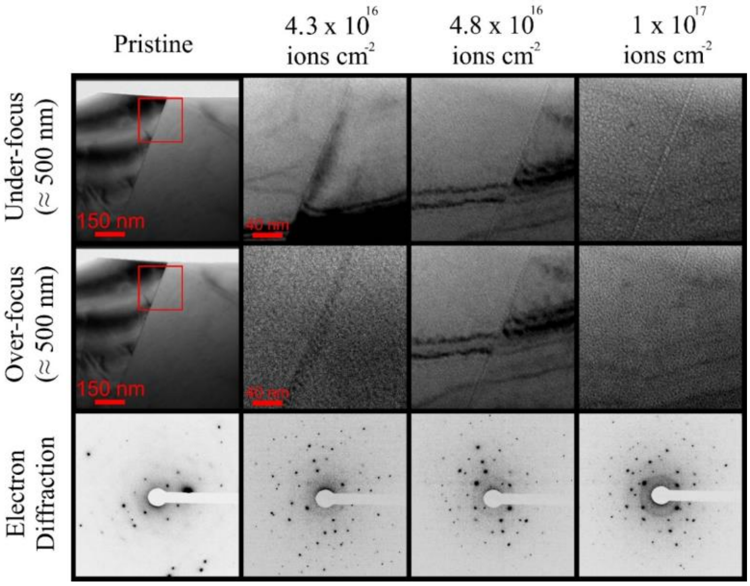

Figure A3.7 Bright field TEM micrographs and SAEDPs of the ion milled x = 0.6 sample in the pristine and ion implanted at room temperature with 6 keV He$^+$ to fluences of 3.8 x 10^{16}, 4.3 x 10^{16} and 1 x 10^{17} ions cm^{-2}. Under- and over-focus images are defocused by ≈ 500 nm, respectively. Ion implanted micrographs are presented as magnifications of the region identified by the red box in the pristine micrographs to ease identification of bubble formation.

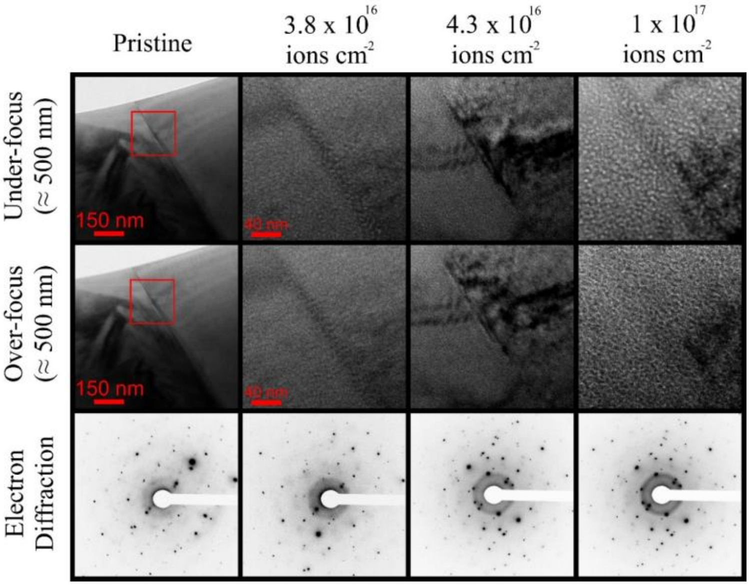

Figure A3.8 Bright field TEM micrographs and SAEDPs of the ion milled x = 0.4 sample in the pristine and ion implanted at room temperature with 6 keV He$^+$ to fluences of 4.3 x 10^{16}, 4.8 x 10^{16} and 1 x 10^{17} ions cm^{-2}. Under- and over-focus images are defocused by ≈ 500 nm, respectively. Ion implanted micrographs are presented as magnifications of the region identified by the red box in the pristine micrographs to ease identification of bubble formation.

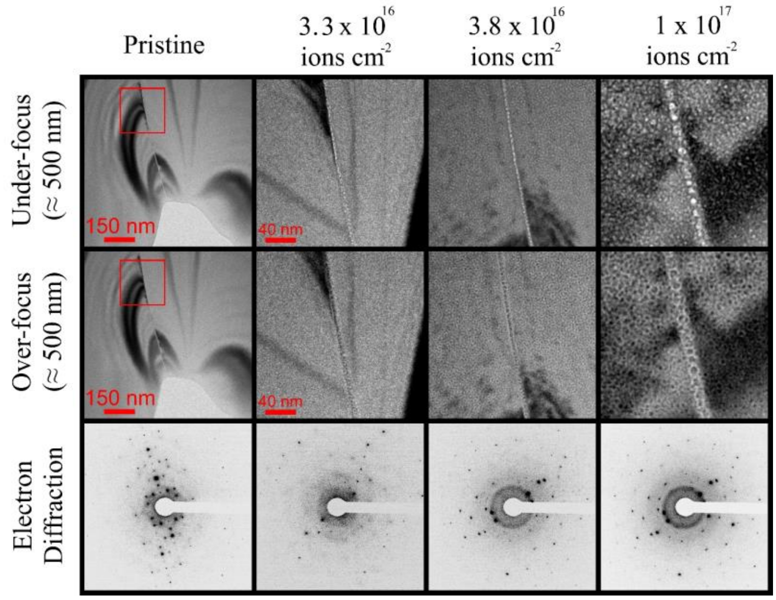

Figure A3.9 Bright field TEM micrographs and SAEDPs of the ion milled x = 0.7 sample in the pristine and ion implanted at room temperature with 6 keV He^+ to fluences of 3.3 x 10^{16}, 3.8 x 10^{16} and 1 x 10^{17} ions cm^{-2}. Under- and over-focus images are defocused by ≈ 500 nm, respectively. Ion implanted micrographs are presented as magnifications of the region identified by the red box in the pristine micrographs to ease identification of bubble formation.

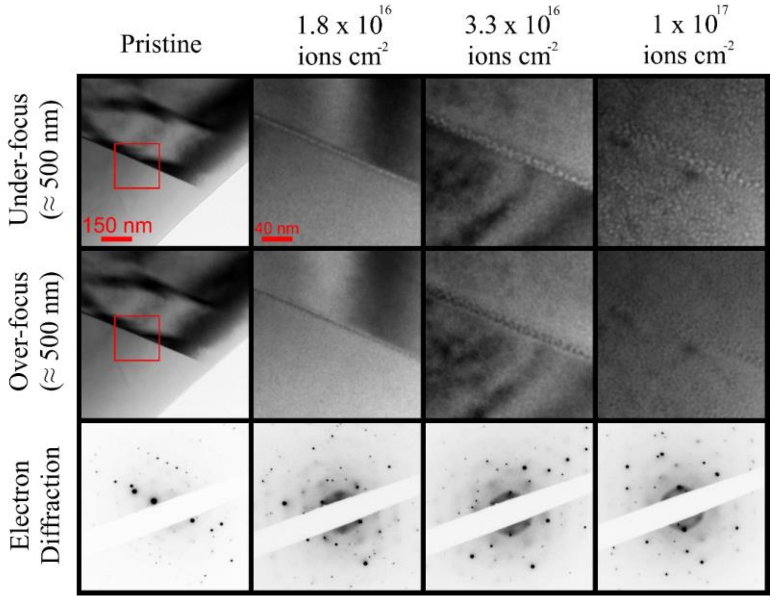

Figure A3.10 Bright field TEM micrographs and SAEDPs of the ion milled x = 0.9 sample in the pristine and ion implanted at room temperature with 6 keV He^+ to fluences of 1.8 x 10^{16}, 3.3 x 10^{16} and 1 x 10^{17} ions cm^{-2}. Under- and over-focus images are defocused by ≈ 500 nm, respectively. Ion implanted micrographs are presented as magnifications of the region identified by the red box in the pristine micrographs to ease identification of bubble formation.